Application of Lead-Halide Perovskite Nanocrystals in Light-Emitting Diodes

Dissertation

zur Erlangung des akademischen Grades
Doctor rerum naturalium (Dr. rer. nat.)

eingereicht an der

Mathematisch-Naturwissenschaftlich-Technischen Fakultät
der Universität Augsburg

von

Tassilo Naujoks

Augsburg, August 2023

Universität
Augsburg
University

Erstgutachter: Prof. Dr. Wolfgang Brütting
Zweitgutachter: Prof. Dr. Henning Höppe

Tag der mündlichen Prüfung: 14.12.2023

Contents

1. Introduction

There was light. Ever since humanity has learned how to control fire, further leaps in evolution have been enabled not only because of the heat it provides but also its light emission.[1] The sole source of artificial light for millennia had been a flame. With its inherent danger to ignite surroundings, the brightness and usability had been very limited. The invention of a light-bulb marked the first major step towards disentangling light from a hazardous chemical reaction. The light source's brightness as well as its safety has been elevated to unprecedented levels from this day forth. However, the complete disentanglement of heat and light had not yet been fully achieved until the era of light-emitting diodes (LEDs) and gas-discharge lamps (e.g. neon lamps) began. The emitted spectrum is narrower than that of an incandescent light and lacks the warming infrared rays. The narrowing can be designed to an extent that pure, single coloured light is emitted. Compared to the bulky fluorescent lamps the LEDs feature a widely more scalable form factor. Recent innovation has made it possible to construct devices as small as a few micrometers, especially LEDs.[2] Flat screens with high pixel densities have revolutionised everyday life. Towards bendable, foldable, stretchable and transparent screens with bright vibrant colours, a variety of solutions have been researched on, with all having their respective advantages and drawbacks. While classical semiconductor based LED are most suited for point light sources, their relatively high cost render them less favourable for large area application.[2] The organic LED (OLED) excels at this point with less energy-intense refinement and thus manufacturing cost for industrial production.[3] These costs are particularly low, when the device can be fabricated from solution. For example ink-jet printed LED panels have the potential to drop in price comparable to any other printed medium.[4] Inorganic semiconductors generally lack the flexibility and solubility to be handled in solution or on flexible substrates. Then again, soft crystals such as lead halide perovskites (LHPs) show decent solubility, which can be used for solution-processed optoelectronic devices. The LHPs have already proven their potential by revolutionising the research on photovoltaic devices leading to a potential dethroning of silicon in levelised cost of electricity (LCOE).[5,6] With that, a significant fraction of the silicon dominant market share in photovoltaic modules may be replaced by the perovskite technology in the near future. Also, the LHPs can be prepared in the form of nanocrystals (NCs) for achieving extraordinarily efficient light-emission.[7,8] However, the application of the LHPs for bright LEDs has still not lead to a comparable break-through yet. Creating perovskite light-emitting diodes (PeLEDs) featuring LHPs face some challenges and new phenomena that shall be elaborated in the following. The NCs are subject to an intrinsic instability, which propagates to the operational lifetime of resulting PeLEDs. Additionally, the deposition of NCs from solution has implications on the other functional layers of the PeLED. After detailing the theoretical issues with respect to the materials' properties, three fundamentally different approaches to achieve enhanced PeLEDs are provided. A colour-conversion approach proves to be promising by avoiding any electrical and thermal stress on the NCs. Consequently, the devices' performance is not limited by the perovskite material but the driving LED and the colour-conversion process itself. Apart from this only-optical application, directly driven NC emission is facilitated by either doping them with an organic alkaline salt or exchanging the molecules on the surface with functionalised ones, which prove to enhance stability and/or charge injection of such. Finally, a method for determining such charge carrier imbalances by investigating displacement currents on half-capacitive devices is explained. In total, this work elucidates the first steps to create and enhance prototypical NC based PeLEDs. Even though significant advancements can be reported, the presented PeLEDs are still far from being competitive in context of application in commercial display technologies. However, the astonishing rate of advancement may render them relevant in the years to come if the detailed issues can be fully addressed. Herein, the perovskite's fundamental properties allow for PeLEDs exceeding some of the limits set for conventional LEDs. A brief overview of such performance limits shall also be given in this work.

2. Properties of Lead-Halide Perovskite Nanocrystal Emitters

Essential for any high level application, that is, a photovoltaic or electroluminescent device is to get an understanding of its constituents. Certainly, for an LED of any kind the light-emitting material is of high interest; so it is for a PeLED. Even though there are less toxic, lead-free perovskites for optoelectronic applications, due to their enhanced stability and for the purpose of unravelling the fundamental scientific challenges with these materials, this work focuses solely on LHPs. Firstly, the basic properties are introduced. At this point, the peculiarities rendering this class of material so unique are elucidated. With a detailed understanding of the bulk material, the implications of down-sizing to the nanoscale, by manufacturing the LHP as tiny colloids, are explained.

2.1. Physics and Chemistry of Lead-Halide Perovskites

Perovskite, named after L. A. Perovski, is the retained name of the mineral $CaTiO_3$. However, since its discovery in the early 19th century many other minerals with similar crystal structure have been found. It features a mixed fcc arrangement of three O^{2-} anions and a cation, A. Thereby six oxide anions surround an additional cation, B, as an octahedron. Put another way, the structure can also be described as ABO_3.[9] Ever since, the term perovskite has been used more generally for the crystal structure rather than for the material, that is calcium titanate, only. But it was not until 1986, that a suitable application for the material has been found. The first discovery of a high temperature superconductor, attributed to Bednorz and Müller [10] with a Nobel prize the year after, was of such perovskite structure. In context of optoelectronics the perovskites have not emerged, however, until Kojima et al. [11] reported dye-sensitised solar cells based on hybrid organic-lead halide perovskites.

With that, the definition of a perovskite has been even further generalised to ABX_3 where X is an anion, here a halide. Even though all original ions have been replaced, a perovskite structure is still established. That is because their Goldschmidt's tolerance factor, t, remains in the range between 0.75 and 1, where one denotes the ideal cubic case.[12] This tolerance factor is determined with the ionic radii denoted by $r_{\square}$, where $\square$ = A, B or X, with the equation:[12]

$$t = \frac{r_{\mathrm{A}} + r_{\mathrm{X}}}{\sqrt{2} \cdot \left(r_{\mathrm{B}} + r_{\mathrm{X}} \right)}. \tag{2.1}$$

With the ionic radii at given oxidation states of, e.g., r_{Cs} = 181 pm, r_{Pb} = 133 pm and r_{Br} = 182 pm,[13] t equals 0.81 which is not optimal. Therefore an orthorhombic perovskite structure is correctly predicted for $CsPbBr_3$ (cf. figure 2.1 a)), even though this factor may have limited validity.[14]

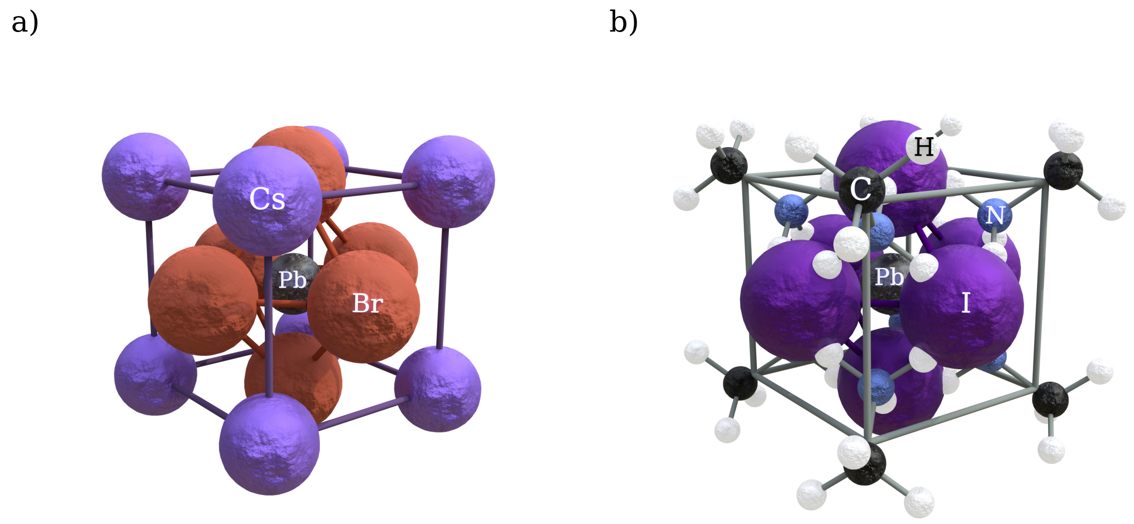

Figure 2.1.: Illustration for visualising the structure of LHPs. The halides (X^-) form an octahedron around a Pb^{2+} ion. Monovalent A-cations fill the gap and are of importance for structural integrity. $CsPbBr_3$ is shown in a), while $MAPbI_3$ is depicted in b).[S.1, S.2]

While the structure may be comparable to the oxide perovskite the bond character of the compounds differ significantly. When comparing $CaTiO_3$ with $CsPbBr_3$, the former originates from real ionic bonds, as indicated by the high disparity in electronegativity between oxygen and the metals, on Pauling scale 2.4 resp. 1.9. However in case of $CsPbBr_3$, for caesium and bromine this difference may be similar, 2.2, but for lead and bromine it is as low as 1.1.[15] This very weak ionic or even polar covalent feature is also known for silver halides.[16] Likewise, as one of the few metal halides, the solubility in water is low and the melting points are below 500 °C (cf. TiO_2 at 1843 °C).[17–19] Furthermore, properties from the silver halides that were utilised in analogous photography, like the high Frenkel defect density as well as their sensitivity to light[20] are indeed propagated to the LHPs.[21] In fact, the similarity to silver is used in pursuance for lead-free perovskite applications. However, silver has incompatible oxidation states, so a blend with bismuth is used, resulting in $CsAgBiX_3$ perovskites.[22] Apparently, the soft crystal lattice allows for ion blends to be incorporated. Also, entire small molecules like the methyl ammonium can be used to compensate for the bigger iodine ion in e.g. $MAPbI_3$ (cf. figure 2.1 b)).

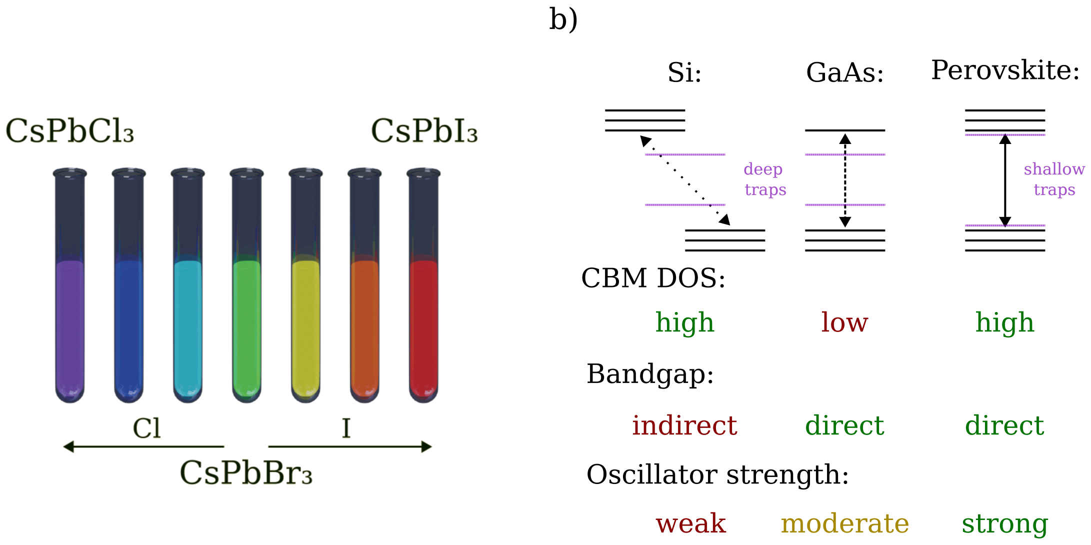

Figure 2.2.: a) Illustration for visualising the influence of the halide composition on the colour of the LHPs. Higher chlorine content results in a blue-shift, while higher iodine content shifts towards red colours.[S.3] b) Sketch for explaining the difference in oscillator strength between different semiconductor material classes. The perovskite combines high DOS with a direct bandgap for highest transition rates. Additionally, the trap states are close to the band edges rendering them more defect tolerant.[S.4]

In comparison to other established semiconductors, LHPs feature a unique combination of properties which renders them especially interesting for optoelectronic applications. Figure 2.2 b) provides an overview of the key features enabling a high oscillator strength and consequently light-emission or absorption. These are a high density of states (DOS) around the band edges and the band-gap type. Additionally, purple lines indicate the position of trap states, originating from defects, that impair the optical quantum yield. Silicon as an indirect semiconductor has a comparably weak optical transition probability. Even though it has a decent density of states, its indirect bandgap requires a considerable momentum change for the optical excitation resp. relaxation reducing the process likeliness. The relatively thick solar panels ($d_{Si} \approx 150\,\mu m$) are a real-life proof for this circumstance. Considering the direct band-gap semi-conductor GaAs the absorber thickness can be reduced to less than a few micrometers.[23] However, its conduction band edge is not as densely populated with states as for silicon. Overall, the LHPs combine a

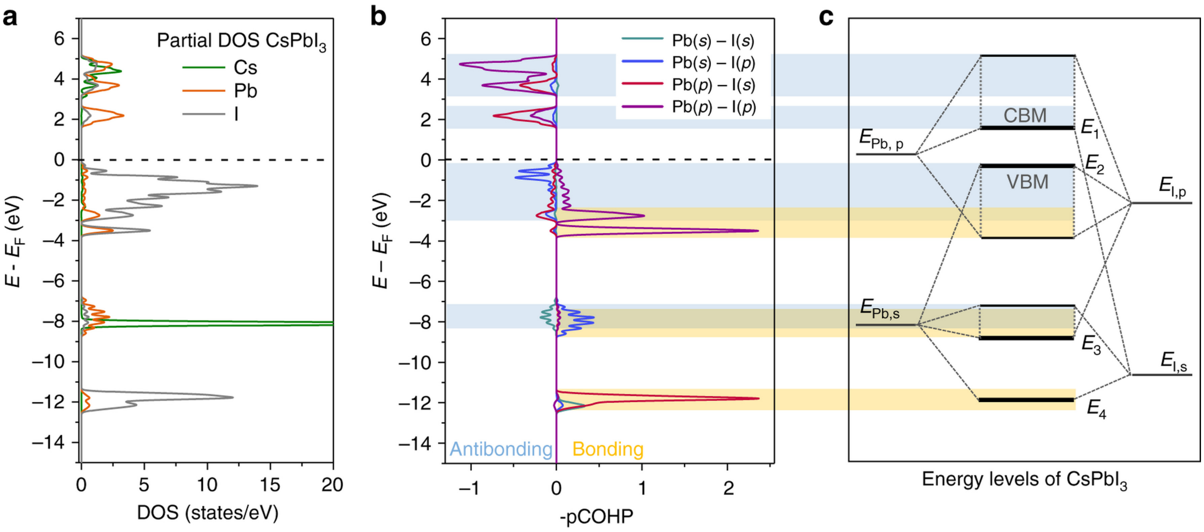

Figure 2.3.: Contributions to the energy bands of $CsPbI_3$ arising from the resp. original orbitals. With a) the calculated partial DOS for the Cs, Pb, and I atoms. A positive (negative) sign denotes a bonding (anti-bonding) feature in the orbital-resolved COHP, b). Which atomic orbitals are involved in the bonds (anti-bonds) are shown by the line colours. c) A schematic depiction of energy levels taken from the COHP investigation. Bonding connections are highlighted in yellow, and anti-bonding ones in blue. Reproduced under CC BY 4.0 from reference 25.[S.5]

high DOS with a direct band gap, predicting a strong optical oscillator strength.[24]

The direct band-gap and the high DOS can be explained by investigating the constituents and their interaction upon forming an ABX_3 perovskite. While the A-site cation has been found to show minor primary influence on the DOS, its size appears to cause lattice distortions mainly altering the extent of the B-X interaction.[25, 26] The B metal cation and the respective halides are ruling the DOS. Consequently, exchanging the lead with tin or silver-bismuth has serious implications on it. Although highly interesting, the scope of this work restricts considerations on lead; so only the influence of the halides are key to the optoelectronic properties of the LHPs. Increasing electronegativity and concurrently decreasing size of the anion leads to major increases in the band-gap of the material. As depicted in figure 2.2 a), the luminescence colour is shifted over the entire visible spectrum. Hence, for triple chlorine LHP violet, near-ultra-violet (UV) and for the triple iodine deep-red, near-infrared (NIR) light is emitted. The tight-binding model analysis on $CsPbX_3$, that is with various halides X, performed by Tao et al. [25] revealed that the contributions of the halides to the DOS, and by implication its colour resp. band-gap, show a similar distribution yet its position on the energy scale changes. Thus, it is sufficient to discuss the nature of the conduction band minimum (CBM) and valence band maximum (VBM) by considering one example, such as the $CsPbI_3$, as shown in figure 2.3. Note that for illustrational purposes the VBM position is set to zero. The calculated DOS (cf. figure 2.3 a)) reveals the already mentioned low influence by the caesium on the states around the band-gap edges. Furthermore, the iodine features high contributions to the VBM and still considerable impact of the CBM. In contrast, lead provides a major part of the CBM's states and a minor amount of the VBM's. A deeper understanding to the origin of these states is provided by the crystal orbital hamiltonian population (COHP) analysis. It is presented in figure 2.3 b) . The atomic orbitals giving rise to the DOS distribution of the compound can be identified.[25, 27] In this context, only the four orbital hybridisations with the highest magnitude are shown. Lead's 6p and 6s orbitals hybridise with iodine's 5p and 5s orbitals. Evidently, the VBM is dominated by the anti-bonding Pb-6s and I-5p combination, while for the CBM it is the also anti-bonding Pb-6p and I-5s hybrid. Consequently, with the partial DOS, the VBM prevalently originates from the I-5p and the CBM from the Pb-6p orbital.[25, 28, 29] Herein, the optical transition between these state is not forbidden, as there is, among other effects, a significant spin-orbit coupling. Moreover, a brief wave function symmetry analysis is given in the next section (section 2.2.1 in context of figure 2.4). Anyhow, the optical transition is expected to be along the B-X axis. As a consequence, considering a cubic lattice a direct band-gap is calculated for LHPs (cf. figure 2.4 b)).[25, 28, 29]

Apart from the mentioned theoretical advantages, there is also practical issues to address. By the nature of the soft bond between metal and the halide, the very reason why the silver halide photography worked in the first place – a high Frenkel defect density,[16] is to be expected within LHPs, too. In contrast, silicon as well as gallium arsenide are manufactured ultra-defect free and they remain in that state unless under e.g. mechanical stress. However, it is not to the disadvantage to the LHPs. Unlike the conventional semiconductors, a defect is not severely harming performance of it. That originates in the nature of the traps which are, because of their low activation energy, located not very deep within the band-gap, also called shallow traps.[24, 30, 31] Surprisingly, the high defect affinity of LHPs is more like its strength rather than its weakness. This enables the processing from solution with less pure ingredients.

Anyway, the softness of the LHPs comes also with new major issues, which the conventional semiconductors cannot exhibit because of their rigidity or robustness. For example, environmental influence by water and oxygen leave latter mostly intact. In contrast, the LHPs feature multiple phase transitions at low temperatures, these are severely altered by water. The oxidation of the LHPs is also an issue, since the halides are easily removed, thus replaced by oxygen. The facile halide migration within an application also severely harms any of the adjacent materials, which are usually not really resistant to it. Not only the halides may migrate. For example it has been reported that methylammonium (MA), the cation of e.g. $MAPbI_3$, irreversibly gases out as methylamine and the respective halide acid. Moreover, a light-induced direct reduction of lead accompanied by an elemental halide gas release is also observed.[32] Water, oxygen and light exposure accelerate most of the degradation processes. As this work is also going to reveal, strong electric fields also degrade LHPs significantly.

Summarising one can say, that the perovskites, especially LHPs, feature ideal properties for the application in optoelectronic applications. Subsequently, remarkable photovoltaic devices have been achieved. However, along with the novel material and its promising peculiarities comes its environmental and intrinsic chemical susceptibility.

2.2. Implications of Downsizing to Nanocrystals

Some of the aforementioned issues can be avoided by processing the LHPs as nanocrystals (NCs). By transferring the system to the nanoscale the surfaces gain importance while bulk properties lose significance. Upon shrinking the LHPs to particles with just a few tens of unit cells edge length, the chemistry on the surface becomes relevant for the confinement of the ions as well as excitons resulting in quantum confinement. This section will provide an overview of the important differences between NCs and the bulk state of a LHP.

In general, a LHP can be easily synthesised with precursor substances of AX and PbX_2. Thus, in case of e.g. $CsPbBr_3$:

$$\mathrm{CsBr} + \mathrm{PbBr_2} \rightarrow \mathrm{CsPbBr_3}. \tag{2.2}$$

LHPs itself are soluble in polar, aprotic solvents such as dimethylformamide (DMF) or dimethylsulfoxide (DMSO). Thus, common practice to grow crystals from solution is to supersaturate it. This can be achieved by either using anti-solvents, decreasing temperature or drying off the liquid.[33] Growing a perfect single crystal may be an art in itself, but so is the growth of stable, monodisperse NCs. There are, among others, two established ways of LHP-NC synthesis, which is the ligand assisted reprecipitation (LARP) and the hot-injection. LARP takes place with room-temperature solvents where a tiny amount of polar precursor solution is gradually dropped into an apolar solvent, such as toluene. The solubility imbalance will lead to precipitation of crystals whose size is ruled by the solvents.[34, 35] The subsequent addition of oleic acid and/or oleylamine stabilises the freshly synthesised NCs. In contrast to that, the hot-injection procedure uses warm solvents to keep the precursors in a less polar solvent and induces the precipitation by injecting a small amount of polar anti-solvent as crystallisation seed.[36] More advanced, recent techniques feature a quick cooling in an ice-bath right after injection of the anti-solvent.[7] Furthermore, the AX precursor or ligand-halide can also be solved directly in latter prior to injection.[37] At this point, the temperature of the hot precursor solution can be used to control the NC size and shape. Cubical and spherical shapes can be synthesised.[7, 30] Also, even entirely different dimensionalities, such as nanoplatelets and nanowires, can be engineered.[38, 39]

2.2.1. Changes to Excitonic Properties

Bulk semiconductors in general have quasi-free, Wannier-Mott excitons. Their binding energy is in the order of the thermal energy at room-temperature; $\mathrm{k_B T} \approx 25\,\mathrm{meV}$. Not only silicon or germanium fulfil this condition but also LHPs.[40, 41] However, for any semiconductor the situation changes if the exciton is spatially confined. The hamiltonian, $\mathcal{H}$, of a free particle with mass m confined in a cube-shaped potential, $\mathcal{V}$, with edge length a, that is, a 3-D quantum well is given with the Laplace operator, Δ, by:

$$\mathcal{H} = -\frac{\hbar^2}{2m}\Delta + \mathcal{V}, \tag{2.3}$$

$$\mathcal{V} = \begin{cases} 0, & \text{if } (x, y, z) \in [0, a]^3. \\ \infty, & \text{else.} \end{cases} \tag{2.4}$$

Ultimately, the lowest eigenstate, that is energy being a solution to the resp. Schrödinger equation yields (cf. A.2.5):

$$\mathrm{E_0} = \frac{3\hbar^2\pi^2}{2ma^2}. \tag{2.5}$$

A very similar equation has been published for spherical potentials, with radius r:[42–44]

$$\mathrm{E_0} = \frac{\hbar^2\pi^2}{2mr^2}. \tag{2.6}$$

Apparently, at a certain size any shape of NC will induce a significant energy to a particle such as electrons. Consequently, after Brus [42], also an exciton will receive this confinement energy. Furthermore, the Coulomb energy of an exciton will also change if the electron-hole distance is forced to be smaller then the Bohr radius (a_B). In these cases, the excitons are considered to be in a 'strong confinement' regime. Anyhow, there are NC sizes, where the quantum confinement effects become already relevant, but the Bohr radius is still distinctly smaller than the particle size, referred to as 'weak confinement' regime.[45] Excitons within these NCs behave hydrogen-like, to put it another way, their energy obeys Coulomb's law, where only the permittivities and effective masses differ from the hydrogen system. The exciton Bohr radii within LHPs are around 3-4 nm (values for $\mathrm{CsPbX_3}$).[46, S.7] Therefore, perovskite nanocrystals (PNCs) sized bigger than 10 nm, which are the focus of this work (cf. figure 2.4 d)), can be categorised in the weak confinement regime.[29, 47]

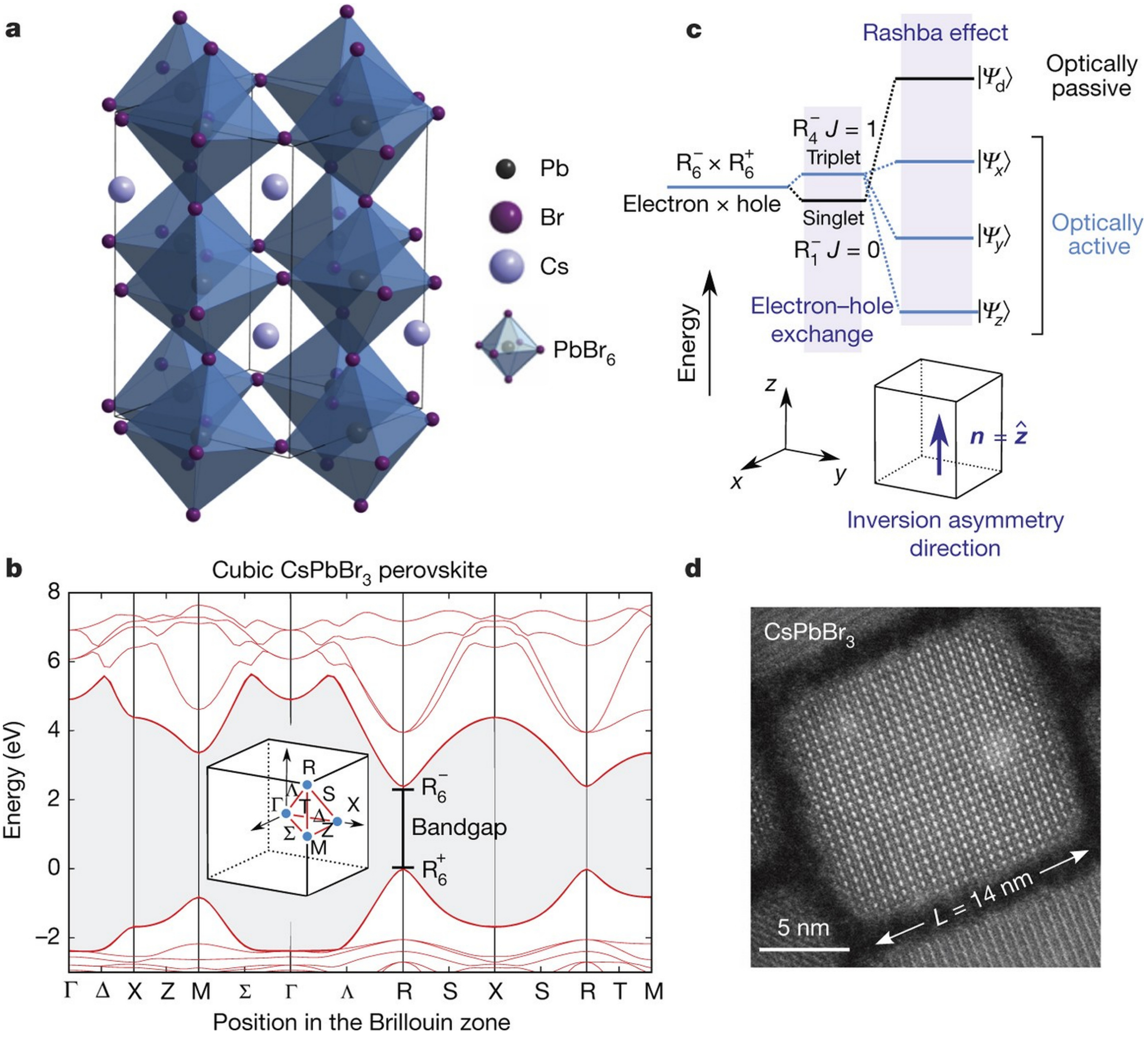

Figure 2.4.: The crystal structure of $CsPbBr_3$, a), is not perfectly cubic, but orthorhombic caused by the $PbBr_6$ octahedron's tilt within the unit cell (indicated as a frame). The calculated band structure of cubic $CsPbBr_3$ perovskite is shown in b). The first Brillouin zone of the cubic crystal lattice is presented as inset. At the R point of the band structure the electronic band gap is located. The valence (conduction) band maximum (minimum) exhibits R_6^+(R_6^-) symmetry. c) shows the derived fine structure of the band-edge exciton considering short-range electron–hole exchange (middle) while factoring in the Rashba effect (right) under orthorhombic symmetry. The excitonic states are separated into three bright states with transition dipoles oriented along the orthorhombic symmetry axes (x, y and z) and a higher-energy dark state ('d') by the Rashba effect. The energetic order of the three lowest sublevels is determined by the lattice strain. d) TEM image of a $CsPbBr_3$-NC with a lateral dimension of 14 nm. Reproduced with permission from reference 29.[S.6]

In any case, with this additional confinement energy contribution the exciton becomes localised, and is more of Frenkel type. Hence, the selection rules apply for any optical transitions. While in case of atoms or small molecules, the angular momentum change required for a photon to be emitted is either fulfilled by a spin-flip (e.g. $\uparrow \rightarrow \downarrow$) or a change of orbital symmetry (e.g. $s \rightarrow p$). The former process requires considerable spin-orbit coupling or an interaction with a third particle and is therefore often referred as 'forbidden' transition. Anyway, this usually leads to the simple picture of having three (<u>triple</u>t) forbidden and one (<u>single</u>t) allowed transition, as observed in organic semiconductors.[48, 49] However, in case of NCs, especially if they consist of heavy metal atoms (e.g. lead, caesium), there is a significant spin-orbit coupling involved which blurs the lines between orbital momentum and spin. In case of $CsPbBr_3$-PNCs, Even et al. [50] showed that the VBM inherits the radial symmetry from lead's 6s orbitals. The halide's p-orbitals are not breaking this symmetry since they are centrosymmetrically arranged in an octahedron around the centre of the Brillouin zone (cf. figure 2.4 a) and b)). On the other hand, they also showed that the CBM has an anisotropy arising from the Pb-6p orbitals. Since the VBM has a vanishing orbital momentum there is no observable spin-orbit coupling, while for the CBM it is very strong.[50] Comparing to many other semiconductors, there the situation is flipped (e.g. GaAs, CdSe, InP), here the VBM shows the known band-splitting into light, heavy and split-off hole dispersion. Actually, for LHPs the spin-orbit coupling dominates the band-structure of the conduction band entirely so that the dispersion around the CBM ultimately arises from a parabolic, twofold degenerate split-off state (total angular momentum $J = \pm 1/2$).[29, 50] Finally, an R^6 symmetry is expected for both of the band edges of a cubic $CsPbBr_3$-NC. By implication, two VBM states combining with two of the CBM lead to the formation of three triplet ($J = 1$) and one singlet ($J = 0$) state. However, unlike the case for organic semiconductors, the singlet transition is not permitted, as the required total angular momentum does not change by ± 1. These selection rules by symmetry observations are confirmed by respective calculations by Becker et al. [29], which also verify that indeed the triplet states are optically active. Moreover, with the calculation at hand, the energy splitting between singlet and triplet is determined to be negative rendering the singlet state the lowest. Anyway, when considering the Rashba effect, the distortions by having an orthorhombic crystal lattice instead (as in a real $CsPbBr_3$ crystal) rearranges the fine structure completely so that the triplet states are finally predicted to be the lowest state and optically active (cf. figure 2.4 c)).

For the efficient application in an LED it is generally important to have the lowest state at the CBM to be optically active, but in this case the energy splitting between the lowest optical states, that is e.g. singlet-triplet, is below 3 meV,[29, 46, 47] which makes all states interchangeable at room temperature. While that may be true for the $CsPbBr_3$-PNCs, the organic perovskite such as $MAPbI_3$ exhibits a splitting of less than 15 meV.[51] Further decreasing dimensions will lead to relevant splittings as high as 32 meV for nanoplatelets.[46] Moreover, Qin et al. [52] showed that if combining PNCs with organic semiconductors their triplet levels have to be considered, since an exciton may be trapped in such an optically passive triplet state. This issue is discussed in context of chapter 3 and 7.

2.2.2. Defect Management and Passivation with Ligand Chemistry

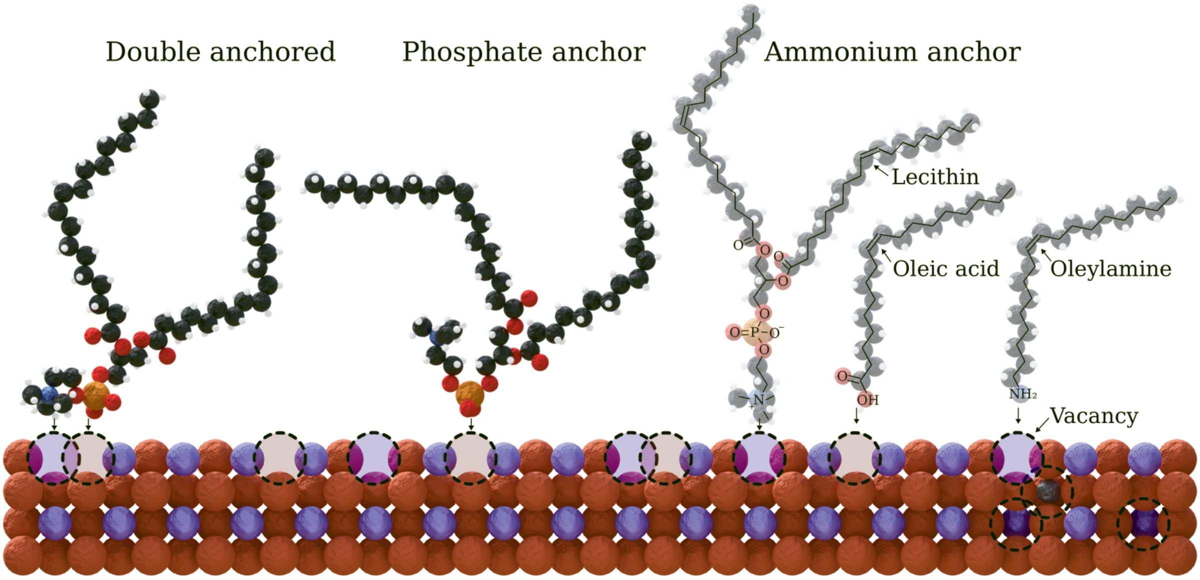

Figure 2.5.: Ligand attachment scheme with (left to right) lecithin, oleic acid and oleylamine. The purple, brick-red and gray balls represent Cs^+, $Br^-$and Pb^{2+} respectively. White, black indicate hydrogen and carbon, while oxygen, nitrogen and phosphor are depicted in pure red, blue and orange. The dashed circles highlight ion defects in the crystal surface. Some of them are passivated by the ligands where oleic acid binds to a bromine vacancy, oleylamine to a caesium vacancy and lecithin to either one or both at the same time.[S.8]

Certainly, the band-structure of LHP-NCs shows novel, unprecedented properties, which implies remarkable superior features to the conventional semiconductor materials. With these ideal theoretical preconditions processing and maintaining LHPs with retained attributes poses a major challenge. Since for NCs a high quantity of unit cells are on the surface, it is of uppermost importance to avoid and/or passivate the surface defects.

For LHP-NCs the use of ligands on the surface is essential, even if the synthesis yielded perfect defect-free particles. That is because of the soft nature of the material itself, defects can and are induced at any time. Additionally, the particles have to be made soluble and since polar solvents will disintegrate or enable further growth of the NCs they are processed in apolar solvents. As already mentioned while detailing the synthesis above, aliphatic molecules like oleic acid or oleylamine can be used for this purpose. The molecules are depicted in figure 2.5. They are drawn at a spot where they would attach to the surface of a PNC. At a vacancy of the A cation, that is caesium, the positive oleylammonium can attach. Opposed to that, the negative carboxylate group of the oleic acid may bind to a halide vacancy, in case of $CsPbBr_3$ bromine.

Depending on the synthesis the PNC surface can be terminated by an AX (CsBr) or BX_2 ($PbBr_2$) plane.[53] For example, a synthesis with excess CsBr will result in a termination layer as shown in figure 2.5. Synthesis of PNCs with PbX_2 surface-termination are mostly avoided, since the inherently broken PbX_6 octahedra have stronger impact on the integrity of the crystal.[53] The AX terminated LHP-PNCs are considered in this work. For them various post-synthetic treatments with the respective ligand salts may leave the surface more halide or more cation abundant. Finally, the quality of PNCs, benchmarked by photoluminescent quantum yield (PLQY), is not controlled by the amount or the type of defects, but rather the adequate stoichiometrically correct passivation of such. Surely, the interplay of oleic acid, oleylamine and the PNC is a very delicate balance to tare because the binding of the respective groups to the PNCs is not very strong. Anchoring moieties, such as thiols, sulphates, phosphates, tertiary amines and many more are found to have stronger binding to a LHP surface.[54] Even double anchor groups are explored. Figure 2.5 features such a double anchor group on the centre to left; a lecithin molecule has a phosphate as well as a trimethylammonium group, which has the potential to passivate a A, X or both (from right to left in fig. 2.5) vacancies.

Especially when considering the bidentate ligands it becomes evident that a molar balance of them with respect to the types of vacancies is not necessary because the more excessive the ligand surplus is, the more vacancies may be passivated until fully passivated. Any unbound ligand is residing in the solution without influence on the optical properties of the PNCs. So, for optical investigations of all kinds the high stability and quantum yields ensured by the ligand excess may be beneficial, but for electrical investigations and applications they pose a major issue, since a substantial part of them stays in the thin-film. In case of aliphatic ligands, they may be optically transparent, however electrically they are the opposite equivalent, which is highly insulating. Hence, for an efficient electroluminescent (EL) device any unnecessary surplus of resistive ligands has to be avoided. In fact, even a slight impairment of the PLQY by sparsely passivated PNCs can be made up with by the gain in conductivity as detailed in chapter 7.

Thus, an exact quantification of the ratio between the PNC and the ligand is required. A PNC with edge length of 11 nm is illustrated in figure 2.6 a). This dimension corresponds to about 19 (primitive, $CsPbBr_3$) unit

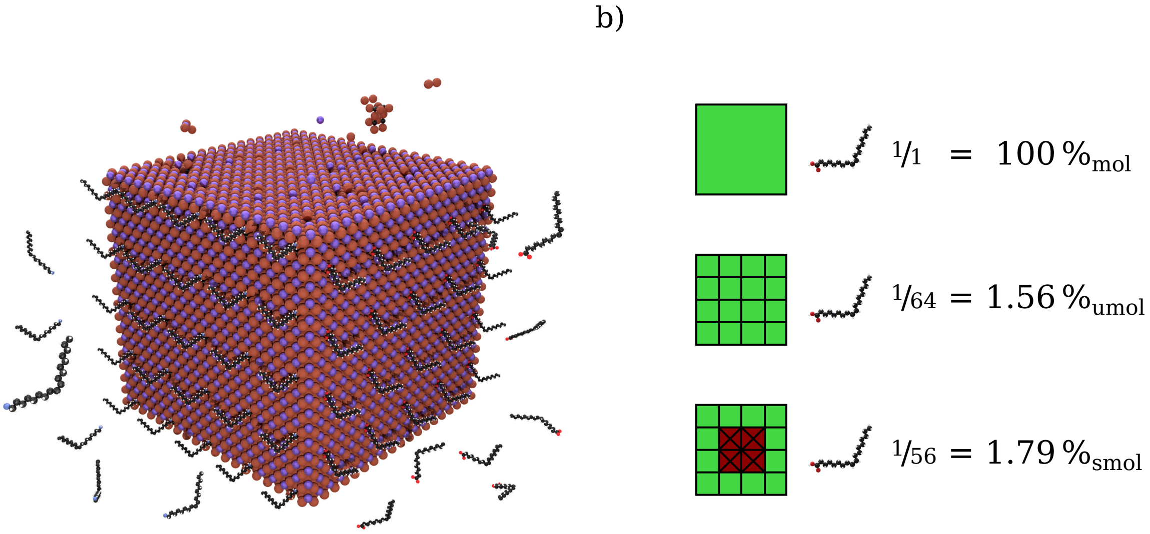

Figure 2.6.: The actual size of a PNCs with edge length 11 nm in relation to the single ions and ligands is depicted in a) and demonstrates the ratio between surface and core unit cells. The top face illustrates an imperfect surface while the left is oleylamine and the right is oleic acid passivated.[S.9] b) presents schematically the different percentage symbols that can be defined in order to quantify the ligand to PNC ratio. It shows a centred cross-section of a PNC with only 4 unit cells edge length to ease the understanding. Either the entire PNC is counted as a particle ($\%_{\mathrm{mol}}$) or each unit cell ($\%_{\mathrm{umol}}$). It is very convenient to define the quantity $\%_{\mathrm{smol}}$ which only counts those unit cells that are actually accessible to the ligands, omitting all core cells. In the present sketch the $2 \times 2 \times 2 = 8$ core is inaccessible and thus subtracted from the total $4 \times 4 \times 4 = 64$ cells resulting in 56 effective unit cells for $\%_{\mathrm{smol}}$.[S.10]

cells per edge, which means 6859 unit cells per NC. If e.g. 20 oleic acid and 25 oleylamine molecules bind to the surface, one could treat the PNC as one entity, thus the molar ratio will be 20:25:1. Considering the same number of oleic acid molecules but on each of the six faces of the cube, $6 \times 20 = 120{:}1 = 12000\,\%_{\mathrm{mol}}$ molar ratio. This high number suggest a large ligand excess, which is certainly not the case (cf. figure 2.6 a), since one PNC can potentially bind more than just a few ligands. Another approach is to define each unit cell as an entity. However, with that the ratio suggests a very small amount of ligands: $120{:}6859 = 1.7\,\%_{\mathrm{umol}}$. Certainly, a quantity that weights the molar ratio on the number of available binding sites is required in order to get representative numbers. The theoretical maximum ligands that can be attached to a NC is one at each unit cell facet at the *surface* of it. Though, two ligands per unit cell might be possible but shall be ruled out because of steric reasons. Anyway, now only the unit cell facets on the surface are counted as entities: $6 \times 19^2 = 2166$. Consequently, $120{:}2166 = 5.5\,\%_{\mathrm{smol}}$; a quantity which is more intuitive ‘surface weighted mol’, smol, is introduced in this work to state molar ratios between ligands and NCs conveniently. Accordingly, $100\,\%_{\text{smol}}$ ratio denotes that for each unit cell facet on the surface of a NC there is one entity of the respective counterpart, e.g. the ligand. In the present example, the $5.5\,\%_{\text{smol}}$ correspond to a little more than $^1/_{20}$ of the PNC's surface (unit cells) being covered by oleic acid. Figure 2.6 b) summarises the key differences between these three different molar ratios. Herein, it shall be pointed out that the molar fraction, denoted with mol %, commonly used in chemistry is not meant with the notation $\%_{\text{mol}}$. The difference between these to values resides in its reference. The molar fraction between molar amount of substances x and y is defined as: $^x/_{x+y}$. In contrast, the molar ratio is simply the ratio: $^x/_y$. Principally, like that one could also define and use smol % as surface molar fraction ($100\,\%_{\text{smol}} \mathrel{\hat{=}} 50\,\text{smol}\,\%$), but this quantity lacks the proportionality to the surface coverage, which makes it less intuitive in context of NC defect passivation considerations.

3. Charge Transport in Perovskite Light-Emitting Diodes

The fabrication of a PeLED inherits the challenges of creating any conventional LED. On top of that, when processing NCs the emitting layer is deposited from solution, which gives rise to new issues. This chapter will give a short overview of the basic parameters ruling the performance of an LED, and discuss workarounds to emerging impairments. Furthermore, the additional difficulties when working with solution-processed layers are detailed and approaches to circumvent those are provided.

The key parameter of interest for any electrical device, that are generators, motors, heat pumps, solar cells and light emitting devices is the power (conversion) efficiency (η_{PE}). It is defined by the ratio of useful desired output to input power ($^{\mathrm{P}_{\mathrm{out}}}/_{\mathrm{P}_{\mathrm{in}}}$). For LEDs that is the total radiated power ($\mathrm{P}_{\mathrm{rad}}$) by the electric driving power (P_{el}):

$$\eta_{\mathrm{PE}} = \frac{\mathrm{P}_{\mathrm{out}}}{\mathrm{P}_{\mathrm{in}}} = \frac{\mathrm{P}_{\mathrm{rad}}}{\mathrm{P}_{\mathrm{el}}} = \frac{\mathrm{P}_{\mathrm{rad}}}{\mathrm{I} \cdot \mathrm{V}}, \tag{3.1}$$

with driving current, I, and voltage, V. The total radiated power is ruled by the number of photons exiting the device per second, $\dot{\mathrm{N}}_{\mathrm{ph}}$, and their average energy, $\bar{\mathrm{E}}_{\mathrm{ph}}$:

$$\mathrm{P}_{\mathrm{rad}} = \dot{\mathrm{N}}_{\mathrm{ph}} \cdot \bar{\mathrm{E}}_{\mathrm{ph}} = \eta_{\mathrm{EQE}} \cdot \dot{\mathrm{N}}_{\mathrm{el}} \cdot \bar{\mathrm{E}}_{\mathrm{ph}} = \eta_{\mathrm{EQE}} \cdot \frac{\mathrm{I}}{e} \cdot \bar{\mathrm{E}}_{\mathrm{ph}}. \tag{3.2}$$

Herein, $\dot{\mathrm{N}}_{\mathrm{el}}$ equals the number of electrons (with charge e) per second. Consequently, the external quantum efficiency (EQE), η_{EQE} is defined as:

$$\eta_{\mathrm{EQE}} = \frac{\dot{\mathrm{N}}_{\mathrm{ph}}}{\dot{\mathrm{N}}_{\mathrm{el}}} = \eta_{\mathrm{out}} \cdot \eta_{\mathrm{QY}} \cdot \gamma. \tag{3.3}$$

Combining the relations 3.1, 3.2 and 3.3 yields:

$$\eta_{\mathrm{PE}} = \eta_{\mathrm{EQE}} \cdot \frac{\bar{\mathrm{E}}_{\mathrm{ph}}}{e \cdot \mathrm{V}} = \eta_{\mathrm{out}} \cdot \eta_{\mathrm{QY}} \cdot \gamma \cdot \eta_{\mathrm{ph}}. \tag{3.4}$$

Ultimately, the power efficiency of an LED is determined by four factors.

The built-in loss per photon, η_{ph}, arises from the discrepancy between the energy that each electron receives, that is $e \cdot \mathrm{V}$, and the energy of the emitted photon. For example, an indigo-violet LED has a photon energy of 3 eV ($\approx$ 414 nm); if it is driven at 3 V, η_{ph} reaches ideality becoming unity. However, the same device emitting a 2 eV ($\approx$ 619 nm) red light, would have $\eta_{ph} = 2/3$. Apparently, the LED's driving voltage has to match the emitted photon energy. It can be kept low with conductive materials and low energy barrier junctions. Note that η_{ph} may only reach values above one if up-conversion processes, such as e.g. triplet-triplet-annihilation up-conversion,[55] are involved.

The charge carrier factor, γ, describes the losses that arise if carriers pass the device without potentially forming excitons, that is, passing the device on the conduction resp. valence band only. Put another way, it is the non-radiative recombination at the metallic electrodes. Hence, it is one if no charge carriers reach the opposite electrode but all recombine with their counterpart inside the LED.

Whether such recombination results in emission of a photon is determined by the effective quantum yield, η_{QY}:

$$\eta_{QY} = \eta_{PLQY} \cdot \eta_{rad.}. \tag{3.5}$$

It accounts for all losses that can occur for an electron-hole pair in the emissive layer. Thus, it is proportional to the PLQY (η_{PLQY}). Furthermore, $\eta_{rad.}$ accounts for the optically passive excitons. In case of LHPs this factor is one since all excitons are optically active at room-temperature. However, if there are dark states, which cannot be converted into a bright one thermally, this factor may reduce. For conventional fluorescent dyes, the three triplets are not accessible so this factor will be only $1/4$, that is, the singlet fraction.

The first term of eq. 3.4, the out-coupling factor, η_{out}, describes all optical influences. Any light that may be reabsorbed, quenched or trapped in modes within the device are summarised within this factor. Also, effects like e.g. the Purcell factor, arising from interaction of the excitation with the geometry resp. cavity of the LED,[56] shall be included in this term. For isotropic emitters in planar LEDs this factor can be as high as 20 %.[57] Moreover, it can be enhanced with horizontal emitter orientation or using out-coupling optics.[57] Novel phenomena found in LHP-NCs such as the reported photon-recycling can bring this factor up to unity.[58] For the application of LHPs in LEDs the out-coupling has already been discussed in detail by Morgenstern et al. [59]. The performance limit in terms of η_{out} is estimated to be in the same range of isotropic emitters for cubic PNCs because a slightly vertical orientation is compensated by a beneficial higher refractive index.[60]

Consequently, for the design of an efficient PeLED with given geometry, auxiliary layers are introduced to optimise the individual factors. The fundamental concepts behind organic light-emitting diodes (OLEDs) are also applied in order to incorporate PNCs for electroluminescence. Details about the organic semiconductors and their application in OLEDs can be read in textbooks by Köhler and Bässler [49] and Forrest [61]. Without the transport layers simple anode-LHP-cathode structures lead to enormous amount of charges bypassing the emitter, so that $\gamma \rightarrow 0$. Furthermore, a direct metal contact leads to significant carrier assisted quenching of the excitons in an emitter.[62] This would decrease η_{QY} as well. The introduction of any additional transport layer to a PeLED has primary implications on η_{ph} and γ. By using adequate semiconductors the charge carriers and excitons are confined to the emission layer posed by a PNC thin-film, so $\gamma \rightarrow 1$. However, any resistance between the layers, that are, metal to transport layer and transport layer to PNC will increase the driving voltage of that device; thus decreasing η_{ph}. Herein, it is important to note, that the injection from the electrodes may be even enhanced at the same time so that the driving voltage is decreased. Secondarily, there are also impacts on the factors η_{out} and η_{QY}, as the thickness alter the cavity size and therefore change the interference within the device significantly.[57] Especially, η_{QY} may be decreased by non- or radiative decay of the transport layers themselves or from a charge transfer state between them and the emitter.

For LHPs the additional challenge of a decreased PLQY by a chemical interaction comes on top as detailed in chapter 6. Additionally, the layers have to be compatible; the subsequent layer must not harm the integrity of the one below. In context of solution-processed LEDs that means the layer below has to be resistant to the solvent of the current one. This can be achieved by using polymers, cross-linkable molecules or orthogonal solvents. Latter means alternating polar and apolar soluble layers. Even if these conditions are met, the solution-processed PNC film itself has to form smooth and closed films in order to avoid field induced degradation and/or parasitic escape paths for excitons and charge carriers. Moreover, LHPs tend to dope adjacent layers with their mobile ions,[63] so they need a resilience especially against an electrochemical doping of halides.

While the long shot goal for industrial application may be fully solution-processed PeLEDs to decrease cost, for this work the high complexity by using more than three solution-processed functional layers, that are hole-, electron transport and emissive layer is avoided. Consequently, only the bottom half of the PeLED is manufactured solution-processed. The LHP-NCs feature two properties which renders them very challenging to incorporate on a solution-processed underlying layer. They are dispersed in an apolar solvent, and they feature very deep VBM (for $CsPbBr_3$ at -5.9 eV, for $CsPbBr_2Cl$ at -6.1 eV)[70, 72]. Most of the organic semiconductors are also soluble in an apolar solvent which impedes an orthogonal solvent design.

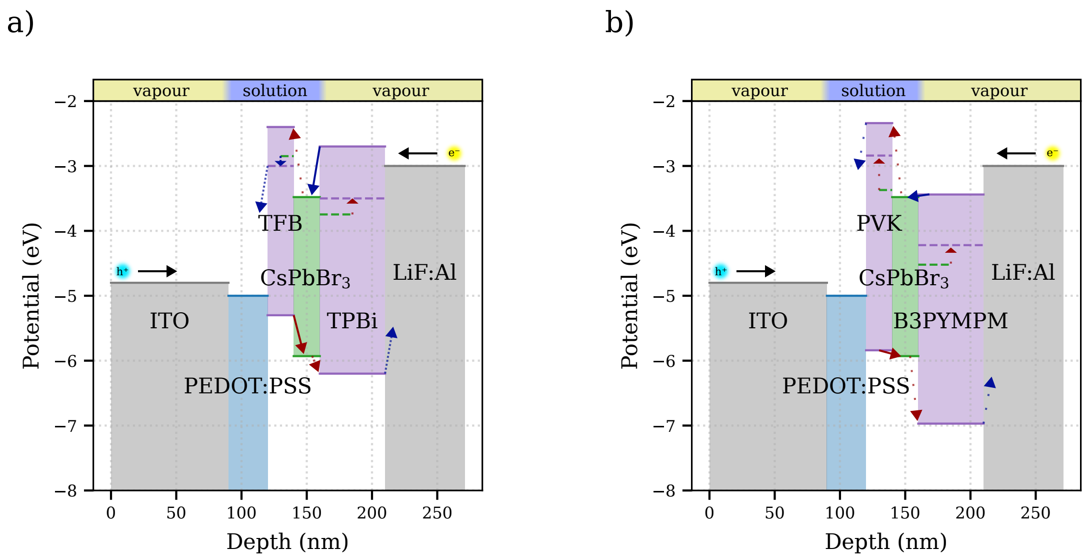

Figure 3.1.: Illustration of PeLED stacks with different band energy level alignments. Solid lines represent desired transitions, dotted lines losses with the dot-density indicating the probability. Blue colour denotes an energy loss of the particle (cooling), while red illustrate a required energy gain. The TFB-TPBi setup, a), has a loss path for excitons via TFB's triplets (dashed lines) and the hole blocking ability of TPBi may be not efficient enough. Furthermore, injection of holes into CsPbBr$_3$ from TFB requires a high amount of energy. Additionally the electrons lose a significant amount of energy at the TPBi-CsPbBr$_3$ interface.[S.11] On the other side, in the device structure used for the PeLEDs of this work, b), that is PVK-B3PYMPM, the PVK efficiently blocks triplets, while B3PYMPM's deeper LUMO position features less carrier cooling.[S.12] Energy levels are taken from references.[64–75]

For hole transport there are polymers that utilise triphenylamines (e.g. TFB and poly-TPD, cf. figure S14 d) and e)) or carbazole (e.g. PVK, cf. figure S14 f)), while showing a decent stability against apolar solvents. At the same time, they feature a high lowest unoccupied molecular orbital (LUMO) for electron confinement. The triphenylamine based hole transport layers (HTLs) feature highest occupied molecular orbital (HOMO) levels as deep as -5.3 eV,[66, 67] which still poses a significant barrier to the VBM of CsPbBr$_3$ and especially for CsPbBr$_2$Cl. However, even though the bandgap is around 2.9 eV,[68] the triplet energy of the triphenylamine based polymers (2.3 eV for TFB)[69] is too low for a considerable exciton confinement of even CsPbBr$_3$'s excitons of energy 2.44 eV (510 nm). Consequently, PVK is left over. The triplet energies of carbazoles are generally higher, so for PVK,[71] and its HOMO is deeper -5.8 to -5.9 eV.[70, 76] The new challenge is to inject from the anode into this deep HOMO, but this can be solved, by depositing PEDOT:PSS (cf. figure S14 i)) or molybdenum oxide below.[65, 77] The biggest issue with PVK is its low hole mobility (10^{-6} $\mathrm{cm^2/V\,s}$).[78] This resistance can be partially circumvented by making the layer thinner for the moment.

Note that not many materials enable efficient charge injection to the deep VBM level of the perovskite and are insoluble in apolar solvents. The CBM is comparably easy to reach, therefore the use of colloidal ZnO has been found a to be a feasible solution-processed electron transport layer by many groups.[79, 80] However, the ZnO shows quenching (cf. chapter 6) and very inconsistent film roughnesses with a subsequent high short-cut rate of resulting PeLEDs. Thus, it could not be reproducibly used for PeLEDs of this work. Other solution-processable electron transport layers mostly lack a deep HOMO for hole blocking or an adequately high triplet level for exciton confinement.

The electron injection can now be achieved with an organic semiconductor deposited on top of the LHP. As material with high triplet level (2.7 eV) and deep HOMO (-6.2 eV) TPBi (cf. figure S13 i)) is used widely.[73] Still, the HOMO may be insufficiently deep for $CsPbBr_2Cl$. Moreover, its high LUMO (-2.8 eV)[73] causes η_{ph} to decrease unnecessarily, since the electron loses the energy difference to the LHPs' CBM. This accounts in case of $CsPbBr_3$ for 0.7 eV for each electron. This energy loss leads to Joule heating of the perovskite leading to degradation, thus decreasing η_{QY} as well.[81] Additionally, the reported giant surface potential of TPBi[82] has unknown implications on the field-susceptible PNCs. Because of these impairments, B3PYMPM (cf. figure S13 h)) has been chosen as electron transport layer (ETL). Its HOMO is very deep (-7 eV) while its LUMO is also quite deep (-3.5 eV)[74] The LUMO aligns well with $CsPbBr_3$'s CBM, while the high triplet (2.7 eV)[74] also ensures exciton confinement even for $CsPbBr_2Cl$'s sky-blue excitons 2.65 eV (467 nm). With respect to PVK, the electron mobility of B3PYMPM is around $10^{-5}\,\mathrm{cm^2/V\,s}$,[74] which is higher but still not too far from PVK's hole mobility, so a slight electron excess can be expected in the sample by the mobilities. Herein, the contact resistance to PVK being probably also higher than the one to B3PYMPM may even further promote this trend.

4. Experimental Methods of Characterisation

The setups and concepts to characterise the components, that is, the thin-films and the LEDs are elaborated in the following. Initially, issues with the common techniques to visualise the thin-films' morphology such as its coverage on different substrates, its thickness as well as its roughness are explained. Consequently, the photoluminescence consideration of mentioned thin-films are elucidated. Finally, optoelectronic measurement procedures to get the key parameters of LEDs are presented. Note that exact quantities, full recipes and characterisation procedures are detailed in section A.1.

4.1. Topology of Thin-Films

In order to work with any LHP the morphology of the film is important to be engineered according to the application. Admittedly, for PNCs impairments like grain boundaries and major crystal dislocations are not expected in a thin-film. Anyway, the formation of agglomerates and the uneven distribution of NCs on a substrate are similar issues that have to be avoided for a successful optoelectronic application. Depending on the ligands, PNCs may become very insulating. Therefore, the desired film thickness is of a few monolayers to avoid high resistances. Hence, the films should be of thickness in the range of less than a few dozen nanometres. Furthermore, a very important point for PeLEDs is a full coverage. Any hole in such thin film poses a direct contact of the two adjacent layers and may give rise to significant losses. Another issue arises if there are steep trenches or sharp steps within the film, since electric fields will be significantly higher at this point leading to degradation and/or breakdown.

Actually, the latter mentioned optimisation may apply to any optoelectronic material, however the inspection of such poses a major challenge for LHP-NCs. The general setups for characterising nanometre-sized films or objects are either atomic force microscope (AFM) or electron microscopy (scanning electron microscope (SEM) or transmission electron microscope (TEM)). Especially, electron microscopy is particularly easy on LHPs since lead ensures a nice contrast, while the halides and in case of $CsPbBr_3$ also the caesium are also suitable materials because of their high nuclear mass. But the organic part of the PNC is not observable with electron microscopy. The issues do not stop there; the organic ligands are contaminating the electron microscope and therefore reducing the resolution significantly over time.[83] This effect is even stronger for less stable PNCs, as they degrade in the electron beam.[84] Consequently, only particles with a limited amount of organic ligands could be imaged by SEM.

The AFM technique has no inherent problem with organic materials. So even higher concentrated ligands in the PNC film can be tolerated. Furthermore, it is even possible to image the organic part. But the lateral resolution of the present AFM restricts the identification of ligands in between PNCs. Only bigger patches of organic can be made visible with the AFM. Anyway, not all organic ligands can be analysed intensely. The oleic acid–oleylamine mixture showed serious AFM-tip contamination. At higher ligand concentration a tip did not even last long enough for more than a dozen lines of measurement. It is suspected, that these ligands attach to the SiN tip leading to a significant change of resonance frequency and also increasing the effective diameter. The ligands with phosphate anchor, like the lecithin prove to be easier to analyse in the AFM. The removal of excess ligands always improved the situation, also for the electron microscopy.

Optical methods, such as ellipsometry of PNC thin film has basically been impossible so far by the lack of a proper model for the rough surface. The film is, if not perfectly defined as an integer monolayer, always full of one NC deep steps. For the present samples that is around 10 nm. So the model has to incorporate random thickness steps of around $1/2$ to $1/3$ of the whole thickness. X-ray reflectometry (XRR), has similar issues, however because of LHP's high contrast to X-rays and the X-rays featuring a substantially lower wavelength a suitable model is easier to apply.

LHP NCs, are mostly spin-coated which is a simple and reproducible deposition technique. Herein, high rotation speeds turned out yielding more holes in the film than the one at low speeds. Issues with too low rotation velocities arise because excess solution is not discarded from the edges and corners of the substrate and will flow back into the centre of the sample upon stopping the rotation. This backflow is destroying the flat integrity of the fresh film by redissolving it. That is why, a two step rotation speed process is used for the spin-coating procedure. A slow 500 rpm rotation is performed until the solvent in the region of interest, that is the pixel area, is (partially) dried. This takes around 30 seconds for toluene or chlorobenzene (less for e.g. hexane). Subsequently, with a short five second 2000 rpm pulse the edges are cleaned. With that a very consistent film thickness can be manufactured (±5 nm, less than a monolayer deviations). While within the same batch the thicknesses may be highly reproducible, it is strongly sensitive to the concentration of the solution, so that a change from e.g. 1 mg/ml to 1.1 mg/ml already added more than a monolayer to the thickness.

4.2. Photoluminescence of Thin Films

While the topology of the thin-films dictates its electrical properties, it influences the luminescence only to a minor extent. The photoluminescence (PL) of a substance gives insights into its light-emission colour, exciton dynamics and its underlying processes. Since principally the emission from an electronically excited and optically excited state is identical, characterisation of PL yields very valuable insights for the application of the emitter in an LED.

4.2.1. Photoluminescent Quantum Yield – PLQY

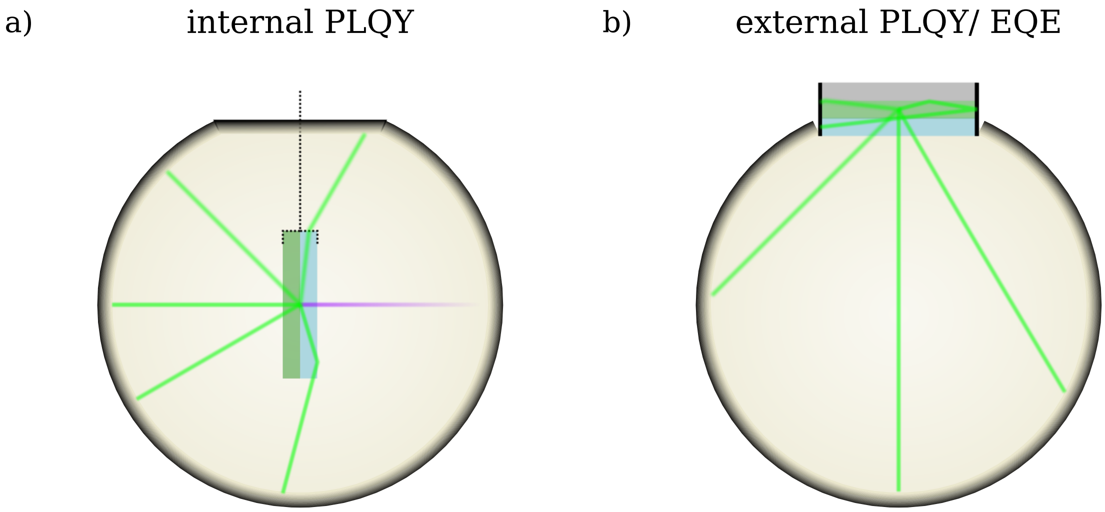

Figure 4.1.: Integrating sphere setup for accurately determining the PLQY: a) setup for measuring the PLQY and b) setup for measuring the external PLQY or EQE. The (internal) PLQY is determined by measuring all the emitted light (4π steradian) and the external PLQY or EQE is obtained by only taking light that leaves a certain defined cavity in one direction (2π) into account.[S.13, S.14]

The concept behind the photoluminescent quantum yield (PLQY) is to benchmark a luminescent material by its ability to re-emit light with respect to non-radiative losses. Herein, the loss of photons rather than energy is considered. Basing this value on energy would result in a strong excitation dependence, since even for an ideal one-photon absorption-emission process, the energy difference between excitation and emission is lost. Even though in LEDs energy efficiency is the ultimate goal, a loss through absorption can be avoided with electrical excitation generation. Thus, the PLQY is fundamentally defined by the ratio of emitted to absorbed photons, $\dot{N}_{em}/\dot{N}_{abs}$. $\dot{N}_{em}$ is obtained by integrating the emission spectrum while $\dot{N}_{abs}$ is determined by the reduction of the excitation signal by the sample. Initially, a spectrum is taken and the photon flux ($\dot{N}$) is calculated by summing the spectral radiant flux ($\Phi(\lambda)$ with unit W/nm) while dividing the average energy of the photons of the respective channel:

$$\dot{N} = \sum_{i=0}^{n} \Phi(\lambda_i) \cdot \frac{\lambda_i}{hc} \cdot (\lambda_{i+1} - \lambda_i)\,. \tag{4.1}$$

When considering the PLQY it is usually referred to the internal PLQY (η_{PLQY}), which deviates from the external PLQY ($\eta_{ext.PLQY}$) by an outcoupling factor η_{out}. Indeed, if the geometry of the sample is equal to an LED, this factor equals the one defined for the EQE eq. 3.3. Consequently,

$$\eta_{ext.PLQY} = \eta_{out} \cdot \eta_{PLQY}. \tag{4.2}$$

$$\eta_{EQE} = \eta_{ext.PLQY} \cdot \eta_{rad.} \cdot \gamma. \tag{4.3}$$

Or in case of LHPs (with $\eta_{rad.} = 1$):

$$\eta_{EQE} = \eta_{ext.PLQY} \cdot \gamma. \tag{4.4}$$

Apparently, the efficiency of a PeLED is ruled by only two factors, and the PLQY is experimentally accessible, which makes it a very important quantity to optimise prior to operating PeLEDs. Figure 4.1 shows a schematic measurement approach for both η_{PLQY} and $\eta_{ext.PLQY}$. In case of measuring the (internal) PLQY, a), all the light that may be trapped within the film or substrate has to be detected or corrected for. A measurement with the sample attached on a transparent hemisphere has shown the exact same PLQY as the measurement without. With that, it is verified that no light is trapped in the substrate and the light can indeed be fully extracted through the cutting-edges. Like that, ideally the full 4π steradian is measured. However various experimental facts, such as reabsorption, may result in deviation from the real internal PLQY. Another way to determine the PLQY is to already include losses in the measurement. As motivated with eq. 4.4, especially in context of LEDs the external PLQY is more feasible. But, for that the entire PeLED has to be investigated. If only a film is considered the change of η_{out} has to be corrected for. Anyway, the fundamental difference is that only a 2π steradian is detected and the light that is trapped in the substrate or device is not entering the integrating sphere (cf. figure 4.1 b)). Only the light that has been able to exit such stack including the reflection by the electrode is detected.

Another approach to accurately determine the internal PLQY is to measure a highly dilute solution. In doing so, any reabsorption or light trapping is avoided entirely. However in case of LHP NCs the investigation on PLQY revealed that there may be a significant difference of the one measured from solution and thin-films which also depends on the solvent and concentration (apart from the known inter-particle influences such as e.g. reabsorption). Interaction with the solvent as well as degradation is not excluded. Furthermore, not only the solvent but also the film shows this: there is a strong influence of the substrate on the internal PLQY (cf. figure 6.2 a)). Therefore, for accurate PLQY estimation the thin-film data shall be taken, as it is closer to the application conditions of the PeLED.

4.3. Optical and Electrical Investigations on LEDs

An ideal optical emitter, that is one exhibiting high external PLQYs, is not necessarily ideal for the application in an LED. Properties as for example the already described film formation are crucial for the LED's performance because it strongly influences the current. Even with a perfect film morphology, balancing the electric charges on the functional layers of the LED proves to be especially challenging in case of nanocrystal based LEDs. Furthermore, many conventional methods of characterising the issues in LED are less straightforward: That is, many slight changes to the PeLED stack have major implications on the emissive layer and vice-versa. To name one of such cross-correlation: Exchanging the hole transporting polymer has proven to not only change the PNC film coverage entirely, but also the polymer itself could turn out to be susceptible to the PNC's solvent and redissolve within it. Furthermore, chemical cross reactions with the ionic LHP can never be fully ruled out including a change in ion permittivity leading to a potential contact resistance change. Same issues occur, if the solvent or concentration of the PNCs is changed. All these challenges have rendered a bottom-up investigation very hard. Any isolated property that may be identified on a sample of a certain state, that is, a specific substrate or solution could be subject to change entirely in a PeLED stack. Because of that, this work is pretty limited to top-down characterisations so that the start of an investigation is posed by a PeLED which is altered and the implications are studied. Reverse engineered setups like half-devices or thin-films with the parameters of the PeLEDs thin-film, such as the external PLQY considerations, are investigated after an (locally) optimal PeLED has been achieved.

4.3.1. Current-Voltage-Luminance Characteristics (j–V–L)

Without doubt, the most common way of characterising the performance of an LED is its current density (j) and luminance (L) depending on the driving voltage (V). While j–V characteristics are crucial to get insight on the electric behaviour of the diode isolated from any luminance effect, so is the L–V dependence to investigate actual light emission. Note that also the radiance can be used for this characterisation if the photopic weighting is not of interest (especially when considering NIR, UV). Anyway, the j–V curve can be split into three regions of interest. At negative or low bias voltage, the diode will be blocking and only an ohmic leakage current is measured. Hence, $j \propto V$ in this region. At a certain threshold voltage (V_{th}) the diode turns on and an exponential current as well as luminance onset is expected for ideal devices, marking the second region. Herein, for real devices the position of V_{th} as well as the slope at the onset provides information about the carrier injection state of the device. As an example, for some devices two current onsets can be identified, while the luminance only has one which is located at or after the latter current onset. This scenario is explained by a difference in hole and electron injection, as the luminance will only turn on if both carriers are present. At elevated voltages, that is the third region, the current increase and as a consequence also the luminance will flatten. For an ideal device, a space charge limited current is expected where ($j \propto V^2$). However, for most of the devices characterised in this work these currents are never reached, because other resistances from e.g. injection are too high. For PeLEDs the luminance starts proportionally to the currents in the onset region, but degradation leads to an over-proportional decrease of the luminance slope. At a certain operation voltage a breakdown of the emitter can be observed, which is indicated by a drop in luminance while the currents still increase.

4.3.2. External Quantum Efficiency - EQE

The ratio of luminance to current, that is the luminance efficiency, as the proportionality factor between current and luminance is closely related to the EQE. If the radiant emission profile is lambertian, it is even proportional, since the luminance is proportional to the radiant flux and consequently to the flux of photons ($\dot{N}_{ph}$). The flux of charge carriers ($\dot{N}_{el}$) is given by the current itself, so according to eq. 3.3 the EQE can be estimated with the known geometry of the setup. This estimated EQE, $\eta_{EQE,lamb.}$, can also be directly accurately determined with the integrating sphere setup depicted in figure 4.1 b). The lambertian emission profile is verified by angular dendent photoluminescence (ADPL) for some of the present PeLEDs. Additionally, the EQEs obtained from the integration sphere are systematically bigger than the ones from the lambertian approximation for PNC-LEDs; the factor determined to be 1.1, so that: $\eta_{EQE} = 1.1 \cdot \eta_{EQE,lamb.}$. Consequently, the EQEs determined by lambertian estimation in this work, are systematically slightly underestimated. With the EQE versus current considerations, the changes of carrier balance depending on driving current or even exhibited luminance can be studied. For example a constant EQE implies either a good carrier balance with a stable external PLQY, or they compensate each other. On the other side, if it monotonically decreases a degradation or a voltage-dependent imbalance is present in the device. Furthermore, maxima or minima denote a compensation of influences.

4.3.3. Displacement Currents

One of the two major factors ruling the EQE of PeLEDs, that is the PLQY, can be investigated in an isolated system. However, for the charge carrier balance γ, apart from investigating the PeLEDs itself and assuming a known PLQY for each voltage, there is no characterisation technique presented so far. One approach to investigate each charge carrier contribution is using single carrier devices. Herein, only half of the PeLED is investigated by replacing the other half with a non-injecting contact. While this gives direct insights into the carrier injection properties, this approach is not very robust to manufacturing errors such as bad or changed film morphology. The mentioned cross-correlation of NC layer with the substrate has tremendous influence on the single carrier performance. This is especially prominent for an electron-only device where the bottom contact has to be electron conducting. Because of the different underground the film morphology changes and the deposition procedure has to be adjusted in order to mitigate the changes. A very crucial disadvantage of the investigation by single carriers is that the film thickness as well as defect density have to be kept constant between samples and LEDs for any statements to make. The main problematic issue arises from the fact, that pin-holes in the film or a thinner film may be mistaken as a better resp. more conductive film. This issue can only be identified by the lack of or inefficient light-emission in a PeLED, but the single carrier device exhibits none by design.

In order to circumvent this issue, displacement currents on a capacitive device shall be investigated. The LHPs are deposited on an insulating film, such as PMMA, and the top contact can be evaporated with minor impact. A defect, such as a hole, in the LHP-NC film does not have a big impact on a capacitor since its locally infinite capacitance is added reciprocally to the overall capacitance. Thus, considering these metal insulator semiconductor (MIS) devices, they have an inherent robustness against film morphology changes and allow for a better investigation of charge injection. However, a slow j–V measurement as performed for LEDs does not yield considerable displacement currents. Rather fast and alternating voltages are applied and the current response can be investigated. For a proper analysis of these currents a simple model of two leaky capacitors is developed and analysed.

The considered devices can be simplified to a system of two layers sandwiched between two electrodes. One of these layers is the insulator (PMMA), which has a known high resistance R_i and permittivity ϵ_i and

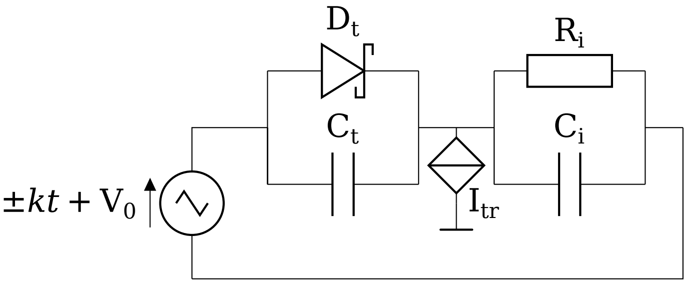

Figure 4.2.: Double RC circuit with a diode and a source to simulate trapped charges.

with its dimensions also C_i. Also the investigated (transport) semiconductor layer has a capacitance C_t. For simplicity the injection and bulk resistance of the semiconductor is approximated as a single Schottky diode, D_t, parallel to the capacitor (cf. figure 4.2). Moreover, the diode is approximated by resistors, since it is either blocking, thus a high resistance, or conducting with a low resistance ($R_t(V)$) (cf. figure 4.3 a)). The turn-on voltage V_D denotes the switching point:

$$R_t(V) = \begin{cases} R_{block.} & \text{if } V < V_D. \\ R_{inj.} & \text{if } V \geq V_D. \end{cases} \tag{4.5}$$

This voltage is controlled by a potential step, Δ, at the metal-semiconductor interface and bulk properties, such as band-bending, giant surface potential or charge screening. A detailed investigation on the stated effects can be found in reference 85. At this point it is just important to note, that there is a potential barrier at the metal-semiconductor interface which shall be generalised as changes to either the bulk properties V_B (region II of figure 4.3 b)-d)) or interfacial dipoles Δ (region I of figure 4.3 b)-d)).

When considering highly conductive and very pure semiconductors, the model is complete. Since neither the organic semiconductors nor LHPs fulfil this criterion, at V_D the semiconductor may turn-on but this voltage is not observable in the current. That is because trapped charges at interfaces or within the materials are compensated first. Therefore, a controlled current source represents the charge carrier drain by traps in the system. Any trapped charges, Q_{tr}, are assumed to neutralise all incoming charges until the charge reservoir is depleted,

$$\int_0^t I_{\hat{R}}(t')\mathrm{d}t' = Q_{tr}. \tag{4.6}$$

This time t can be correlated to a threshold voltage (in this work: $V_{th} = kt + V_0$), where the fundamental behaviour of the circuit change.

$$I_{tr}(t) = \begin{cases} -I_{\hat{R}}(t) & \text{if } \int_0^t I_{\hat{R}}(t')\mathrm{d}t' \leq Q_{tr}. \\ 0 & \text{if } \int_0^t I_{\hat{R}}(t')\mathrm{d}t' > Q_{tr}. \end{cases} \tag{4.7}$$

Again, for high performance contacts, Q_{tr} is reached instantaneously since the currents are high and Q_{tr} itself is not very high in magnitude. In that case: $V_{th} = V_D$. Note that for $\hat{R}$, the reciprocal sum (eq. 4.8), is used to sum up currents from both layers. Considering the resistors in series would not be sensible as long as there are traps present, since the insulator has no influence on the voltage between the applied and the traps' potential and vice versa.

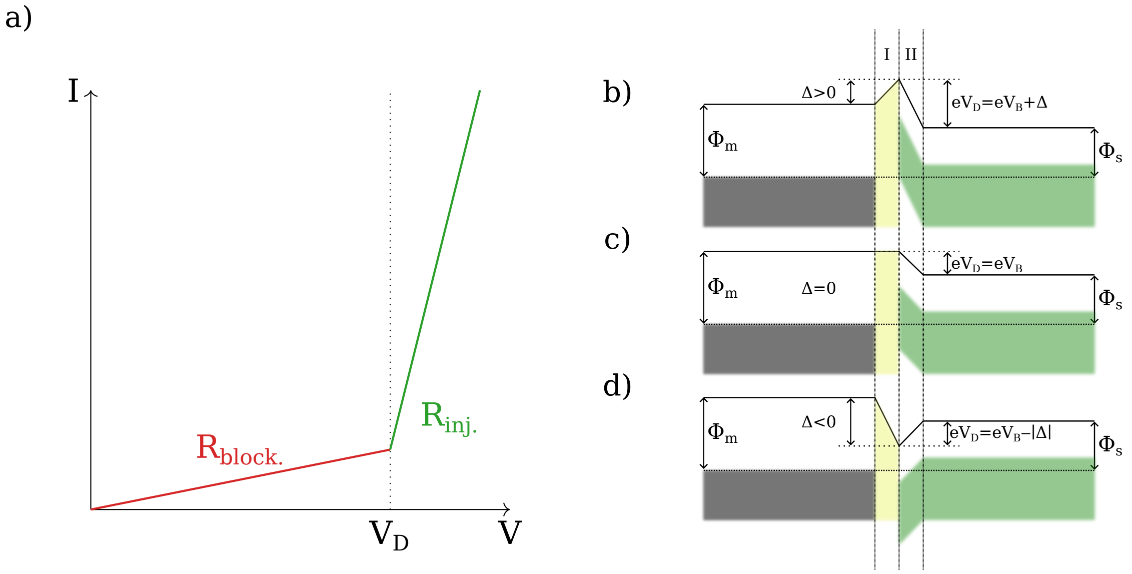

Figure 4.3.: a) Illustration of the j–V characteristics of a piecewise approximation of a diode with two resistors. After a certain voltage (V_D) the diode is assumed to switch from blocking to injection regime, as inferred by a rectifying property. b)-d) illustrate the origin of this voltage in energy level diagram. The Fermi level is indicated as densely dotted line and the vacuum level as a solid line. The metal (gray, workfunction Φ_m) – semiconductor (green, workfunction Φ_s) interface creates a potential (Δ) that may block (here: electron) injection (depicted in yellow, region I). This interface dipole can either impair, b), or enhance, d), the contact. Fields that primarily originate from the bulk film, such as band bending, giant surface potential or others are summarised within V_B (region II).[S.15]

Single RC Circuit

Consequently, in case of applying voltages below V_{th}, the circuit simplifies to Fig. 4.4. The RC cross connection, that is from C_t to R_i or R_t to C_i, is open, since charge carriers will fill the vacancies located on the connection first until Q_{tr} are filled. The trapped charges will compensate the current of only the resistors, since the capacitors won't compensate trapped charges, but rather redistribute them only. The circuit simplifies to a single RC

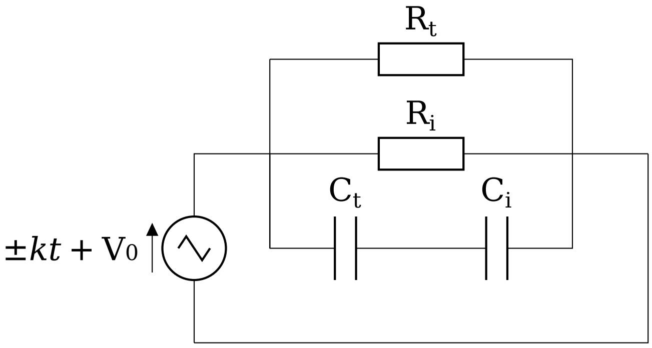

Figure 4.4.: Double RC circuit simplified in case of no or compensated injection $V < V_{th}$.

circuit with:

$$R = \hat{R} = \frac{R_t R_i}{R_t + R_i}, \tag{4.8}$$

and

$$C = \hat{C} = \frac{C_t C_i}{C_t + C_i}. \tag{4.9}$$

In this voltage region the diode is approximated with the high resistor (R_t=$R_{block.}$). The impedance of a capacitor can be expressed with the angular frequency ω and the imaginary unit i as (with $s = i\omega$):

$$Z_C = \frac{1}{i\omega C} = [sC]^{-1}\,. \tag{4.10}$$

So, the impedance of a single RC circuit is the parallel combination of both individual impedances (reciprocal sum):

$$Z = \left[\frac{1}{\hat{R}} + s\hat{C}\right]^{-1}. \tag{4.11}$$

The response of the circuit to an alternating ramp driving voltage $V(t) = \pm kt + V_0$ is derived to be (see section A.2.6):

$$I(t) = \pm\frac{kt}{\hat{R}} \pm k\hat{C} + \frac{V_0}{\hat{R}} + V_0\hat{C}\delta(t). \tag{4.12}$$

For t>0:

$$I(t) = \pm\frac{k}{\hat{R}}t \pm k\hat{C} + \frac{V_0}{\hat{R}}. \tag{4.13}$$

$$I(t) = \pm\frac{k}{\hat{R}} \cdot \left[t + \hat{R}\hat{C} \pm \frac{V_0}{k}\right]. \tag{4.14}$$

The current response is linear with a slope of $^{k}/_{\hat{R}}$ and an offset of $k\hat{C}$ (if V_0=0). Hence, a time-constant current is proportional to a capacitance and a slope is proportional to a conductance, with the proportionality constant being the sweep rate k.

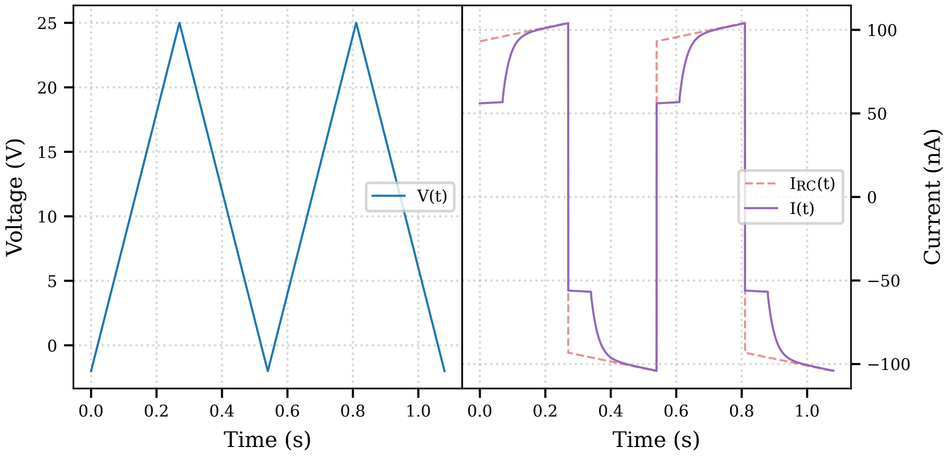

Figure 4.5.: Plot of an exemplary simulated DCM procedure. On the left the applied triangular voltage function with 100 V/s is plotted. On the right are responses of two systems: dashed red is the single RC system, which responds as a rectangular function with a tilt by the leakage through the resistors. The purple solid line is the function that has been derived to model the MIS response. Initially the device behaves like a single RC, but at a threshold voltage the diode's injection bypasses the first capacitor partially leading to an exponential charging until it saturates into again a single RC circuit behaviour.[S.16, S.17]

Double RC Circuit

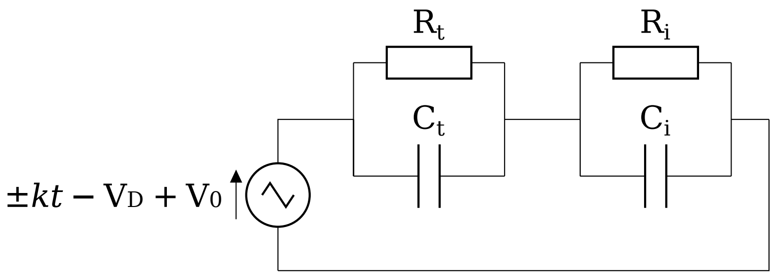

Figure 4.6.: Double RC circuit with the diode approximated as resistor for $V \geq V_{th}$.

In case of exceeding the threshold voltage, $V \geq V_{th}$, all traps are filled. The current source simulating the traps is depleted, and the diode takes a constant resistance. So the diode is approximated with a low resistor (R_t=$R_{inj.}$), and the resulting circuit is depicted in figure 4.6. The cross-currents are no longer compensated by trapped charges. Herein, the currents are dominated by the charging of C_i. That arises from the resistance of the insulator being designed to be as high as possible. The impedance is basically the previous single RC problem in series:

$$\mathrm{Z} = \left[\frac{1}{\mathrm{R_t}} + s\mathrm{C_t}\right]^{-1} + \left[\frac{1}{\mathrm{R_i}} + s\mathrm{C_i}\right]^{-1}. \tag{4.15}$$

The response of the circuit to a driving voltage $\mathrm{V}(t) = \pm kt + \mathrm{V_0}$ is derived to be (see section A.2.6):

$$\begin{aligned}\mathrm{I}(t) = {}& \pm\frac{k}{\tilde{\mathrm{R}}} \cdot \left[t + t_\times - \left(t_\times - \tilde{\mathrm{R}}\hat{\mathrm{C}}\right)\exp\left[-\frac{1}{\hat{\mathrm{R}}\tilde{\mathrm{C}}}t\right]\right] \\ & + \frac{\mathrm{V_0}}{\tilde{\mathrm{R}}} \cdot \left[1 + \left(\frac{t_\times - \tilde{\mathrm{R}}\hat{\mathrm{C}}}{\hat{\mathrm{R}}\tilde{\mathrm{C}}}\right)\exp\left[-\frac{1}{\hat{\mathrm{R}}\tilde{\mathrm{C}}}t\right] + \delta(t)\tilde{\mathrm{R}}\hat{\mathrm{C}}\right].\end{aligned} \tag{4.16}$$

With $t_\times = \mathrm{R_t C_t} + \mathrm{R_i C_i} - \hat{\mathrm{R}}\tilde{\mathrm{C}}$ and tildes $(\tilde{\square})$ denoting the sum resp. hats $(\hat{\square})$ the reciprocal sum of the respective quantity $(\square)$. A linear component comparable to the single RC circuit, $k/\tilde{\mathrm{R}}$, can be found again. With the difference that the resistors are in series.

However, the constant part has become quite complex. The introduction of $t_\times$ simplifies the equation for that matter. The first two terms of $t_\times$ represent the charging of the individual capacitors ($\mathrm{R_t C_t}$ and $\mathrm{R_i C_i}$) which is reduced by the third term, that is, an exchange component ($\hat{\mathrm{R}}\tilde{\mathrm{C}}$). For an ideal insulator:

$$\mathrm{R_i} \to \infty \text{ and } \tilde{\mathrm{R}} \to \infty \text{ and } \hat{\mathrm{R}} \to \mathrm{R_t}. \tag{4.17}$$

$$\frac{\mathrm{R_i}}{\tilde{\mathrm{R}}} \to 1 \text{ and } \frac{\mathrm{R_t}}{\tilde{\mathrm{R}}} \to 0: \tag{4.18}$$

$$\pm\frac{k}{\tilde{\mathrm{R}}}\,t_\times = \pm k\,\mathrm{C_i}. \tag{4.19}$$

The constant part is equals that of a single RC circuit. Yet, the slope will also diminish at the same time.
Apart from that, a new exponential decay component arises from the double RC arrangement. For better understanding the limiting cases of this decay can be analysed. For $0 < t \ll \hat{\mathrm{R}}\tilde{\mathrm{C}} \Rightarrow \exp\left[-\frac{1}{\hat{\mathrm{R}}\tilde{\mathrm{C}}}t\right] \approx 1 \wedge \delta(t) = 0$:

$$\mathrm{I}(t) = \pm k \cdot \left[\frac{t}{\tilde{\mathrm{R}}} + \hat{\mathrm{C}}\right] + \frac{\mathrm{V_0}}{\tilde{\mathrm{R}}} \cdot \left[1 + \left(\frac{t_\times - \tilde{\mathrm{R}}\hat{\mathrm{C}}}{\hat{\mathrm{R}}\tilde{\mathrm{C}}}\right)\right]. \tag{4.20}$$

For $t \gg \hat{\mathrm{R}}\tilde{\mathrm{C}} \Rightarrow \exp\left[-\frac{1}{\hat{\mathrm{R}}\tilde{\mathrm{C}}}t\right] \approx 0 \wedge \delta(t) = 0$:

$$\mathrm{I}(t) = \pm k \cdot \frac{t + t_\times}{\tilde{\mathrm{R}}} + \frac{\mathrm{V_0}}{\tilde{\mathrm{R}}}. \tag{4.21}$$

In the limit of long times, where the exponential function has fully decayed, the current behaviour is identical to a single RC with capacitance $t_\times/\tilde{\mathrm{R}}$. The onset of the exponential has also the identical shape as a single RC circuit. Even though the capacitive contribution may be equal ($\pm k\hat{\mathrm{C}}$) to the $\mathrm{V}<\mathrm{V}_{\mathrm{th}}$ case, the total resistance is derived by a series combination and V_0 has a correction term. Apparently, the boundary condition for equal currents at $\mathrm{V}=\mathrm{V}_{\mathrm{th}}$ is not fulfilled, yet.

This arises from the fact, that the voltage drop at the diode, which is simulated by a resistor has not been considered yet. The overall applied voltage is shifted by the turn-on voltage V_{D} as part of this diode approximation with two resistors. Since the current is expressed with respect to time it results in a time-shift: the double RC solution has to be delayed by $\Delta t = {}^{\mathrm{V}_{\mathrm{D}}}/_{k}$. In order to piece-wise model the displacement-current-measurement (DCM) curves with the single RC part and neglecting $\delta(t>0)$ using eq. 4.16 as $\mathrm{I}_{\mathrm{DRC}}(t)$ results in:

$$\mathrm{I}(t) = \begin{cases} \pm\frac{k}{\hat{\mathrm{R}}}\left(t + \hat{\mathrm{R}}\tilde{\mathrm{C}} \pm \frac{\mathrm{V}_0}{k}\right) & \text{if } \mathrm{V} < \mathrm{V}_{\mathrm{th}}. \\ \mathrm{I}_{\mathrm{DRC}}\left(t - \frac{\mathrm{V}_{\mathrm{D}}}{k}\right) & \text{if } \mathrm{V} \geq \mathrm{V}_{\mathrm{th}}. \end{cases} \tag{4.22}$$

The shape of the curve plotted against time can be seen in figure 4.5. Two linear regimes are connected by an exponential piece. With that a very powerful method to extract the capacitances and resistances is found. However some of these may have a certain covariance, e.g. V_{D} and R_{t}, which impairs a non-linear numerical fitting process. Linear, single-RC, fits are used to fit the extreme regions in order to disentangle them to some extent. More measurements with different ramp rates and different layer thicknesses can give more constraints if needed.

5. Colour-Conversion from Organic Emitters

The discussed challenges, when applying a lead-halide perovskite to an electrical device are predominantly linked to the solution-processing and erosion during operation. In contrast, the remarkable optical properties are rather simple to control and easily stabilised. The operational instability arises primarily from applied electrical fields, which are obviously inevitable in LEDs. Furthermore, for nanocrystals, their stability is ensured by a well-insulating ligand shell, which pose a major drawback because of their inherent electrical insulation. Their impaired electrical accessibility requires even higher fields for the charge injection. A detailed discussion about this issue is presented in chapter 7.

Anyway, this chapter details an approach to make use of the nearly ideal optical traits in an LED. Enabled by their spectrally broad and high absorption coefficient, the PNC excel at converting high-energy, for instance blue, light to low-energy, red-shifted light. Basically, the outstanding solar-cell feature is redirected into re-emission instead of charge separation. A conventional blue LED can be used to empower a thin layer of down-converting PNCs. The combination, now a PeLED, has intrinsic advantages to conventional PeLEDs as well as OLEDs, since the high efficiency of the well-researched OLED is implemented, while the colour-pure, narrow-band spectrum of the PNC is radiated.

5.1. Spatial Separation of Electrical and Optical Operation

5.1.1. Advantages for Display Technologies

The most conspicuous advantage of separating the light-generation and the colour tuning has already been widely explored by the industry of display technologies. The majority of modern displays are backlit TFT LCDs, rivalled only by the emerging OLED and micro-LED technology.[86] The basic concept involves a strong white light source, that is tuned in colour and intensity by filtering elements that are controlled electronically via TFTs. From an engineer's viewpoint the success of this principle is given by the circumstance that the crucial components, that is light source, electronics and colour tuning, are operating separately. Though

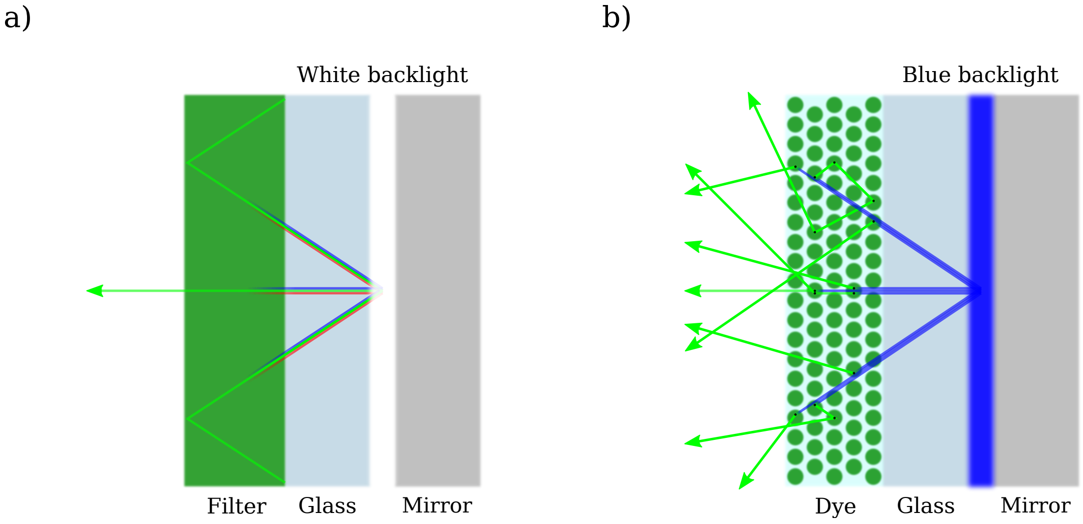

Figure 5.1.: Illustration for visualising the conceptual differences between conventional LCD and down-conversion LEDs. A sketch depicts an ideal a) filtering[S.18] and b) down-conversion[S.19] layer with arrows indicating escape and loss paths of the generated light. In the shown, exemplary case of colour-pure green emission the subtractive approach is inferior to the down-conversion.

there are disadvantages in the current state-of-the-art LCDs, these can be addressed with the incorporation of a down-converting layer. At first glance one could infer that down-conversion is already widely used in mentioned displays, but there is an important difference between a filtering and a down-converting material. The colour and intensity tuning in LCDs is actually performed subtractively where the liquid crystals determine which fraction of light is filtered. By design, if a single colour is emitted, a substantial part of light, that is, the other colours, is lost in the filters (confer figure 5.1). Considering an ideal backlight, this theoretical loss is quantified to be $^2/_3$, since two of three colours have to be dimmed out. This estimation is still too optimistic, since necessary filters for intensity and polarisation have not been taken into account yet.

Opposed to that, down-converters are regulating the conversion of only a certain fraction of light. That is why these devices are driven with a blue light source. Put another way, LCDs wouldn't be able to emit any green or red light at all, if powered by a blue source. The fundamental difference is that LCDs subtract light from the source only, while the down-converter subtracts and subsequently adds the same fraction back. When considering an ideal down-converter (PLQY = 1), each photon that has been absorbed is re-emitted with decreased energy (red-shifted). That reveals an inherent flaw of the down-conversion concept: even if all photons are red-shifted conserving quanta, the energy difference between incident and radiant photons is lost, anyway. While this discrepancy is low for blue to green conversion, it, being $1 - \eta_{ph}$ (cf. eq. 3.4), can grow up to 50 % in the extreme case of converting over the entire visible spectrum, that is from the near UV (3.2 eV) to NIR (1.6 eV). Still, especially for blue, green and high contrast images the LCDs are theoretically inferior to down-converter based displays.

5.1.2. Reduced thermal and electrochemical influences

Energy losses are especially critical when using PNC as down-converters. Because of their inherent susceptibility to heat, the thermal influence by dissipated energy pose a threat to the tiny crystals. Though, having the dye separated from the warming injecting contacts reduces this threat significantly. At the same time, there is more space for designing a potent heat-sink.

In any case, the decomposition of the PNCs is promoted by strong electric fields.[87, 88] Between the two electrodes of an LED there are typically high fields, while they are diminishing outside. The absence of considerable fields is another benefit of having the particles far away from the electronics. Additionally, a field-free operation restricts the residuals of a decomposed PNC from migrating through the device. Therefore potential damage to the transport layers or the electrodes can be entirely avoided.

5.1.3. Enhanced Optical Out-Coupling

The approach of using layers beyond the electric circuit of the LED to enhance the optical output by optimising out-coupling (η_{out} of eq. 3.3) efficiency is not new. The otherwise optically trapped luminance is made available with scattering layers or high refractive index media.

Hence, these are designed to absorb as less as possible. In contrast to that, the down-converter need to absorb as much as possible. Owing to their high absorption coefficient perovskite are the ideal candidate when processed as nanocrystals with near unity PLQY. Here, the PNC acts as a scattering layer since the absorption and subsequent emission exhibits the same deflecting feature. Common coumarin or rhodamine based laser dyes may fulfil the requirement in quantum efficiency,[89, 90] but they are accompanied by a considerable Stokes shift and ultimately thermalisation losses. Stokes shifts in weakly confined PNCs have been reported to be below the mean thermal energy at room temperature; $\Delta E < k_B T = 25\,\mathrm{meV}$.[91]

This unique combination of near unity quantum yield and negligible Stokes shift gives rise to a photon-recycling process, where a photon undergoes multiple bounces before exiting the device. This results in a over-proportional dependence on the PLQY.[58, 92] Thus, in case of PNCs as down-converter, misdirected light is randomised multiple times and its direction is reevaluated, effectively avoiding all losses from trapped light by internal reflection. Leveraged by photon-recycling the theoretical EQE limit of such device can be raised to 100 % (confer figure 5.1).[58] Simulating an OLED via combined classical dipole model with matrix transfer method, previously developed in-house,[93] reveals that the fraction of light that leave a device in real-life conditions is only 18 %[S.20]. Assuming the PNCs to have a constant refractive index about 2.2,[60] the perovskite acts as a high-index medium[94] which increases the available light to 38 %[S.21], more than doubling ($\eta_{\mathrm{out}}(n{=}2.2)/\eta_{\mathrm{out}}(n{=}1) = 2.09$)[S.22] the output.

5.2. Enhanced Stabilisation by Doubling Protection Featuring Micelles

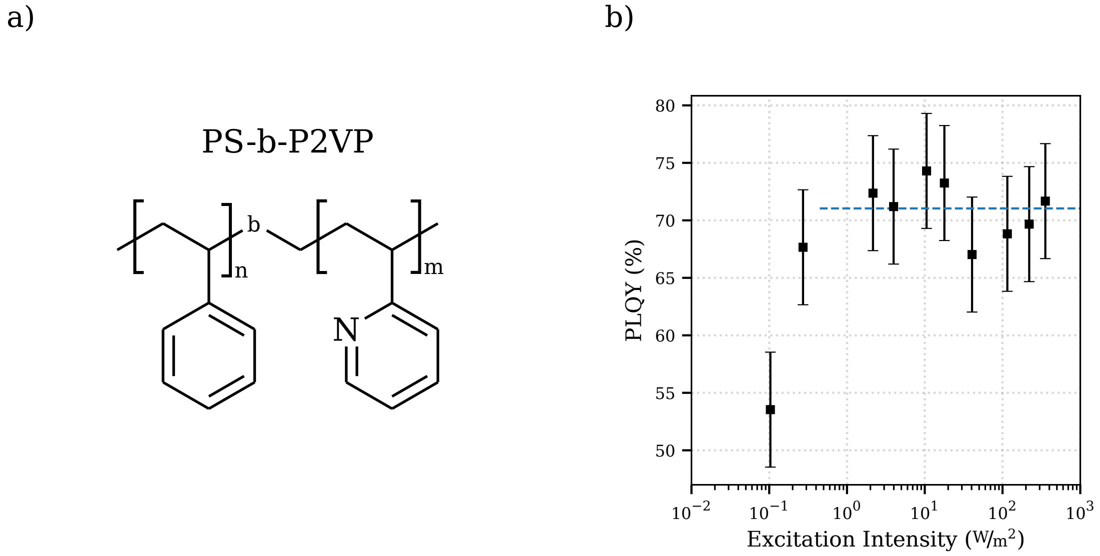

Figure 5.2.: a) Lewis structure of the micelle-forming polymer. n polystyrene parts are combined with m more polar pyridine parts and seperated by b CH_2 groups.[S.23] In an apolar solvent: micells with pyridine groups in the core are built. b) PLQY of the doubly stabilised PNC-DC thin film vs excitation intensity: at radiative intensities higher than 1 W/m² the PLQY settles at 71 %.[S.24, S.25, 95]

Without the necessity of injecting charge carriers into the PNC, the only remaining properties that needs to be addressed are PLQY and stability. As a matter of fact, both can be enhanced by fortifying the encapsulation of the PNC. Exchanging ligands can, in general, serve this purpose to a significant extent. But their ability to insulate against small, polar solvents, especially water is limited. A detailed discussion about engineering ligands for better performance can be read in chapter 7.

This section elucidates an unprecedented concept using a second encapsulation layer around the existing ligands to excel in stability. A polystyrene-b-poly(2-)vinylpyridine (PS-b-P2VP) co-polymer (confer figure 5.2 a)) is used to form micelle structures in an apolar solution. The polystyrene part of the polymer will face towards the solvent, while the polar pyridine is building up the hollow core of the micelle. The PNCs are synthesised inside of the micelles through LARP, as described in-depth in the corresponding publication by Xue et al. [95]. The method is fairly generic, allowing also the use of different ligands. Alkyl-chain lengths ranging from 6 to 18 carbon atoms are successfully incorporated in the micelles. However, for proving the concept of a down-converter LED, a simple MAPbBr$_3$-PNC, capped with oleic acid and oleylamine, is utilised.

The excitation fluence dependent PLQY, measured with a 442 nm HeCd laser and an adjustable ND filter wheel, of these particles reveals minor flaws of the PNCs: the PLQY peaks not as high as for octylamine passivated ones reported in reference 95. Furthermore, at low excitation densities the quantum yield is apparently lower. Both features indicate, that the surface passivation is not optimal yet, since the low quantum yields can be explained by an optical trap-filling process,[96, 97] which is compensating insufficiently at low laser excitation intensities. Consequently, for an LED based on the present PNCs the EQE is expected to start low and rise at elevated pump radiances.

5.3. Perovskite Nanocrystal Down-Converter LEDs

For proving the still only theoretical advantages, a deep-blue fluorescent emitter OLED is fabricated. The stack design with used materials and the layer sequence is detailed in context of figure S1 a) . The pump OLED (cf. figure 5.3 b)-d)) turns on at around 3 V, exhibiting a deep-blue spectral emission peaking at 405 nm, while reaching luminances higher than 1000 $\mathrm{cd/m^2}$ at an elevated voltage of 10 V. The EQE of 0.4 % is maximal at lower and drops towards higher currents.

While the low efficiency may arise from suboptimal triplet-confinement,[98] the decline is explained by already studied phenomena such as exciton-exciton and exciton-polaron quenching.[99] Note that high efficiency is not required for this proof-of-concept. The issues with this pump device are only of minor interest for the down-conversion. More importantly, the emitter is chosen for an optimal overlap of its emission and the down-converting PNCs' absorption spectra. Indeed, the emission of the OLED appears to be negligibly low beyond the absorption of the PNCs (consider figure S1 c)).

The down-converter (DC) is deposited onto backside of the glass, which poses the base substrate for the bottom-emitting pump OLED. That way, all the PNCs are illuminated as depicted in figure 5.3 a) . However, the initial trials with spin-coating the colloids on the glass has yielded PeLEDs with substantial parasitic pump light in the resulting spectrum. Also, reducing

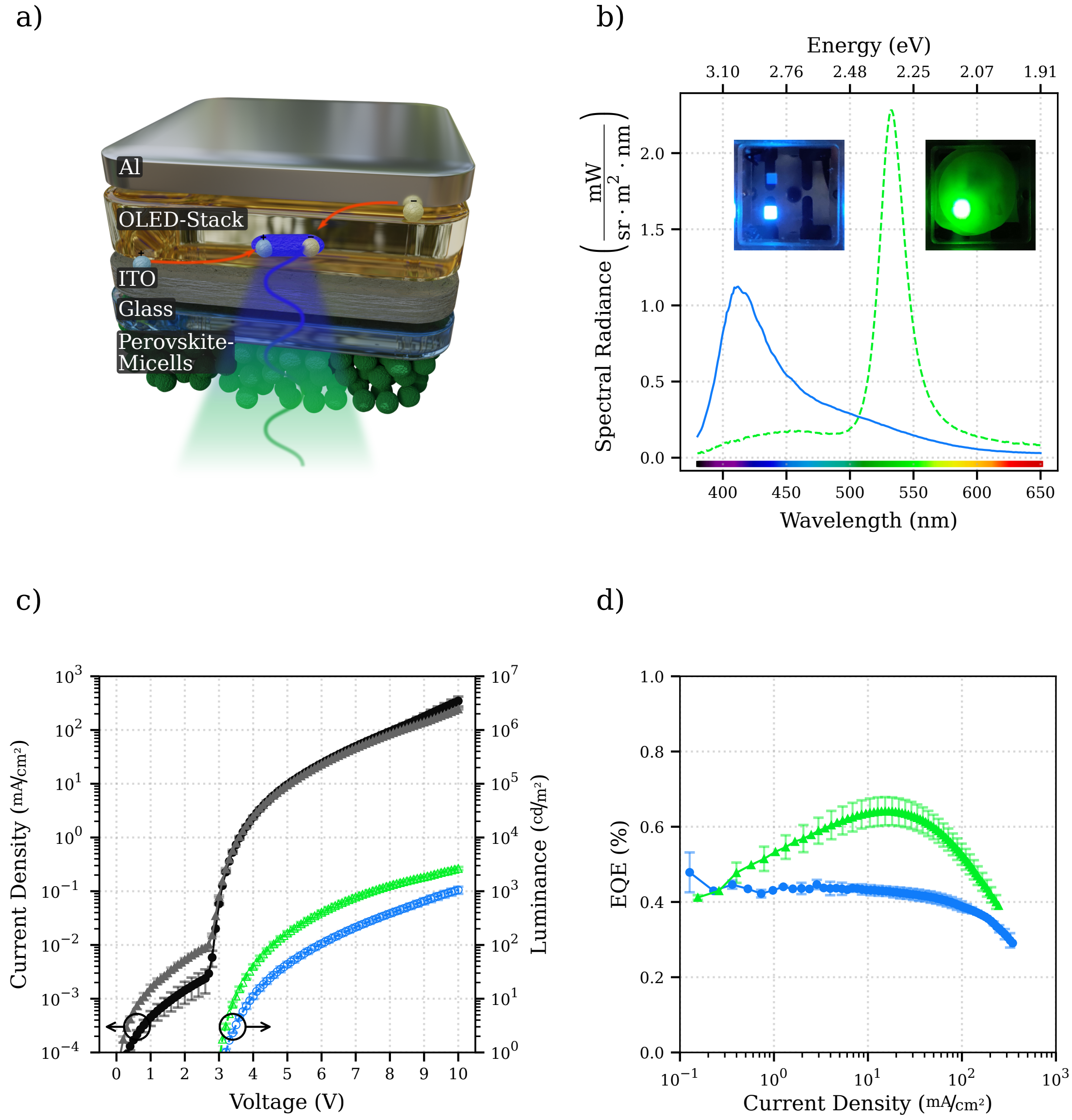

Figure 5.3.: a) On the top side of a glass substrate, the blue pump OLED is deposited, as shown in this schematic layer stack, and the perovskite NC down-conversion layer is placed to the bottom side of the substrate.[95, S.26] b) EL emission from the complete device (green, dashed) and the bare OLED (blue, solid). Insets provide photos of the two devices.[S.27–S.29] c) The driving voltage affects the current density and brightness of the complete device (grey, green) as well as the bare OLED (black, blue) very similarly.[S.30] d) The DC-(green, triangles) OLED's and the raw OLED's (blue, circles) EQE as a function of current density exhibits an expected optimum.[S.22, 95, S.31, S.32]

the rotation speeds down to zero, that is, drop-casting as well as increasing the concentration to the limit by the solvent shows a more pure but still mixed spectrum.

With the named approaches the thickness of the down-converter layer stays below 1 µm (determined by AFM) which apparently is not sufficient for full colour conversion. To achieve extremely thick films, a substantial amount of polystyrene is added to the PNC solutions, rendering them highly viscous. After drop-casting these solutions, the films dried unevenly to a thickness of around 0.5-1.5 mm (measured with vernier caliper). The roughness of this layer is not a disadvantage, since it, if at all, facilitates out-coupling as already discussed briefly.

Finally the device is able to convert nearly all the pump light. Figure 5.3 b) displays the extent of conversion as well as the photographs in the inset demonstrate a strong effect of the thick layer of PNCs. The new device is still highly luminescent, emanating colour-pure green light peaking at wavelength of 532 nm and a full width half maximum (FWHM) of only 24 nm. The detailed analysis (in context of figure S1 c)), reveals that the DC-spectrum consists of a superposition of red-shifted photoluminescence (PL), absorption spectrum of the micelle-PNCs and EL spectrum of the pump-OLED. Thus other potential processes apart from the investigated down-conversion are, if present, negligible.

The electrical characteristics have stayed almost identical, but the luminance has significantly increased at all voltages, outperforming also the peak brightness at 10 V by a factor of around 2.5 by reaching 2650 $\mathrm{cd/m^2}$ (see figure 5.3 c)). Generally, an increase in luminance upon down-converting from blue to green is expected, as photometric quantities are weighted by the perceptivity of the human eye. Nevertheless, the radiance (cf. figure S1 b)), the radiometric equivalent, is also slightly increased. Without a significant change in radiation pattern and thus the radiance being proportional to the total emitted power, a simple down-conversion can only decrease the output power, since the red-shift inherently leads to an energy respectively power loss. To stay in accordance to the law of conservation of energy, light that has originally been lost in the pump device has to be recovered by the DCs. At this point, the already mentioned theoretical considerations concerning out-coupling (see section 5.1.3) are enabling this radiation power to be extracted, which has been denied exiting in the pump device. In order to quantify this increase, an investigation based on quanta, that is examining the EQE, reveals the scale of this effect in this PeLED, since the colour-shift losses are not affecting this quantity by its nature.

Anyway, the EQE for the down-converter LED is increased by a factor of 1.4 peaking at 0.6 %. The EQE is low at low current densities and rises towards its peak at 25 $\mathrm{mA/cm^2}$. This correlates perfectly with the determined PLQYs (cf. figure 5.2 b)): a current density of 25 $\mathrm{mA/cm^2}$ corresponds to a radiant intensity of 6 $\mathrm{W/m^2}$, which is on one side the power where the thin-film's PLQY has just reached its high saturation, when pumped by the spectrally different, yet comparable HeCd laser. Presumably the traps-states are sufficiently filled. On the other side, it is the point where the down-converter device reaches its highest efficiency.

Actually, the down-conversion efficiency (DCE, η_{DCE}), which shall be defined by the ratio of DC-EQE to pristine EQE, is very comparable to the external PLQY ($\eta_{\mathrm{ext.PLQY}}$), since the excitation conditions are similar in wavelength and intensity. At that point, probing the PLQY of the film rather than the solution, directly yields $\eta_{\mathrm{ext.PLQY}}$ as any reabsorption, photon-recycling processes are already accounted for (see section 4.2.1). It is however altered by the out-coupling enhancement factor ($^{\eta_{\mathrm{out}}(n=2.2)}/_{\eta_{\mathrm{out}}(n=1)}$):

$$\eta_{\mathrm{DCE}} = \eta_{\mathrm{ext.PLQY}} \cdot {}^{\eta_{\mathrm{out}}(n=2.2)}/_{\eta_{\mathrm{out}}(n=1)}. \tag{5.1}$$

With the simulated out-coupling factor of 2.09[S.25] and the measured PLQY of 71 %, the DCE is predicted to be 148 %. That value is surprisingly close to the one obtained by the ratio of EQEs, regarding the uncertainty by the crude flat refractive index assumption of the simulation and the uncertainties from PLQY as well as EQE measurements.

6. Enhancing Optoelectronic Properties by LiTFSI Doping

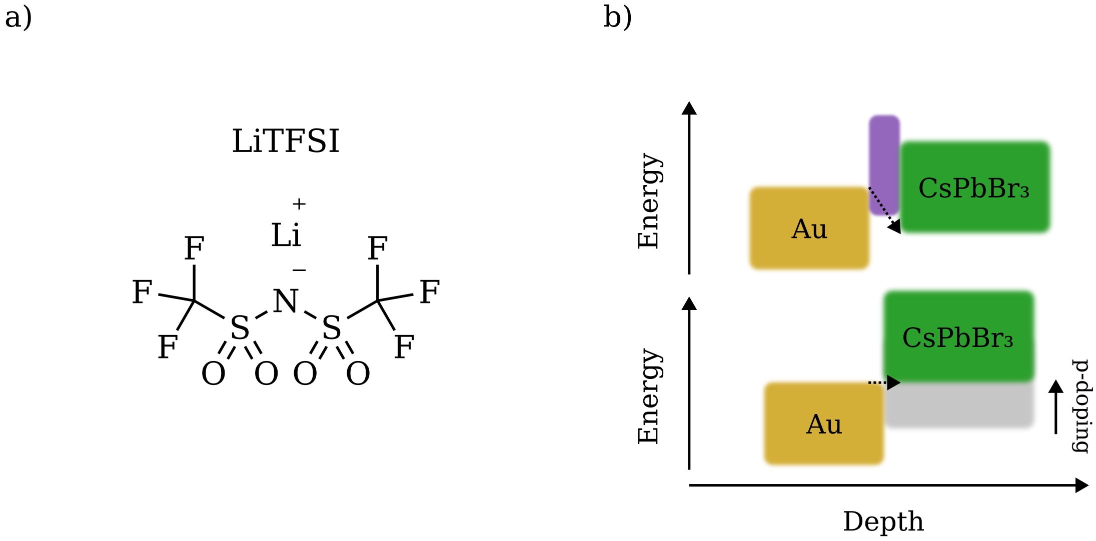

Figure 6.1.: a) Lewis structure of LiTFSI.[S.33] The Li^+ ion is weakly bound to the $TFSI^-$ ion. b) Illustration of two hole-injection enhancement approaches.[S.34] By p-doping, the valence level of the LHP is raised to better match the noble metal (e.g. gold). Otherwise the auxiliary HTL(s), indicated as purple rectangle, has (have) to bridge the high energy gap.

Though at the time of writing this text the QD-DC technology is emerging to the consumer market, its mentioned inherent energy losses by the colour-conversion together with its performance limitation by the pump lighting device renders it to be more of a compromise application of QDs in lighting devices. A more elegant way to incorporate the peculiar yet remarkable properties of nanocrystals into an LED is by facilitating the high quantum yields for directly driven emission. However, the challenges that have been avoided by the down-converter technique have to be overcome. Especially, the injection of charge carriers and the stability of the PNC during the electrical stress with respect to heat dissipation, high fields and polaron-quenching has to be addressed thoroughly. A major cause of hot devices is a suboptimal contact between the functional layers of an LED. A misalignment in the according energy levels at the interfaces gives, among others, rise to a potentially high contact resistance. For perovskites in general the proper alignment of the valence levels to the organic semiconductor poses more of a challenge than the conduction levels. That is, as already elucidated in chapter 3, the low VBM has to be matched with an adjacent transport layer. Engineering a very low HOMO respectively high work function, potentially solution-processed and transparent contact poses a substantial obstacle.

To this end, it may be easier to render the PNCs VBM less deep. Positively doping, (p-doping) the PNCs in order to lift its VBM to the level of a conventional contact while simultaneously increasing carrier mobility is explored by the exemplary use of LiTFSI as p-doping agent (cf. figure 6.1). Note that this chapter augments the already published results in reference 70 by additional findings and its implications.

Lithium bis(trifluoromethanesulfonyl)imide (LiTFSI), structure formula shown in figure 6.1 a), is used extensively as a source for ions used in organic electrolytes applied in lithium ion batteries and capacitors.[100, 101] Besides that it has become quite common to use lithium salts, most prominently LiTFSI, for p-doping of the HTL[102] in dye sensitised solar cells[103] and subsequently also perovskite solar cells.[104] From a different perspective, an exceptionally well passivation of defects in perovskites by respective lithium halides has also been reported concurrently by various other groups.[105–107] Based on this promising prospect, research on the interplay of LiTFSI and PNC has been initiated.

6.1. Invoked Changes of Luminescent Properties

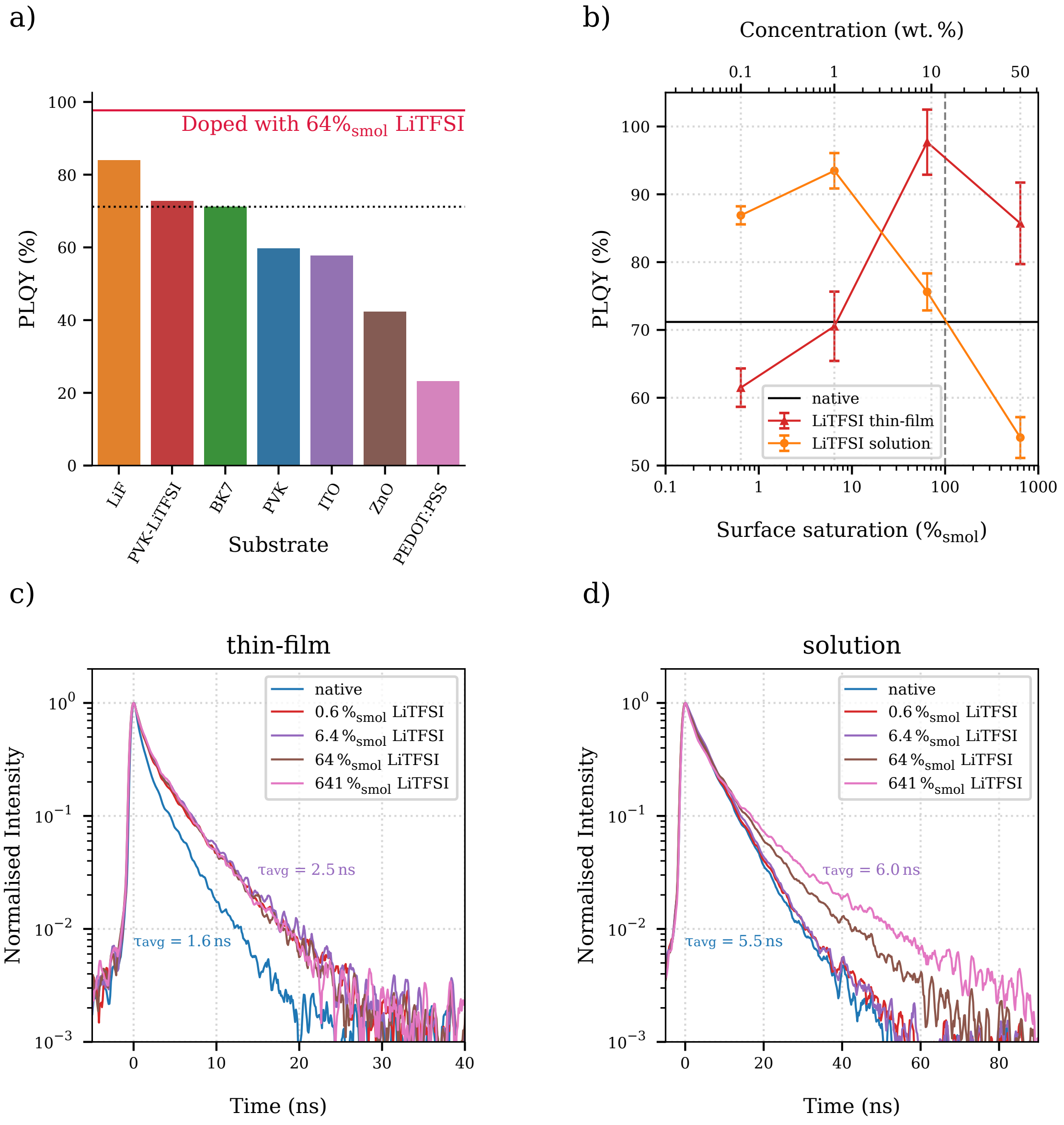

Figure 6.2.: a) PLQY of a thin-film of $CsPbBr_3$-NC on various substrates. It is increased on Li^+ substrates and lowered on conductive specimen.$^{S.35}$ b) The PLQY on a LiTFSI doped thin-film on fused-silica and its original solution.$^{S.36, S.37}$ Different optima are reached, the liquid phase promotes lower concentrations, while the solid phase prefers higher ones. c), d) The respective TRPL decays of thin-film$^{S.38}$ and solution$^{S.39}$ show a step-up for the former, while the latter gradually extend their excited state lifetimes.$^{S.40, S.41}$

Preliminary work on PNC thin-films shows a significant influence of the substrate on the quantum yield. Accordingly, most transport layers impair the PLQY of the PNC thin-film. In general, a decrease is expected, since excitons may dissociate more easily if a suitable electric contact is maintained.[108] That opens a loss path which will consequently lead to said decrease of its luminance.[109] Figure 6.2 a) gives insight on the magnitude of this effect. Shown are pristine $CsPbBr_3$-PNCs (native) spin-coated on various substrates. Highly conductive materials like ITO, ZnO and PEDOT:PSS act most detrimental to the PLQY compared a common glass substrate (BK7). Especially weak quantum yield is exhibited on PEDOT:PSS, which can be attributed to residual water content and the caused subsequent deterioration of the PNC.[110, 111] However, the lowering on the dry indium tin oxide (ITO) and ZnO originates from a different mechanism. For example, their high carrier densities may enable the mentioned exciton-charge quenching or the oxides could also facilitate a degradation of the PNCs.[112]

The material of most interest because of its usage as HTL in this study, PVK, shows a slight impairment on PLQY. The first contact of PNCs with LiTFSI is made unintentionally in order to facilitate hole-transport via PVK: a p-doping on PVK reported by Shi et al. [113] is reproduced. Astonishingly, the LiTFSI doping of the PVK proved to be beneficial to the quantum yield. Generally an enhanced conductivity, but also specifically LiTFSI doping, is expected to cost optical performance.[114] So the otherwise delicate PNCs appear to stabilise in contact with this lithium super acid[115] that is LiTFSI. Following a suspicion of an impact caused by the lithium ion itself rather than the $TFSI^-$, PNC layers are prepared on top of a thin layer of LiF. The resulting samples yield the highest PLQY of all investigated thin-films so far. Though a benefit by LiF on perovskite layers has been reported,[116] it has been ascribed to bigger grain sizes and less pin-hole defects of a bulk perovskite film. This explanation is not satisfactory for NCs, since their size and defects are predefined during and by the synthesis and are not expected to significantly change when spin-coated on a chemical passive layer such as a lithium fluoride.[7] Clearly, a novel process is responsible for this substantial enhancement in PLQY.

The immediate question, whether an inter-diffusion or the nature of the substrate alone is the main driver for this effect, is answered in case of LiTFSI by a ‘happy little accident’[117]. The importance of serendipity and embracing the outcome of miscommunication shall be boldly stressed at this point.[118] Anyway, by mixing the highly polar LiTFSI in chlorobenzene with the PNC in solution prior to spin-coating a distinct increase in brightness can be noticed bare-eyed. Despite using polar solvents and super acid agents the PNC improves its PLQY considerably over a wide range of mixing ratios. Also on thin-films, the PLQY can be raised strikingly to values near unity as plotted on figure 6.2 b).

While in both states, solution and thin-film, the quantum yield is increased by equal amounts, the concentration dependence is evidently different. For thin-films at low mixing ratios smaller than $6.4\,\%_{\mathrm{smol}}$, the PLQY is lowered compared to the native’s 71 %. But at higher ratios the quantum yield is raised to near unity before dropping back down to roughly the native level at a 1:1 weight ratio or put it another way an LiTFSI excess by doping with 641 $\%_{\mathrm{smol}}$. In contrast to that, the solution's PLQYs are already elevated at low concentrations. Furthermore, at higher ratios they drop below the native level. Note that the PLQY of the native, untreated PNCs (solid black line in figure 6.2 b)) stays within error margins regardless whether measured in film or solution. The solution maximum PLQY is generally lower and peaks sooner than the one for the thin-film. Apparently, conditions in a thin-film differ substantially from that in the solution. A reason for that could be that for proper PLQY measurements the solutions have to be diluted in order to minimise reabsorption,[119] but dilution with any solvent of PNC solutions leads to degradation.[120] In order to avoid damages by dilution, a less polar solvent, toluene, is used. Then again, the polarity of the solvent mixture used for the solution-PLQY, is now less polar than the one used to spin-coat the thin-films, which is in favour of the stability of the PNCs. The decline in polarity could turn out to be more beneficial than the impairments by the dilution process itself. That explains the concentration offset between the maximal PLQY of the PNCs in their respective states.

It seems that also the reduction in PLQY at exalted concentrations is correlated to the polarity. At higher doping ratios hypothetical, dispersed LiTFSI crystallites could parasitically absorb the excitation. This proposed absorption by LiTFSI agglomerates is more prominent in the solution-samples, where they are more prone to form as the solvent's polarity is lower. This suspicion is reasonable as LiTFSI proved to precipitate entirely at elevated concentrations. Furthermore, the high PLQY at low doping ratios can be motivated by the less polar solvent effectively pushing the polar LiTFSI molecules towards the PNCs. The existence of a separate LiTFSI-phase may also be established in the thin-film, as indicated with an x-ray diffraction spectroscopy (XRD) measurement on a highly doped film, shown in figure 6.4 d) . A new peak pair arises at a concentration of 237 $\%_{\mathrm{smol}}$. This peak could not be reproduced with concentrations of 64 $\%_{\mathrm{smol}}$ and 6.4 $\%_{\mathrm{smol}}$ (not shown). Concluding, the PLQY drop at 641 $\%_{\mathrm{smol}}$ for the thin-film and 6.4 $\%_{\mathrm{smol}}$ for the solution, can be preliminarily attributed to this undesired phase.

Anyway, the PL spectra as well as the transient PL (TRPL) decays disclose a strong impact by LiTFSI even at the lowest investigated doping ratio. An immediate red-shift at 0.6 $\%_{\mathrm{smol}}$ is observed in both states, even though the magnitude of the shift is stronger for the solution (see figure 6.3). Additionally, for the thin-film the red-shift reduces on elevating concentrations, while it stays constant or if at all increases for the solution. Interestingly, the sudden shift is observed in terms of lifetime for the TRPL characteristics of the thin-film shown in 6.2 c) , but for the solution, confer 6.2 d) , it is more gradual. The mean lifetimes are little more than double as high as the ones for the thin-film. Considering the respective components of a bi-exponential fit, figures S2 to S5, it is conspicuous that the lifetime of the long part for the thin-film is greater or equal to the prompt part for the solutions (cf. figure S3 c) and S5 c)). Additionally, the solutions long decay part lifetime is also roughly around double the lifetime of the respective thin-film's long part. With the absorption processes in LHP-PNCs happening within a few picoseconds,[121] negligible on the considered scale, one can speculate that the doubling in lifetime arises from a reabsorption and subsequent secondary emission. As already, explained in context of photon-recycling for the DCs, such reabsorption reduces the measured PLQY. This circumstance further supports the argumentation given to explain the more pronounced drop of PLQY at elevated concentrations of the solution measurements versus the thin-films. Especially, the lifetimes deviate from this doubling at the two investigated concentrations where the solution's PLQY drops, that is $64\,\%_{\mathrm{smol}}$ and $641\,\%_{\mathrm{smol}}$, leaving further indication of an alien process, which could also be addressed to such LiTFSI crystallites absorption.

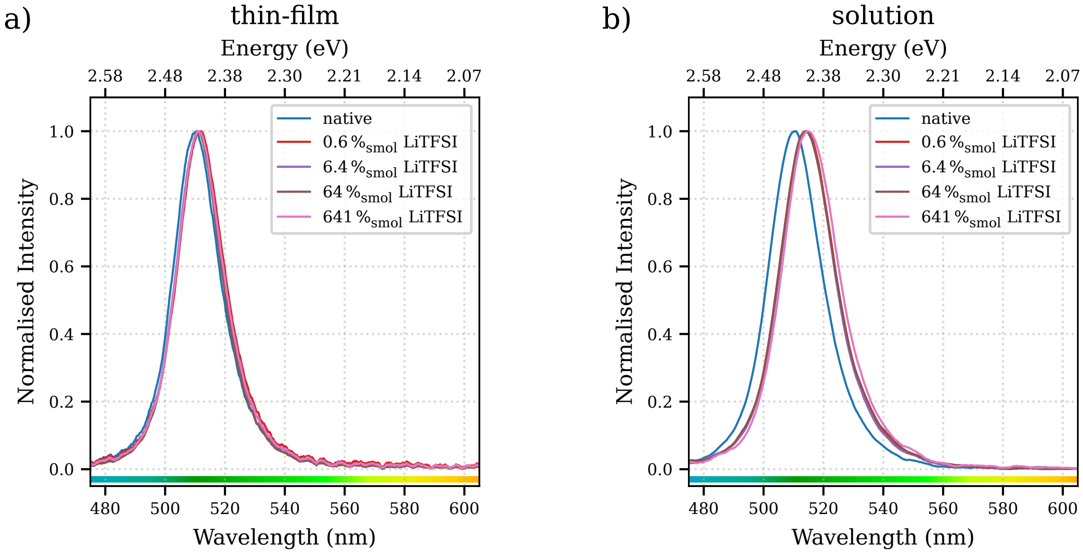

Figure 6.3.: Photoluminescent spectra of LiTFSI PNC a) thin-films[S.42] and b) solutions[S.43] doped at various concentrations. For the solutions, a constant, moderate redshift of around 180 meV (4 nm) is exhibited even at the lowest concentration, but for the thin-film the redshift is less pronounced, about 80 meV (2 nm), and decreases at higher ratios to only 40 meV (1 nm).[S.44]

In conclusion, the sudden TRPL decay change and the spectral shift of the thin-film imply a passivation occurring which outweighs the detrimental effect of the polar solvent at higher LiTFSI content.[122] The nature of this passivation is most probably a ligand exchange already in solution as similar observations have been made on the dynamic respectively labile binding conditions of the oleic acid and oleylamine on a red PNC's surface.[123, 124] Still, if there is an actual passivation of the NC surface, the TRPL liftimes are expected to gradually increase just as the PLQY does. However, the PLQY is reduced if there is an absorption of the UV excitation without a subsequent re-emission in the detected, visible range. Such absorption can arise from the already mentioned solvent degraded PNCs. The proposed LiTFSI agglomerates are not contributing at the investigated low concentrations. On the other hand, the TRPL decay rates do not necessarily have to be affected by this undesirable absorption. If the degradation by-products are not interacting with the optically active ones, the obtained TRPL characteristics originate solely from intact NCs without any impairment, while the PLQY is very sensitive to it. Even so, the unharmed PNCs' TRPL reveals that, while having comparable lifetimes, the weighting of the amplitudes shifts towards higher times. Keeping the PLQYs in mind, within the prompt decay there have to be more nonradiative decay processes. This indicates a trap-assisted recombination is being suppressed by the presence of LiTFSI. Several papers on surface trap passivation using different halide salts have been published. They concur on a halide abundance-based passivation process, which has already been documented by researchers utilising lithium-free halide salts.[37, 125–127] But in the present situation, the halide-free LiTFSI appears to have a comparable impact. The reported passivation by Liu et al. [128] via H^+TFSI^- accompanies a substantial blue-shift and a shrinkage in NC size. Although, these peculiarities are not present (cf. SEM images on figure 6.4), a similar chemical reaction may still take place at a unit cell on the PNC surface:

$$CsPbBr_3 + Li^+TFSI^- \rightleftharpoons CsPbBr_2TFSI + Li^+Br^- . \qquad (6.1)$$

The main difference to the H^+TFSI^- passivation is that the generated lithium halide salt is less volatile than the associated halide acid, in this context, LiBr being less volatile than the gaseous HBr[129], successfully preventing a continuous degradation of the NC surface and avoiding a potential shrinkage. This procedure is energetically attractive because bromine has a stronger affinity to bind Li^+ than $TFSI^-$.[130] This may account for why adding LiTFSI passivates $CsPbBr_3$-NCs without affecting their size or form. In addition, the present LiTFSI-treated NCs show improved stability to polar solvents, just as reported by Liu et al. [128], too.

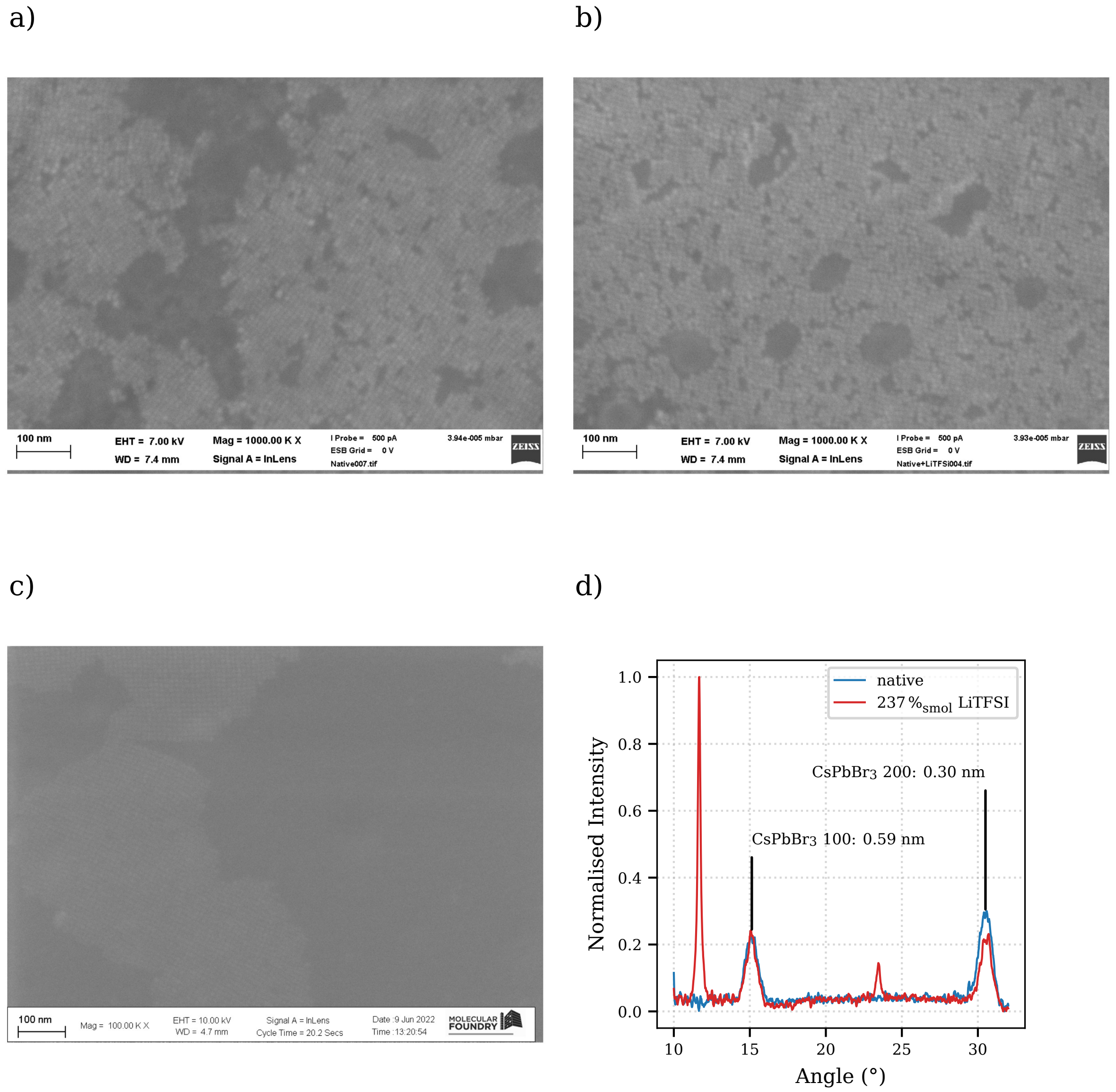

Figure 6.4.: SEM images of a thin film of $CsPbBr_3$ NC deposited on PVK a) without, b) with 6.4 $\%_{smol}$ and c) with 237 $\%_{smol}$ LiTFSI doping. The dark areas are not holes but a subsequent layer of PNCs, which has been verified by its energy-dispersive x-ray spectroscopy (EDX) mode for no and 6.4 $\%_{smol}$ doping.[S.45, S.46] d) XRD spectrum of $CsPbBr_3$ NC films on 1 mg/ml PVK on a silicon wafer.[S.47, S.48] At high doping concentrations a new phase arises, and the film becomes highly ordered as seen in c) its SEM image.[S.49]

6.2. Beneficial Electrical Characteristics

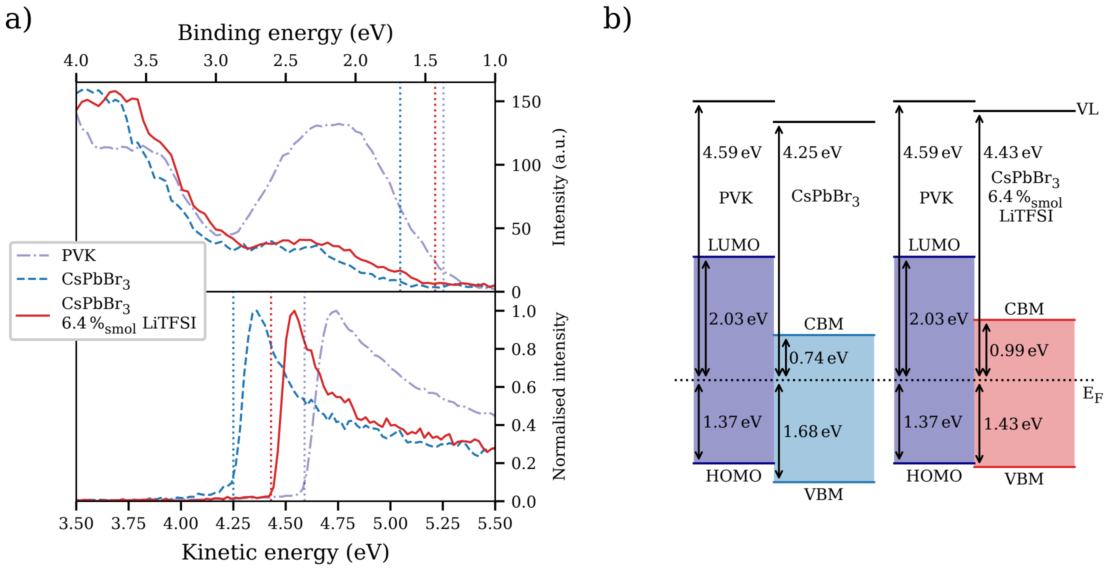

Figure 6.5.: a) UPS spectrum of the hole-injection relevant thin-films with the lower plot showing the SECO and the upper the valence region.[S.50] b) Schematic plot of energy levels obtained from the plot on the left, CsPbBr$_3$ appears to become less n-type upon doping, promoting a potentially enhanced hole injection from PVK.[S.51, S.52]

The dopant has proven to be eligible for the application on PNCs in terms of chemical compatibility. The requirement to not severely alter or impair the optical properties is fulfilled. Actually, it exceeds expectations and even improves key properties of the PNC. With that, the initial goal to achieve a beneficial effect on the electric accessibility has yet to be shown. With ultra-violet photoelectron spectroscopy (UPS) and x-ray photoelectron spectroscopy (XPS) the surface valence respectively the core energy levels of thin-films can be reliably determined. Since a p-doping affects primarily the structure around the VBM, the PNCs are probed on a hole transporting thin-film. For maximal comparability, the same PVK layer, as used for the PeLEDs of this study, is chosen as such HTL. Four combinations with two sublayers and two PNC layers are investigated. Firstly, just the PVK layer is investigated to get familiar with the substrate. The two perovskite layers, pristine and 6.4 %$_{\text{smol}}$ doped CsPbBr$_3$-NCs, are spin-coated on a PVK layer such as the first sample. Also, for observing the possible inter-diffusion of LiTFSI to the adjacent perovskite layer, a 1 wt. % LiTFSI-doped PVK layer is substrate to another native CsPbBr$_3$ thin-film. Note that as the PNC specimen of interest the 6.4 %$_{\text{smol}}$ doped CsPbBr$_3$ is chosen to be used. This doping ratio is used for the detailed characterisation as a compromise based on the PeLED's performance discussed in the next section. For a better overview the spectrum of the doped PVK sublayer underneath the untreated PNCs is omitted from figure 6.5. It exhibited very similar behaviour as the sample with the doped $CsPbBr_3$ layer on pristine PVK. This circumstance implies a non-negligible diffusion and provides a different glance on the initially determined increased PLQY of PNCs on this layer from figure 6.2 a).

Anyway, the top part of figure 6.5 a) plots the valence region while the bottom part represents the secondary electron cut-off (SECO). Latter shows the released electron's energy from PVK relative to a vacuum level, according to Einstein's [131] photoelectric effect. By setting the scale in a way, that the Fermi level (E_F) equals the photons' energy resp. zero for kinetic energy resp. binding energy, this edge is located at its workfunction, avoiding dipole and HOMO influences. Details about this rescaling method can be found in references 132, 133. In any case, the workfunction of PVK is determined as deep as 4.59 eV. The work function drops to 4.25 eV when $CsPbBr_3$ NCs are deposited, most likely as a result of band bending and/or the establishment of an interface dipole at the buried interface.[134] Then, in relation to E_F, 1.68 eV is extrapolated as the valence band (VB) onset of $CsPbBr_3$. With the energy gap of the present PNCs of around 2.42 eV (512 nm), this implies that E_F is placed above mid-gap indicating a strong n-type character on the surface of the NCs. Additional surface photovoltage measurements made under white light illumination reveal no variations in the energy levels of the $CsPbBr_3$-NC, confirming a flat band state across the LHP-NC layer.[135] Therefore, it is envisaged that the surface energy levels will likewise reflect the electrical characteristics of the LHP-NC thin-film. Upon applying LiTFSI-doped $CsPbBr_3$-NCs instead, the workfunction settles deeper by 0.2 eV at 4.43 eV. Concurrently, the obtained VBM shifts by 0.25 eV in the same direction to 1.43 eV with respect to E_F. However, due to the sensitivity of the $CsPbBr_3$-NCs the UPS has to be performed at very low excitation intensities, as higher UV fluxes are found to change the electronic structure quickly and irreversibly. Consequently, the signal-to-noise ratio at the upper valence band region is insufficient for an extraction of the VBM on a logarithmic intensity scale of the photoelectron signal. In order to more accurately infer the band edge clearer signals are required, because of the low density of states at said region.[136, 137]

Fortunately, XPS can be done accurately without the low intensity impairments and shifts of the same magnitude are observed by it (see figure S6). The consistent energy level shift from core to valence levels distinctly demonstrates a potent p-doping of the $CsPbBr_3$-NCs by LiTFSI. Additionally, a weak fluorine signal can be measured (cf. figure S6 d)), which is not obtained for the untreated perovskite thin-film. By the considerations of Liu et al. [128] such peak is indicative of an attachment of $TFSI^-$ on the surface of the NCs. Note that in the present XPS measurement the sulphur and nitrogen peaks could not be identified, since the excitation is still kept too low. The full energy level landscape of the PVK-$CsPbBr_3$ interface is illustrated in figure 6.5 b). The initial HOMO-VBM level mismatch can be reduced from 0.31 eV to as low as 0.06 eV. Reducing this offset and by implication improving the hole transport ability of this interface can be conclusively ascribed to the successful p-doping of the $CsPbBr_3$-NCs by LiTFSI.

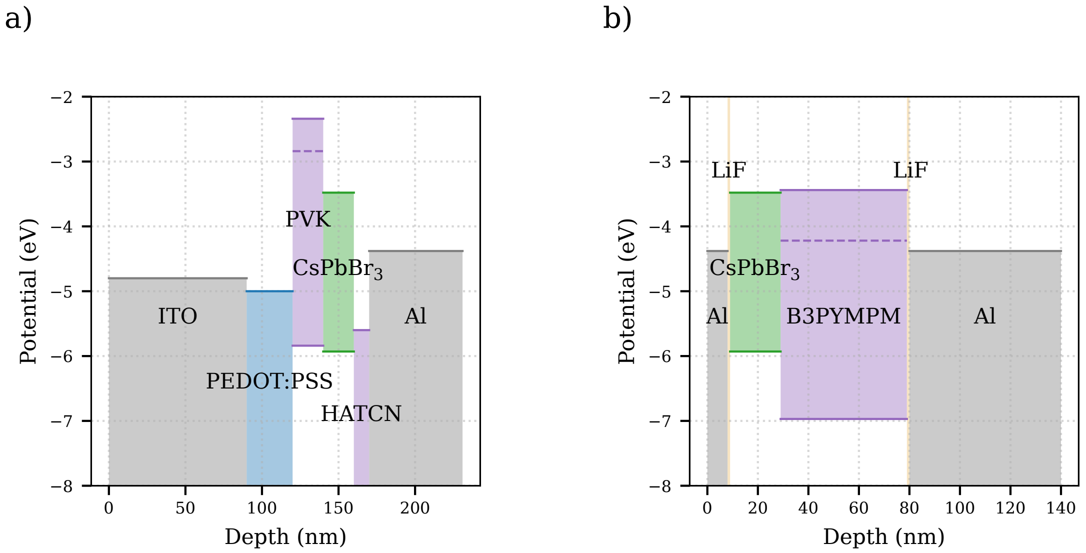

Figure 6.6.: Schematic sketch of the layer sequence for an a) hole-only[S.53] and b) electron-only device.[S.54] An ITO-$CsPbBr_3$ contact can not be established: either the etching-edge, general contamination or roughness lead to shortcuts. A thin aluminium layer with LiF excels.[S.55] Energy levels taken from references.[64, 65, 70–72, 74, 75, 138]

This proposed reduction in hole injection barrier is manifested in the electrical transport behaviour. In pursuance of proving an enhanced hole transport across the PVK-$CsPbBr_3$ interface a so called ‘single carrier’ device is designed. The purpose of such setup is to allow current of only one carrier type to pass it. For a hole-only device the current is restricted to the valence bands while for an electron-only the conduction band of the semiconductor is used. For investigating interface effects the layer thicknesses should not be extensively big, because the currents should be limited by the interfacial resistance rather than the resistivity of the bulk materials. Practically the single carrier devices are created in a way, that the tested contacts are as much comparable to the PeLEDs’ contacts as possible (compare figures 6.9 c) and 6.6). Figure 6.7 shows the current density – voltage characteristics of the single carrier devices applied in forward bias, that is positive charge at the bottom contact respectively negative at the top contact. Like that, only the charge injection occurring during the PeLED operation is probed. Specifically, only the currents in direction of the PVK-$CsPbBr_3$ (for hole-only) and the B3PYMPM-$CsPbBr_3$

(for electron-only) contacts are investigated.

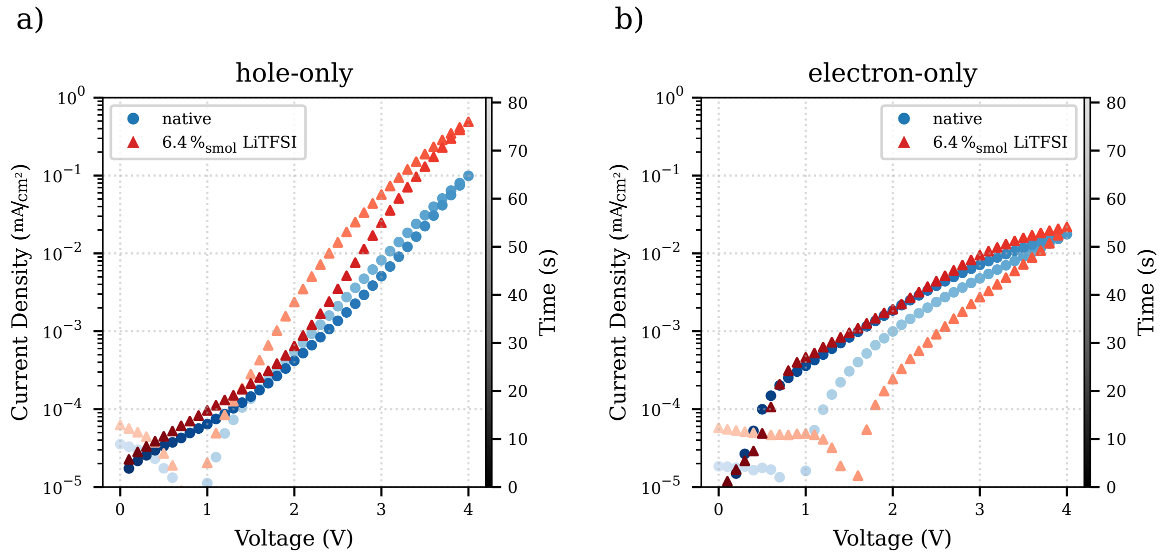

Figure 6.7.: Current density vs voltage plot for single carrier devices: a) hole only[S.56] b) electron only.[S.57] The LiTFSI-doping significantly enhances current only for the hole dominated device.[S.58]

Indeed, the currents of the hole-only device are overall increased to a maximum difference by a factor of two at 4 V, while the electron-only currents remain during the ascending voltage ramp unchanged for the most part and are even significantly decreased during the descending voltage ramp. Additionally, on the descending ramp the current for the doped sample reaches zero at around 1.5 V, which is higher than other devices' zero current voltage. The samples are measured in darkness so a photo-voltage can be ruled out, leaving an increased capacitance respectively a displacement current as cause for this offset change. This hysteresis reveals that the electron-only currents contain a non-negligible displacement current. With the slow ramp speed in mind, it most probably arises from ion migration, which may even be enhanced since the p-doping introduced additional mobile Li^+ ions. A small displacement current is present in any of the thin-film devices and it originates mostly from its geometry, which is the reason the three other curves' (both hole-only and the native electron-only) nulls are at comparable values. A detailed explanation and consideration on displacement currents is given in chapter 8. Anyhow, the electron-only currents are not enhanced and most probably even suppressed. On the other side, the hole-only device exhibits increased currents on backwards ramps, with the generally elevated current the capacitance plays a minor role at voltages higher than 2 V. The pitfall to assume an enhanced contact when in reality the thin-film got thinner or developed holes from the LiTFSI treatment, can be excluded by the present morphological characterisation of the same. The SEM images, printed in 6.4, imply that the neither the film morphology nor the coverage changed towards higher conductance. If at all, the LiTFSI addition even slightly improves the coverage which would increase its resistance. Also, the thickness remained constant, that is, within a 5 nm error margin around 20 nm, as confirmed by AFM measurements (not shown).

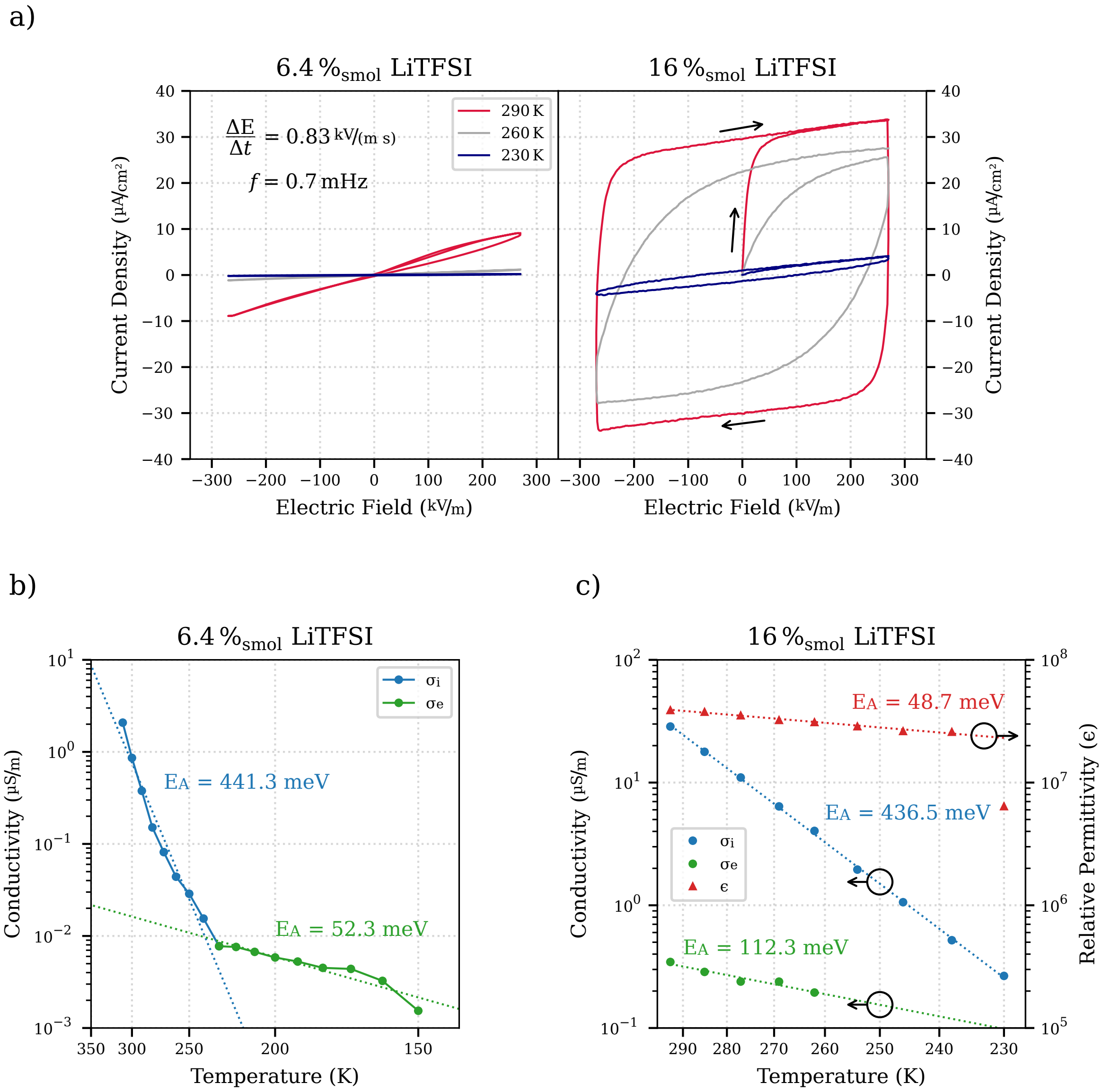

Figure 6.8.: A PNC-TFT without gate contact is characterised at various temperatures: a) j-E plots on two doping concentrations reveal a non-negligible displacement current.[S.59] Arrhenius plots, b) and c),[S.60, S.61] imply a thermally activated conductance. Same for the permittivity in case of c).[S.62]

In order to focus more on the transport and less on the interfacial effects of the perovskite layers, the LHP-NCs are investigated in a gate-less Thin film transistor (TFT) structure. By the geometry of a transistor device potential charge injection without a gate-voltage is strongly suppressed enabling detailed consideration on charge transport. Figure 6.8 a) shows the current density vs electric field dependence at doping concentration $6.4\,\%_{\mathrm{smol}}$ and $16\,\%_{\mathrm{smol}}$. Note that the measured currents originate from a saw-tooth waveform applied voltage and measured current. The electric field and current density are calculated from the dimensions of the TFT. That is, the area for current density comprising the film's thickness and the channel width, and the channel length is used to obtain the electric field from the voltage. Anyhow, for the native sample no considerable current beyond the noise was obtained, so the current density stayed below $0.1\,{}^{\mu\mathrm{A}}\!/\!{}_{\mathrm{cm}^2}$, with both LiTFSI treatments leading to orders of magnitude higher charge transport. Consequently, the doping has not only enhanced the hole injection but also conductivity. Furthermore, a strong temperature dependence of the charge transport through the devices is observed (cf. figure S7). For room temperature measurements a displacement current can be extracted. While being just a perturbation at $6.4\,\%_{\mathrm{smol}}$ it accounts for the major part of the current within the $16\,\%_{\mathrm{smol}}$ doped thin-film. The $6.4\,\%_{\mathrm{smol}}$ j–V curve is fitted with a linear function, representing a simple resistor, and the capacitive deviation at elevated temperature is neglected. But for the $16\,\%_{\mathrm{smol}}$ sample, there is a very distinct exponential behaviour which is modelled by a leaky capacitor in series with a resistor (RRC, see section A.2.6) matching well with the data over all temperatures as shown in figure S7 b). The extracted conductivities are plotted versus temperature in figures 6.8 b) and c). The temperature scale is set to be reciprocal and the ordinate is semi-logarithmic. This view, also called Arrhenius plot, facilitate the identification of a potential thermal activated quantity, since exponential functions of inverse temperatures (T) are depicted as straight lines. For the conductivity (σ) holds:

$$\sigma = \sigma_0 \exp\left[-\frac{T_A}{T}\right]. \tag{6.2}$$

with the Boltzmann constant (k_B):

$$T_A = \frac{E_A}{k_B}.$$

$$\ln\left[\frac{\sigma}{\sigma_0}\right] = -\frac{E_A}{k_B}\cdot T^{-1}. \tag{6.3}$$

With this relation an activation temperature (T_A) resp. energy (E_A) is introduced as a measure for temperature dependence.[139] For both thin-films a strongly temperature dependent conductivity component is observed. Activation energies as high as 0.4 eV imply an ionic hopping rather than charge carrier hopping transport.[140–142] In case of non-negligible capacitance the giant permittivity of more than ten million reveals to be also thermally activated. Even though high relative permittivities are quite common in perovskites as well as in LiTFSI blends,[143–146] the obtained giant dielectric constant exceed reported values by at least an order of magnitude. This further hardens the evidence for a strongly ionic system, especially with the fact that the displacement current increases with higher concentration and is absent for untreated films (not shown). Then again, due to the geometry of the samples and the sensitivity limit of the measurement device this measurement was performed at a very low sweep speed resp. frequency of less than 1 mHz which enables ions to significantly contribute to the displacement currents boosting the dielectric constant to unprecedented values. In contrast to this ionic conductivity, σ_i, a second temperature dependence is identified at energies more close to electronic hopping transport, σ_e. The exact origin of this second contribution remains elusive. Whether it actually arises from an electron hopping process can not be decided with the present data. However, even this second conductivity is increased by roughly one order of magnitude from less than $0.03\,{}^{\mu\mathrm{S}}/_{\mathrm{m}}$ to $0.4\,{}^{\mu\mathrm{S}}/_{\mathrm{m}}$ when using $16\,\%_{\mathrm{smol}}$ instead $6.4\,\%_{\mathrm{smol}}$ and using the extrapolations for comparison. At the same time the activation energy approximately doubled, which indicates also at least a correlation to the ionic nature of the LHP thin-film. Note that σ_e can not be determined by the RRC fit for temperatures below 260 K since the substantially slowed charging of the capacitor is limiting the overall current, causing this, supposedly electronic, part to vanish and consequently its based resistance to diverge erratically.

So while for the in-plane configuration, that is, the TFT setup, there are major ionic movement detectable, for the out-of-plane setup, the single-carrier devices, ions pose only a perturbation if at all. The main difference of these arrangements is the electric field that the thin-film is exposed to. That is a few volts over a thickness of less then hundred nanometres, the total thickness of the non-metallic layers of the stack, for the single carriers, which equals electric fields of magnitude greater than $10\,{}^{\mathrm{MV}}/_{\mathrm{m}}$. It is two orders of magnitude smaller at around $100\,{}^{\mathrm{kV}}/_{\mathrm{m}}$, by applying a voltage of few tens of volt over slightly more than hundred micrometres, the TFT channel length. In other words, the same electric field as in the in-plane at 10 V is roughly realised at 0.1 V. Herein, the field sweep rate is inherently higher. The sweep rate of $0.1\,{}^{\mathrm{V}}/_{\mathrm{s}}$, used for the single carrier devices in figure 6.7, corresponds to, $0.1\,{}^{\mathrm{V}}/_{\mathrm{s}}$ divided by a) $d = 80\,\mathrm{nm}$ b) $d = 70\,\mathrm{nm}$, an electric field rate of a) $1.25\,{}^{\mathrm{MV}}/_{(\mathrm{m\,s})}$ and b) $1.43\,{}^{\mathrm{MV}}/_{(\mathrm{m\,s})}$. Compared to the field rate of $0.83\,{}^{\mathrm{kV}}/_{(\mathrm{m\,s})}$ of the in-plane device it sweeps three orders of magnitude faster. Notably, the charging current, I, of any capacitor does primarily only depend on time, t: $\mathrm{I} \propto \exp\left[-{}^{t}/_{\mathrm{RC}}\right]$. With that, by comparing the TFT and the single carrier, one could assume that the sweep rate is too fast for the slow ion movement. However, if the resistor, R, and/or the capacitance C is field or time dependent, the charging current will also be secondarily. Additionally, the resistor is not even comparable between the two setups, for the single carrier it is a diode-like resistor and the area is tremendously bigger. Such strongly decreased contact resistance already reduces the RC-time to a value that the ion movement may become significant again. Furthermore, the field and time dependence of the capacitance of the single carrier device is unknown, and expected not to be constant for various reasons. To name some, the degradation of PNCs in high fields lead to change in ion quantity or the injection of charge carriers may contribute to significant field screening effects. All these issues, render a comparison of the transistor and the single carrier device very challenging, so that the role of ions movement in the single carrier device remains elusive.

Finally, the electrical characterisation of the PNC thin-films yields some insights about the effect of LiTFSI doping on it. A substantial energy level shift is induced by a moderate doping concentration, rendering the PNCs less n-type and therefore enhancing a potential hole injection from PVK. This implication is proven with considerably increased currents in a hole-only device, while the corresponding electron-only device shows no such clear current increase. Furthermore electrical hystereses, also measured in a transistor structure, reveal a contribution from ionic movement, which is tremendously increased by higher doping concentrations. However the current increase is identified to be not only of ionic nature. Even though the ionic displacements do not seem to influence the current of the single carrier device by a big extent, the presence of these highly mobile ions in this device is undeniable, and may propagate to play a major role in light-emitting devices.

6.3. Improved Perovskite Nanocrystal Light-Emitting Diodes

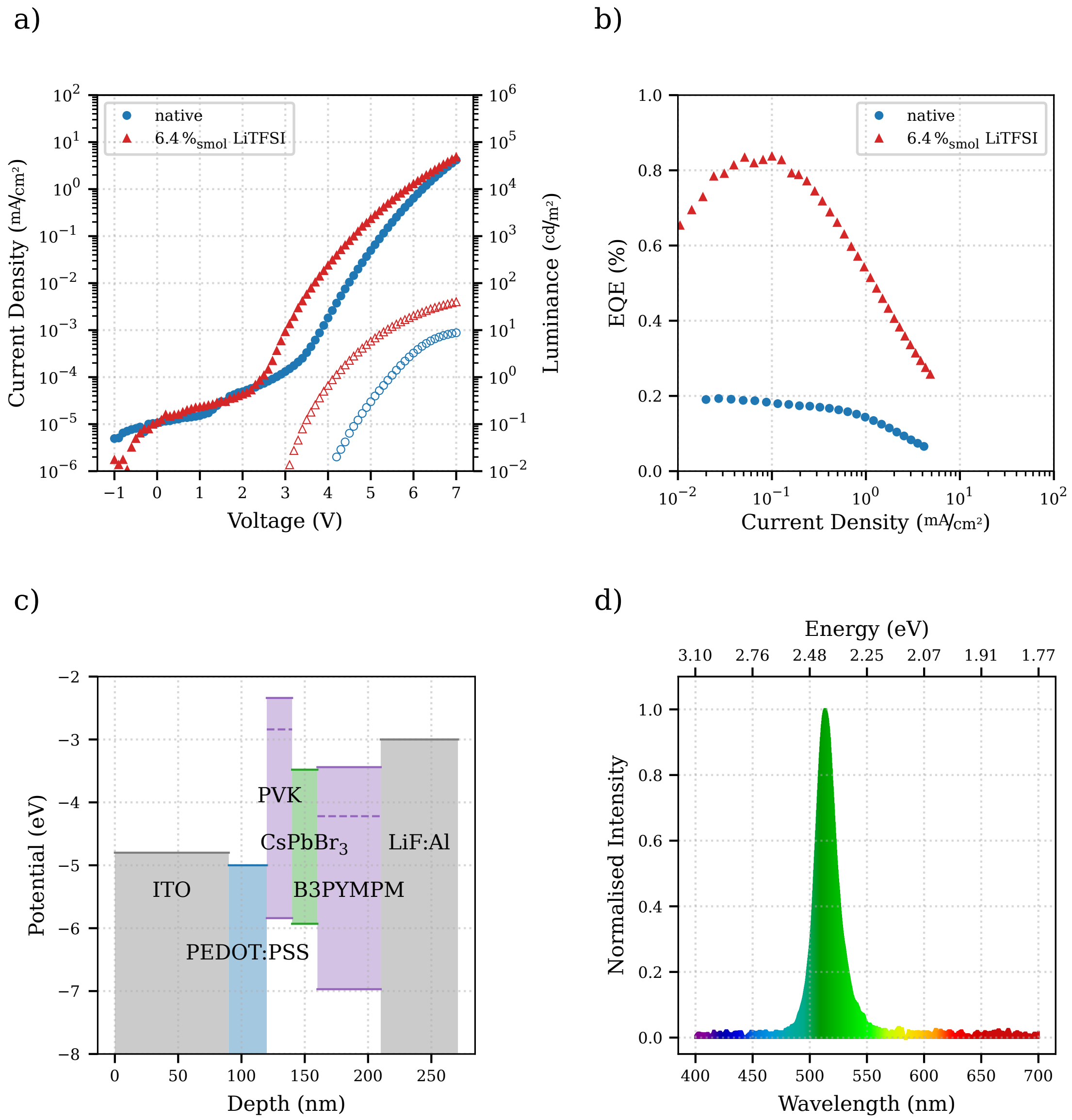

Figure 6.9.: PeLEDs made from $CsPbBr_3$-NC thin-films: the, a), j-V-L plot exhibits improved currents as implied from the single carrier devices, at the same time an over-proportional increase in luminance is detected.[S.63] The surplus brightness is proven by the EQE-j plot, b), showing a quadrupled efficiency.[S.64] c) illustrates the energy levels, taken from references,[64, 65, 70–72, 74, 75] of the materials comprising the PeLED.[S.65] Their EL-spectra, d), showed no notable colour-shift neither during the time of operation nor induced by doping.[S.44, S.55, S.66, S.67]

So far, key parameters ruling the performance of PeLEDs, η_{QY} and γ considering eq. 3.3, are enhanced substantially. With that, this section will detail the implications of these improvements. The tested injection contacts are combined to assemble a thin-film stack for light-emission. The choice of materials has been elucidated in context of chapter 3. While the thickness of PVK is, because of its very low hole mobility, optimised experimentally, the dimension of the ETL, B3PYMPM with refractive index n, is kept roughly around $^{\lambda}/_{4n}$ avoiding destructive interference within the created micro-cavity between the electrodes. Actually, the simple consideration with a single wavelength (λ) turns out to be very close to a simulation of the device with the PL spectrum according to this group's previously reported method. This simplification is justified by the very narrow-band spectrum. General details on this can be found in reference 147 and more PeLED-specific considerations are undertaken by Morgenstern et al. [59]. A PeLED-stack as depicted in 6.9 c) is used for all the LEDs in this study, if not explicitly stated otherwise.

The current – voltage – luminance characteristics, plotted in figure 6.9 a), feature two current onsets for the native sample: one occurs just above 1 V while the second is located as late as 3.5 V. The first onset can be assigned to an early electron injection, due to the n-type nature of the PNCs discussed in the previous section. After a short accumulation, respectively stagnating current, the steep current increase followed by a luminance onset at around 4 V is accordingly identified as hole injection. In contrast to that, the double-step property vanishes for the LiTFSI-doped NCs. The two onsets seemingly meet in the middle to form a single steeper current increase at 2 V accompanied by a proportionally sooner luminance start at 3 V. On top of that onset mismatch, the current and luminance rises substantially quicker for the treated PeLED than for the pristine. At elevated voltages the LiTFSI doped PeLED's current also flattens more rapidly than the native so that they meet at 7 V. However, the luminance stays significantly higher, while being two orders of magnitude apart at 4 V, a factor of four remains at the maximal voltage. This discrepancy is projected on the efficiency: the EQE is also increased fourfold, from 0.2 % to 0.8 % and remaining at double the native value at higher currents as shown in 6.9 c). During the operation the native as well as the treated sample are emitting the same narrow green EL-spectrum with only changes to the intensity value but none to the spectral distribution.

As for the PLQY series, a batch of PeLEDs with varying LiTFSI concentrations is fabricated (cf. figure 6.10 a)). The current and luminance onsets are not shifted further towards lower voltages at higher doping ratios. The lowest considered doping ratio even decreased currents indicating insufficient influence by the dopant supporting the previously given explanation in context of the lowered PLQY for the same concentration. However, for LiTFSI contents higher than that, the current and luminance curves become continuously steeper with the exception of the excessively doped sample of 641 $\%_{\mathrm{smol}}$. Considering the new XRD peaks (cf. fig-

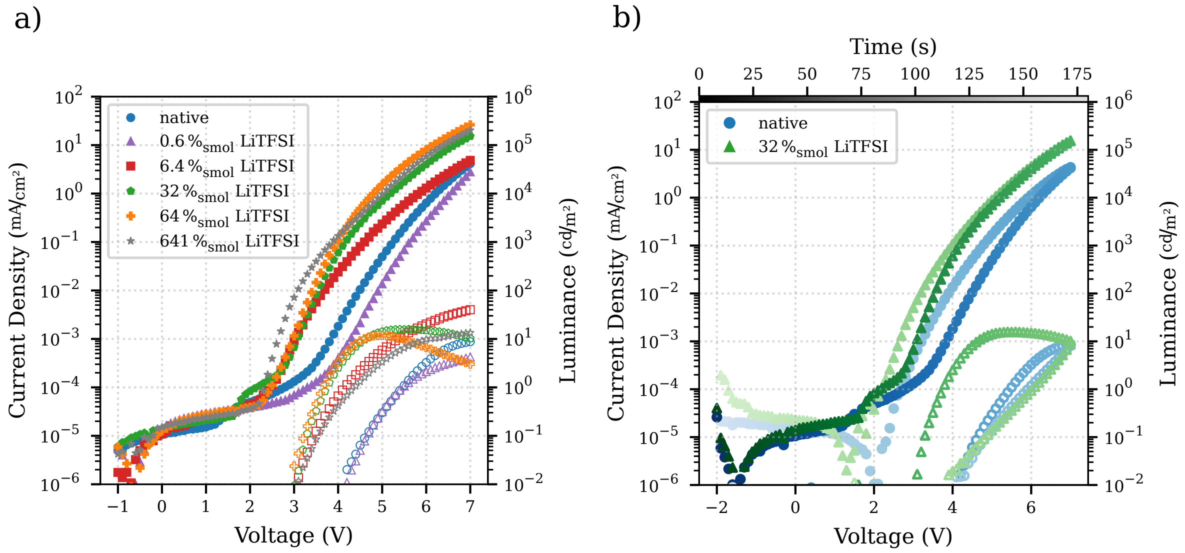

Figure 6.10.: The j-V-L curves, a), of PeLEDs with various LiTFSI doping concentrations reveal also an optimum comparable to the PLQY series and b) with a sweep-back for the champion device with 32 $\%_{\mathrm{smol}}$. Ionic movement are expected and surprisingly suppressed.[S.67–S.69]

ure 6.4 d)) taken at 237 $\%_{\mathrm{smol}}$, and reminiscing the definition of the unit $\%_{\mathrm{smol}}$ it becomes evident that a significant amount of LiTFSI molecules are unable to influence the PNC. Any potential LiTFSI crystallites could impair the integrity of the thin-film and lead to even higher currents and significant luminance losses, just as observed in the plot. Apart from that, when using less than 100 $\%_{\mathrm{smol}}$ the luminance onset is the most rectified. Consequently, the EQE reaches the highest values for 32 $\%_{\mathrm{smol}}$ at 1.3 % and for 64 $\%_{\mathrm{smol}}$ at 1.0 % (plotted in figure S8 a)). In opposition to that, the sample with only 6.4 $\%_{\mathrm{smol}}$ with its EQE peaking at only 0.8 % reaches higher luminances, while all the higher concentrated samples stay below 20 $\mathrm{cd/m^2}$. In case of the latter, elevated voltages induce a more pronounced degradation. This can be derived from the fall of luminance at voltages exceeding 5 V. Further insight on this degradation gives the investigation on the subsequent reverse sweep of the voltage. The j-V-L curve with such sweep-back is shown in figure 6.10 b) for the 32 $\%_{\mathrm{smol}}$ doped sample, the champion device that already exhibits this degradation. The hysteresis of currents is decreased for the moderately doped sample compared to the native, in contrast to the single carrier hystereses which are amplified by the doping (cf. figure 6.7). With that in mind, it can be concluded that the ionic movements may compensate to result ultimately in a decreased difference on forward and backwards measurement. Anyway, the detrimental irreversible luminance drop to the native level is telling. Apparently, along with the proposed increased ion migration the beneficial effect of the doping vanishes.

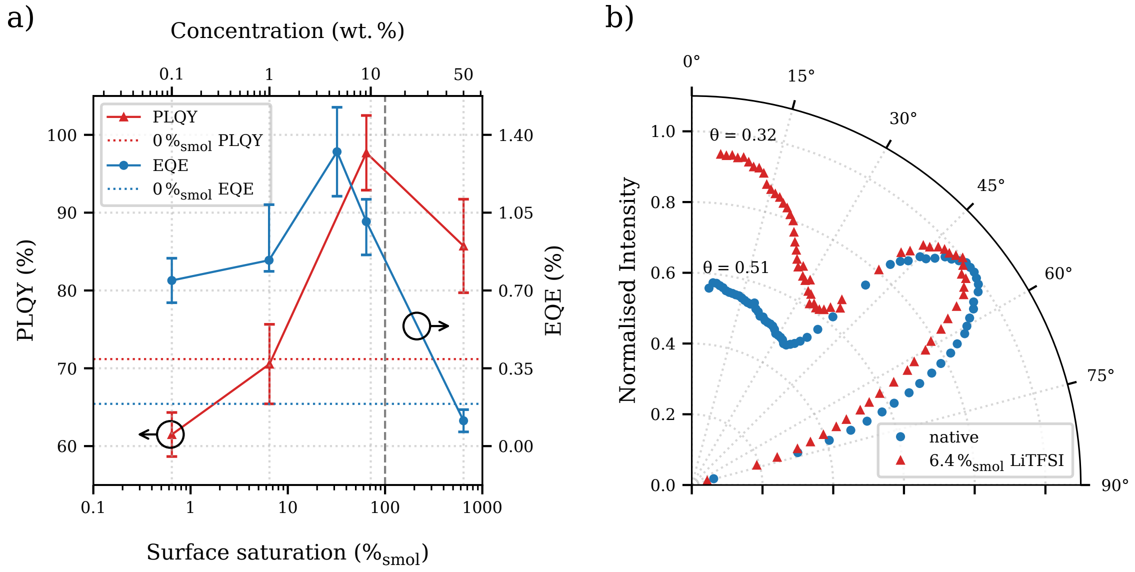

Figure 6.11.: a) The plot of concentration dependent PLQY and EQE describes a correlation with deviances at the extremes. It suggests a change in charge carrier balance or light out-coupling.[S.37, S.70] b) ADPL spectrum: the doped sample radiates significantly more light at the preferred low angles, which indicates said better light out-coupling.[S.71, S.72]

This disadvantage of high doping with LiTFSI is not projected on its PLQY, since in the absence of an electric field such voltage induced degradations fade. Figure 6.11 a) compares the concentration dependent PLQY (thin-film) to the EQE. The droop at high concentrations has already been elaborated, but for the EQE it is more prominent because any impairments on the PLQY will propagate to the EQE (see eq. 3.3). On the other hand, the EQE breaks its proportionality to the PLQY at low concentrations. The other two factors, that is, the light-extraction, η_{out}, and the charge carrier balance, γ, remain to influence the EQE to distort its proportionality to the PLQY. While the discussed research clearly indicate a beneficial change in γ, its extent of this dependence can only be further elaborated on once the magnitude of η_{out} is known. Figure 6.11 b) shows the parallelly polarised ADPL of the films manufactured identically to the PLQY samples. Such radiation patterns provide key information about the mean orientation of the transition dipole moments (TDMs) of the electronically active optical transition between excited and ground state. This concept has been detailed by studies for organic emitters as well as LHP-NCs.[60, 148, 149] Furthermore, the average TDM is a crucial factor to understand and improve LEDs and PeLEDs.[59, 148] In particular, the orientation parameter θ, defined as the fraction of power emitted by vertically oriented TDMs, directly displays the degree of anisotropy of the TDM orientation distribution. Accordingly, a θ of 0.33 denotes an isotropic case while larger, resp. smaller values, indicates more vertical, resp. horizontal, TDM orientation. The radiation pattern is changed drastically upon addition of LiTFSI compared to the pristine $CsPbBr_3$-film. A significantly higher portion of light is emitted at vanishing angles for the doped film. Consequently, the obtained TDM orientation parameter is nearly isotropic for 6.4 $\%_{smol}$ doped LiTFSI, $\theta_{LiTFSI} = 0.32$, while being more vertical for the native thin-film, $\theta_{native} = 0.51$ (cf. fits shown in figure S10). This results in a transition from the native NC film's undesirable vertical TDM orientation to an isotropic emission profile that matches the cubic structure of $CsPbBr_3$-NCs. An Al_2O_3 overcoating of LHP nanoplatelets has also been discovered to have a similar effect.[60, 150] In order to prevent the imbalance in the electrostatics between the substrate and the free surface of the NCs, it is thus assumed that LiTFSI functions as a dielectric layer. No doubt, the light-extraction is of high importance for any light emitting setup, in case of present PeLEDs the gain in EQE can be up to a factor of 1.3 (simulated according to Morgenstern et al. [59]). On the other side, it is limited to a factor, which is not sufficient to explain any of the enhanced EQEs in the concentration sweep (cf. figure 6.11 a)). The EQE of the native 0.19 % is increased to 0.74 %, 0.84 % and 1.32 % for concentrations 0.6, 6.4, 32 $\%_{smol}$. In none of the samples the enhancement is even close to the upper limit of 1.3, the improvement factors are more between three to seven. Especially, the sample with 0.6 $\%_{smol}$ shows a higher EQE than the native even though the PLQY is lowered by 10 %. Under the reasonable assumption that the orientation not being be more horizontal than the 6.4 $\%_{smol}$ sample, it proves that this improvement has to predominantly arise from γ. With that, even the PeLEDs' data prove, that the the carrier balance is optimised by the LiTFSI treatment. While the enhancement factors for PLQY and for η_{out} can be estimated to be smaller than 1.4 resp. 1.3, the charge carrier balance is identified to be key to gain the missing two orders of magnitude in EQE (from the native's 0.2 %) to match the one of commercialised OLED.

Finally, the beneficial effect of LiTFSI treatment of PNCs is not limited to $CsPbBr_3$. When using an altered halide composition, introducing iodine or chlorine to replace bromine, for red ($MAPbBrI_2$) or blue ($CsPbBr_2Cl$) LHPs, the lithium salt treatment leads to comparable efficiency boosts. In case of red PNCs, even the caesium cation is exchanged to MA. This shows that the doping is very versatile and applicable over a wide range of compositions. In case of the $MAPbBrI_2$ the conduction band and valance band are closer together due to the lowered energy gap compared to $CsPbBr_3$. Additionally, the VBM is not moved deeper towards 6 eV but rather to 5.4 eV.[72, 136] In contrast to that, the blue $CsPbBr_2Cl$-PNCs have a higher band-gap and consequently deeper VBMs beyond 6.1 eV.[72] So a charge injection into $MAPbBrI_2$ from PVK is inherently easier than into $CsPbBr_2Cl$. Actually, a shift of valence levels is no longer beneficial since the levels are below PVK's even without LiTFSI treatment (PVK: $E_{HOMO} = 5.96$ eV, cf. figure 6.5). For the blue PNCs, on the other side, the injection enhancement by the doping is expected to be even more pronounced. Considering the respective devices' currents presented in figure 6.12, it becomes evident that LiTFSI immensely increase currents for the blue device, while having insignificant influence on the red, partly even reducing the currents. For the $CsPbBr_2Cl$ based PeLED, the same argumentation as for $CsPbBr_3$ can be applied, to achieve EQEs up to factor of seven higher than the native (six for the resp. maximum EQE). The more prominent increase in current and EQE matches well with the hypothesised trend by the energy level landscape. On the other side, a five-fold increase in luminance and consequently EQE for the $MAPbBrI_2$ based devices is rather unexpected. Unlike all other considered PeLEDs of this research, the $MAPbBrI_2$ based device reveals a significant spectral change. Figures 6.12 b) and d) show the EL-spectra of the resp. PeLEDs. For the blue $CsPbBr_2Cl$ its narrow distribution does not change during operation as degradation only affects the intensity, comparable to the $CsPbBr_3$ based PeLEDs. The $MAPbBrI_2$ EL spectrum is initially very similar to its resp. PL spectrum and degrades to a spectrum reminiscent of a pure $MAPbI_3$ spectrum within 100 s of operation at $2.5\,{}^{\mathrm{mA}}\!/\!_{\mathrm{cm}^2}$. Interestingly, the degraded spectrum may look alike, the course towards degradation differs substantially. The LiTFSI treated device shows a gradual change in spectrum proportional to its intensity decay. Opposed to that, the pristine $MAPbBrI_2$ EL shifts abruptly within the first ten seconds close to this $MAPbI_3$ spectrum then exhibiting a luminance recovery over the next 70 seconds, only to very rapidly decay within the next 20 seconds to a flatline after 100 seconds of running. This non-monotonic behaviour arises presumably from a rapid halide composition change followed by a recrystallisation in the single iodine phase. The bromine ions may be expelled from the NC in order to temporarily stabilise as $MAPbI_3$, before degrading completely. The role of LiTFSI in this device is assumed to either stabilise the device by immobilising bromine ions via the already mentioned LiBr salt or to hinder electron injection, in order to delay the reduction of lead within the PNC. The latter explanation is based on the research on LHP degradation which identify the reduction of lead as a major part.[151, 152] Under the assumption that a surplus of electrons facilitates such reduction function, impairing electron injection may lead to an increased stability.

Summarising one can say that, using an LiTFSI doping process for the application of LHP-NCs in PeLEDs poses a viable approach. Firstly the the optical properties of the PNCs, that is, PLQY and emitter orientation is changed in favour. Additionally, the energy levels of the PNCs are lifted indicating a successful p-doping. Initially, the shifts are measured by UPS/XPS and further verified by the single carrier devices and PeLEDs. Furthermore, TFTs reveal a concomitantly enhanced conductivity. At the same time, significant ion migration processes are identified. Applied to PeLEDs these ionic movement do not exhibit a notable influence, as the boost in luminance and efficiency can be mostly explained by the valence level shift and the optical improvements. The overall efficiencies are not exceptionally high and the operational stability is still very low compared to OLEDs. During this study a very prominent efficiency spread between several synthesis batches has been observed. Also the shelf lifetime as well as operational lifetime changed considerably batch-wise. Nevertheless, over all the received batches the LiTFSI treatment showed similar improvements. There are several reports of high efficient PNC PeLEDs from several groups, who do not use a fundamentally different PeLED stack. This implies, that the main cause for degradation may originate from the particle itself, and the LiTFSI doping is a process to refine the PNC into perfection rather then fixing PNCs of poor quality. Then again, the red $MAPbBrI_2$ based PeLED reveals that an ion balance may also provide an approach to increase operational stability. Because of the more volatile nature of the iodine ions, balancing and confining ions has emerged as key feature to optimise for perovskite solar cells, and such management may also be of interest for PNCs at the surface. Also for the $CsPbBr_3$ and $CsPbBr_2Cl$, the anions may be generally less mobile during device operation, still their migration could play a major role for the degradation of the PeLEDs, which apparently is not fully compensated by the LiTFSI treatment.

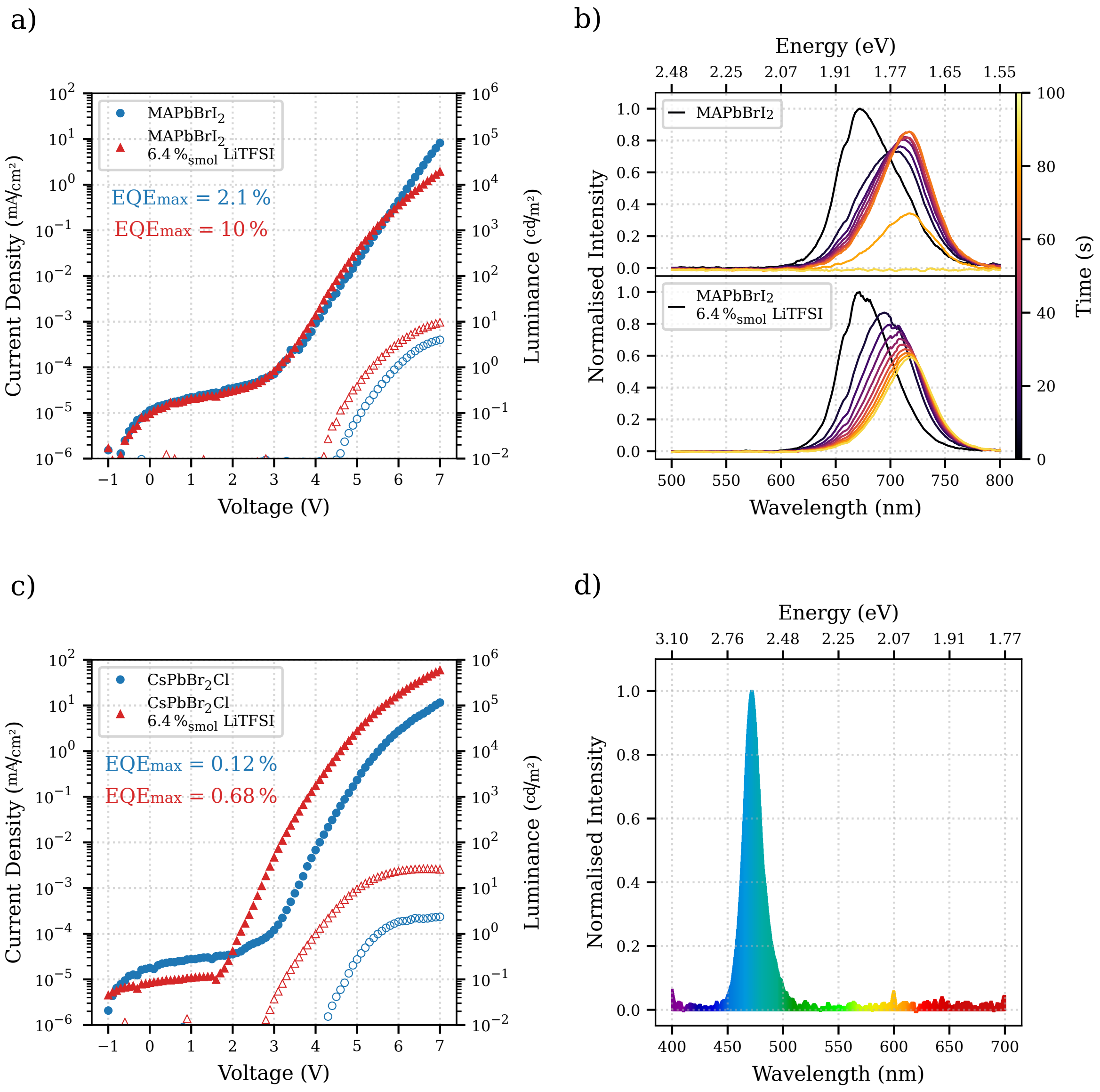

Figure 6.12.: PeLEDs made from red $MAPbBrI_2$-NCs: the, a), j-V-L plot reveals only minor initial current increase with a concurrently raised luminance leading to annotated peak EQEs (cf. fig. S9).[S.73] The turn-on voltage is comparable to the blue and green native counterparts. Their EL-spectra, b), show degradation-induced colour-shifts into the NIR. This change takes place step-wise for the native (upper plot) and gradual for the doped sample, indicating different processes.[S.74]
The PeLEDs featuring blue $CsPbBr_2Cl$-NC thin-films do not show such colour-shifts just like the $CsPbBr_3$ ones. Its EL-spectra, d), shows clear blue narrow-band emission.[S.75] c): At the same time, it also receives a major current boost with simultaneously overly raised luminance, respectively EQE, if LiTFSI-treated.[S.44, S.67, S.76]

7. Ligand-Engineered Nanocrystals

Up to this point, the PNCs themselves have been kept in their pristine state. Their core as well as the ligand shell remained mostly untouched. For the downconverters the NCs have simply gained an additional shell of insulation, while the LiTFSI treatment is aimed to alter the dielectric environment. Here, the native ligands, that is, oleic acid and/or oleylamine, have most probably unintentionally, at least partially, been replaced. This motivates into investigating further the intentional exchange of ligands on the surface of the NCs. Three different approaches of alterations to the ligand shell are investigated, ranging from a brief exploration of the impact of the ligand density on the surface of the PNCs to their exchange with a more strongly binding ligand such as lecithin and furthermore, based on that, developing a more electronically accessible ligand utilising carbazole moieties.

7.1. Optimising Ligand Density

The aliphatic ligands at the PNCs' surface are introduced during their synthesis and stay of most importance to their optoelectronic properties. This becomes evident when imagining the extreme case of removing all the ligands and its implications. Having no ligands attached to the PNC surface enables a recrystallisation towards forming aggregates which will ultimately end up in a state reminiscent of a polycrystal.[153, 154] However, the beneficial properties induced by the nano-crystallinity vanish at the same time. The other extreme, that is, over-saturating the surface with aliphatic ligands, leads to high stability and PL quantum-yield. In this case, the benefits are gained at the expense of a diminishing electrical conductivity at the same time. This simple picture already suggests that for the application into an optoelectronic device a compromise is needed. A photovoltaic device, for instance, does not rely on high quantum yields nor quantum confinement effects since the conductivity is crucial. Polycrystalline films with additives rather than NCs with ligands are state-of-the-art.[155] For LEDs on the other side, high quantum-yields are more important, so the research shifts more towards thin-films of nanostructures when optimising for efficiency especially for blue coloured devices.[156]

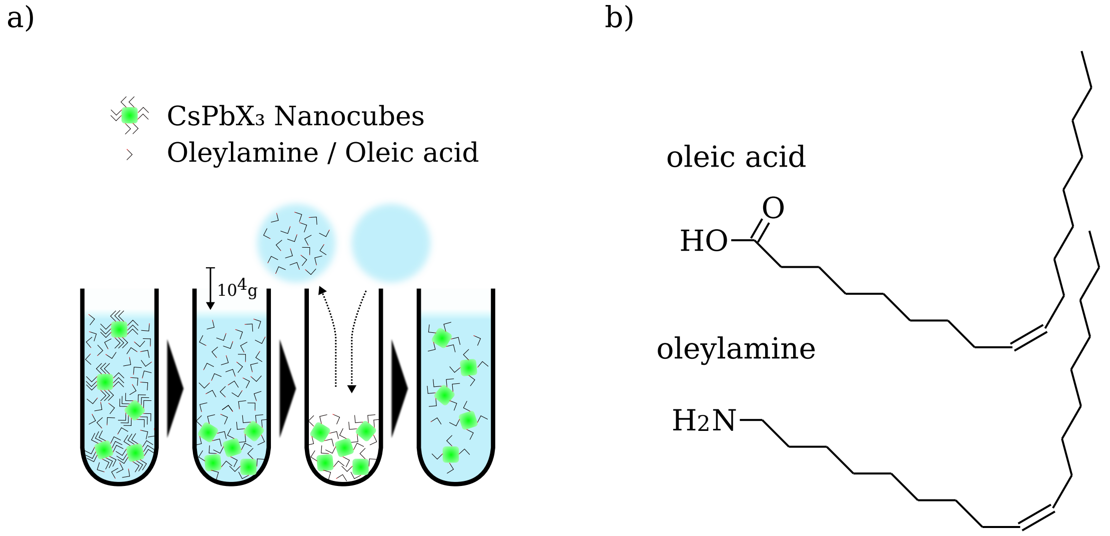

Figure 7.1.: a) Sketch detailing the washing procedure featuring centrifugal forces. At specific solvent mixtures the particles will precipitate while ligands stay in solution.[S.77] b) Lewis structure of the canonical ligands during synthesis: oleic acid and oleylamine.[S.78, S.79]

Generally, as part of the synthesis, a purification of the NC suspension is conducted. That purification can be repeated multiple times in order to reduce the ligand concentration in the solution. By utilising the labile binding of the oleic acid and oleylamine (cf. figure 7.1 b)) to the PNC, a mere dilution of the dispersed particles leads to a substantial disattachment of those.[157] As depicted in figure 7.1 a), the purification process continues by centrifugal forces separating free floating ligands from the NCs. The initial dilution is done with a slightly polar solvent, so that the solution is optimised towards keeping the ligands dissolved. Consequently, oleic acid and oleylamine are still decently soluble in solvents such as methylacetate (MeAc), ethylacetate (EtAc) or tetrahydrofuran (THF), since they coordinate with the ligand's polar carboxy resp. amine group. In contrast to that, the highly passivated NCs, have the ligands' anchors close to its ionic, polar surface and the apolar aliphatic chain is faced outwards, towards the solution. Thus the NCs, though being highly polar in its core, are, if sufficiently passivated, less polar on their outermost region, comparable to the already discussed micelles. This is the reason the NCs are generally dispersed in an apolar solvent like hexane, octane or toluene. Concluding, by applying centrifugal accelerations of magnitudes around 10^4 g the heavy NCs will receive a higher force while being in a suboptimal solvent leading to considerable precipitation, while the ligands remain in the solution. This method is used to tune the ligand density.[158] Even though the quantification of the ligands in solution and thin-film is very challenging, a single washing process already results in huge changes in current density of a resulting PeLED. Three orders of magnitude higher currents are observed on washed devices shown in figure 7.2 a). At the same time the EQE is also significantly enhanced, since the lower injection barriers enable light-emission at lower voltages, which inherently leads to lower electric fields and thermal losses. Additionally, a less passivated surface may change the energy landscape. Indications of this influence are discussed in chapter 8 (in context of figure 8.3). Anyway, the altered energy levels can also enhance the charge carrier balance. A higher resistance below turn-on voltage is also indicative of a change in electrical response of any kind.[159, 160] With this proof-of-concept device in mind, it is evident that not only the type of ligand is of importance for the successful application of LHPs to PeLEDs, but also its surface concentration on the PNCs.[158]

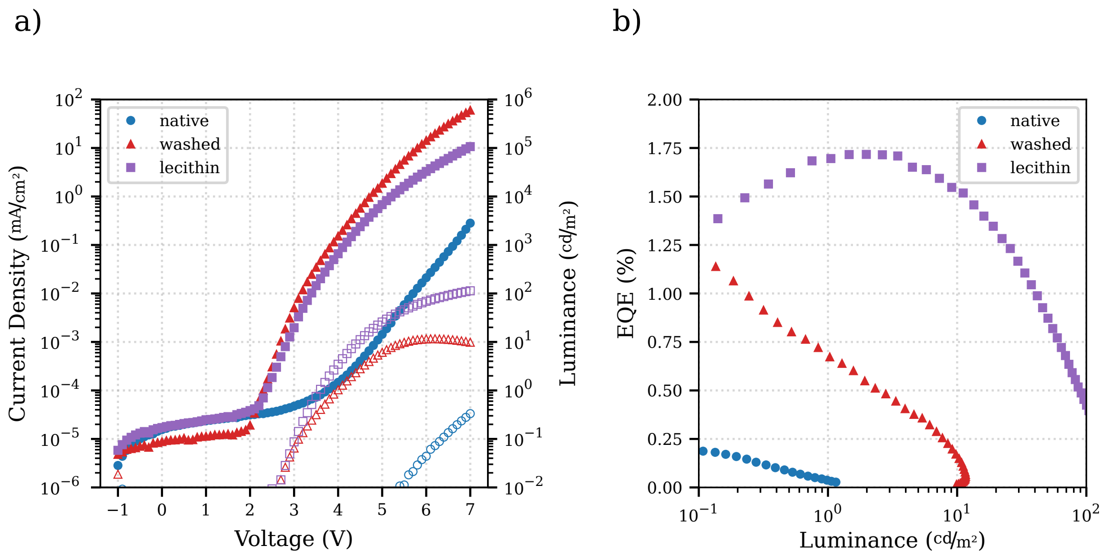

Figure 7.2.: The, a), j–V–L characteristics show that the ligands' quantity and quality is key to efficient PeLEDs.[S.80] Reducing ligand concentration leads to significant current increases, while an exchanged ligand like lecithin stabilises light-emission at elevated luminances. The, b), EQE-L characteristics shows that efficiency is also highly depending on the ligand type and density.[S.81, S.82]

7.2. Exchange of Ligands

A brief overview of the types of ligands eligible and its implications upon applying them to PNCs has been given in section 2.2.2. Phosphonates have shown great potential in passivating lead surfaces as present at a halide vacancy.[161, 162] As not all vacancies need to be of halide type, for example, the also common caesium vacancy can effectively be filled by an ammonium moiety, consequently a zwitterionic anchor such as the phosphocholine can passivate both most relevant defect types.[120, 163–165] By using soy-lecithin (cf. figure 7.3 a)), Krieg et al. [120] have shown that a more stable ligand shell compared to the carboxylic oleic acid is achieved. In this section the use of a π-conjugated functional group instead of a passive aliphatic residue at the glyceric part of the lecithin is explored (cf. figure 7.3 a)).

The previous consideration on the influence of the ligand's quantity has revealed that a significant part of resistivity of a PNC thin-film is posed by free ligands present in the original solution. The washing procedure renders the particles less stable in solution, as the chemical reaction equilibrium between the PNC's surface and the solution gradually reduces the ligand density attached to the PNC. The general observation that PNC solutions become less stable upon dilution is also indicative to the facile detachment; therefore, a substantial amount of ligand in solution is expected. This equilibrium can be shifted in favour of a better surface coverage by anchoring with stronger bonds such as phosphonic compared to carboxylic acid. Using that, Krieg et al. [120] report stable, concentration-independent PNCs.

This fact can be used to create PNC-thin-films with low resistance and reasonable stability, with little to no negative impact on the PNCs' integrity due to dilution and washing. PeLEDs made from these films show comparable current enhancement as already shown by PeLEDs with washed oleic acid based PNCs (cf. figure 7.2 a)). Additionally, higher EQEs are obtained, while exhibiting a decent stability implied by peaking EQEs at elevated luminances instead of simply descending as the native's EQEs do (cf. figure 7.2 b)). This behaviour is rather intuitive, since, in case of lecithin, the PNCs are still sufficiently covered by ligands, while for the washed ones the surface coverage may have become insufficient. Another indication for a stronger binding with concurrently less ligands is that in the case of the washed PNCs the increased currents are caused by decreased surface coverage, but at the cost of EQE resp. its stability[158]. The decline in EQE is similar to the native but steeper while the current even outmatches the lecithin device. At comparable currents, the latter exhibits a much more stable and higher EQE.

Even though this major electrically resistive part of a PNC thin-film posed by free ligands can be compensated by the more stable ligand attachment, the inherent resistivity posed by the aliphatic (oleic, linoleic, palmitic, stearic, and other residues as part of lecithin) residues remain. While using shorter alkyl chains has already been widely and successfully explored as a solution to this issue, it ultimately just reduces the degree of an impairment and induces new challenges, rather than tackling the root cause.[166–168] Utilising a functional group known for its semiconducting properties may provide additional electronic accessibility while not sacrificing stability.[124] Still, the criteria for this novel ligand are the same as for traditional charge transport layers. If one charge carrier type is already adequately well transported between the PNCs, a match in energy levels for at least the other carrier type combined with a greater bandgap than the LHP-NCs assures potentially excellent performance. Moreover, the triplet energy of such ligand has to be sufficiently high, too.[52] Since the n-type nature of these NCs leads to the assumption that they have a decent enough electron mobility, it shall be focussed on increasing the hole injection in this case.[70, 169] The carbazole moiety is compatible with the low valence band edge of LHPs in this aspect, and it also has sufficient solubility in organic solvents, a wide bandgap, and a high triplet level for use in conjunction with blue emitters.[170–172] With a strong research foundation in that area, carbazoles have been used in a number of reliable, cutting-edge optoelectronic systems.[173–175] In order to successfully attach carbazole groups to the glycerin core a propyl group is used as spacer to avoid steric issues. Ultimately, two carbazoyl-propanoyl groups are linked to the glycero-phosphocholine backbone via a Yamaguchi esterification process as described in the corresponding publication by Kirsch et al. [121] resulting in dicarbazol-9-yl-propanoyl-glycerophosphocholine (DCzGPC), depicted in figure 7.3 b).

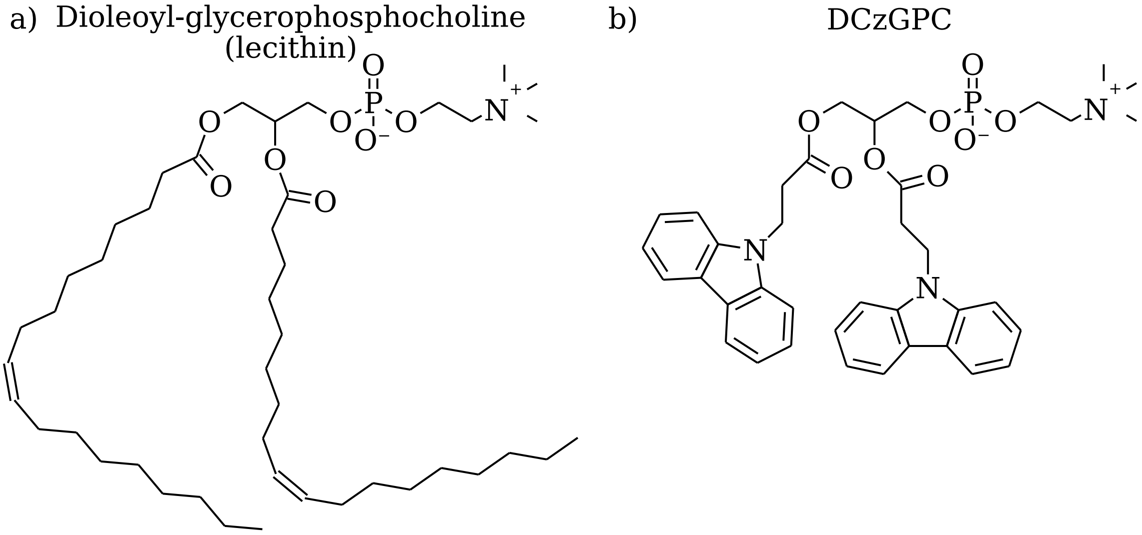
a) Dioleoyl-glycerophosphocholine (lecithin)

b) DCzGPC

Figure 7.3.: a) Lewis structure of a lecithin configuration based on oleic acid.[S.83] b) Lewis structure of DCzGPC.[S.84]

The ligand-exchange with DCzGPC is performed post-synthetically. Like that, the delicate synthesis is not altered ensuring the quality and key properties like size and stoichiometry of the PNCs. However, while the addition of lecithin is performed with same solvents, that are toluene, hexane or the like, and subsequent removal of excess ligand is performed by the mentioned washing procedure, DCzGPC exhibits poor solubility in such apolar solvents. More polar solvents like chloroform or THF are used, which renders its mixture with the PNCs turbid. This indicates that the solvent blend is already suboptimal for the DCzGPC-PNCs, which is getting worse upon addition of more hexane. Though, this circumstance already induces the first step of a washing procedure. The situation in the solution is flipped, now the PNCs are more polar, while the undesired aliphatic ligands stay in solution. Upon centrifugation, the particles will again precipitate and the original ligands stay in the apolar solution. The washing procedure is analogous but is at the same time in contrast to the usual washing procedure, where the passivated particles are not polar enough and therefore precipitate, while the ligands stay in the slightly polar solution. This circumstance poses a major advantage over the polar washing procedure, since the aliphatic ligand can be extracted more efficiently. In the other side, because of the PNCs' surface and the ligand itself having comparable solubility, an effective removal of excess DCzGPC from the solution has not been achieved by any solution blend. Consequently, any further quantitative ligand engineering after the exchange procedure is impossible at this point.

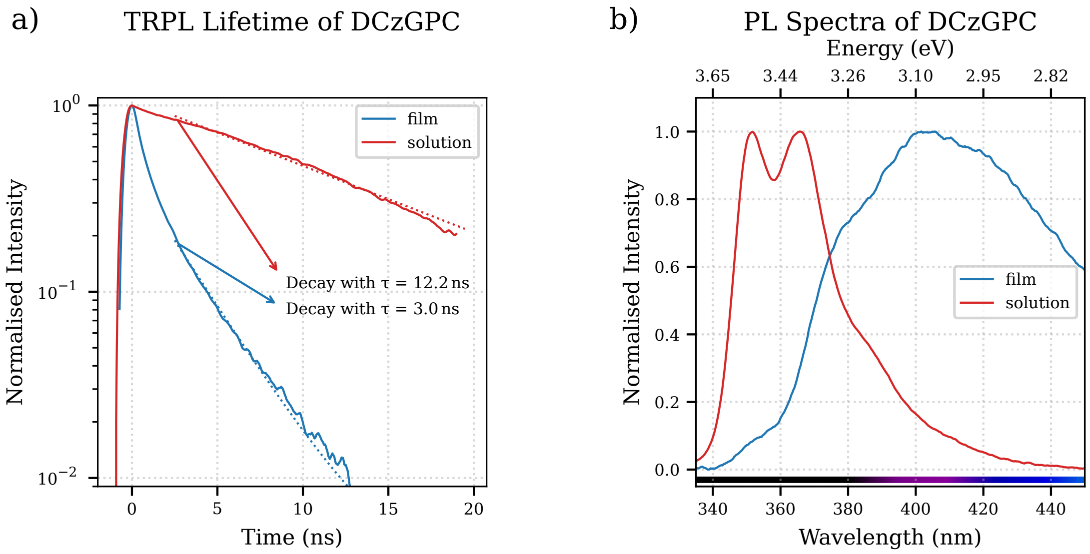

Figure 7.4.: The TRPL lifetime of only DCzGPC as thin-film and solution, a),[S.85] and its spectra, b),[S.86] show great discrepancies. Lifetime is reduced drastically and concurrently the entire spectrum is changed into a broad one with multiple peaks.[S.87]

Initially, only the optical properties of DCzGPC are studied. The PL lifetimes for thin-film as well as for solutions are higher than the ones obtained for LHP-NCs. Figure 6.2 c) and d) imply lifetimes of around 1.6 ns for thin-films, and 5.5 ns for the solution of PNCs, which is lower than the respective lifetimes of DCzGPC of 3 ns resp. 12.2 ns (cf. figure 7.4). While the thin-film TRPL in general contains inter-particle interactions because of their inherent proximity to each other, the solutions are diluted sufficiently to show, if at all, only contributions of the solvents which are usually negligible. Anyway, the ligands' decay rates are not significantly faster than the LHP's, which would pose an issue where the ligands PL signal or non-radiative decay could compete with the PNC's radiative decay. Upon combining both materials in a PNC thin-film, because of low distances, limited by the attachment itself, and high spectral overlap between PNC absorption and DCzGPC emission, very high energy transfer rates can be expected.[176] The lower radiative lifetime of the PNCs avoids any issues arising from exciton-accumulation on the PNC, which would lead to e.g. biexcitons on the PNCs or potential non-radiative decay.

Apparently, the effects of aggregated carbazoles, which has been widely explored for PVK, is also measured on the DCzGPC, this becomes evident when comparing the PL spectra of the thin-film with the one of the solution.[177] While in solution the peaks at 351 nm, 365 nm and 387 nm are reminiscent of isolated carbazole,[178] the former peak is strongly suppressed and the latter two are supposedly redshifted to 375 nm resp. 400 nm and the last one enhanced. Considering the investigations on various vinylcarbazole-chains towards PVK by Johnson [177], this shift in intensity towards higher wavelength peaks, has also been measured as vinylcarbazole-chains increase in length. With this, it is highly reasonable to expect a moderate interaction of carbazoles, also if attached to the PNCs.

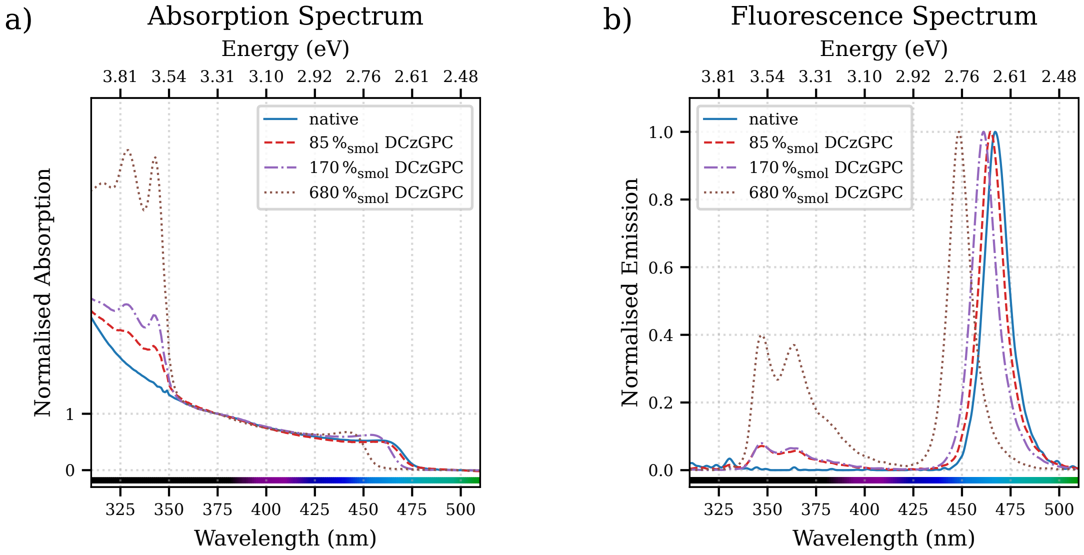

Figure 7.5.: Absorption, a),[S.88] and photoluminescence, b),[S.89] spectra of PNC solutions with addition of DCzGPC ligands. A substantial and continuous blueshift in both PNC spectra is exhibited, while the DCzGPC-specific contributions gain significance.[S.90]

As expected, upon addition of DCzGPC to the $CsPbBr_2Cl$ solution an increasing absorption as well as emission contribution by the ligand arises. The double absorption peak at below 350 nm, here 328 nm and 342 nm, is characteristic for the carbazole group[179, 180] and it has also been identified for the DCzGPC ligand itself.[121] Furthermore, the addition of DCzGPC to the solution immediately induces a reproducible and linear blue-shift of both PL and absorption indicating a band-gap change. This colour-shift persists even after the initial washing procedure. Figure 7.5 shows the respective absorption and fluorescence spectra of the solutions. Initially, this shift has been tentatively ascribed to a hypothetical chlorine enrichment within the PNCs, that is, a halide exchange from $CsPbBr_2Cl$ to $CsPbBrCl_2$ or even $CsPbCl_3$. However, this linear blue-shift is also occurring to a comparable extent for the green $CsPbBr_3$ perovskite (cf. figure S11). With that, a halide-stoichiometry as origin for the colour change can be excluded since there are no other halide types present in this solution. As opposed to the peak positions, a potential linearity between DCzGPC content and its PL signal, the peak-pair at 347 nm and 363 nm, cannot be identified. That is because elevated surface saturations exceeding 170 $\%_{smol}$ deviate strongly. At the same time, its absorption signal strength scales linearly with the concentration for all concentrations. Here, because of the normalisation the DCzGPC-PL signal seems to be suppressed, but the absolute units reveal, that actually the PNC emission got significantly enhanced at 170 $\%_{smol}$ instead. Independent PLQY measurements of these solutions verify this PL increase by reaching its maximum PLQY value also at 170 $\%_{smol}$.[121] The drop in PLQY may have various reasons, but at this point it shall be mentioned that the previously detailed consideration on the TRPL suggests a competition between ligand and PNC decay rate. This issue only arises as PNCs are getting sparse compared to the ligands, since the energy transfer rate towards it decreases over-proportionally (to the power of six) with the distance to the excited ligand.[176] This is, of course, only possible with a significant amount of disattached ligands in the film. Note that the carbazole's PL signal detected even at the lowest concentration suggests already unbound ligands even if the theoretical saturation is not reached yet. Anyway, the initial PLQY increase together with respective nuclear magnetic resonance (NMR) considerations[121] and the colour-shift itself pose strong evidence that the novel ligand is bound to the surface of the PNC for concentrations below 170 $\%_{smol}$.

Despite that, it is reasonable to anticipate that not all ligands added to the PNCs solution are actually tightly bound to the surface of such even at low concentrations. Firstly, excessively adding ligand to the solution, exceeding 100 $\%_{smol}$, lead to a continuous and linear blue-shift verified up to 680 $\%_{smol}$ (cf. figure 7.7 d)). Secondly, the PLQY is reaching its maximum also beyond the theoretical full saturation. Herein, it is assumed, that the increase in PLQY originates solely from surface passivation and any unbound ligand in solution has minor beneficial effect on it. Both points are indicative that the actual full NC coverage has not yet occurred. If the blue-shift originated from ligand attachment it would saturate at some point. On the other side, the peak in PLQY does not necessarily need to indicate the full saturation point, since at the considered concentration, losses from the free, abundant ligands themselves could decrease it considerably. Additionally, apart from the theoretical, stoichiometric considerations, AFM images of thin-films, which are also used for the PeLEDs described later, show that even at the lowest considered mixing ratio, 85 $\%_{\mathrm{smol}}$, a major volumetric part is filled by smooth supposedly organic domains (cf. figure 7.6 on the right). On the other hand, the same film without DCzGPC (cf. figure 7.6 on the left), reveals that the film consists of a soft, featureless foundation compound, where PNCs are stacked up to 45 nm height corresponding to an average height of two to three NCs. The cuboids are strung together densely rendering organic residues only visible around the thin-film's holes. In contrast to that, the DCzGPC ligands hide any potential regular arrangement revealing only a few PNCs seemingly separated from each other. The maximum height does not exceed 25 nm indicating that no more than two NCs are stacked. It is clearly apparent, that the ligands' volume is severely higher in the DCzGPC compared to the oleic acid and oleylamine passivated PNC-film. It shall be mentioned that the oleyl-based system is known for having a labile binding, implying a significant amount of unbound ligand in solution, thus consequently to a certain extent also in the thin-film. Yet, the DCzGPC sample seems to have a vastly higher organic fraction. Furthermore, unlike the e.g. LiTFSI treated samples, it is unlikely that a bulky ligand such as the DCzGPC can anchor at each unit cell as implied by a 100 $\%_{\mathrm{smol}}$ ratio. The bulky carbazole will also not arrange as easily as the long oleyl based ligands. All together it is reasonable to assume that even in the lowest investigated mixing ratio, 85 $\%_{\mathrm{smol}}$, the amount of ligands would be enough to fully saturate the PNC, but the given chemical and steric conditions do not allow them to be fully utilised.

The lecithin ligand features a tight binding, rather than a labile one.[163] Its AFM image (not shown) looks very similar to the native one with even less organic residues, depending on the purification grade. All together the DCzGPC does not seem to have comparable tight binding, as indicated by the high ligand amount required to induce significant changes to its optical properties. This discrepancy is rather unexpected considering that the identical anchor group is used. However, there are, among others, two intuitive approaches to explain it. A very easy explanation could just be that the required, increased polarity of the solvent is favouring the DCzGPC to stay in solution rather than replacing the apolar oleyl-based ligands. A detailed optical analysis on the characteristics of a thin-film, thus excluding the solvent's influence,

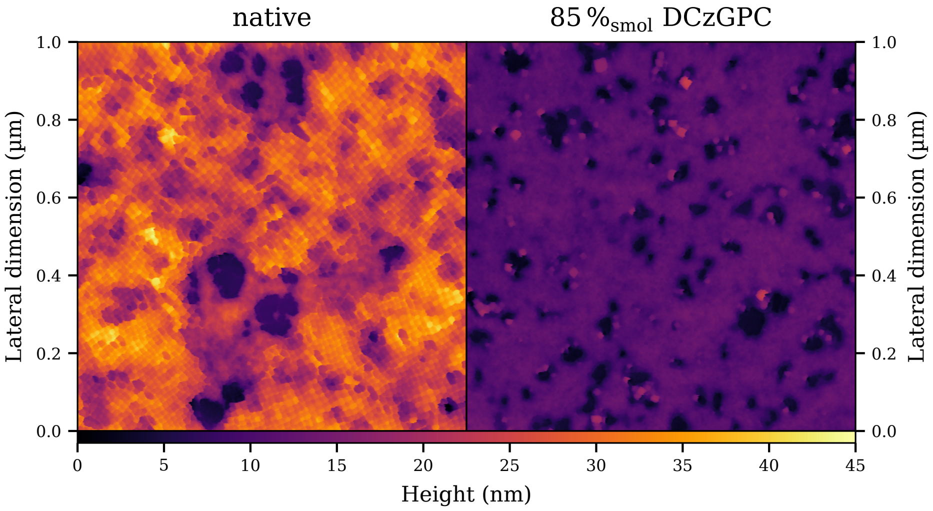

Figure 7.6.: AFM images of PNC thin-films deposited on PVK. The native NCs, on the left, can be clearly identified as regularly arranged cuboids with average height of between two and three cubes. The DCzGPC augmented PNCs, on the right, are partially hidden by a smooth organic layer, which makes up a higher volume ratio within the film compared to the native. Additionally the DCzGPC-PNC film is formed with decreased thickness of less than two cubes.

may give additional insight on this matter. Another circumstance that may give rise to a weaker binding of the phosphocholine group, is the fact that, the conjugated π-system of the carbazole can have an impact on the zwitterionic anchor by a hypothetical, partial compensation of the charges present on the phosphocholine via electrical screening by the carbazole groups. This proposed hybridisation coupling could be decreased by redesigning the ligand with a longer junction between phosphocholine and the carbazole. In particular, the propanoic acid may be replaced with e.g. hexanoic acid for a greater spatial separation.

The influence of the carbazole moieties in proximity to the phosphocholine and ultimately the PNC along with the origin of the induced blue-shift by this ligand exchange remains elusive. Especially, since the particle size does not shrink to induce a stronger quantum confinement nor does a change in halide composition explain it.[121] However, with simple analytic considerations it can be hypothesised that it arises from a change in effective mass rather than an exclusive change of permittivity. The fundamental relation for describing the energy gap in weakly confined NCs, Brus' equation, is considered:[42–44]

$$E_{\mathrm{gap,PNC}} = E_{\mathrm{gap,bulk}} + E_{\mathrm{exciton}} + E_{\mathrm{confinement}}, \tag{7.1}$$

with the energy gap of the bulk LHP, $E_{\mathrm{gap,bulk}}$, the exciton Coulomb energy, E_{exciton}, and the confinement energy, $E_{\mathrm{confinement}}$.

While the bulk energy gap is controlled by the halide composition, the exciton's attractive, and therefore negative, binding energy is determined by the effective masses of electron (m_e) and hole (m_h) respectively its reduced mass, $\mu = {}^{(m_\mathrm{e} \cdot m_\mathrm{h})}/_{(m_\mathrm{e}+m_\mathrm{h})}$, and the permittivity ($\epsilon_\mathrm{r}$). The Rydberg-energy ($\mathrm{E}_\mathrm{Ry} = \mathrm{R}_\infty \cdot \mathrm{hc}$) is defined as the Coulomb energy of an electron orbiting an infinitely heavy proton.[181, 182] This energy is approximately equal to the binding energy of the hydrogen's electron, but the exact expression would be: $\mathrm{E}_\mathrm{H} = \mathrm{E}_\mathrm{Ry} \cdot {}^{\mu}/_{m_0}$ (m_0: the mass of an electron). With this correction term, the mass of the electron, that is included in the Rydberg constantR_∞, is replaced with the reduced mass μ. While for the hydrogen atom this factor may be just a nitpick (${}^{\mu}/_{m_0} \approx 0.9995$), when considering excitons the reduced mass does differ from m_0 significantly. Additionally, the permittivity is no longer that of vacuum ($\epsilon_\mathrm{r} \neq 1$). By summing up the corrections and defining a Rydberg-velocity (v_Ry):

$$v_\mathrm{Ry}^2 = \frac{2\mathrm{E}_\mathrm{Ry}}{m_0}, \tag{7.2}$$

$$\mathrm{E}_\mathrm{exciton} = -\mathrm{E}_\mathrm{Ry} \cdot \frac{\mu}{m_0} \cdot \frac{1}{\epsilon_\mathrm{r}^2} = -\frac{v_\mathrm{Ry}^2}{2} \cdot \frac{\mu}{\epsilon_\mathrm{r}^2}, \tag{7.3}$$

an expression for the energy of an exciton is derived. Note that, these consideration is only valid if the exciton within the NC is hydrogen-like so that the electron-hole distance is equal to the resp. Bohr-radius (weak confinement regime). Moreover, influences by polarisation of the NC are neglected.[183] A detailed discussion on these influences can by found in Brus' [42] publications.

Now, the confinement energy is only depending on the cube size and the reduced mass. It is estimated by the already mentioned (cf. A.2.5) 3-D particle in a box with edge length a, just as in common textbooks on quantum physics, with the wave vector ($\vec{k}$) and an effective radius $\bar{a} = {}^{a}/_{\sqrt{(3)}}$:[184]

$$\mathrm{E}_\mathrm{confinement} = \frac{\hbar^2 \vec{k}^2}{2\mu} = \frac{\hbar^2}{2\mu} \cdot \sum_i^3 \left(\frac{n_i \pi}{a} \vec{e}_i\right)^2 = \frac{3 \cdot \hbar^2 \pi^2}{2\mu a^2} \tag{7.4}$$

$$= \frac{\hbar^2 \pi^2}{2\mu (\frac{a}{\sqrt{3}})^2} = \frac{\hbar^2 \pi^2}{2\mu \bar{a}^2}. \tag{7.5}$$

Using effective masses ($m_\mathrm{e} = 0.15\, m_0$ and $m_\mathrm{h} = 0.14\, m_0$) and permittivity ($\epsilon_\mathrm{r} = 4.96$) from Protesescu et al. [7] and bulk energy gaps from references 185, 186, the individual contribution can be tabulated as shown in table 7.1. The calculated PNC energy gaps coincide very well with the measured PL peaks for the native $\mathrm{CsPbBr_3}$ as well as $\mathrm{CsPbBr_2Cl}$-NCs. However, it becomes evident that the measured blue-shift of 100 meV / 22 nm in case of DCzGPC-covered $\mathrm{CsPbBr_3}$-PNCs and 120 meV / 19 nm in case of DCzGPC-covered $\mathrm{CsPbBr_2Cl}$-PNCs cannot arise from a dielectric

Composition	$E_{gap,bulk}$	μ	$E_{exciton}$	$E_{confinement}$	$E_{gap,PNC}$
$CsPbBr_3$	2.29 eV / 541.4 nm	0.072 m_0	-40 meV	+156 meV	2.41 eV / 515.4 nm
$CsPbBr_2Cl$	2.59 eV / 478.1 nm	0.072 m_0	-40 meV	+105 meV	2.65 eV / 467.1 nm

Table 7.1.: Energy contributions according to eq. 7.1 for native PNCs. Reducing coulomb interaction via dielectric screening may only blue-shift as much as 40 meV.[S.7, S.91]

Composition	$E_{gap,bulk}$	μ_{DCzGPC}	$E_{exc,DCzGPC}$	$E_{conf.,DCzGPC}$	$E_{gap,DCzGPC}$
$CsPbBr_3$	2.29 eV / 541.4 nm	0.045 m_0	-25 meV	+250 meV	2.51 eV / 493.0 nm
$CsPbBr_2Cl$	2.59 eV / 478.1 nm	0.031 m_0	-17 meV	+195 meV	2.77 eV / 448.0 nm

Table 7.2.: Reduced mass and the implied energies after the 680 $\%_{smol}$ DCzGPC ligand exchange. The reduction of effective mass affects the coulomb as well as the confinement part towards a higher energy gap.[S.7, S.91]

screening thus increasing the permittivity. Apparently the only term that shows the potential to induce such strong blue-shifts is $E_{confinement}$. The particle size does not decrease,[121] so the only variable that is left is the reduced mass. Combining eq. 7.1 with eq. 7.3 and eq. 7.5:

$$E_{gap} - E_{gap,bulk} = -\nu_{Ry}^2 \cdot \frac{\mu}{2\epsilon_r^2} + \frac{\hbar^2\pi^2}{2\mu\bar{a}^2}. \tag{7.6}$$

With:

$$\Delta E = E_{gap} - E_{gap,bulk}, \tag{7.7}$$

a quadratic equation is derived:

$$0 = -\nu_{Ry}^2 \cdot \frac{\mu}{2\epsilon_r^2} + \frac{\hbar^2\pi^2}{2\mu\bar{a}^2} - \Delta E. \tag{7.8}$$

$$0 = -\mu^2 \cdot \frac{\nu_{Ry}^2}{2\epsilon_r^2} - \mu \cdot \Delta E + \frac{\hbar^2\pi^2}{2\bar{a}^2}. \qquad (\mu \neq 0) \tag{7.9}$$

By solving eq. 7.9 using the experimentally determined optical gap as an approximation for the band-gap, an estimate for the change in reduced mass can be obtained. Shown in table 7.2, in case of $CsPbBr_3$ the decrease in reduced mass from 0.072 m_0 to 0.045 m_0 can be realised by halving e.g. the effective hole mass to 0.07 m_0. Analogously, for $CsPbBr_2Cl$ an even stronger reduction of the respective effective mass can be the root cause. Note that without loss of generality also the electron's effective mass can be concurrently reduced.

Here, it shall be pointed out, that the mentioned polarisation effects could also have become relevant, since the ligand may induce a dipole at the surface which potentially alters the dielectric environment entirely. A more detailed investigation on the conditions on the NC's surface will tell if the exciton energy term, eq. 7.3 as part of eq. 7.1, has to be corrected accordingly.

Anyways, following the current equations, a reduced effective mass implies a lowered inertia and consequently a more 'free' carrier. According to the Drude model the hole (resp. electron) mobility, μ_h, is inversely correlated to the mass of the carrier m_h,[187] with a constant average collision time τ and the elementary charge e even inversely proportional: $\mu_h = {}^{e\tau}/_{m_h}$.[188] So the initial goal of rendering the PNCs electronically more accessible may be achieved, by exchanging the insulating ligands with DCzGPC.

With implications from the optical considerations, the PeLEDs as electrical device will elucidate this issue. Indeed, in figure 7.7 a) the currents are increased after the onset by more than an order of magnitude by adding 85 $\%_{\mathrm{smol}}$ DCzGPC. Regrettably, this increase in current does not necessarily need to originate from the proposed mobility increase, as the film thickness decreased concurrently (cf. figure 7.6). However, the magnitude of the enhancement along with a substantial luminance onset shift towards lower voltages suggest a non-negligible contribution by the hypothesised enhanced carrier mobility. The addition of excess ligands shows that apparently the molar ratio of ligand to PNC has an enormous impact on the currents. A 170 $\%_{\mathrm{smol}}$ DCzGPC treatment causes currents to decrease overall with up to an order of magnitude at 7 V, while the film-thickness has not increased substantially compared to the 85 $\%_{\mathrm{smol}}$ treated sample. Here, one can assume, that even the latter has no optimal ligand to PNC ratio for the electrical operation yet, since the AFM image also implies a ligand excess. As already detailed, any passive, unbound ligand deteriorates the electrical performance of such film. In case of the oleyl or lecithin based PeLEDs excess ligands in solution could be removed, resulting in ultimately highly covered PNCs while minimising the amount of unbound ligands in the film. However, for DCzGPC a high ligand excess is required to fully passivate the PNC's surface as indicated by the optical investigations, but these excess ligands will stay present in the thin-film used in the PeLED. Effectively, the j–V–L curves reveal that at 170 $\%_{\mathrm{smol}}$ DCzGPC this excess outweighs any PLQY and PNC-specific mobility enhancements. This circumstance provides further hints, that the current increase of the 85 $\%_{\mathrm{smol}}$ sample has higher currents not solely because of reduced film thickness, since it could be tremendously higher without the observed excess ligands in the resulting thin-film.

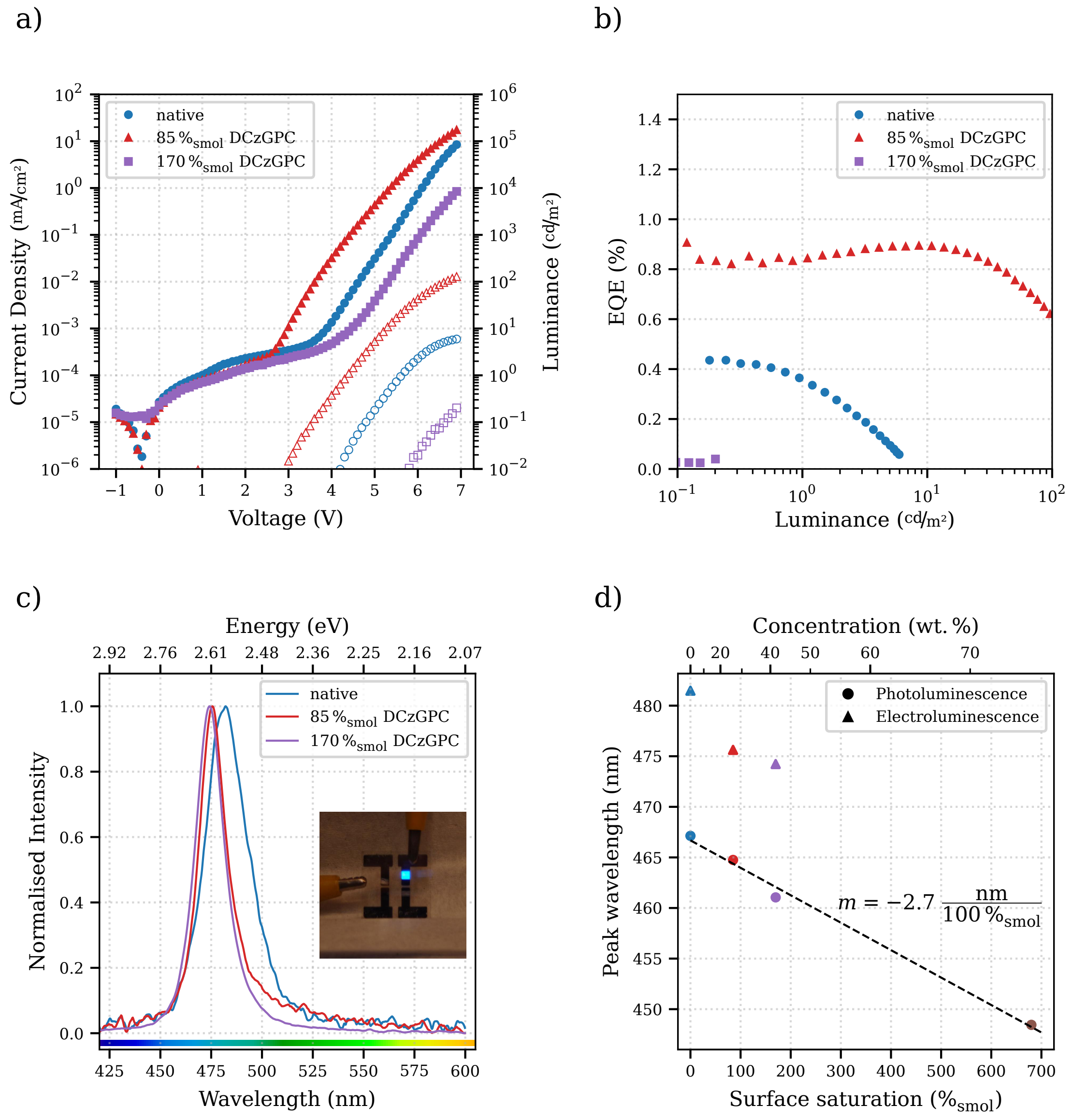

Figure 7.7.: PeLEDs made from $CsPbBr_2Cl$-NCs with ligands exchanged to DCzGPC: the, a), j–V–L plot reveals a significant current change depending on the ligand concentration. Luminances are also correlated, but not proportional to the current changes.[S.82, S.92] The extent of this disproportionality is depicted by the EQE-L plot, b). Herein, the EQE can also be enhanced and stabilised with the right ligand quantity.[S.82, S.93] The EL-spectra, c), show a similar blue-shift as already measured for PL in solution. However, a narrowing of the spectra accompanied by a general red-shift differ from the PL. A photograph of the PeLED driven at 7 V is provided in the inset.[S.94–S.96] A molar ratio vs peak-wavelength plot, d), compares EL with the PL and illustrates the PL to EL peak position change along with a non-linearity in only the EL blue-shifting.[S.96, S.97]

Considering the EQEs of the DCzGPC treated PeLEDs in figure 7.7 b), two remarkable enhancements are induced by the new ligands. Firstly, the EQE is generally higher and has been increased from the native's just above 0.4 % to the 0.8 % for the 85 $\%_{\mathrm{smol}}$ sample. Secondly, the EQE remains stable and reaches its maximum close at the elevated luminance of 10 $^{\mathrm{cd}}/_{\mathrm{m}^2}$. Also the 170 $\%_{\mathrm{smol}}$ sample shows this stability, even though its EQE being very low because of the, for this stack, suboptimal driving voltages. Again, the increased EQE indicates an actual direct electrical benefit of the ligand since it has a strong influence on the charge carrier balance. Anyhow, the 16-fold change in EQE between the two samples cannot be explained by changes in PLQY or out-coupling factor following the same argumentation as already provided for the LiTFSI-PeLEDs.

In contrast to the previously investigated PeLEDs, the DCzGPC treatment induces a blue-shift to the EL spectrum (cf. figure 7.7 c)). The blue-shift determined in solution is propagated to the thin-film and ultimately to the electroluminescence. Additionally, the spectral distribution narrows from an original native FWHM of 25 nm down to 15 nm for the DCzGPC treated sample. There is no emission by the ligand itself visible, though with the PL of the pure DCzGPC film in mind one could expect a broad band spreading over the deep-blue (<450 nm) part of the spectrum. This indicates that even when using 170 $\%_{\mathrm{smol}}$ DCzGPC the exciton transfer may still be faster than its own radiative decay. Interestingly, even the EL of the native PeLED is red-shifted by 14 nm compared to its PL (cf. figure 7.7 d)). However this has practical reasons, the mixed halide LHP-NCs tend to colour-shift depending on various environmental conditions. Since the PL has been measured without transport from the University of Tübingen to Augsburg and the EL is measured in Augsburg after the transport where temperature, oxygen and water exposure could not be kept strictly constant. Nevertheless, the linear relation between ligand content and blue-shift is not propagated from the PL to the EL. The EL peak rather leaps by 5 nm from 481 nm to 476 nm on the first 85 $\%_{\mathrm{smol}}$, but for the next step it seems to saturate by only shifting 1 nm over the same interval. An EL measurement for DCzGPC contents exceeding 170 $\%_{\mathrm{smol}}$ has not been possible, as the device becomes too insulating for a detectable emission at reasonable driving voltages.

Still, the DCzGPC-augmented PeLEDs can be driven at higher voltages without a comparably fast degradation. The photo of the PeLED shown in figure 7.7 c), could not be taken for the native as it degraded too quickly. The luminance decay is studied in detail (cf. figure 7.8) and it is verified that it takes 15 times longer for the initial luminance to be halved (LT_{50}) if treated with DCzGPC. At a constant current density of 0.1 $^{\mathrm{mA}}/_{\mathrm{cm}^2}$, the native reaches LT_{50} after only 6 seconds, while the ligand exchanged sample takes 91 seconds. This matches with the argumentation concerning the EQE maximum at higher luminance. Indeed, the PeLED is more stable, which is also confirmed by the change of conductivity during constant

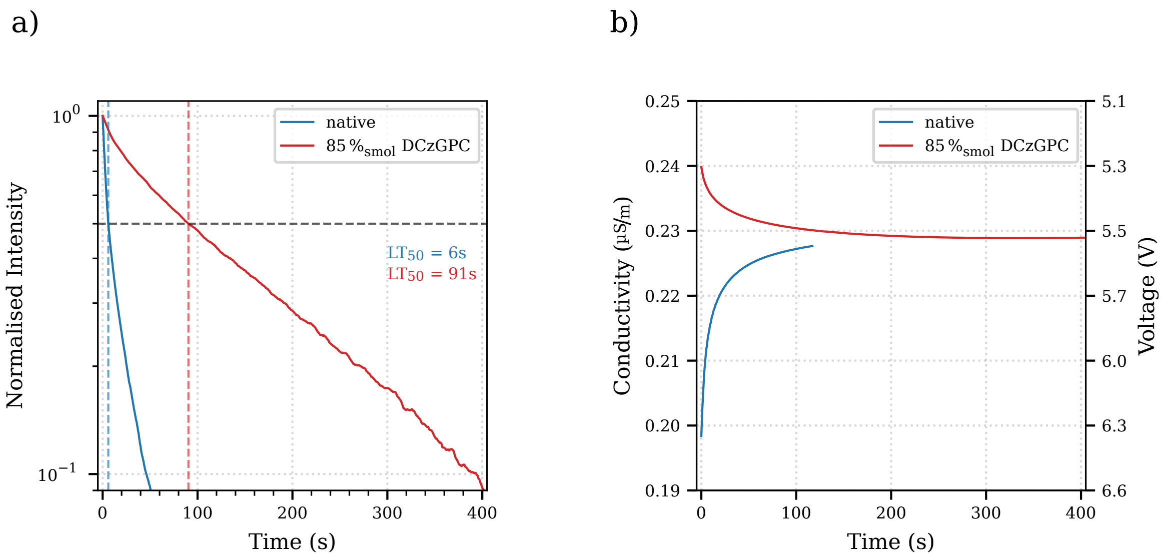

Figure 7.8.: The, a), L–t plot reveals a significant increase in operational lifetime of the PeLEDs.[S.98] Also the, b), conductivity vs time indicates a different origin of degradation, since the course of the curves are completely changed.[S.99, S.100]

current operation (cf. figure 7.8 b)). Now, not only does the conductivity change more rapidly but also, in case of the native, it got higher while DCzGPC decreases the conductivity over time. Apparently, the nature of this degradation has changed fundamentally. One explanation for this discrepancy is given by considering ionic movements. A PNC disintegration will inevitably lead to free ions as by-products. In case of the native, these ions are free to penetrate the adjacent transport layers, which could increase its conductivity as well as the contacts. On the other hand, the excess of DCzGPC ligands may keep the ions within the emission layer, concurrently the ions' interaction with the ligand could render it less conductive.

Overall, this chapter has revealed that successfully applied ligands in terms of quantity and type are of key importance for efficiency as well as operational stability of resulting PeLEDs. While engineering the ligand density of the aliphatic ligands already shows crucial enhancements, the use of a suitable semiconducting residual group such as the carbazole in case of DCzGPC shows potential to surpass even these enhancement. However, there are new challenges concerning the proper attachment of such ligands to the PNCs, as the new moieties apparently change the binding situation. Anyway, other anchoring groups or applying the ligands already during synthesis may be a solution to this issues. Finally, also the blue-shift remains interesting for fundamental research as it cannot be explained with the current models.

8. Displacement Currents in Perovskite Thin-Films

So far, it has become very clear that a major challenge for efficient PeLEDs is balancing the charge carrier injection into the PNC thin-film. Consequently, by arguing with the energy levels of the adjacent layers, several trends have been found. A direct observation of a charge carrier specific influence is possible with single carrier devices. However, by the nature of the device, the current in such device is comprised of the thin-film's bulk and its injection resistance. A better conductivity of the film may show similar currents as an enhanced injection may do. This includes the issue of perforated or otherwise insufficient film coverage being misinterpreted as enhanced conductivity. In order to better disentangle the parts to focus more on the injection properties, displacement currents in a capacitive, that is a metal insulator semiconductor (MIS) device, can be considered. This chapter gives a brief overview to the technique along with some preliminary results. The MIS devices are designed to be transparent for future experiments allowing to obtain operando PL signal as reported by Noguchi et al. [189]. This method allows spotting potential quenching mechanisms within a charged PNC. Therefore, PMMA is used as insulator and ITO acts as metallic contact. Here, it is shown how the model of a double resistor-capacitor can be used to explain some of the charge carrier dynamics present in PeLEDs. Note that this method is not very far developed and the statements made in this chapter are still preliminary and will need additional considerations to prove the points made. The model is explained in detail in section 4.3.3.

These transparent MIS devices are driven close to their operational limit. That is because the electric field reaches values close to 100 MV/m, which exceeds the reported dielectric strength of the insulating PMMA (<30 MV/m).[193, 194] Thicker PMMA layers may circumvent this issue, but it reduces the overall displacement currents costing resolution at this point. Furthermore, smooth and defect-free PMMA films prove to be harder to achieve with increasing thickness. The engineered thickness of 160 nm experimentally turned out to be the best compromise. However, the MIS devices with direct PNC-metal contact prove to be too unstable in any case, so the PNC thin-films are investigated as an interlayer below an organic transport layer. In order to probe electron and hole injection, B3PYMPM resp. TCTA is used. The materials and consequently the con-

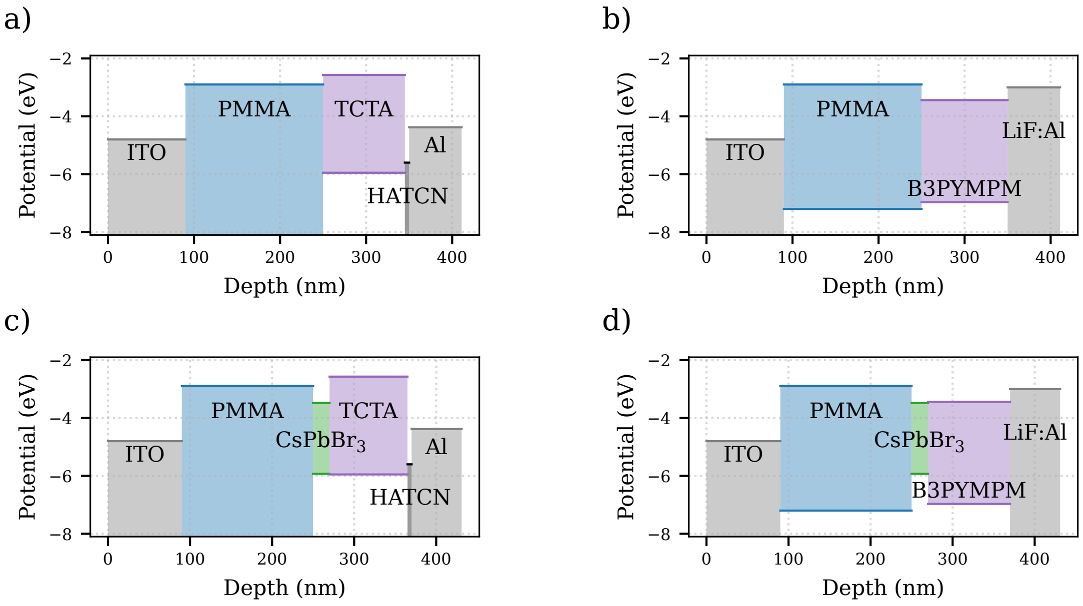

Figure 8.1.: Device layer stack illustrations show the used device for DCM: a) and b) are the all-organic hole-only resp. electron-only devices,[S.101, S.102] while c) and d) are the equivalents with the PNC as a thin layer in between the transport layer and the PMMA.[S.103–S.105] Energy levels taken from references.[64, 65, 70–72, 74, 75, 138, 190–192]

tacts are chosen to stay as comparable as possible to the manufactured PeLEDs. Here TCTA is used as an alternative to PVK, which cannot be evaporated. Figure 8.2 shows the displacement currents measured for the all-organic MIS reference devices, with stacks depicted in figure 8.1 a) and b) .

The hole-only sample (left) shows an expected behaviour: noticeable charge carrier injection occurs at $V_{th} = -0.9\,V$ resp. at $V_{th} = -0.5\,V$. The fitted model suggests a turn-on voltage at reverse bias voltages of $V_D = 1.6\,V$ resp. at $V_D = 3.5\,V$. Apparently, the underlying depletion region has already vanished at shortcut conditions ($V = 0\,V$) and an external field is needed to establish it. This phenomenon can be explained by dipoles created at the interfaces by the contact materials. While some organics are known to exhibit a giant surface potential, which is able to create enormous electric fields, TCTA does not build such.[82] However, in the case of HATCN, its use as hole injection contact is basically enabled by a strong interfacial dipole as explained by Park et al. [138]. In contrast, in the absence of such dipoles, the electron injection into B3PYMPM occurs at voltages around $V_D = -0.1\,V$.[195] At voltages higher than $V_{th} = 3.6\,V$ the electron injection exceeds the geometric displacement current, that is, the current without injection simulated by the single RC. Evidently, the contact has an elevated turn-on voltage; this discrepancy between V_D and V_{th} is determined by the quality of the contact. The better the contact the sooner the injection currents reach a non-negligible magnitude. The injection resistance R_{inj}, equivalent to R_t

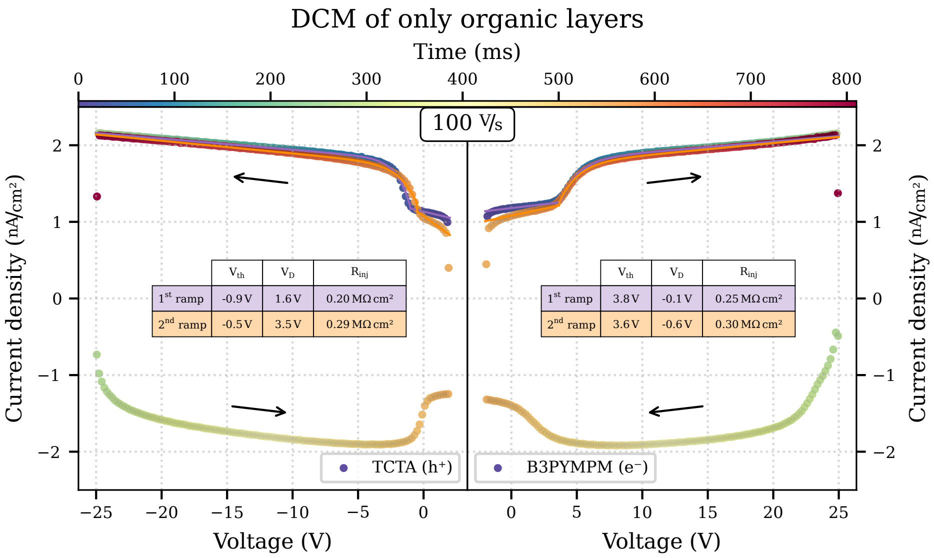

Figure 8.2.: DCM curve of organic only MIS device. These curves reveal inherent limitation by the organics and are measured for reference to compare with the other PNC based ones.[S.106, S.107]

in figure 4.6, denotes the resistance of the metal-organic interface plus the resistance caused by the mobility of the carriers within the layer. Thus, for better cross-comparability the unit is only corrected by area but not the layer thickness, resulting in an area-corrected resistance rather than resistivity, thus a unit: $\mathrm{M\Omega\,cm^2}$. For both devices the injection resistance is very comparable at the second ramp and lower during the first one. After stressing the devices with one DCM loop, an electric field remains in the stacks, which further shifts the injection voltage. At the same time, the resistance is increased, which ultimately induces only minor changes to the threshold voltage. Additionally, the permittivity of the PMMA, calculated from the pixel area and layer thickness, layer is in reasonable range ($\epsilon_{\mathrm{PMMA}} = 3.1$).[196] The obtained permittivity of the organic layers ($\epsilon_{\mathrm{TCTA}} = 3.5$ and $\epsilon_{\mathrm{B3PYMPM}} = 4.0$)[S.107] are also reasonably in the typical range for organic semiconductors. Overall, with the comparable injection resistances, it is reasonable to infer that an OLED made from these materials will experience a well balanced carrier injection. As a matter of fact, these materials are incorporated in very well performing OLEDs.[197, 198] Even though the DCM considerations on these organics may also be subject of its own research, in the scope of this work they shall only be used as reference to discuss changes when used in conjunction with PNCs, as illustrated in figure 8.1 c) and d).

Upon applying the PNCs as an additional layer between the PMMA and the transport layer, conceptually, another RC has to be introduced to the equation and a double step feature in the DCM curve may be the result. However, with the PNC layers being comparably thin and the

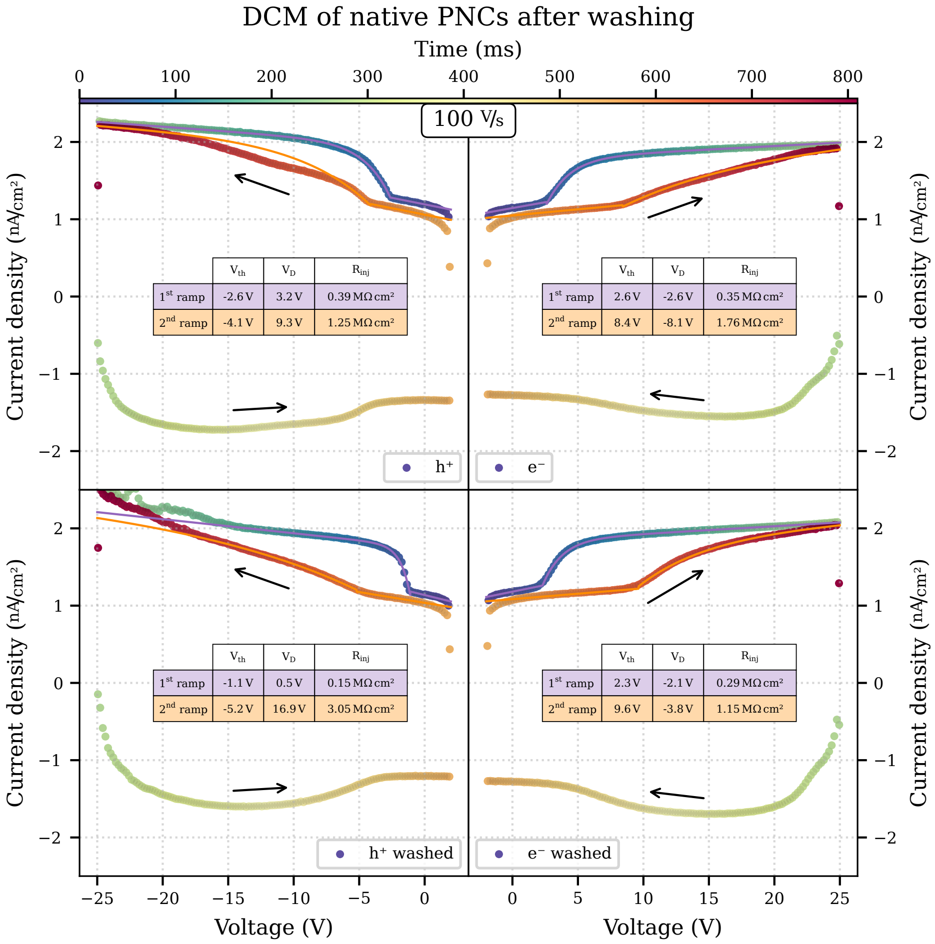

	V_{th}	V_D	R_{inj}
1st ramp	-2.6 V	3.2 V	0.39 MΩ cm²
2nd ramp	-4.1 V	9.3 V	1.25 MΩ cm²

	V_{th}	V_D	R_{inj}
1st ramp	2.6 V	-2.6 V	0.35 MΩ cm²
2nd ramp	8.4 V	-8.1 V	1.76 MΩ cm²

	V_{th}	V_D	R_{inj}
1st ramp	-1.1 V	0.5 V	0.15 MΩ cm²
2nd ramp	-5.2 V	16.9 V	3.05 MΩ cm²

	V_{th}	V_D	R_{inj}
1st ramp	2.3 V	-2.1 V	0.29 MΩ cm²
2nd ramp	9.6 V	-3.8 V	1.15 MΩ cm²

Figure 8.3.: Four DCM of the native PNCs (top) and washed PNCs within a MIS device. On the left the hole-only devices and on the right the electron only configurations are displayed. The perovskite induce major changes to the DCM curves with the washing procedure pronouncing the effects. A major difference between first and second measurement is also exhibited by higher resistances and threshold voltages.[S.108, S.109]

permittivities quite high, this step will be negligibly small. Consequently, the PNCs are considered to be a 'perturbation' to the organic layer and the DCM curves are still investigated with the double RC formulas. Assuming the hypothetic scenario of the PNC layer being trap-free and electrically passive, the influence on the injection properties, that is the resistance R_{inj}, as well as the threshold voltage V_{th} would be very limited. Only the permittivities are expected to change. Opposed to that, the PNC has tremendous impact on the injection properties (cf. figure 8.3). In case of the unwashed PNC hole-only MIS device (top-left), considering the first ramp (blue), V_D has settled around the value of the second ramp for the TCTA-only sample at a value of 3.2 V and R_{inj} has increased 1.5-fold. Furthermore, the second ramp measurement (red), now differs more significantly from the first one. Though, the first ramps of the PNC and the all-organic sample are similar, the second ramp reveals a tripled resistance along with a very high injection voltage. The electron-only counterpart (top-right) shows the same trend for the resistance and the voltages, between first and second ramp. However, the threshold voltage is decreased with respect to the B3PYMPM-only sample. Here, with the absence of an initial dipole, the perovskite apparently has a notable influence on the injection voltage but less on the resistance. Additionally, both second ramps feature a more or less pronounced double-step, which deviates from the model.

Since the underlying processes are unknown at this point, more data on different PNCs are obtained. Washing the PNCs has proven to increase the conductivity of such at the cost of stability. The corresponding DCM-curves are exposed at the bottom part of figure 8.3. Considering the first ramp, it becomes evident that the dipole, which has been tentatively ascribed to HATCN, is partly compensated and on top of that the resistance is not only decreased with respect to the unwashed PNC sample but also compared to the TCTA sample. The changes for the electron-only MIS stack are not as dominant but follow the same trend. Strongly contrasting the implications of the first ramp, the second exhibits an unprecedentedly high resistance along with even higher injection bias for the hole-only device. The electron-only stays comparable to the unwashed second ramp, even though the properties stay closer to the first ramp this time.

Considering the hole-only devices (left), it is not very surprising that the washing procedure enhances the electrical properties. However, rather surprising is the feature that they are enhanced even beyond the level of the pristine contact of the TCTA-only sample. Consequently, the PNCs are undeniably influencing the 100 nm far apart HATCN-aluminium contact. Most probably, the ionic nature of the perovskite and therefore the high response on electric fields have significant implications. The fact that they are increased on the washed sample, which contains more active perovskite and less passive ligands, further support this hypothesis. Even though the situation is initially enhanced, the second ramp reveals that this effect is not very persistent. Also, the washed sample shows higher susceptibility to this deterioration. Multiple consecutive measurement with various pre-conditioning proved the ultimate irreversibility of these changes. So it can be considered a degradation process leading to the high resistances and bias voltages. With that in mind, the irreversible increase in resistance can be ascribed to be a direct influence of PNC degradation products. Such influence may be migrating ions to the metal contacts through the organic layers and substantially undermine their initial purpose. An indication of such process can be observed at voltages of value below -15 V: the DCM-curve points start to noisily divert from the plateau. Since currents at this points are limited by the thickness and permittivity of the PMMA layer only, the insulation ability of

PMMA is apparently severely harmed and leads to a breakdown of many other pixels. The electron-only devices (right), do not show any signs of accelerated degradation by the washing procedure. Nevertheless, the electron-only devices show stronger degradation compared to the hole-only if not washed. So ultimately, for the electron-only device the degradation of the PNCs seems to even be slowed down by the washing procedure. Clearly, the DCM curves prove carrier selective degradation speeds, even though the mechanisms are unknown at this point. The formerly measured n-type nature of the pristine PNCs could be a start for explaining this carrier asymmetric behaviour. When comparing this findings with the corresponding PeLEDs (cf. figure 7.2), one can actually spot correlations: The initial EQE boost does not last long so that at 6 V the washed sample underperforms the unwashed one. That is well correlated with the observation of the changes between first and second ramp of the hole-only sample. Initially, the hole injection is enhanced compared to the unwashed one, the lowered injection resistance is reflected in the higher EQE. However, things quickly change to a worsened scenario, which explains the EQE flipping at the said voltage. The electron injection seems to play a minor role according to this comparison. Undoubtedly, this investigation proves that the ligand density plays a significant role for the properties of these MIS devices to the extent that it may render charge injection ability asymmetric.

Among the analysed PeLEDs, the one featuring lecithin ligands showed an optimum EQE rather than a monotonous drop. If the DCM curves of the single carrier MIS devices can be correlated with the respective PeLEDs, this optimum has to be notable in such. Figure 8.4 shows the measurements of the MIS stack with lecithin PNCs. The first ramp is very comparable to the previously considered ones. The hole-injection resistance is lower than the unwashed PNC sample and in range of the all-organic counterpart. Also, the injection voltage is not significantly out of the ordinary. The electron-only stack behaves more similar to the organic analogue, too. Intuitively, one could describe the situation as a better passivated PNC influence while not costing conductivity. However, the condition changes completely when analysing the second ramps. The electron injection resistance does not change at all, while the hole injection resistance is only slightly more than doubled. Still, the resistances remain less than half as high as they are for all non-lecithin samples on the second ramp. A extremely strong novel effect can be noticed, when investigating the voltages: These samples shift their injection voltage in the opposite direction. After the first ramp, the PNC layer induces a carrier depletion at positive bias. This is especially prominent for the electron-only sample, where the depletion region already breaks down at negative bias of -1.7 V at the first ramp, just as all the other investigated PNCs, but for the second ramp voltages as high as 16.3 V are required for an injection.

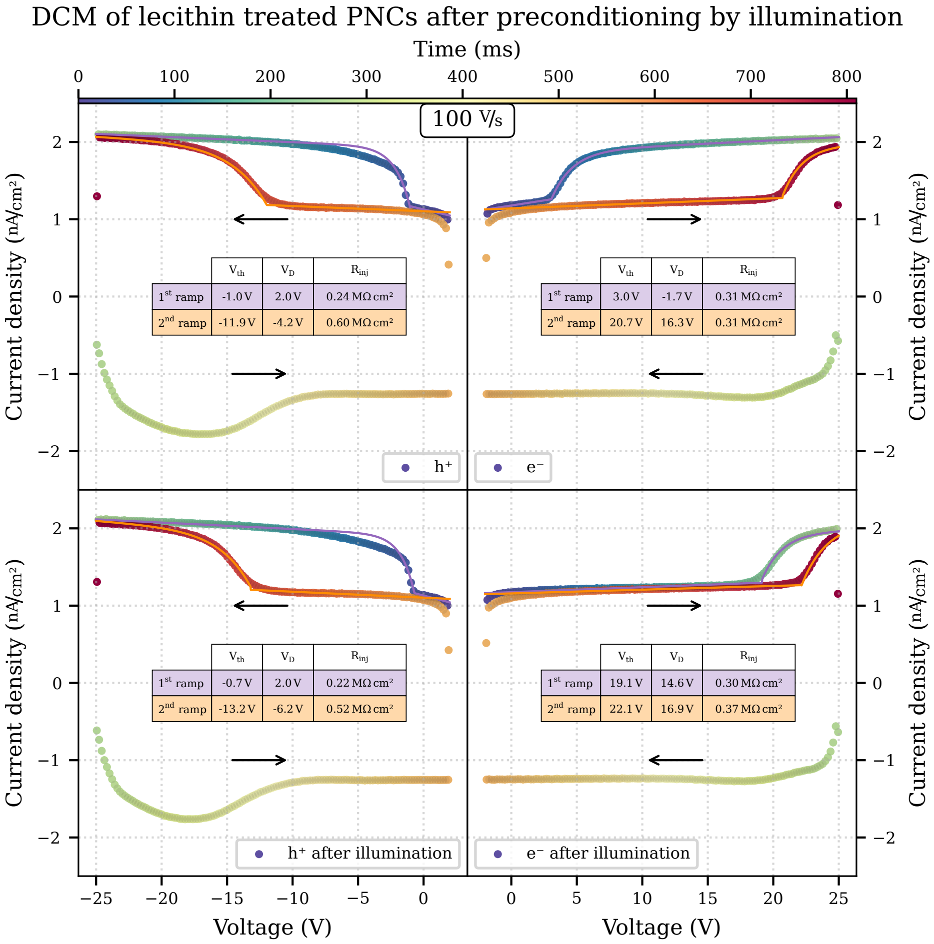

	V_{th}	V_D	R_{inj}
1st ramp	-1.0 V	2.0 V	0.24 MΩ cm²
2nd ramp	-11.9 V	-4.2 V	0.60 MΩ cm²

	V_{th}	V_D	R_{inj}
1st ramp	3.0 V	-1.7 V	0.31 MΩ cm²
2nd ramp	20.7 V	16.3 V	0.31 MΩ cm²

	V_{th}	V_D	R_{inj}
1st ramp	-0.7 V	2.0 V	0.22 MΩ cm²
2nd ramp	-13.2 V	-6.2 V	0.52 MΩ cm²

	V_{th}	V_D	R_{inj}
1st ramp	19.1 V	14.6 V	0.30 MΩ cm²
2nd ramp	22.1 V	16.9 V	0.37 MΩ cm²

Figure 8.4.: DCM curves of lecithin passivated PNCs. The bottom DCM are measured after an illumination treatment. The properties of the lecithin sample's first ramps are between the all-organic and the native sample. However, the second ramp shows a stronger shift. Also, evidently, a illumination treatment recovered the initial properties mostly.[S.110, S.111]

Regarding the lower DCM branch (green), the reverse ramp gives insight in the carrier extraction. The extraction regime, that is the plateau of higher negative currents, fades also at the elevated voltages compared to the all-organic samples. Apparently, this high voltage is induced by charges that are not extracted starting at this backwards-threshold. Since an area between both forward DCM curves is proportional to a sheet charge density,[189] it becomes evident that a significant amount of charge remains in the device without being extracted on the backwards ramp. Opposed to the native samples the shift is reversible. After illuminating the samples with white light, the injection properties can be completely recovered for the hole-only sample (cf. figure 8.4 bottom-left). Apparently, the trapped charges can be released by light. This effect is not exclusive to the lecithin samples, but for the other samples the irreversible degradation is too strong to investigate it properly (cf. figure S12). Anyhow, it can be observed only to a minor extent for the electron-only sample. Then again, the second ramp reveals also some irreversible part even for the lecithin samples. This asymmetric extraction behaviour can also be motivated by the energy landscape. The energy gap between TCTA's HOMO and the PNC's VBM allows for extraction of holes, while B3PYMPM's LUMO is less compatible to the PNC's CBM for extraction. Given the fact that experimentally determined LUMOs are generally underestimated,[199, 200] this incompatibility may be worse than indicated by figure 8.1 d). Additionally, the fact that the lecithin PNC seems to store more charges along with the observation that the degradation is significantly avoided, leads to the assumption that there are less undefined or unpassivated sites in these PNCs. In case of the native PNCs the charges can be more easily transferred to the adjacent organic transport layers via these sites. With that, the DCM curves can also give a glimpse on the passivation implications of a ligand on a PNC.

The correlation between the injection properties obtained by the DCM curves and the EQEs of the corresponding PeLEDs is still valid. While the injection resistances imply a slight hole abundance in the beginning, crossing equality until finally reaching a disbalance towards electron abundance. However the injection voltages of the second ramp differ considerably so that they may also break this correlation. Then again, the reason for these voltage shifts originate from a charge up of the device. This effect will be weakened substantially, since the PeLED is a device where the carriers will annihilate for the light emission and therefore counteract this charging effect to a considerable extent. Nevertheless, a non-monotonic EQE curve is made plausible with all these mechanisms adding up.

Finally, to further strengthen the evidence on the obtained injection resistance of the MIS devices being correlated to the non-insulating counterpart, which are PeLEDs and actual single carrier devices, LiTFSI-treated PNC layers are investigated (cf. figure 8.5) in a hole-only MIS device. Again, the injection voltage has not changed substantially, but as expected the resistance is decreased. Also at this point, the change in injection resistance is directly correlated to the EQE change between native and LiTFSI, as it shows resistance comparable to the lecithin sample. Though, the EQEs are lower for LiTFSI treated samples compared to the lecithin, but in a comparable range. Then again, this discrepancy, may also arise from the LiTFSI treatment not contributing to operational stability unlike lecithin. This is also indicated by investigating the second ramp, which resembles more the native. Also, here the shifts are mostly irreversible. However, the double step is more pronounced for the LiTFSI samples. Figure 8.5 shows a fit on both steps, with the same formulas. Interestingly, unlike the native sample only the second step showed

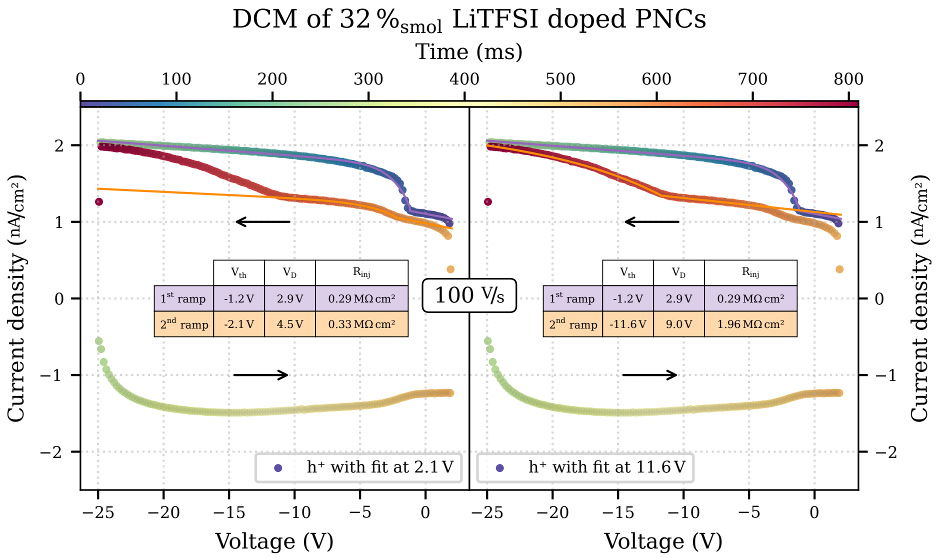

Figure 8.5.: DCM on LiTFSI treated PNCs reveal also an enhanced hole injection and a more pronounced double-step feature. Unlike the other measurements the double-step does not degrade considerably.$^{\mathrm{S.112,\ S.113}}$

degradation. The position and slope of the first step stayed until breakdown. Apparently, there is a novel not yet discussed feature which can be most likely ascribed to the more complex binding situation of LiTFSI to the PNCs and also its inherently free Li ions.

Summarising one can state that the DCM curve analysis can yield very valuable information on charge carrier specific influences in terms of stability as well as conductance. With proper analysis, estimates about the potential performance in a PeLEDs can be made. Though, there is a set of parameters in the formulas, which are not discussed in this work, there is still a lot of information to gain from further analysis. Especially, when combining the considerations with concurrent PL measurements, just as reported by Noguchi et al. [189], important implications on the quantum-yield changes upon specific carrier excess can be systematically analysed. Preliminary measurements have revealed that there are severe impairments by the adjacent transport layer with and without voltage bias.

9. Conclusion and Outlook

During the course of this study, LHP-PNCs have been successfully employed in LEDs. Starting from highly stabilised and therefore also electrically insulating PNCs, the initial devices exhibited no luminance or only such of the transport layers. Parallel to this work global research gained experience with the material providing a basic understanding and achieving better stability of the PNCs with less insulation. Consequently, a successful application in PeLEDs has been accomplished. However, after various initial improvements and overcoming the challenges posed by the nature of spin-coating a delicate NC thin-film, an efficiency limit of around 0.2 % EQE has been identified.

Three approaches for PeLED improvements are presented, that are the down-conversion process, the p-doping via LiTFSI and an exchange of ligands with stronger surface binding. While the colour-conversion path entirely avoids many of the challenges posed by the novel, delicate PNC material, the techniques using the dopant LiTFSI or exchanging the ligand with a more functionalised one predominantly deal with issues arising from the PNCs intrinsically. The colour-conversion may be very interesting for industrial application at some point since the mechanism is already known and easy to apply to existing supply chains and automation. However, the direct emission from PNC pose a more elegant way for light-emission, which may achieve similar efficiencies with less engineering and/or materials resp. parts in the stack. The inherent energy loss during the colour-conversion can be avoided. Though, the presented LiTFSI enhances the carrier balance leading to a remarkable increase in efficiency, the stability remains very low. For improved stability the ligand exchange approach achieved some success. Overall the EQEs of the green and blue devices have not exceeded 2 %, and all the PeLEDs showed operational lifetimes of less than a few minutes. Nevertheless, concurrently performing competing research reports ten times higher efficiencies and lifetimes without any special engineering and sometimes with same stack designs. With the fact that also the different batches received from collaborators fluctuated in quality, as determined by shelf-lifetime and PLQY, by up to several orders of magnitude, raises the suspicion that the PNC synthesis itself has still higher implications on the PeLEDs performance than many of the approaches detailed in this work. Especially, the stoichiometry of the perovskite components with respect to each other, mixed halides as well as the cations during synthesis combined with a tuned oleic acid to oleylamine ratio proved to be a very delicate balance making a substantial difference in the resulting PeLEDs performance and lifetime.

Nevertheless, this work presents some universally applicable techniques to enhance LHP-NC LEDs. EQEs can be enhanced by a successful p-doping of the surface of such PNC from the mentioned native limit by a factor of up to seven by realigning the energy levels in the stack. The stability of PeLEDs can be increased by using different, more affine phosphocholine anchor groups for the attachment of the ligands. Furthermore, a novel approach to quantify the injection properties with DCM has been presented. With that, a better understanding in the mechanisms behind some of the major issues can be obtained. Anyway, all of the presented improvements can be further developed and applied.

The colour-conversion device requires more engineering in order to become relevant for the commercial application. Such could be to further improve the particles within the micelles to have a real unity PLQY. Additionally the pump-device has to be upgraded to a high-performance LED and its spectrum has to match with the thickness and absorption spectrum of the PNCs.
The LiTFSI approach has also opened ways to optimise by using different alkaline or even earth alkaline metal ions instead of lithium. Potassium TFSI has proven to also increase the PLQY substantially, while the ion migration could turn out to be weaker because of the bigger ion size. Also, approaches with the TFSI acid have been published. A blend of these chemicals may be used to continuously tune stability and/or energy levels.
For the DCzGPC ligand an employment during the synthesis may overcome the solubility induced limitation of the exchange procedure. Furthermore, theoretical investigation on the underlying mechanism on the blue-shift by the ligand may open new ideas for further optimisation. Overall, the presented DCzGPC devices are far from optimal, since the ligand density is too high, nevertheless significant improvements can be reported, which makes the process even more promising.

Especially a more detailed DCM with potentially a concurrent PL investigation will give more insights in the role of the ion movement on the LiTFSI treated sample as well as for the DCzGPC exchanged one. With the PL part exciton dynamics of charged particles may reveal new insights on the role of the carbazole in proximity of the PNC. This could also be studied on a helium cooled device to investigate the supposed energy transfer from the carbazole moiety.

Not only this work but also the research regarding the perovskite photovoltaic or the work of other NCs for light emission will benefit from each other, which will give rise to unprecedented novel applications and improvements. These innovations are hitting the consumer market at the time of writing this thesis. However, the toxicity of lead will remain an issue for any product based on LHPs. Arguably, the devices usually require very low quantities, so a perovskite solar cell has a lower lead concentration than urban soil. On the other side, the bioavailability is significantly higher which may cause a lead poisoning by such LHP contamination. Anyway, effective encapsulation or exchanging the lead with other suitable ions is explored.[201] With that, even if the LHP may not be used for the discussed large scale applications, the research on this material class of soft metal-halides has already evolved into different fields such as batteries[202] or catalysis[203, 204].

A. Supplemental Data

A.1. Details on Processing

The following details are, except the displacement current parts, identical to the procedures reported in references 70, 121 and are copied for the sake of completeness of the chapter 4 on methods.

A.1.1. Materials

The indium tin oxide (ITO) substrates with dimensions 2 by 2 cm have been purchased by Kintec (Hongkong) with and without custom pattern of layer thickness 100 nm on a 23 nm SiO_2 buffer on a 0.7 mm thick glass substrate. Fused Silica (SiO_2) substrates with dimensions 2 by 2 cm have been bought with a thickness of 0.7 mm from Nano Quarz Wafer Germany GmbH. PEDOT:PSS is used in a low-conductive ratio of 1 : 20, having the descriptor CH8000, by Heraeus Germany GmbH & Co. KG. ZnO has been synthesised from Zincacetate with the sol-gel method.[205] $CsPbBr_3$ solution ($c = 10$ mg/ml in toluene, ProductID: 900746) and lithium bis(trifluoromethanesulfonyl)imide (LiTFSI) (99.95 % trace metal basis, ProductID: 544094) have been ordered from Merck Germany KGaA. poly(9-vinylcarbazole) (PVK) ($M_w > 10^5$, ProductID: LT-N4078) has been obtained from Luminescence Technology Corp. (Lumtec, Taiwan).

A.1.2. Nanoparticle Preparation

Preparation of oleylammonium halide (OLA^+-X^-) To prepare a 1.1 mmol/ml OLA^+-X^-precursor solution, 10 ml of oleylamine (OLA) has been placed in a 25-ml three-neck flask and either 1 ml of concentrated hydrochloric acid (HCl(aq.)) or 1.28 ml of concentrated hydrobromic acid (HBr(aq.)) has been added slowly. Subsequently, the solidified reaction mixture has been heated at 120 °C under nitrogen atmosphere for 2 hours. The reaction temperature has then been increased to 150 °C for 30 minutes and afterwards allowed to cool to room temperature. The mixture has been kept in a glovebox and heated to 80 °C before injection.

$CsPbBr_2Cl$ nanocrystals $CsPbBr_2Cl$ nanocrystals have been made by a hot-injection synthesis using a modified literature method.[37] To synthesise 7 nm $CsPbBr_2Cl$ nanocrystals, 49 mg (0.15 mmol) Cs_2CO_3, 67 mg (0.3 mmol) PbO and 1.5 ml oleic acid (OA) have been degassed in 15 ml ODE in a 50 ml three-neck flask under reduced pressure at 120 °C for 1 hour. The temperature has been increased to 240 °C under nitrogen atmosphere, 1 ml OLA$^+$-Br$^-$and 0.5 ml OLA$^+$-Cl$^-$precursor have been quickly injected and after one minute the reaction mixture has been cooled to room temperature using an ice-bath (below 180 °C). $CsPbBr_2Cl$ NCs have been collected by centrifuging the suspension (7000 rpm, 10 min.), decanting the supernatant, and collecting the precipitate. The precipitate has been centrifuged again without addition of a solvent (7000 rpm, 5 min.), and the resulting supernatant has been removed with a syringe to separate the traces of residual supernatant. The precipitate has been dissolved in 2 ml hexane and centrifuged again (2500 rpm, 5 min.) to remove aggregates and larger particles. The resulting supernatant has been filtered through a 0.2 µm PTFE syringe filter and stored as stock solution inside of a glovebox with a typical concentration of 25 mM following Maes et al. [206].

LiTFSI treatement The LiTFSI solutions are diluted from a stock which is created by dissolving 200 mg LiTFSI with 2 ml dimethylformamide (DMF) and 18 ml chlorobenzene (CB) by stirring overnight resulting in a volume concentration of 10 mg/ml. Dilution to 1, 0.1 and 0.01 mg/ml concentration is done with CB only.
Equal volumes of LHP-NC solution and LiTFSI solutions are mixed to obtain a LiTFSI-doped solution. Mixing equal volumes of 10 mg/ml LHP-NC and 10 mg/ml LiTFSI yields a 5 mg/ml LHP-NC solution with 50 wt. % (resp. 641 %$_{\text{smol}}$) LiTFSI doping. Analogously, a 9.09, 0.990 and 0.099 wt. % (resp. 64, 6.4, 0.6 %$_{\text{smol}}$) doped solution is obtained by using 1, 0.1 and 0.01 mg/ml concentrated LiTFSI solution and mixing with the 10 mg/ml LHP-NC solution by equal volumes. All LHP-NC solutions are created within a nitrogen filled glovebox and have exhibited stable luminescence for at least 3 months at room temperature.

A.1.3. Sample Preparation

Photoluminescence Fused Silica is used as a substrate for all PL measurements, that is PLQY, TRPL and ADPL. The substrates are spin-coated on in a nitrogen-filled glovebox by dropping 50 µl (p.r.n. LiTFSI-doped) LHP-NC solution before starting the rotation of the spin-coater. After a settling time of 30 seconds it is accelerated to 500 rpm and kept at that speed for another 30 seconds. To remove residuals from the edges, spinning for 5 seconds at 2000 rpm is applied before stopping the procedure.

Gate-less transistors and transparent MIS devices The gate-less transistors are built by using a just described PL sample and subsequently evaporating two 70 nm thick gold (rate: 20 pm/s) contacts. The two contacts are designed as bars which are 3 mm long and 150 µm far apart. However, deviations are measured with an optical microscope and taken into consideration.

As for the transparent MIS devices, they are manufactured mostly identical to the corresponding single carrier devices, described in the next paragraph. The only difference is, that the bottom transport layers, that are, the ones between ITO and the PNCs are replaced by a single layer of PMMA with a thickness of 160 nm. This layer is deposited by spin-coating 25 mgml PMMA in toluene at 1000 rpm for 50 s and heated on a hotplate at 160 °C for 20 minutes.

UPS/XPS, SEM, LEDs and single-carrier devices For UPS/XPS and SEM the unpatterned, and for the electrical devices the patterned substrates are used. For the electron-only device a fused-silica substrate is smoothed with a 0.8 µm thick PMMA layer, spin-coated by 100 mgml in toluene at 1000 rpm for 60 s and heated on a hotplate at 230 °C for 30 minutes, before depositing 7.5 nm aluminium and 1 nm LiF as a bottom electrode. Initially, PEDOT:PSS is spin-coated in the cleanroom, at 4000 rpm for 30 s, and heated on a hotplate at 130 °C for 15 minutes, resulting in a smooth approx. 40 nm thin film. The samples are transferred to a nitrogen-filled glovebox immediately. As second layer, the approx. 20 nm thin PVK film is deposited by spin-coating a 3 mg/ml concentrated PVK-chlorobenzene solution at 3000 rpm for 30 seconds and heating at 175 °C for 30 minutes. The LHP-NC solutions are spin-coated as described for the PL samples after cooling the substrate to room-temperature, resulting in a closed film of about 2-3 monolayers (effective thickness approx. 20 nm).
The sample in current state, that is the bottom-half LED, is used for UPS/XPS and SEM investigations. For devices, the samples are transferred without ambient exposure into a high vacuum chamber, with a pressure smaller than 0.1 mPa. For hole-only, 10 nm HATCN (rate: 50 pm/s), for LEDs and electron-only devices 55 nm B3PYMPM (rate: 100 pm/s) followed by 0.5 nm LiF (rate: 10 pm/s) is evaporated. The devices are finished with a 60 nm (rate: 100 pm/s) thick aluminium cathode, also deposited by thermal deposition.

A.1.4. Measurement details

PLQY The photoluminescent quantum yield (PLQY) is determined by a two-step-method measurement featuring a $BaSO_4$ coated integrating sphere.[207] The excitation source is a HeCd laser's 442 nm light. The excitation signal as well as the samples fluorescence is collected with a high-OH SiO_2 fibre (OH: hydroxyl ion) and guided into a Princeton Instruments Acton2300i spectrometer, which is connected to a nitrogen cooled CCD camera, that is Princeton Instrument's Pylon BRX100. An absolute calibration of the integrating-sphere- system has been performed with a lamp calibrated for spectral irradiance according to the NIST standard by GigaHertz Optik GmbH Germany. With that system spectra could evaluated to its amount of photons and consequently a

PLQY is calculated.

ADPL The angular dendent photoluminescence (ADPL) measurement and analysis are performed as previously reported by this group.[59] The spectrum is recorded with the same CCD-Spectrometer system as explained for the PLQY.

TRPL Transient photoluminescence (TRPL) was recorded by the C5680 streak camera system by Hamamatsu, after being delayed by DG535 by Stanford Instruments while being spectrally analysed by a Acton Spectra Pro 2300i. Excitation was done with the EKSPLA PT400 Diode Pumped Solid State laser set to wavelength 355 nm.

UPS/XPS Ultra-violet photoelectron spectroscopy (UPS) measurements have been conducted using a SPECS PHOIBOS 100 hemispherical electron analyser equipped with a monochromatised helium discharge lamp (21.22 eV). The UV flux has been attenuated significantly by the monochromator to avoid UV-induced sample degradation. A sample bias of -10 V has been applied to acquire the secondary electron cut-off (SECO) spectra. The base pressure of the analysis chamber has been kept below 0.1 µPa. X-ray photoelectron spectroscopy (XPS) measurements have been performed at a JEOL JPS-9030 ultrahigh vacuum system (base pressure of 0.1 µPa) using monochromatised Al K_α (1486.6 eV) radiation. Anode power of 30 W was applied for XPS measurements, which has not been found to induce noticeable sample degradation.

Gate-less transistors and transparent MIS devices The current through the gate-less transistor is obtained by a 4200A-SCS Keithley Parameter Analyzer by Tektronix. The same device is also programmed to ramp the voltages. The transistors are measured and cooled under a vacuum of lower than 0.1 mPa.
The transparent MIS devices are measured in a nitrogen filled glovebox with the PAIOS system by fluxim AG (Switzerland).

LEDs and single carrier devices j-V(-L) curves are recorded with a Keithley 2612B Source Meter Unit (SMU). A Photodiode of known diameter at known distance is used for Luminance detection. The electroluminescent spectrum is taken with the Phelos system by fluxim AG (Switzerland). With that and a lambertian approximation the EQE is determined. The integrity of the lambertian approximation has been ensured by random sampling with a calibrated integrating sphere (same setup as for PLQY). The sampling revealed that the photodiode's, and consequently in this manuscript reported EQE, is about 10 % underestimated, relatively (not percentage points). For instance, the peak EQE of the $64\,\%_{\text{smol}}$ LiTFSI-doped sample in figure S8 exhibits 1.1 % EQE in the integrating sphere while it has been 1.0 % in the photodiode-setup.

A.2. Additional Analysis

A.2.1. Colour conversion

The pump stack (cf. figure S1 a)) is inspired by Zhang et al. [209] and Kotadiya et al. [208], comprises available materials and is not optimised for efficiency but rather stability. That is the reason why the use of triplet-blocking layers such as DPEPO, CzSi (cf. figure S13 e) and g)) has been avoided. The group has observed stability issues with these materials.

Further evidence on a simple DC process is provided by fitting the obtained PeLED's EL spectrum with a weighted superposition of the down-converting components: $\alpha\Phi_{EL}$, the pump OLED EL emission spectrum and its weight α. $\beta\Phi_{PNC-PL}$, the micelle-PNC film's PL spectrum and its weight β and λ_0 its red-shift. Finally, Ω, the micelle-PNC film's absorption spectrum and its weight σ. For fitting, the interpolations of the spectra are taken and a combined function (Φ_{DC}) is composed (details in ref. S.22):

$$\Phi_{DC}(\lambda) = \alpha\Phi_{EL}(\lambda) \cdot (1 - \sigma\Omega(\lambda)) + \beta\Phi_{PNC-PL}(\lambda - \lambda_0) \tag{A.1}$$

The fit shows good agreement in the blue to green colour regime, while it fails to describe for the red part. However, the unabsorbed tail of the Cz-PS emission may be over-proportionally out-coupled, since the simulation also suggest a spectral dependence. Also, a red-shift (λ_0) has to be introduced. The shift can be ascribed to the change of excitation conditions, the PNC film is, for the PL spectrum, excited with a narrow-band source from a nitrogen atmosphere, while in the blue OLED it is broad-band and from glass.

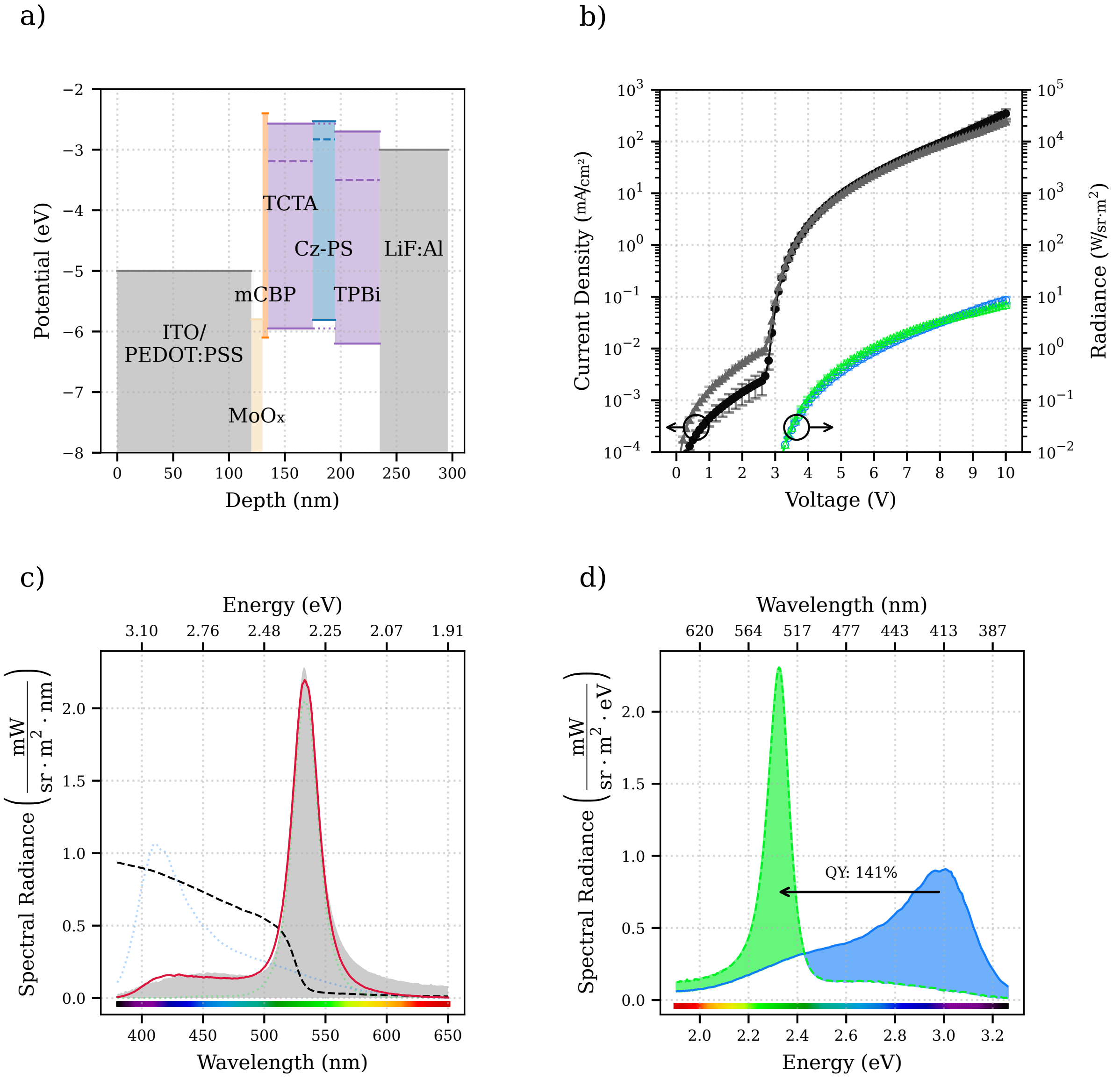

Figure S1.: a) Illustration of the stacked organic semiconductor layers (cf. figure S13) of the OLED that is utilised to pump the PNC down-converters. Energy levels taken from references.[64, 65, 73, 75, 190, 208, 209] The hole injection site is designed according to ref. 208. The transport layers have sufficient carrier confinement, but the triplets (dashed lines) are not well confined.[S.114, S.115]
b) Radiance plot according to figure 5.3 c); the radiance is not increased as dramatically.[S.32, S.116] c) Absorption (black dashed), down-converter device spectrum (filled gray area), superpositional fit (red solid) and its respective parts (dotted). The EL can be fitted by a superposition of pump spectrum reduced by absorption and the red-shifted micelles' PL.[S.22, S.117] d) Spectrum according to figure 5.3 b), but on energy scale with indicated areas for counting photons to obtain a device-PLQY (referenced on pp. 47, 109).[S.22, S.118]

A.2.2. LiTFSI Doped Perovskites

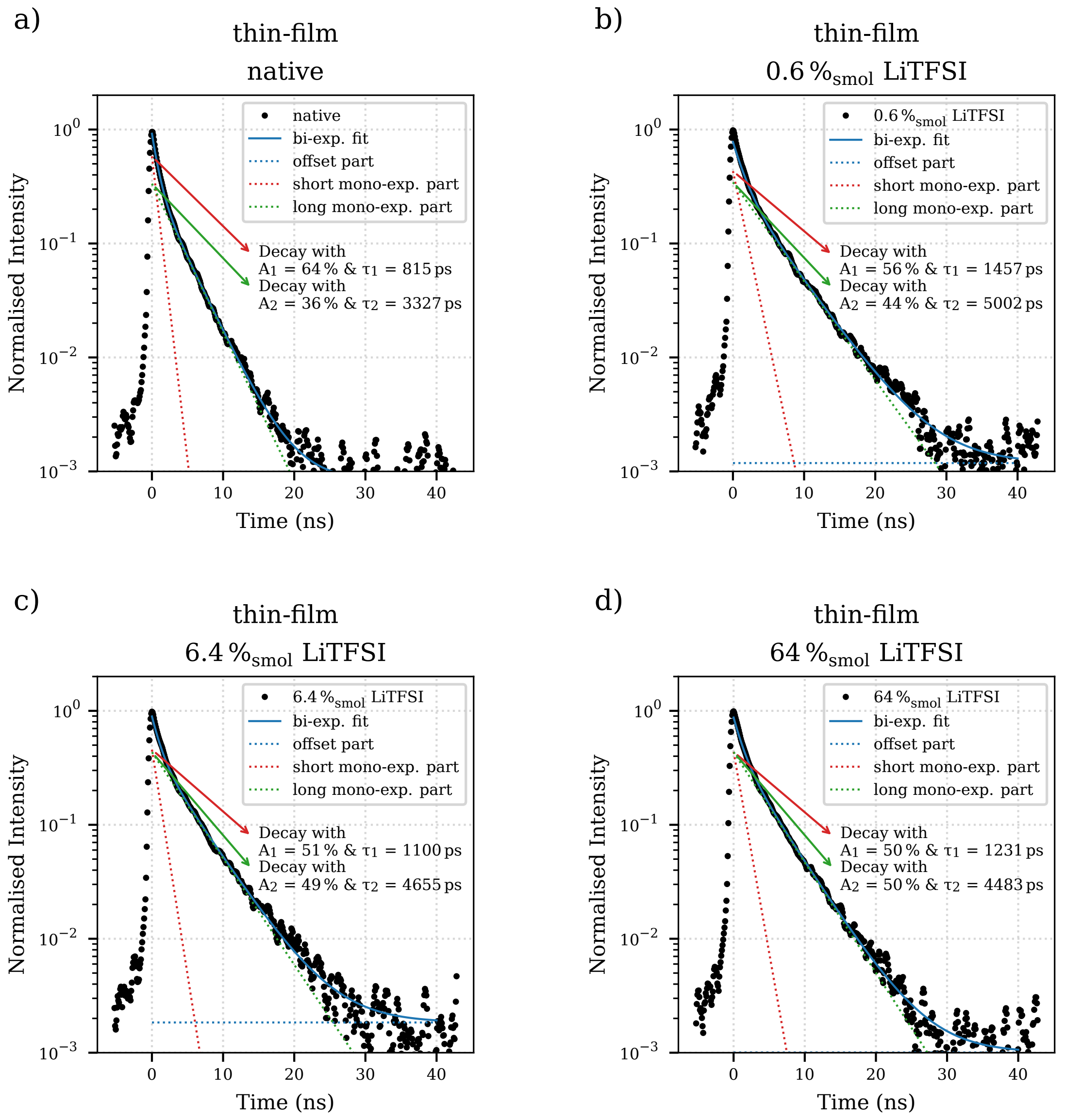

Figure S2.: Transient PL of a $CsPbBr_3$-PNC film with a) no, b) 0.6 $\%_{smol}$, c) 6.4 $\%_{smol}$, and d) 64 $\%_{smol}$ LiTFSI doping (referenced on p. 56).[S.40, S.119–S.122]

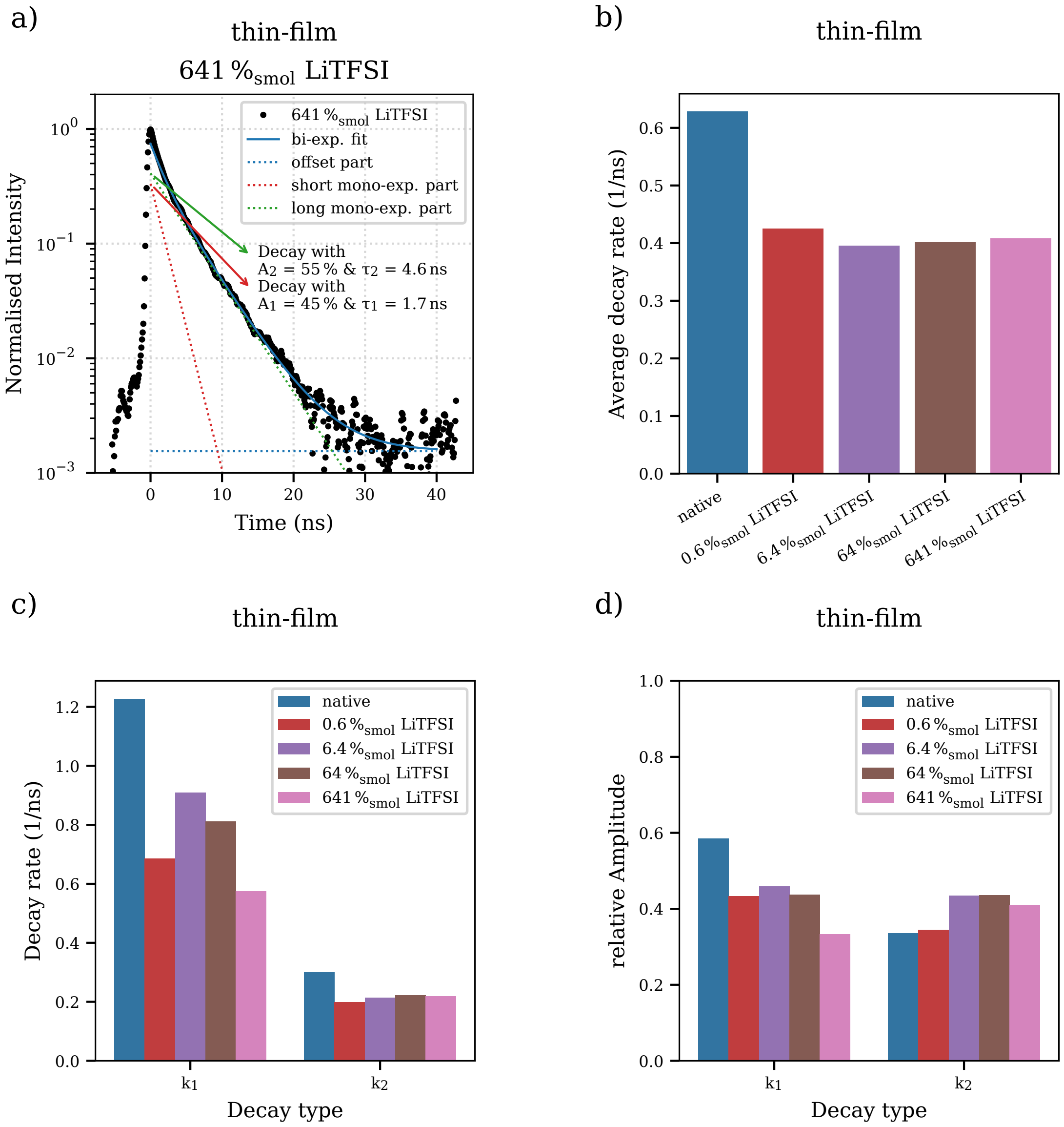

Figure S3.: Transient PL of a $CsPbBr_3$-PNC film with a) 641 $\%_{smol}$ LiTFSI doping. b) average decay rate, c) individual decay rates and d) relative amplitudes against LiTFSI doping concentration (referenced on p. 56).$^{S.40,\ S.123–S.126}$

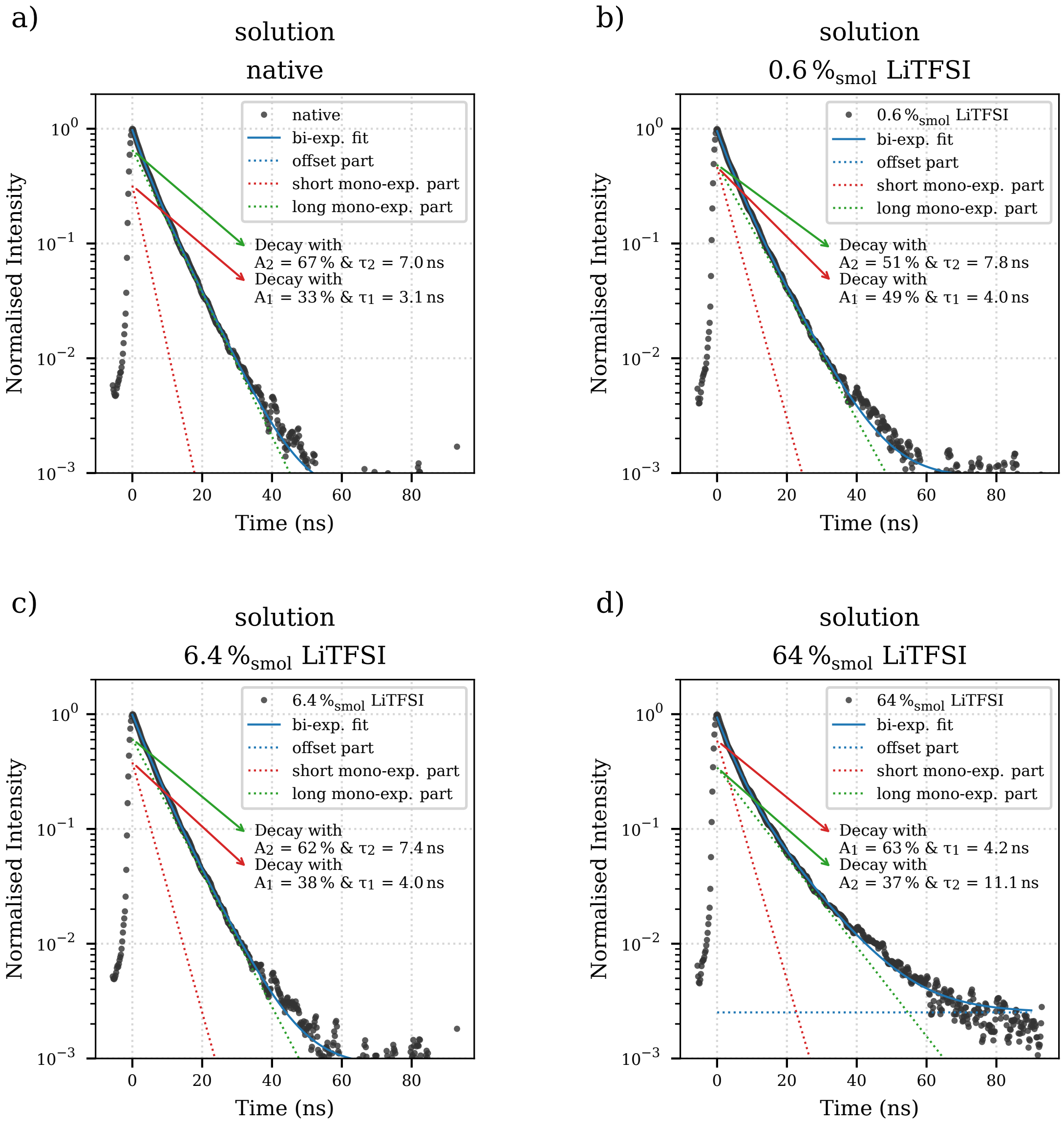

Figure S4.: Transient PL of a $CsPbBr_3$-PNC film with a) no, b) 0.6 $\%_{smol}$, c) 6.4 $\%_{smol}$, and d) 64 $\%_{smol}$ LiTFSI doping (referenced on p. 56).[S.41, S.127–S.130]

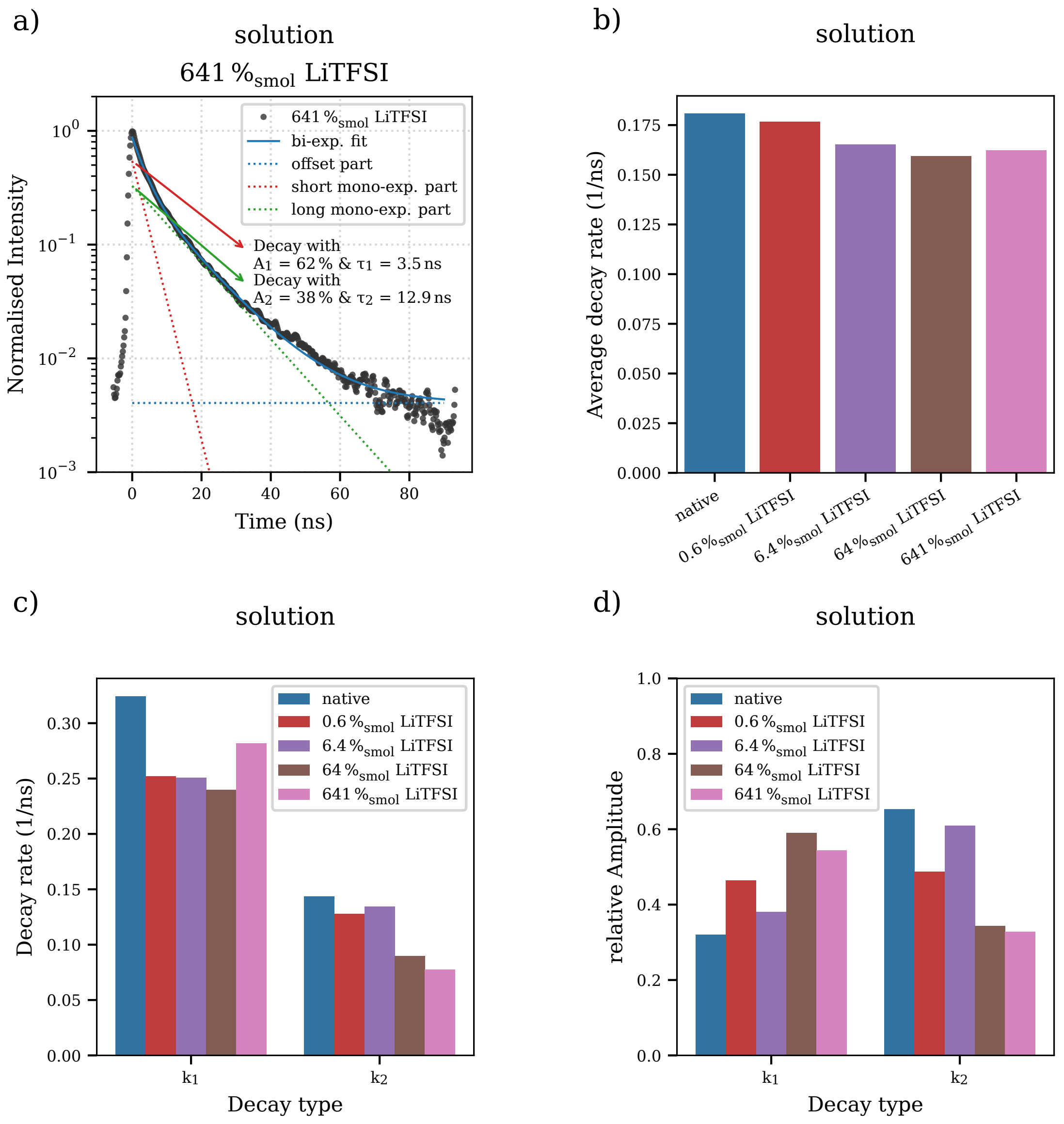

Figure S5.: Transient PL of a CsPbBr$_3$-PNC film with a) 641 %$_{\mathrm{smol}}$ LiTFSI doping. b) average decay rate, c) individual decay rates and d) relative amplitudes against LiTFSI doping concentration (referenced on p. 56).[S.41, S.131–S.134]

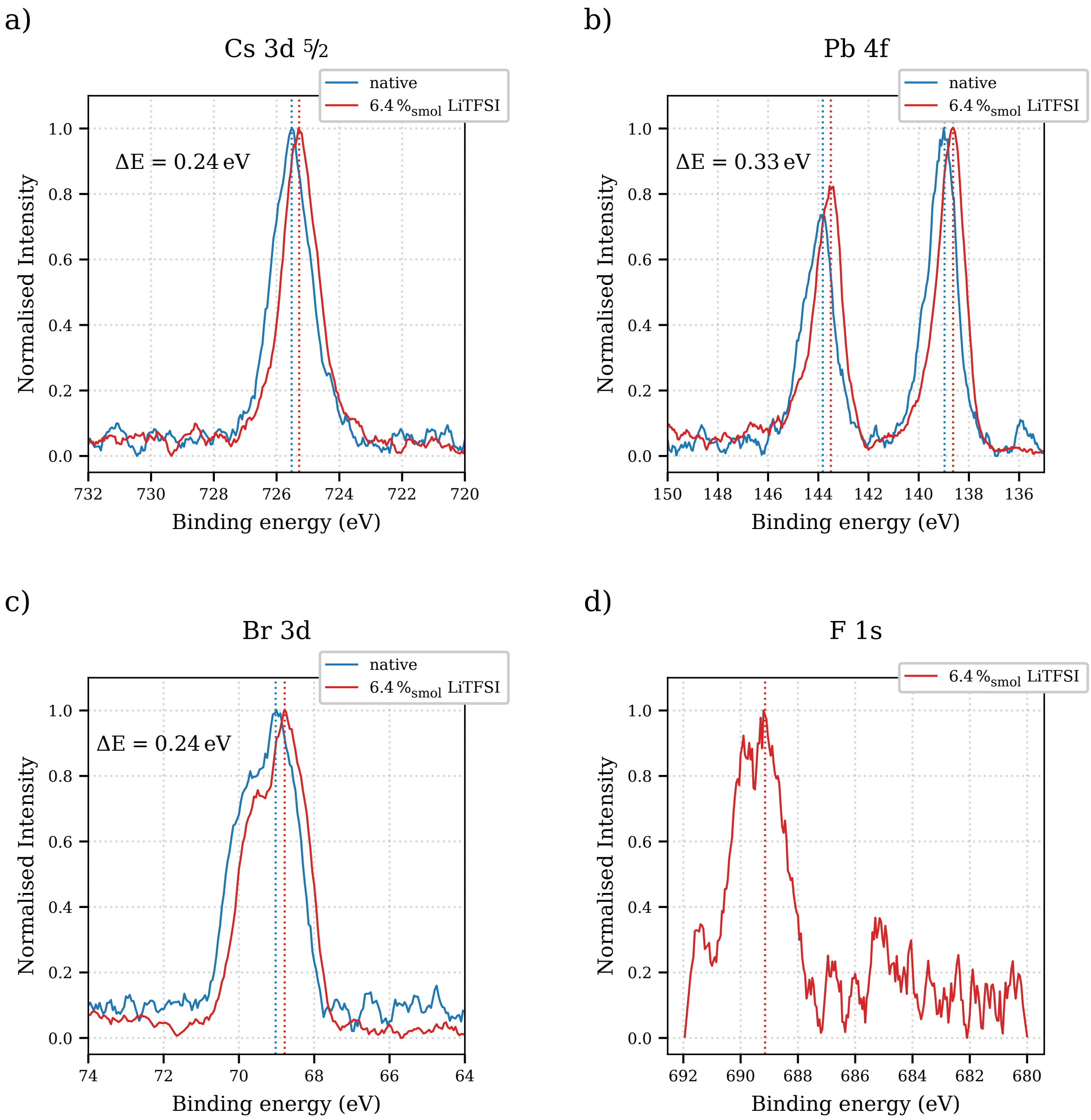

Figure S6.: Binding energy of the a) Cs 3d 5⁄2,[S.135] b) Pb 4f 5⁄2 7⁄2,[S.136] c) Br 3d,[S.137] and d) F 1s[S.138] orbital measured by XPS. The levels are shifted by around 0.25 eV consistently to the valence level shift obtained by UPS shown in figure 6.5. As expected no signal is detected for the native CsPbBr$_3$ NC caused by the absence of TFSI$^-$ (referenced on p. 60).[S.139]

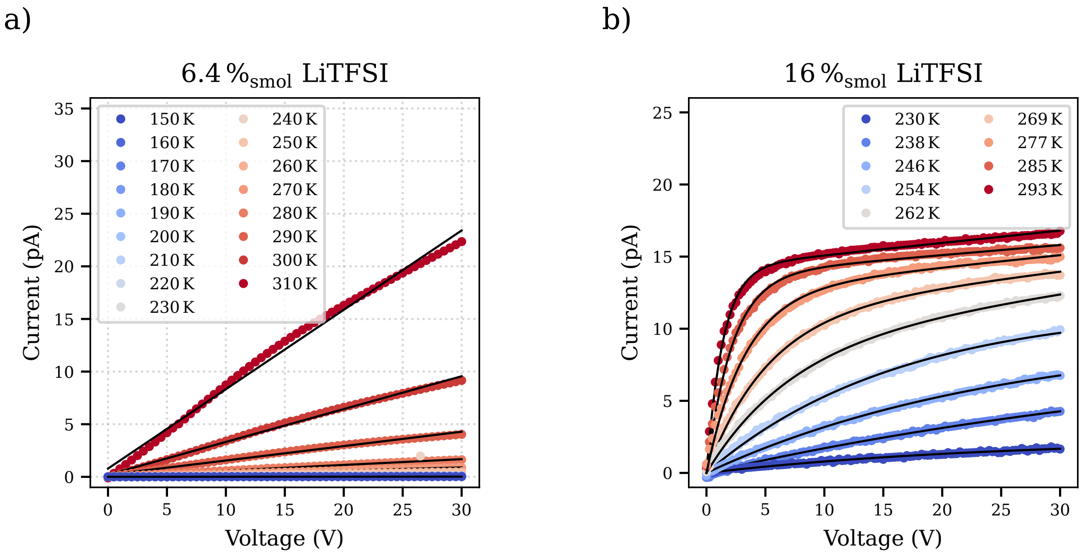

Figure S7.: Linear and RRC fit to obtain the conductances and if possible capacitances at different temperatures (referenced on p. 64).[S.62, S.140, S.141]

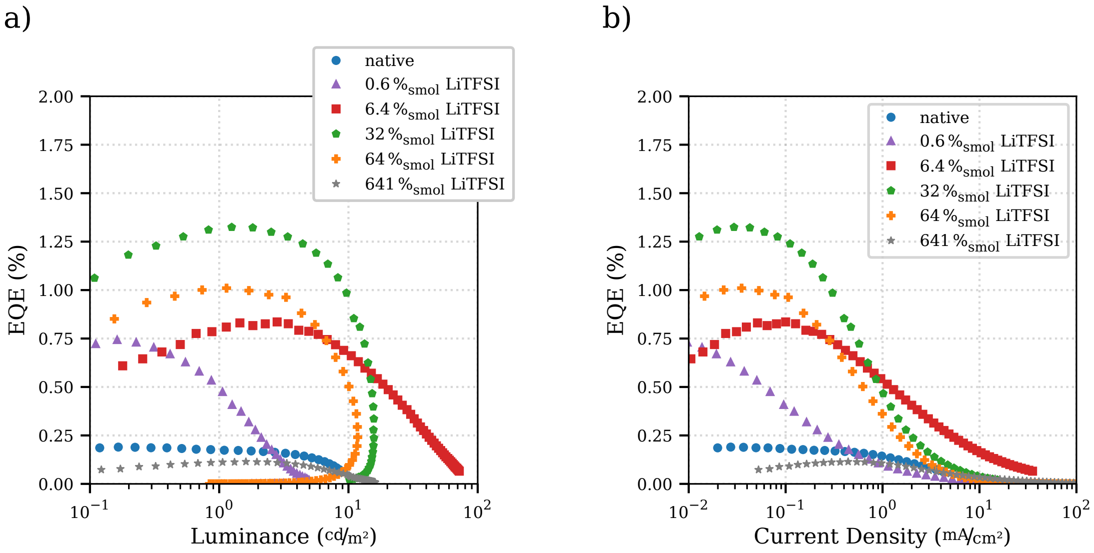

Figure S8.: A doping concentration depending EQE vs a) L[S.142], vs b) j[S.143], gives insight into a degradation limited luminance at concentrations exceeding 6.4 $\%_{\mathrm{smol}}$ (referenced on p. 69).[S.67]

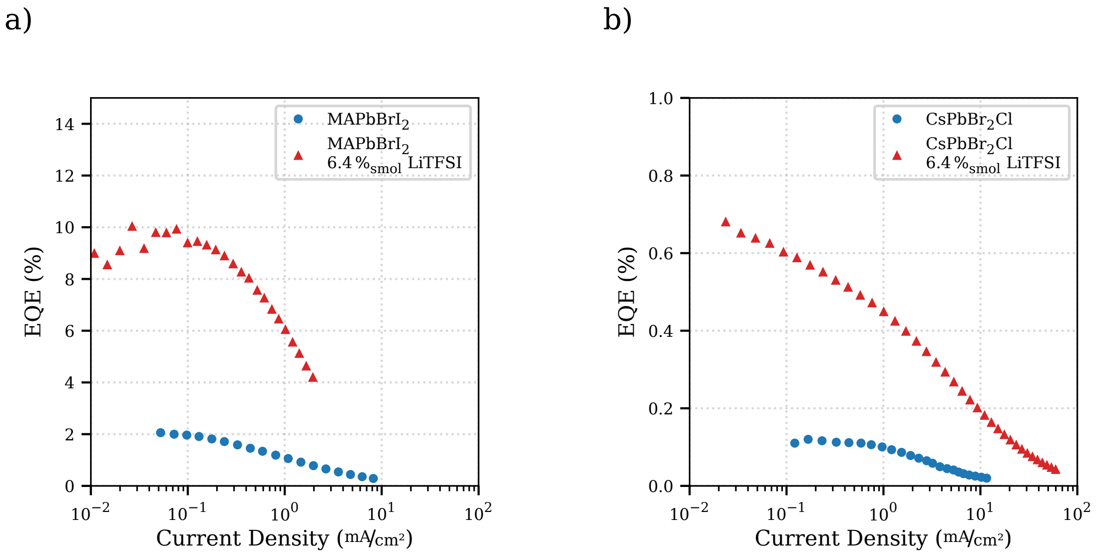

Figure S9.: EQE vs current density plot. Tremendous increases are also found with red and blue PNC (referenced on p. 74).[S.67, S.144, S.145]

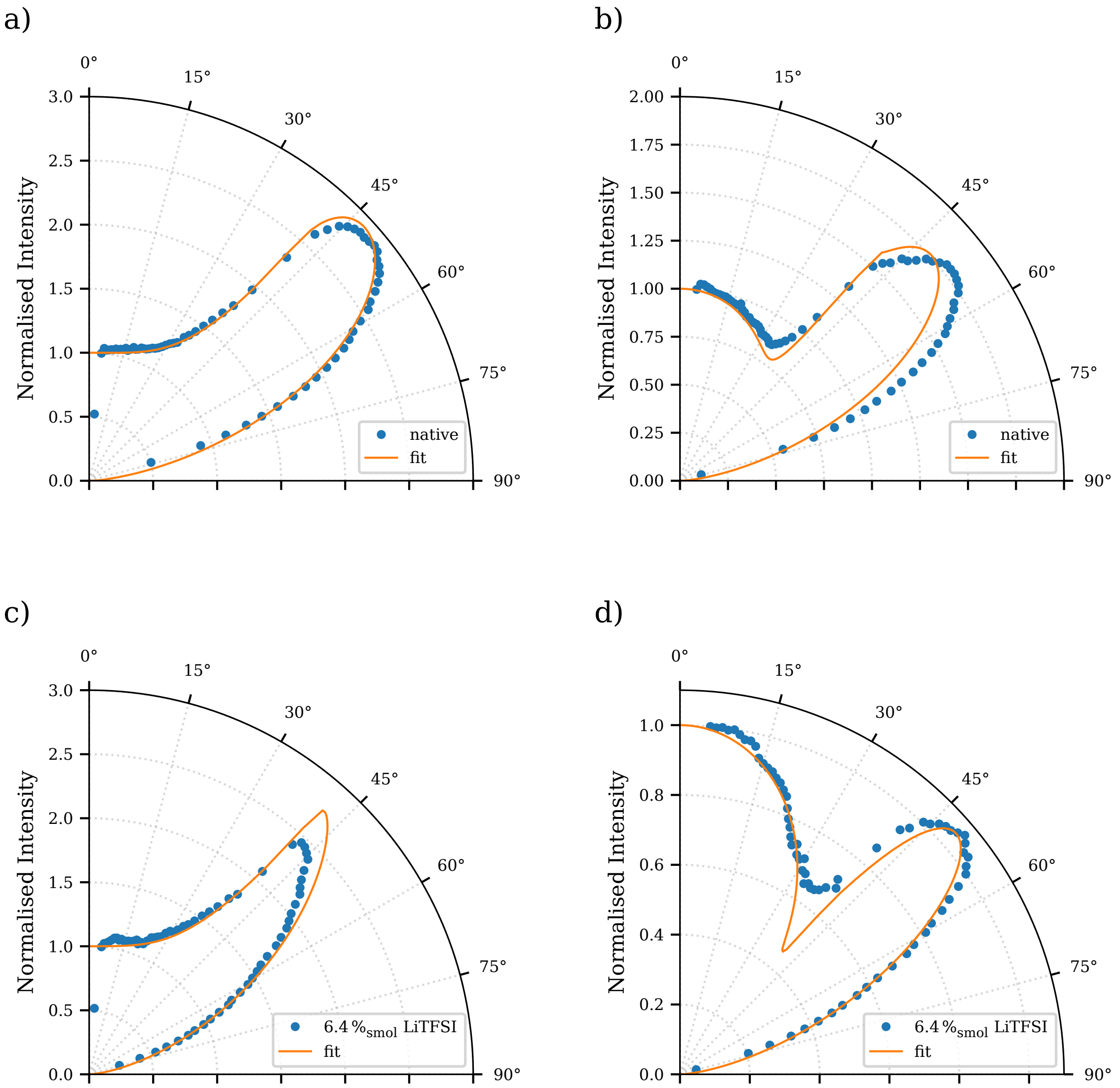

Figure S10.: S-polarised ADPL spectrum taken at 510 nm with a matrix-transfer fit of a) native[S.146] b) 6.4 %$_{smol}$ LiTFSI[S.147] doped CsPbBr$_3$ thin-film on glass (fused silica); the corresponding curves for p-polarised ADPL are shown in c)[S.148] and d) (referenced on p. 71).[S.72, S.149, S.150]

A.2.3. Carbazole Passivated Perovskites

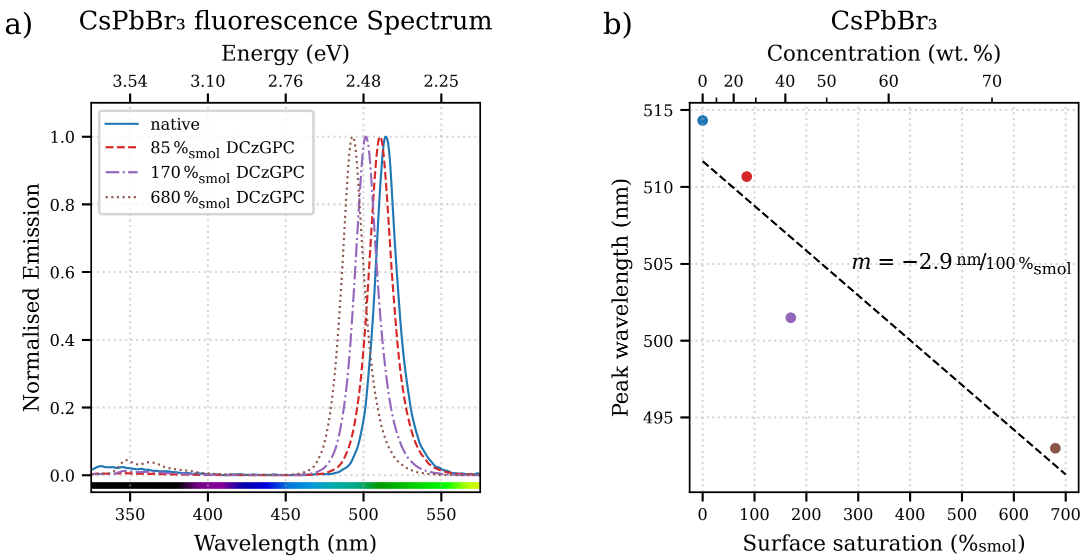

Figure S11.: a) Photoluminescence.[S.151] b) PL peak pos vs DCzGPC content (referenced on p. 82).[S.90, S.152]

A.2.4. Additional DCM curves

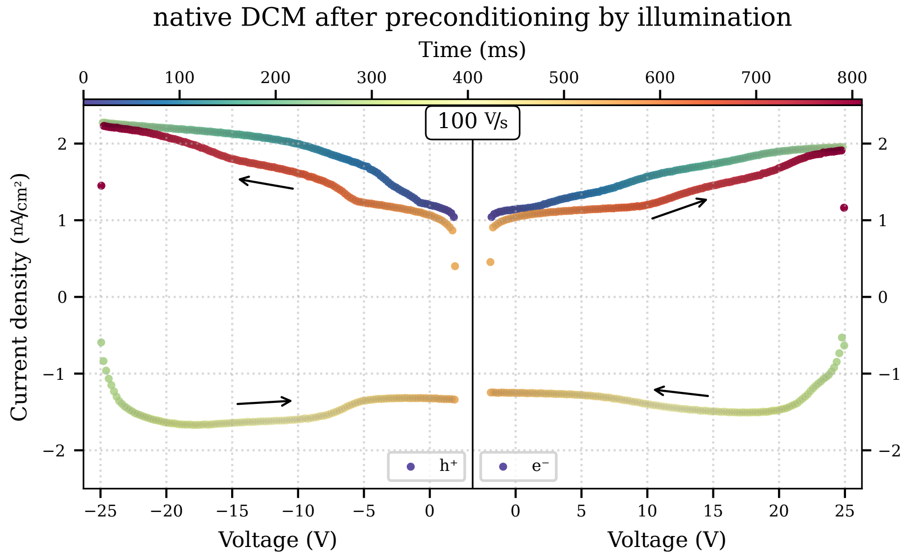

Figure S12.: native DCM after illumination treatment (referenced on p. 98).[S.109, S.153]

A.2.5. Exciton Confinement Derivation

The hamiltonian, $\mathcal{H}$, of a free particle with mass m confined in a cube-shaped potential, $\mathcal{V}$, with edge length a, using planck's constant ($\hbar = h/2\pi$) is given with the Laplace operator, Δ, by:

$$\mathcal{H} = -\frac{\hbar^2}{2m}\Delta + \mathcal{V}, \tag{A.2}$$

$$\mathcal{V} = \begin{cases} 0, & \text{if } (x, y, z) \in [0, a]^3. \\ \infty, & \text{else.} \end{cases} \tag{A.3}$$

With the Schrödinger Equation and a general ansatz for 3 dimensions, a real A ≠ 0, the Energy, E, a wavevector $\vec{k}$ and the spatial coordinate x:

$$\mathcal{H}\Psi = \mathrm{E}\Psi, \tag{A.4}$$

$$\Psi(\vec{x}) = \mathrm{A}\sin\left(\vec{k}\cdot\vec{x}\right) + \mathrm{B}\cos\left(\vec{k}\cdot\vec{x}\right). \tag{A.5}$$

$$= \mathrm{A}\sin\left(\sum_j^3 k_j x_j\right) + \mathrm{B}\cos\left(\sum_j^3 k_j x_j\right). \tag{A.6}$$

With the boundary conditions originating from the infinite potential walls for each dimension x_j all cosine contributions must vanish:

$$\Psi(0,0,0) = 0 = \mathrm{A}\sin(0) + \mathrm{B}\cos(0). \tag{A.7}$$

$$\mathrm{B} = 0. \tag{A.8}$$

Without loss of generality, in case of only z being non-vanishing:

$$\Psi(0,0,a) = 0 = \mathrm{A}\sin(k_z a). \tag{A.9}$$

The sine has to vanish and therefore its argument has to be a multiple of π; with the quantum number $n \in \mathbb{N}$:

$$k_z = \frac{n_z \pi}{a}; \tag{A.10}$$

same holds for the other coordinates, j:

$$k_j = \frac{n_j \pi}{a}. \tag{A.11}$$

$$\Psi = \mathrm{A}\sin\left(\sum_j^3 \frac{n_j \pi}{a} x_j\right). \tag{A.12}$$

Re-evaluating the Schrödinger equation:

$$\mathcal{H}\Psi = -\frac{\hbar^2}{2m}\Delta\left[\mathrm{A}\sin\left(\sum_j^3 \frac{n_j\pi}{a}x_j\right)\right]. \tag{A.13}$$

$$= -\frac{\hbar^2}{2m}\sum_i^3 \frac{\partial^2}{(\partial x_i)^2}\left[\mathrm{A}\sin\left(\sum_j^3 \frac{n_j\pi}{a}x_j\right)\right]. \tag{A.14}$$

$$= -\frac{\hbar^2}{2m}\sum_i^3 -\left(\frac{n_i\pi}{a}\right)^2\left[\mathrm{A}\sin\left(\sum_j^3 \frac{n_j\pi}{a}x_j\right)^2\right]. \tag{A.15}$$

$$= \frac{\hbar^2}{2m}\sum_i^3 \left(\frac{n_i\pi}{a}\right)^2 \Psi. \tag{A.16}$$

$$\mathcal{H}\Psi = \frac{\hbar^2\pi^2}{2ma^2}\sum_i^3 n_i^2\Psi. \tag{A.17}$$

$$\mathrm{E}_n = \frac{\hbar^2\pi^2}{2ma^2}\sum_i^3 n_i^2. \tag{A.18}$$

Finally, the lowest possible energy for in the 3D quantum well is realised at n=(1,1,1):

$$\mathrm{E}_0 = \frac{3\hbar^2\pi^2}{2ma^2}. \tag{A.19}$$

This calculation is used to derive eq. 2.5.

A.2.6. RC Circuit Derivations

Single RC Response on Ramp Voltage Derivation

$$\mathrm{Z} = \left[\frac{1}{\hat{\mathrm{R}}} + s\hat{\mathrm{C}}\right]^{-1}. \tag{A.20}$$

The driving voltage $\mathrm{V}(t) = \pm kt + \mathrm{V}_0$ is expressed in s via Laplace Transformation:

$$\mathrm{V}(s) = \int_0^\infty \mathrm{V}(t)\exp(-st)\,\mathrm{d}t = \pm k\int_0^\infty t\exp(-st)\,\mathrm{d}t + \mathrm{V}_0\int_0^\infty \exp(-st)\,\mathrm{d}t. \tag{A.21}$$

$$= \pm\frac{k}{s^2} + \frac{\mathrm{V}_0}{s}. \tag{A.22}$$

The current at the voltage source, $\mathrm{I}(s)$, can be derived with A.20:

$$\mathrm{I}(s) = \frac{\mathrm{V}(s)}{\mathrm{Z}} = \underbrace{\pm\frac{k}{s^2\mathrm{Z}}}_{\mathrm{A}} + \underbrace{\frac{\mathrm{V}_0}{s\mathrm{Z}}}_{\mathrm{B}}. \tag{A.23}$$

Considering only A from Eq. A.23:

$$\mathrm{I}(s) = \pm k\left[\frac{1}{s^2\hat{\mathrm{R}}} + \frac{\hat{\mathrm{C}}}{s}\right]. \tag{A.24}$$

Invert the Laplace Transformation $\mathrm{I}(t) = \mathcal{L}^{-1}\left\{\mathrm{I}(s)\right\}$:

$$\begin{aligned}
\mathrm{I_A}(t) &= \mathcal{L}^{-1}\left\{\pm k\left[\frac{1}{s^2\hat{\mathrm{R}}} + \frac{\hat{\mathrm{C}}}{s}\right]\right\}. && \text{(A.25)}\\
&= \pm k\cdot\left[\frac{1}{\hat{\mathrm{R}}}\mathcal{L}^{-1}\left\{\frac{1}{s^2}\right\} + \hat{\mathrm{C}}\mathcal{L}^{-1}\left\{\frac{1}{s}\right\}\right]. && \text{(A.26)}\\
&= \pm k\cdot\left[\frac{t}{\hat{\mathrm{R}}} + \hat{\mathrm{C}}\right]. && \text{(A.27)}
\end{aligned}$$

Now considering only B from Eq. A.23 with analogous steps:

$$\begin{aligned}
\mathrm{I}(s) &= \mathrm{V_0}\left[\frac{1}{s\hat{\mathrm{R}}} + \tilde{\mathrm{C}}\right]. && \text{(A.28)}\\
\mathrm{I_B}(t) &= \mathcal{L}^{-1}\left\{\mathrm{V_0}\left[\frac{1}{s\hat{\mathrm{R}}} + \hat{\mathrm{C}}\right]\right\}. && \text{(A.29)}\\
&= \mathrm{V_0}\cdot\left[\frac{1}{\hat{\mathrm{R}}}\mathcal{L}^{-1}\left\{\frac{1}{s}\right\} + \tilde{\mathrm{C}}\mathcal{L}^{-1}\left\{1\right\}\right]. && \text{(A.30)}\\
&= \mathrm{V_0}\cdot\left[\frac{1}{\hat{\mathrm{R}}} + \hat{\mathrm{C}}\delta(t)\right]. && \text{(A.31)}
\end{aligned}$$

Combining $\mathrm{I_A}$ and $\mathrm{I_B}$:

$$\mathrm{I}(t) = \pm\frac{kt}{\hat{\mathrm{R}}} \pm k\hat{\mathrm{C}} + \frac{\mathrm{V_0}}{\hat{\mathrm{R}}} + \mathrm{V_0}\tilde{\mathrm{C}}\delta(t). \tag{A.32}$$

This calculation is used to derive eq. 4.12.

Double RC Response on Ramp Voltage Derivation

$$\begin{aligned}
\mathrm{Z} &= \left[\frac{1}{\mathrm{R_t}} + s\mathrm{C_t}\right]^{-1} + \left[\frac{1}{\mathrm{R_i}} + s\mathrm{C_i}\right]^{-1}. && \text{(A.33)}\\
&= \left[\frac{1 + s\mathrm{R_t}\mathrm{C_t}}{\mathrm{R_t}}\right]^{-1} + \left[\frac{1 + s\mathrm{R_i}\mathrm{C_i}}{\mathrm{R_i}}\right]^{-1}. && \text{(A.34)}\\
&= \frac{\mathrm{R_t}}{1 + s\mathrm{R_t}\mathrm{C_t}} + \frac{\mathrm{R_i}}{1 + s\mathrm{R_i}\mathrm{C_i}}. && \text{(A.35)}\\
&= \frac{\mathrm{R_t}\left(1 + s\mathrm{R_i}\mathrm{C_i}\right) + \mathrm{R_i}\left(1 + s\mathrm{R_t}\mathrm{C_t}\right)}{\left(1 + s\mathrm{R_t}\mathrm{C_t}\right)\cdot\left(1 + s\mathrm{R_i}\mathrm{C_i}\right)}. && \text{(A.36)}\\
&= \frac{\mathrm{R_t} + \mathrm{R_i} + s\mathrm{R_t}\mathrm{R_i}\left(\mathrm{C_t} + \mathrm{C_i}\right)}{1 + s\left(\mathrm{R_t}\mathrm{C_t} + \mathrm{R_i}\mathrm{C_i}\right) + s^2\left(\mathrm{R_t}\mathrm{C_t}\mathrm{R_i}\mathrm{C_i}\right)}. && \text{(A.37)}
\end{aligned}$$

The same simplifications as for the single RC is are used. Thus, considering only A from Eq. A.23, with $\tilde{R} = R_t + R_i$ and $\tilde{C} = C_t + C_i$:

$$= \pm\frac{k}{s^2}\cdot\frac{1 + s\left(R_tC_t + R_iC_i\right) + s^2\left(R_tC_tR_iC_i\right)}{\tilde{R} + sR_tR_i\tilde{C}}. \tag{A.38}$$

$$= \pm\frac{k}{s^2}\cdot\left[\frac{1}{\tilde{R} + sR_tR_i\tilde{C}} + s\frac{R_tC_t + R_iC_i}{\tilde{R} + sR_tR_i\tilde{C}} + s^2\frac{R_tC_tR_iC_i}{\tilde{R} + sR_tR_i\tilde{C}}\right]. \tag{A.39}$$

$$I_A(s) = \pm k\cdot\left[\frac{1}{s^2\left(\tilde{R} + sR_tR_i\tilde{C}\right)} + \frac{R_tC_t + R_iC_i}{s\left(\tilde{R} + sR_tR_i\tilde{C}\right)} + \frac{R_tC_tR_iC_i}{\tilde{R} + sR_tR_i\tilde{C}}\right]. \tag{A.40}$$

Invert the Laplace Transformation $I(t) = \mathcal{L}^{-1}\left\{I(s)\right\}$:

$$I_A(t) = \mathcal{L}^{-1}\left\{\pm k\cdot\left[\frac{1}{s^2\left(\tilde{R} + sR_tR_i\tilde{C}\right)} + \frac{R_tC_t + R_iC_i}{s\left(\tilde{R} + sR_tR_i\tilde{C}\right)} + \frac{R_tC_tR_iC_i}{\tilde{R} + sR_tR_i\tilde{C}}\right]\right\}. \tag{A.41}$$

$$\begin{aligned} &= \pm k\cdot\left[\mathcal{L}^{-1}\left\{\frac{1}{s^2\left(\tilde{R} + sR_tR_i\tilde{C}\right)}\right\}\right. \\ &\quad + \mathcal{L}^{-1}\left\{\frac{R_tC_t + R_iC_i}{s\left(\tilde{R} + sR_tR_i\tilde{C}\right)}\right\} \\ &\quad \left. + \mathcal{L}^{-1}\left\{\frac{R_tC_tR_iC_i}{\tilde{R} + sR_tR_i\tilde{C}}\right\}\right]. \end{aligned} \tag{A.42}$$

With $\hat{R} = \frac{R_tR_i}{R_t+R_i} = \frac{R_tR_i}{\tilde{R}}$ & $\hat{C} = \frac{C_tC_i}{C_t+C_i} = \frac{C_tC_i}{\tilde{C}}$:

$$\begin{aligned} &= \pm k\cdot\left[\frac{\hat{R}\tilde{C}}{\tilde{R}}\left(\exp\left[-\frac{1}{\hat{R}\tilde{C}}t\right] - 1\right) + \frac{t}{\tilde{R}}\right. \\ &\quad + \frac{R_tC_t + R_iC_i}{\tilde{R}}\left(1 - \exp\left[-\frac{1}{\hat{R}\tilde{C}}t\right]\right) \\ &\quad \left. + \hat{C}\exp\left[-\frac{1}{\hat{R}\tilde{C}}t\right]\right]. \end{aligned} \tag{A.43}$$

$$\begin{aligned} &= \pm\frac{k}{\tilde{R}}\cdot\left[t\right. \\ &\quad + \left(R_tC_t + R_iC_i - \hat{R}\tilde{C}\right)\left(1 - \exp\left[-\frac{1}{\hat{R}\tilde{C}}t\right]\right) \\ &\quad \left. + \tilde{R}\hat{C}\exp\left[-\frac{1}{\hat{R}\tilde{C}}t\right]\right]. \end{aligned} \tag{A.44}$$

with $t_\times = \mathrm{R_t C_t} + \mathrm{R_i C_i} - \hat{\mathrm{R}}\tilde{\mathrm{C}}$:

$$\mathrm{I_A}(t) = \pm\frac{k}{\tilde{\mathrm{R}}} \cdot \left[t + t_\times\left(1 - \exp\left[-\frac{1}{\hat{\mathrm{R}}\tilde{\mathrm{C}}}t\right]\right) + \tilde{\mathrm{R}}\hat{\mathrm{C}}\exp\left[-\frac{1}{\hat{\mathrm{R}}\tilde{\mathrm{C}}}t\right]\right]. \tag{A.45}$$

$$\mathrm{I_A}(t) = \pm\frac{k}{\tilde{\mathrm{R}}} \cdot \left[t + t_\times + \left(\tilde{\mathrm{R}}\hat{\mathrm{C}} - t_\times\right)\exp\left[-\frac{1}{\hat{\mathrm{R}}\tilde{\mathrm{C}}}t\right]\right]. \tag{A.46}$$

Now considering only B from Eq. A.23 with analogous steps:

$$\mathrm{I_B}(s) = \mathrm{V_0} \cdot \left[\frac{1}{s\left(\tilde{\mathrm{R}} + s\mathrm{R_t R_i}\tilde{\mathrm{C}}\right)} + \frac{\mathrm{R_t C_t} + \mathrm{R_i C_i}}{\tilde{\mathrm{R}} + s\mathrm{R_t R_i}\tilde{\mathrm{C}}} + s\frac{\mathrm{R_t C_t R_i C_i}}{\tilde{\mathrm{R}} + s\mathrm{R_t R_i}\tilde{\mathrm{C}}}\right]. \tag{A.47}$$

$$\begin{aligned}
\mathrm{I_B}(t) = \mathrm{V_0} \cdot \Bigg[&\mathcal{L}^{-1}\left\{\frac{1}{s\left(\tilde{\mathrm{R}} + s\mathrm{R_t R_i}\tilde{\mathrm{C}}\right)}\right\} \\
&+ \mathcal{L}^{-1}\left\{\frac{\mathrm{R_t C_t} + \mathrm{R_i C_i}}{\tilde{\mathrm{R}} + s\mathrm{R_t R_i}\tilde{\mathrm{C}}}\right\} \\
&+ \mathcal{L}^{-1}\left\{s\frac{\mathrm{R_t C_t R_i C_i}}{\tilde{\mathrm{R}} + s\mathrm{R_t R_i}\tilde{\mathrm{C}}}\right\}\Bigg].
\end{aligned} \tag{A.48}$$

$$\begin{aligned}
= \mathrm{V_0} \cdot \Bigg[&\frac{1}{\tilde{\mathrm{R}}}\left(1 - \exp\left[-\frac{1}{\hat{\mathrm{R}}\tilde{\mathrm{C}}}t\right]\right) \\
&+ \frac{\mathrm{R_t C_t} + \mathrm{R_i C_i}}{\mathrm{R_t R_i}\tilde{\mathrm{C}}}\exp\left[-\frac{1}{\hat{\mathrm{R}}\tilde{\mathrm{C}}}t\right] \\
&+ (\mathrm{R_t C_t R_i C_i})\left(\frac{\delta(t)}{\mathrm{R_t R_i}\tilde{\mathrm{C}}} - \frac{\tilde{\mathrm{R}}}{\left(\mathrm{R_t R_i}\tilde{\mathrm{C}}\right)^2}\exp\left[-\frac{1}{\hat{\mathrm{R}}\tilde{\mathrm{C}}}t\right]\right)\Bigg].
\end{aligned} \tag{A.49}$$

With $\tilde{R}\hat{R} = R_tR_i$:

$$\begin{aligned}
&= V_0 \cdot \Bigg[\frac{1}{\tilde{R}}\left(1 - \exp\left[-\frac{1}{\hat{R}\tilde{C}}t\right]\right) \\
&\quad + \frac{R_tC_t + R_iC_i}{\tilde{R}\hat{R}\tilde{C}} \exp\left[-\frac{1}{\hat{R}\tilde{C}}t\right] \\
&\quad + \delta(t)\hat{C} - \frac{\tilde{R}\hat{C}}{R_tR_i\tilde{C}} \exp\left[-\frac{1}{\hat{R}\tilde{C}}t\right]\Bigg]. && \text{(A.50)} \\
&= \frac{V_0}{\tilde{R}} \cdot \Bigg[1 - \exp\left[-\frac{1}{\hat{R}\tilde{C}}t\right] \\
&\quad + \frac{R_tC_t + R_iC_i}{\hat{R}\tilde{C}} \exp\left[-\frac{1}{\hat{R}\tilde{C}}t\right] \\
&\quad - \frac{\tilde{R}\hat{C}}{\hat{R}\tilde{C}} \exp\left[-\frac{1}{\hat{R}\tilde{C}}t\right] + \delta(t)\tilde{R}\hat{C}\Bigg]. && \text{(A.51)} \\
&= \frac{V_0}{\tilde{R}} \cdot \left[1 - \exp\left[-\frac{1}{\hat{R}\tilde{C}}t\right] + \frac{R_tC_t + R_iC_i - \tilde{R}\hat{C}}{\hat{R}\tilde{C}} \exp\left[-\frac{1}{\hat{R}\tilde{C}}t\right] + \delta(t)\tilde{R}\hat{C}\right]. && \text{(A.52)} \\
&= \frac{V_0}{\tilde{R}} \cdot \left[1 + \left(\frac{R_tC_t + R_iC_i - \tilde{R}\hat{C}}{\hat{R}\tilde{C}} - 1\right) \exp\left[-\frac{1}{\hat{R}\tilde{C}}t\right] + \delta(t)\tilde{R}\hat{C}\right]. && \text{(A.53)} \\
I_B(t) &= \frac{V_0}{\tilde{R}} \cdot \left[1 + \left(\frac{t_\times - \tilde{R}\hat{C}}{\hat{R}\tilde{C}}\right) \exp\left[-\frac{1}{\hat{R}\tilde{C}}t\right] + \delta(t)\tilde{R}\hat{C}\right]. && \text{(A.54)}
\end{aligned}$$

Combining I_A (Eq. A.46) and I_B (Eq. A.54):

$$\begin{aligned}
I(t) &= \pm\frac{k}{\tilde{R}} \cdot \left[t + t_\times - \left(t_\times - \tilde{R}\hat{C}\right) \exp\left[-\frac{1}{\hat{R}\tilde{C}}t\right]\right] \\
&\quad + \frac{V_0}{\tilde{R}} \cdot \left[1 + \left(\frac{t_\times - \tilde{R}\hat{C}}{\hat{R}\tilde{C}}\right) \exp\left[-\frac{1}{\hat{R}\tilde{C}}t\right] + \delta(t)\tilde{R}\hat{C}\right]. && \text{(A.55)}
\end{aligned}$$

This calculation is used to derive eq. 4.16.

Modelling a gate-less transistor (RRC)

A gate-less transistor can also be described with a RC circuit. With sufficiently small channel lengths or giant permittivities a capacitance may be necessary. Instead of applying the single RC, the double RC can be used to model it with a contact resistance. If sweeping from $V_0 = 0$ and no contact capacitance ($C_t = 0$), Eq 4.16 simplifies:

$$I(t) = \frac{k}{\tilde{R}} \cdot \left[t + t_\times - \left(t_\times - \tilde{R}\hat{C}\right) \exp\left[-\frac{1}{\hat{R}\tilde{C}}t\right]\right]. \tag{A.56}$$

with $\hat{\mathrm{C}} \to 0$, $\tilde{\mathrm{C}} \to \mathrm{C_i}$:

$$t_\times = \mathrm{R_t C_t} + \mathrm{R_i C_i} - \hat{\mathrm{R}}\tilde{\mathrm{C}} = \mathrm{R_i C_i} - \hat{\mathrm{R}}\mathrm{C_i}. \tag{A.57}$$

$$\mathrm{I}(t) = \frac{k}{\tilde{\mathrm{R}}} \cdot \left[t + \left(\mathrm{R_i C_i} - \hat{\mathrm{R}}\mathrm{C_i}\right) - \left(\mathrm{R_i C_i} - \hat{\mathrm{R}}\mathrm{C_i}\right) \cdot \exp\left[-\frac{1}{\hat{\mathrm{R}}\mathrm{C_i}} t \right] \right]. \tag{A.58}$$

$$\mathrm{I}(t) = \frac{k}{\tilde{\mathrm{R}}} \cdot \left[t + \left(\mathrm{R_i C_i} - \hat{\mathrm{R}}\mathrm{C_i}\right) \cdot \left(1 - \exp\left[-\frac{1}{\hat{\mathrm{R}}\mathrm{C_i}} t \right] \right) \right]. \tag{A.59}$$

$$\mathrm{I}(t) = \frac{k}{\tilde{\mathrm{R}}} \cdot \left[t + \mathrm{C_i} \left(\mathrm{R_i} - \hat{\mathrm{R}}\right) \cdot \left(1 - \exp\left[-\frac{1}{\hat{\mathrm{R}}\mathrm{C_i}} t \right] \right) \right]. \tag{A.60}$$

A.3. Chemicals

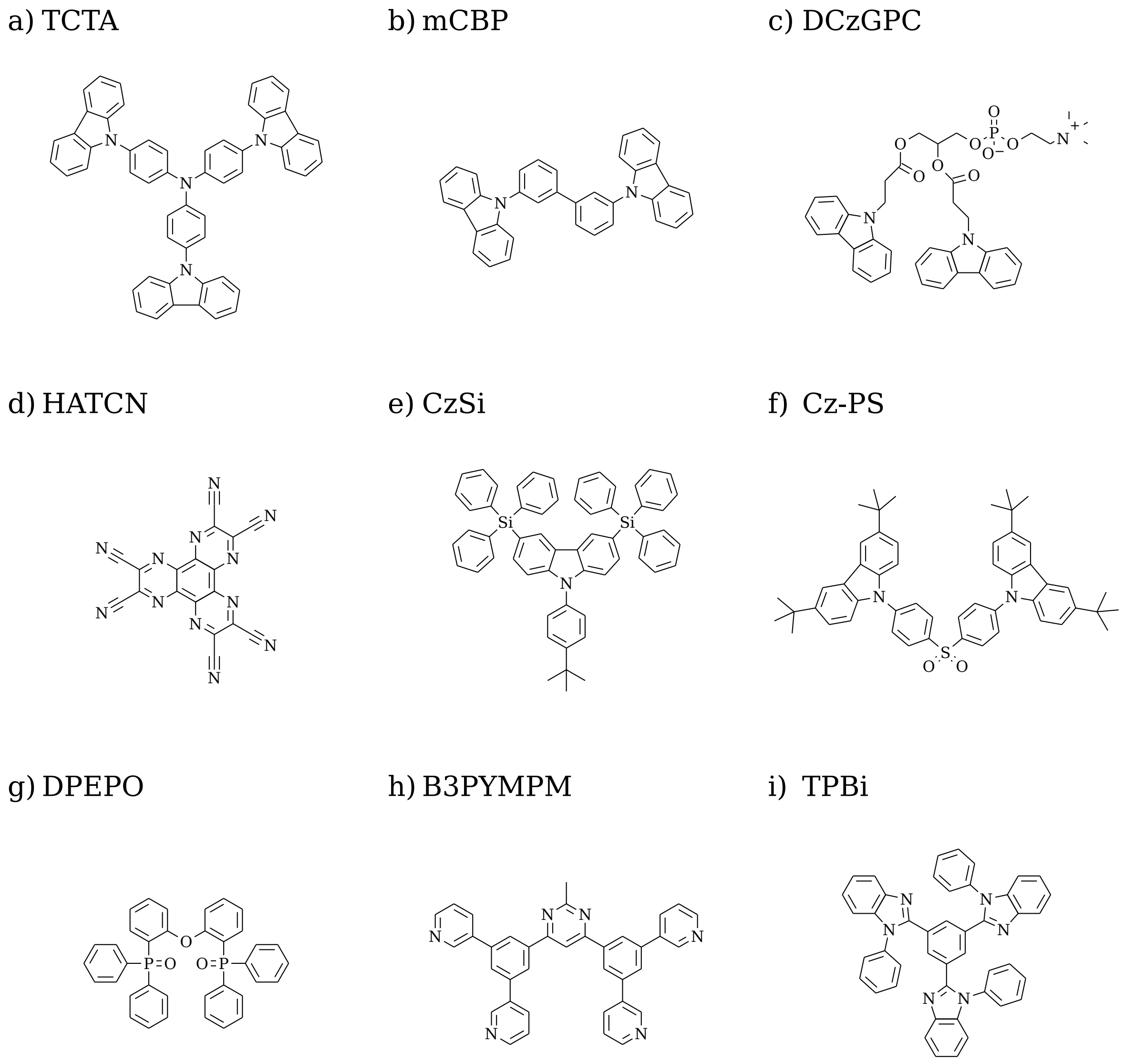

a) TCTA
b) mCBP
c) DCzGPC
d) HATCN
e) CzSi
f) Cz-PS
g) DPEPO
h) B3PYMPM
i) TPBi

Figure S13.: Lewis formula of:
a) tris(4-carbazoyl-9-yl)-tri-phenylamine (TCTA),
b) 3,3′-di(9H-carbazol-9-yl)-1,1′-biphenyl (mCBP),
c) dicarbazol-9-yl-propanoyl-glycerophosphocholine (DCzGPC),
d) lithium bis(trifluoromethanesulfonyl)imide (LiTFSI),
e) 9-(4-tert-butylphenyl)-3,6-bis(triphenylsilyl)-9H-carbazole (CzSi),
f) bis[4-(3,6-Di-tert-butyl carbazole-9-yl)phenyl]sulfone (Cz-PS),
g) bis(2-(diphenylphosphino)phenyl)ether oxide (DPEPO),
h) 4,6-bis(3,5-di-3-pyridinylphenyl)-2-methylpyrimidine (B3PYMPM),
i) 2,2’,2”-(1,3,5-benzinetriyl)-tris(1-phenyl-1-H-benzimidazole) (TPBi).
(referenced on pp. 27, 109).

a) OA b) OLA c) Lecithin

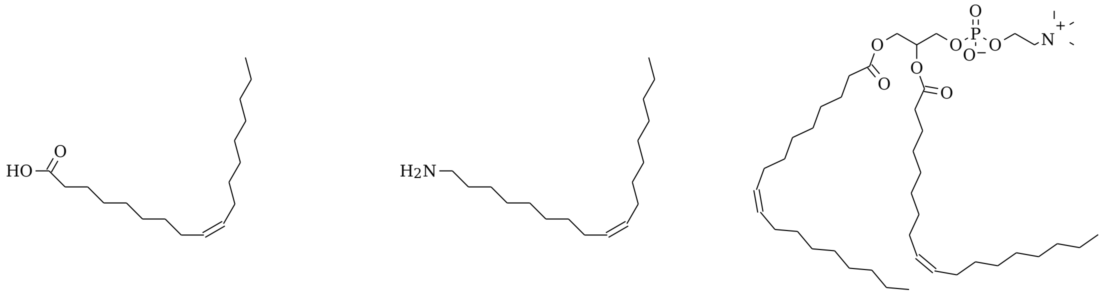

d) TFB e) poly-TPD f) PVK

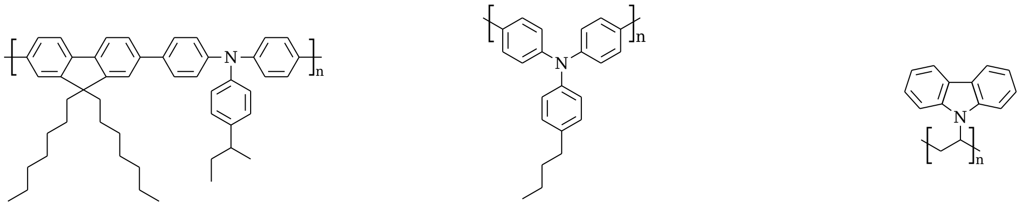

g) PS-b-P2VP h) PMMA i) PEDOT:PSS

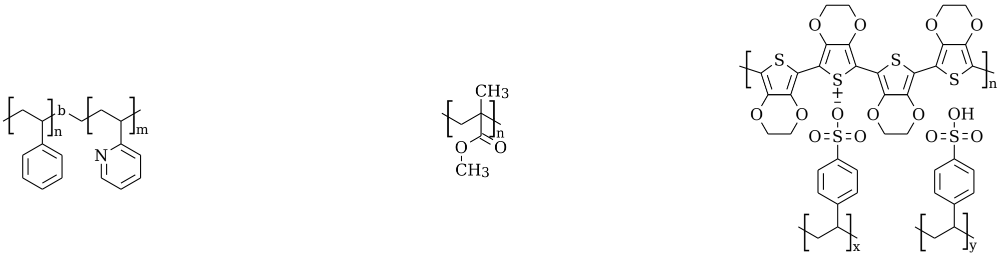

Figure S14.: Lewis formula of:
a) oleic acid (OA),
b) oleylamine (OLA),
c) Lecithin (here with oleic acid residuals),
d) poly(9,9-dioctylfluorene-alt-N-(4-sec-butylphenyl)-diphenylamine) (TFB),
e) poly(4-butylphenyldiphenylamine) (poly-TPD),
f) poly(9-vinylcarbazole) (PVK),
g) polystyrene-b-poly(2-)vinylpyridine (PS-b-P2VP),
h) polymethylmethacrylat (PMMA),
i) poly(3,4-ethylenedioxythiophene) polystyrene sulfonate (PEDOT:PSS).
(referenced on p. 26).

B. Glossary

B.1. Special Terms

biexciton A biexciton, is a combination of two excitons sharing one entity such as for example a molecule or a particle. 81

BK7 N-BK7 by Schott AG, is a borosilicate glass widely used for optical applications. For near-UV light it is not recommended since its absorption is non-negligible. 53, 54

CCD A charge-coupled device, CCD, uses a charged MOSFET to detect, for example, light that leads to the depletion of the charges. 107, 108

EQE The external quantum efficiency, EQE, is the photon weighted efficiency of a light emitting device. It is defined as the photons, exiting the device, in relation to the injected carriers. 23, 31, 32, 34, 35, 46–50, 67–72, 74, 77, 78, 88, 89, 96, 98, 101, 102, 108, 116, 117

Fermi level The Fermi level, E_F, denotes the energy level required to remove an electron from a solid-state body to the VL. It is equal to the work function for metals and located in the middle of the band-gap for intrinsic semiconductors or insulators. 37, 59, 60

Frenkel defect A Frenkel defect, also known as a Frenkel pair, is a type of point defect in a crystalline material. It occurs when an atom in a crystal lattice moves from its normal lattice site to an interstitial site, leaving behind a vacancy in its original lattice site. 10, 13

ITO Indium tin oxide, ITO, is tin doped indium oxide. Because of its oxygen deficiency it is highly conductive. That combined with low workfunction and high transparancy makes it commonly used as an anode in optoelectronic devices. 53, 54, 61, 67, 91, 92, 105, 107, 110

LCOE The levelised cost of electricity, LCOE, is a quantity to provide the net cost per unit of electric energy where all inherent costs including financial aspects are taken into account. 7

ND filter A neutral density filter, ND filter, is a filter that reduces the intensity of passing light by equal amount independently of the wavelength. 47

p-doping Positive doping, p-doping, is a process where an electron-deficient material is added to a substance in order to increase the mobility of charge carriers in the valence level (holes) of a semiconductor. 51, 52, 54, 59–62, 72, 101, 102

RC-time The resistor-capacitor time, RC-time, is the time it takes for a capacitor, with capacitance C, to discharge $1/e$ of its charge via a resistor, with resistance R. Analogously, for the charging of a capacitor, the time to charge it to $1-1/e$ of the final load. 66

SECO The secondary electron cut-off, SECO, is an energy level, that is according to Einstein's photo-effect the lower energy limit of an electron leaving a substance by photo-excitation, due to the material's work function. 59, 60, 108

smol Surface mol, smol, a new quantity for describing molar ratios in context with nanoparticles. Based on the chemical mol, but reduced by the inner unitcells so that effectively only the surface unit cells are taken into account (see 2.2.2). 20, 21, 53–56, 58, 59, 62–65, 67–71, 74, 81–84, 86–90, 99, 106, 108, 111–119

Stokes shift The Stokes shift defines the descrepancy in energy, wavelength or the like, between absorption and emisson from the same electronic transition in a substance. 45

TFT LCD A thin-film transistor liquid crystal display, TFT LCD, is a display technology using thin-film transistors in order to control the liquid-crystals to modify passing light properties such as colour and intensity. 43

B.2. Acronyms

a.u. arbitrary units. 59

ADPL angular dendent photoluminescence. 34, 70, 106, 108, 118

AFM atomic force microscope. 29, 30, 49, 63, 83, 84, 87

AG public limited company (PLC, Aktiengesellschaft). 108

B3PYMPM 4,6-bis(3,5-di-3-pyridinylphenyl)-2-methylpyrimidine. 26, 27, 61, 67, 68, 91–93, 95, 98, 107, 127

c speed of light in vacuum. 85

CB chlorobenzene. 106

CBM conduction band minimum. 11–13, 17, 27, 59, 98

CC BY 4.0 creative commons international attribution 4.0 license (`https://creativecommons.org/licenses/by/4.0/`). 12

cf. confer. 10, 11, 13, 15, 17, 20, 26, 27, 32, 33, 36, 45, 47, 49, 52, 56, 57, 60, 64, 68, 69, 71, 76, 78, 80, 82, 83, 85, 87, 89, 90, 94, 96–98, 109, 110

COHP crystal orbital hamiltonian population. 12, 13

Cz-PS bis[4-(3,6-Di-tert-butyl carbazole-9-yl)phenyl]sulfone. 109, 110, 127

CzSi 9-(4-tert-butylphenyl)-3,6-bis(triphenylsilyl)-9H-carbazole. 109, 127

DC down-converter. 46–51, 56, 109

DCE down-conversion efficiency. 50

DCM displacement-current-measurement. 39, 41, 92–99, 102, 119

DCzGPC dicarbazol-9-yl-propanoyl-glycerophosphocholine. 79–90, 102, 119, 127, 149

DMF dimethylformamide. 14, 106

DMSO dimethylsulfoxide. 14

DOS density of states. 11–13

DPEPO bis(2-(diphenylphosphino)phenyl)ether oxide. 109, 127

e.g. for example (exempli gratia). 7, 10, 11, 13, 14, 17, 20, 21, 24, 26, 30, 31, 33, 34, 41, 51, 81, 83, 84, 86

EDX energy-dispersive x-ray spectroscopy. 58

EL electroluminescence. 19, 48, 49, 67, 68, 72, 74, 88, 89, 109, 110

EtAc ethylacetate. 76

ETL electron transport layer. 27, 68

FWHM full width half maximum. 49, 89

GmbH limited liability company (Gemeinschaft mit beschränkter Haftung). 105, 107

h Planck’s constant. 85, 120

HATCN hexa-aza-tri-phenyl-ene-hexa-carbo-nitrile. 61, 92, 95, 107, 127

HOMO highest occupied molecular orbital. 26, 27, 52, 59–61, 71, 98

HTL hole transport layer. 26, 51, 52, 54, 59

$\mathbf{k_B}$ Boltzmann constant. 15, 64

LARP ligand assisted reprecipitation. 14, 47

LCD liquid crystal display. 44, 45

LED light-emitting diode. 7–9, 17, 23–25, 29, 31–35, 43–45, 47, 49, 51, 68, 70, 75, 101, 102, 107, 108

LHP lead halide perovskite. 7–15, 17–19, 24, 25, 27, 29, 30, 32, 33, 35, 36, 51, 56, 60, 63, 65, 70–72, 77, 79–81, 84, 89, 101–103, 106, 107

LiTFSI lithium bis(trifluoromethanesulfonyl)imide. 51–75, 83, 89, 98, 99, 101, 102, 105, 106, 108, 111–118, 127

LUMO lowest unoccupied molecular orbital. 26, 27, 59, 98

MA methylammonium. 13, 47, 71, 74, 117

mCBP 3,3′-di(9H-carbazol-9-yl)-1,1′-biphenyl. 110, 127

MeAc methylacetate. 76

MIS metal insulator semiconductor. 35, 39, 91–96, 98, 106–108, 149

NC nanocrystal. 7, 8, 14–18, 20, 21, 23–25, 29, 30, 32, 35, 53, 54, 56–61, 63, 67, 68, 70–72, 74–76, 79, 80, 83–85, 87–89, 101, 102, 106, 107, 115

NIR near-infrared. 12, 34, 45, 74

NIST national institute of standards and technology. 107

NMR nuclear magnetic resonance. 82

OA oleic acid. 105, 128

ODE octadecene. 105

OLA oleylamine. 105, 128

OLA$^+$ oleylammonium. 105, 106

OLED organic light-emitting diode. 7, 25, 43, 46–49, 71, 73, 93, 109, 110

p.r.n. as/if needed (pro re nata). 106

PEDOT:PSS poly(3,4-ethylenedioxythiophene) polystyrene sulfonate. 26, 53, 54, 61, 67, 105, 107, 110, 128

PeLED perovskite light-emitting diode. 8, 9, 23–27, 29, 32–35, 43, 47, 49, 59, 61, 67–74, 77, 78, 83, 87–92, 96, 98, 99, 101, 102, 109

PL photoluminescence. 31, 49, 55, 68, 72, 75, 80–82, 85, 88, 89, 91, 99, 102, 106, 107, 109–114

PLQY photoluminescent quantum yield. 19, 24, 25, 31–33, 35, 44–47, 49, 50, 53–57, 60, 68–72, 82, 83, 87, 89, 101, 102, 106–108, 110

PMMA polymethylmethacrylat. 35, 91–93, 95, 96, 107, 128

PNC perovskite nanocrystal. 15, 17–21, 24, 25, 27, 29, 30, 33, 34, 43, 45–47, 49, 51–60, 63, 66, 68, 69, 71–73, 75–87, 90–99, 101, 102, 107, 109–114, 117

poly-TPD poly(4-butylphenyldiphenylamine). 26, 128

PS-b-P2VP polystyrene-b-poly(2-)vinylpyridine. 46, 47, 128

PTFE polytetrafluoroethylene. 106

PVK poly(9-vinylcarbazole). 26, 27, 53, 54, 58–61, 66–68, 71, 81, 84, 92, 105, 107, 128

QD quantum-dot. 51

R_∞ Rydberg constant. 85

RC resistor-capacitor. 92–94

resp. respective(ly). 10–12, 15, 24, 35, 40, 60, 64, 65, 70–72, 76, 78, 80, 81, 85, 87, 91, 92, 101, 106

RRC resistor-resistor-capacitor. 64, 65, 116

SEM scanning electron microscope. 29, 30, 57, 58, 63, 107

TCTA tris(4-carbazoyl-9-yl)-tri-phenylamine. 91–95, 98, 110, 127

TDM transition dipole moment. 70, 71

TEM transmission electron microscope. 16, 29

TFB poly(9,9-dioctylfluorene-alt-N-(4-sec-butylphenyl)-diphenylamine). 26, 128

TFSI tri-fluoro-methane-sulfonyl-imide. 51, 54, 57, 60, 102, 115

TFT thin film transistor. 43, 63–65, 72

THF tetrahydrofuran. 76, 80

TPBi 2,2’,2”-(1,3,5-benzinetriyl)-tris(1-phenyl-1-H-benzimidazole). 26, 27, 110, 127

TRPL transient photoluminescence. 53, 55–57, 80, 82, 106, 108

UPS ultra-violet photoelectron spectroscopy. 59, 60, 72, 107, 108, 115

UV ultra-violet. 12, 34, 45, 57, 60, 108

VBM valence band maximum. 12, 13, 17, 25–27, 52, 59–61, 71, 98

VL vacuum level. 59

wt. weight. 53, 59, 70, 88, 106

XPS x-ray photoelectron spectroscopy. 59, 60, 72, 107, 108, 115

XRD x-ray diffraction spectroscopy. 55, 58, 68

C. References

[1] J. A. J. Gowlett, ‘The discovery of fire by humans: a long and convoluted process’, Phil. Trans. R. Soc. B **371**, 20150164 (2016) (cit. on p. 7).

[2] Z. Chen, S. Yan and C. Danesh, ‘MicroLED technologies and applications: characteristics, fabrication, progress, and challenges’, J. Phys. D: Appl. Phys. **54**, 123001 (2021) (cit. on p. 7).

[3] A. Islam, M. Rabbani, M. H. Bappy, M. A. R. Miah and N. Sakib, ‘A review on fabrication process of organic light emitting diodes’, in 2013 International Conference on Informatics, Electronics and Vision (ICIEV) (May 2013) (cit. on p. 7).

[4] J. Zhao, L.-W. Lo, H. Wan, P. Mao, Z. Yu and C. Wang, ‘High-Speed Fabrication of All-Inkjet-Printed Organometallic Halide Perovskite Light-Emitting Diodes on Elastic Substrates’, Adv. Mater. **33**, 2102095 (2021) (cit. on p. 7).

[5] A. S. R. Bati, Y. L. Zhong, P. L. Burn, M. K. Nazeeruddin, P. E. Shaw and M. Batmunkh, ‘Next-generation applications for integrated perovskite solar cells’, Commun Mater **4**, `10.1038/s43246-022-00325-4` (2023) (cit. on p. 7).

[6] Z. Li, Y. Zhao, X. Wang, Y. Sun, Z. Zhao, Y. Li, H. Zhou and Q. Chen, ‘Cost Analysis of Perovskite Tandem Photovoltaics’, Joule **2**, 1559–1572 (2018) (cit. on p. 7).

[7] L. Protesescu, S. Yakunin, M. I. Bodnarchuk, F. Krieg, R. Caputo, C. H. Hendon, R. X. Yang, A. Walsh and M. V. Kovalenko, ‘Nanocrystals of Cesium Lead Halide Perovskites ($CsPbX_3$, X = Cl, Br, and I): Novel Optoelectronic Materials Showing Bright Emission with Wide Color Gamut’, Nano Lett. **15**, 3692–3696 (2015) (cit. on pp. 7, 14, 15, 54, 85).

[8] A. F. Gualdrón-Reyes, S. Masi and I. Mora-Seró, ‘Progress in halide-perovskite nanocrystals with near-unity photoluminescence quantum yield’, Trends in Chemistry **3**, 499–511 (2021) (cit. on p. 7).

[9] M. E. M. Marc De Graef, *Structure of Materials: An Introduction to Crystallography, Diffraction and Symmetry* (Cambridge University Press, 2007), pp. 671–673 (cit. on p. 9).

[10] J. G. Bednorz and K. A. Müller, ‘Possible highT c superconductivity in the Ba-La-Cu-O system’, Z. Physik B - Condensed Matter **64**, 189–193 (1986) (cit. on p. 9).

[11] A. Kojima, K. Teshima, Y. Shirai and T. Miyasaka, ‘Organometal Halide Perovskites as Visible-Light Sensitizers for Photovoltaic Cells’, J. Am. Chem. Soc. **131**, 6050–6051 (2009) (cit. on p. 9).

[12] M. A. Peña and J. L. G. Fierro, ‘Chemical Structures and Performance of Perovskite Oxides’, Chemical Reviews **101**, 1981–2018 (2001) (cit. on pp. 9, 10).

[13] R. D. Shannon, ‘Revised effective ionic radii and systematic studies of interatomic distances in halides and chalcogenides’, Acta Crystallographica Section A **32**, 751–767 (1976) (cit. on p. 10).

[14] C. J. Bartel, C. Sutton, B. R. Goldsmith, R. Ouyang, C. B. Musgrave, L. M. Ghiringhelli and M. Scheffler, ‘New tolerance factor to predict the stability of perovskite oxides and halides’, Sci. Adv. **5**, `10.1126/sciadv.aav0693` (2019) (cit. on p. 10).

[15] L. Pauling, *The Nature of the Chemical Bond and the Structure of Molecules and Crystals: An Introduction to Modern Structural Chemistry*, 3rd ed., George Fisher Baker Non-Resident Lec (Cornell University Press, 1960), p. 93 (cit. on p. 10).

[16] R. W. Gurney and N. F. Mott, ‘The Theory of the Photolysis of Silver Bromide and the Photographic Latent Image’, Proc. R. Soc. Lond. A **164**, 151–167 (1938) (cit. on pp. 10, 13).

[17] C. C. Chemistry, *Compound Properties, lead bromide, CAS: 10031-22-8*, (2023) `https://commonchemistry.cas.org/detail?cas_rn=10031-22-8` (cit. on p. 10).

[18] C. C. Chemistry, *Compound Properties, silver bromide, CAS: 7785-23-1*, (2023) `https://commonchemistry.cas.org/detail?cas_rn=7785-23-1` (cit. on p. 10).

[19] C. C. Chemistry, *Compound Properties, titania, CAS: 13463-67-7*, (2023) `https://commonchemistry.cas.org/detail?cas_rn=13463-67-7` (cit. on p. 10).

[20] F. Seitz, ‘Lattice Defects in Silver Halide Crystals’, Phys. Rev. **56**, 1063–1064 (1939) (cit. on p. 10).

[21] J. Kim, S.-H. Lee, J. H. Lee and K.-H. Hong, 'The Role of Intrinsic Defects in Methylammonium Lead Iodide Perovskite', J. Phys. Chem. Lett. **5**, 1312–1317 (2014) (cit. on p. 10).

[22] B. Yang, J. Chen, S. Yang, F. Hong, L. Sun, P. Han, T. Pullerits, W. Deng and K. Han, 'Lead-Free Silver-Bismuth Halide Double Perovskite Nanocrystals', Angew. Chem. **130**, 5457–5461 (2018) (cit. on p. 11).

[23] H.-L. Chen, A. Cattoni, R. D. Lépinau, A. W. Walker, O. Höhn, D. Lackner, G. Siefer, M. Faustini, N. Vandamme, J. Goffard, B. Behaghel, C. Dupuis, N. Bardou, F. Dimroth and S. Collin, 'A 19.9%-efficient ultrathin solar cell based on a 205-nm-thick GaAs absorber and a silver nanostructured back mirror', Nat Energy **4**, 761–767 (2019) (cit. on p. 11).

[24] W.-J. Yin, J.-H. Yang, J. Kang, Y. Yan and S.-H. Wei, 'Halide perovskite materials for solar cells: a theoretical review', J. Mater. Chem. A **3**, 8926–8942 (2015) (cit. on pp. 12, 13).

[25] S. Tao, I. Schmidt, G. Brocks, J. Jiang, I. Tranca, K. Meerholz and S. Olthof, 'Absolute energy level positions in tin- and lead-based halide perovskites', Nat Commun **10**, `10.1038/s41467-019-10468-7` (2019) (cit. on pp. 12, 13).

[26] G. J. Man, C. Kamal, A. Kalinko, D. Phuyal, J. Acharya, S. Mukherjee, P. K. Nayak, H. Rensmo, M. Odelius and S. M. Butorin, 'A-site cation influence on the conduction band of lead bromide perovskites', Nat Commun **13**, `10.1038/s41467-022-31416-y` (2022) (cit. on p. 12).

[27] R. Dronskowski and P. E. Bloechl, 'Crystal orbital Hamilton populations (COHP): energy-resolved visualization of chemical bonding in solids based on density-functional calculations', J. Phys. Chem. **97**, 8617–8624 (1993) (cit. on p. 13).

[28] W.-J. Yin, T. Shi and Y. Yan, 'Unusual defect physics in $CH_3NH_3PbI_3$ perovskite solar cell absorber', Applied Physics Letters **104**, 063903 (2014) (cit. on p. 13).

[29] M. A. Becker, R. Vaxenburg, G. Nedelcu, P. C. Sercel, A. Shabaev, M. J. Mehl, J. G. Michopoulos, S. G. Lambrakos, N. Bernstein, J. L. Lyons, T. Stöferle, R. F. Mahrt, M. V. Kovalenko, D. J. Norris, G. Rainò and A. L. Efros, 'Bright triplet excitons in caesium lead halide perovskites', Nature **553**, 189–193 (2018) (cit. on pp. 13, 15–17).

[30] Q. A. Akkerman, G. Rainò, M. V. Kovalenko and L. Manna, 'Genesis, challenges and opportunities for colloidal lead halide perovskite nanocrystals', Nature Mater **17**, 394–405 (2018) (cit. on pp. 13, 15).

[31] M. V. Kovalenko, L. Protesescu and M. I. Bodnarchuk, 'Properties and potential optoelectronic applications of lead halide perovskite nanocrystals', Science **358**, 745–750 (2017) (cit. on p. 13).

[32] E. J. Juarez-Perez, L. K. Ono, M. Maeda, Y. Jiang, Z. Hawash and Y. Qi, 'Photodecomposition and thermal decomposition in methylammonium halide lead perovskites and inferred design principles to increase photovoltaic device stability', J. Mater. Chem. A **6**, 9604–9612 (2018) (cit. on p. 14).

[33] S.-S. Rong, M. B. Faheem and Y.-B. Li, 'Perovskite single crystals: Synthesis, properties, and applications', Journal of Electronic Science and Technology **19**, 100081 (2021) (cit. on p. 14).

[34] S. Pathak, N. Sakai, F. W. R. Rivarola, S. D. Stranks, J. Liu, G. E. Eperon, C. Ducati, K. Wojciechowski, J. T. Griffiths, A. A. Haghighirad, A. Pellaroque, R. H. Friend and H. J. Snaith, 'Perovskite Crystals for Tunable White Light Emission', Chem. Mater. **27**, 8066–8075 (2015) (cit. on p. 14).

[35] F. Zhang, H. Zhong, C. Chen, X.-g. Wu, X. Hu, H. Huang, J. Han, B. Zou and Y. Dong, 'Brightly Luminescent and Color-Tunable Colloidal $CH_3NH_3PbX_3$ (X = Br, I, Cl) Quantum Dots: Potential Alternatives for Display Technology', ACS Nano Nano **9**, 4533–4542 (2015) (cit. on p. 14).

[36] L. C. Schmidt, A. Pertegás, S. González-Carrero, O. Malinkiewicz, S. Agouram, G. M. Espallargas, H. J. Bolink, R. E. Galian and J. Pérez-Prieto, 'Nontemplate Synthesis of $CH_3NH_3PbBr_3$ Perovskite Nanoparticles', J. Am. Chem. Soc. **136**, 850–853 (2014) (cit. on p. 14).

[37] A. Dutta, R. K. Behera, P. Pal, S. Baitalik and N. Pradhan, 'Near-Unity Photoluminescence Quantum Efficiency for All $CsPbX_3$ (X=Cl, Br, and I) Perovskite Nanocrystals: A Generic Synthesis Approach', Angew. Chem. **131**, 5608–5612 (2019) (cit. on pp. 15, 57, 105).

[38] Q. A. Akkerman, S. G. Motti, A. R. S. Kandada, E. Mosconi, V. D'Innocenzo, G. Bertoni, S. Marras, B. A. Kamino, L. Miranda, F. D. Angelis, A. Petrozza, M. Prato and L. Manna, 'Solution Synthesis Approach to Colloidal Cesium Lead Halide Perovskite Nanoplatelets with Monolayer-Level Thickness Control', J. Am. Chem. Soc. **138**, 1010–1016 (2016) (cit. on p. 15).

[39] H. Zhu, Y. Fu, F. Meng, X. Wu, Z. Gong, Q. Ding, M. V. Gustafsson, M. T. Trinh, S. Jin and X.-Y. Zhu, 'Lead halide perovskite nanowire lasers with low lasing thresholds and high quality factors', Nature Mater **14**, 636–642 (2015) (cit. on p. 15).

[40] G. Macfarlane, T. McLean, J. Quarrington and V. Roberts, 'Exciton and phonon effects in the absorption spectra of germanium and silicon', Journal of Physics and Chemistry of Solids **8**, 388–392 (1959) (cit. on p. 15).

[41] M. Baranowski and P. Plochocka, ‘Excitons in Metal-Halide Perovskites’, Adv. Energy Mater. **10**, 1903659 (2020) (cit. on p. 15).

[42] L. E. Brus, ‘Electron–electron and electron-hole interactions in small semiconductor crystallites: The size dependence of the lowest excited electronic state’, The Journal of Chemical Physics **80**, 4403–4409 (1984) (cit. on pp. 15, 84, 85).

[43] T. Kippeny, L. A. Swafford and S. J. Rosenthal, ‘Semiconductor Nanocrystals: A Powerful Visual Aid for Introducing the Particle in a Box’, J. Chem. Educ. **79**, 1094 (2002) (cit. on pp. 15, 84).

[44] A. L. Efros and L. E. Brus, ‘Nanocrystal Quantum Dots: From Discovery to Modern Development’, ACS Nano **15**, 6192–6210 (2021) (cit. on pp. 15, 84).

[45] A. L. Efros and M. Rosen, ‘The Electronic Structure of Semiconductor Nanocrystals’, Annu. Rev. Mater. Sci. **30**, 475–521 (2000) (cit. on p. 15).

[46] M. Gramlich, M. W. Swift, C. Lampe, J. L. Lyons, M. Döblinger, A. L. Efros, P. C. Sercel and A. S. Urban, ‘Dark and Bright Excitons in Halide Perovskite Nanoplatelets’, Advanced Science **9**, 2103013 (2021) (cit. on pp. 15, 17, 18).

[47] P. C. Sercel, J. L. Lyons, D. Wickramaratne, R. Vaxenburg, N. Bernstein and A. L. Efros, ‘Exciton Fine Structure in Perovskite Nanocrystals’, Nano Lett. **19**, 4068–4077 (2019) (cit. on pp. 15, 17).

[48] M. Schwoerer and H. C. Wolf, *Organic Molecular Solids*, 1st ed (Wiley, 2008) (cit. on p. 17).

[49] A. Köhler and H. Bässler, *Electronic Processes in Organic Semiconductors* (Wiley, Mar. 2015) (cit. on pp. 17, 25).

[50] J. Even, L. Pedesseau, J.-M. Jancu and C. Katan, ‘Importance of Spin–Orbit Coupling in Hybrid Organic/Inorganic Perovskites for Photovoltaic Applications’, J. Phys. Chem. Lett. **4**, 2999–3005 (2013) (cit. on p. 17).

[51] M. Kim, J. Im, A. J. Freeman, J. Ihm and H. Jin, ‘Switchable S = 1/2 and J = 1/2 Rashba bands in ferroelectric halide perovskites’, Proc. Natl. Acad. Sci. U.S.A. **111**, 6900–6904 (2014) (cit. on p. 17).

[52] C. Qin, T. Matsushima, W. J. Potscavage, A. S. D. Sandanayaka, M. R. Leyden, F. Bencheikh, K. Goushi, F. Mathevet, B. Heinrich, G. Yumoto, Y. Kanemitsu and C. Adachi, ‘Triplet management for efficient perovskite light-emitting diodes’, Nat. Photonics **14**, 70–75 (2019) (cit. on pp. 18, 79).

[53] M. I. Bodnarchuk, S. C. Boehme, S. ten Brinck, C. Bernasconi, Y. Shynkarenko, F. Krieg, R. Widmer, B. Aeschlimann, D. Günther, M. V. Kovalenko and I. Infante, ‘Rationalizing and Controlling the Surface Structure and Electronic Passivation of Cesium Lead Halide Nanocrystals’, ACS Energy Lett. **4**, 63–74 (2018) (cit. on p. 19).

[54] N. Fiuza-Maneiro, K. Sun, I. López-Fernández, S. Gómez-Graña, P. Müller-Buschbaum and L. Polavarapu, ‘Ligand Chemistry of Inorganic Lead Halide Perovskite Nanocrystals’, ACS Energy Letters, 1152–1191 (2023) (cit. on p. 19).

[55] M. J. Bennison, A. R. Collins, B. Zhang and R. C. Evans, ‘Organic Polymer Hosts for Triplet–Triplet Annihilation Upconversion Systems’, Macromolecules **54**, 5287–5303 (2021) (cit. on p. 24).

[56] E. Yablonovitch, ‘Inhibited Spontaneous Emission in Solid-State Physics and Electronics’, Phys. Rev. Lett. **58**, 2059–2062 (1987) (cit. on p. 24).

[57] W. Brütting, J. Frischeisen, T. D. Schmidt, B. J. Scholz and C. Mayr, ‘Device efficiency of organic light-emitting diodes: Progress by improved light outcoupling’, Phys. Status Solidi A **210**, 44–65 (2012) (cit. on pp. 24, 25).

[58] C. Cho, B. Zhao, G. D. Tainter, J.-Y. Lee, R. H. Friend, D. Di, F. Deschler and N. C. Greenham, ‘The role of photon recycling in perovskite light-emitting diodes’, Nat Commun **11**, `10.1038/s41467-020-14401-1` (2020) (cit. on pp. 24, 45, 46).

[59] T. Morgenstern, C. Lampe, T. Naujoks, M. Jurow, Y. Liu, A. S. Urban and W. Brütting, ‘Elucidating the performance limits of perovskite nanocrystal light emitting diodes’, Journal of Luminescence **220**, 116939 (2020) (cit. on pp. 24, 68, 70, 71, 108).

[60] M. J. Jurow, T. Morgenstern, C. Eisler, J. Kang, E. Penzo, M. Do, M. Engelmayer, W. T. Osowiecki, Y. Bekenstein, C. Tassone, L.-W. Wang, A. P. Alivisatos, W. Brütting and Y. Liu, ‘Manipulating the Transition Dipole Moment of $CsPbBr_3$ Perovskite Nanocrystals for Superior Optical Properties’, Nano Lett. **19**, 2489–2496 (2019) (cit. on pp. 24, 46, 70, 71).

[61] S. Forrest, *Organic Electronics: Foundations to Applications* (Oxford University Press, 2020) (cit. on p. 25).

[62] D. E. Markov and P. W. M. Blom, ‘Exciton quenching in poly(phenylene vinylene) polymer light-emitting diodes’, Appl. Phys. Lett. **87**, 233511 (2005) (cit. on p. 25).

[63] V. M. L. Corre, J. Diekmann, F. Peña-Camargo, J. Thiesbrummel, N. Tokmoldin, E. Gutierrez-Partida, K. P. Peters, L. Perdigón-Toro, M. H. Futscher, F. Lang, J. Warby, H. J. Snaith, D. Neher and M. Stolterfoht, 'Quantification of Efficiency Losses Due to Mobile Ions in Perovskite Solar Cells via Fast Hysteresis Measurements', Solar RRL **6**, 2100772 (2022) (cit. on p. 25).

[64] K. Sugiyama, H. Ishii, Y. Ouchi and K. Seki, 'Dependence of indium–tin–oxide work function on surface cleaning method as studied by ultraviolet and x-ray photoemission spectroscopies', Journal of Applied Physics **87**, 295–298 (2000) (cit. on pp. 26, 61, 67, 92, 110).

[65] W. Kim, N. Kim, J. K. Kim, I. Park, Y. S. Choi, D. H. Wang, H. Chae and J. H. Park, 'Polymer Bulk Heterojunction Solar Cells with PEDOT:PSS Bilayer Structure as Hole Extraction Layer', ChemSusChem **6**, 1070–1075 (2013) (cit. on pp. 26, 61, 67, 92, 110).

[66] Q. Sun, Y. A. Wang, L. S. Li, D. Wang, T. Zhu, J. Xu, C. Yang and Y. Li, 'Bright, multicoloured light-emitting diodes based on quantum dots', Nature Photon **1**, 717–722 (2007) (cit. on p. 26).

[67] M. Redecker, D. D. Bradley, M. Inbasekaran, W. W. Wu and E. P. Woo, 'High Mobility Hole Transport Fluorene-Triarylamine Copolymers', Adv. Mater. **11**, 241–246 (1999) (cit. on p. 26).

[68] W. Renzi, N. J. Cordeiro, H. de Santana, M. F. Costa, M. A. da Silva, E. Laureto and J. L. Duarte, 'Exploring the experimental photoluminescence, Raman and infrared responses and density functional theory results for TFB polymer', Synthetic Metals **236**, 24–30 (2018) (cit. on p. 26).

[69] J. Park, T. Park, W. Jeon, R. Pode, J. Jang, J. Kwon, E. Yu and M. Chae, 'Small molecule interlayer for solution processed phosphorescent organic light emitting device', Organic Electronics **10**, 189–193 (2009) (cit. on p. 26).

[70] T. Naujoks, R. Jayabalan, C. Kirsch, F. Zu, M. Mandal, J. Wahl, M. Waibel, A. Opitz, N. Koch, D. Andrienko, M. Scheele and W. Brütting, 'Quantum Efficiency Enhancement of Lead-Halide Perovskite Nanocrystal LEDs by Organic Lithium Salt Treatment', ACS Appl. Mater. Interfaces **14**, 28985–28996 (2022) (cit. on pp. 25, 26, 52, 61, 67, 79, 92, 105).

[71] J. Pina, J. S. de Melo, H. Burrows, A. Monkman and S. Navaratnam, 'On the triplet state of poly(N-vinylcarbazole)', Chemical Physics Letters **400**, 441–445 (2004) (cit. on pp. 26, 61, 67, 92).

[72] V. K. Ravi, G. B. Markad and A. Nag, 'Band Edge Energies and Excitonic Transition Probabilities of Colloidal $CsPbX_3$ (X = Cl, Br, I) Perovskite Nanocrystals', ACS Energy Lett. **1**, 665–671 (2016) (cit. on pp. 25, 26, 61, 67, 71, 92).

[73] T. Xu, Y.-X. Zhang, C.-C. Huang, J.-G. Zhou, M.-K. Fung and H. Meng, 'Highly simplified blue phosphorescent organic light-emitting diodes incorporating exciplex-forming co-host assisting energy transfer', Journal of Luminescence **206**, 554–559 (2019) (cit. on pp. 26, 27, 110).

[74] H. Sasabe, D. Tanaka, D. Yokoyama, T. Chiba, Y.-J. Pu, K.-i. Nakayama, M. Yokoyama and J. Kido, 'Influence of Substituted Pyridine Rings on Physical Properties and Electron Mobilities of 2-Methylpyrimidine Skeleton-Based Electron Transporters', Adv. Funct. Mater. **21**, 336–342 (2010) (cit. on pp. 26, 27, 61, 67, 92).

[75] R. Schlaf, B. A. Parkinson, P. A. Lee, K. W. Nebesny, G. Jabbour, B. Kippelen, N. Peyghambarian and N. R. Armstrong, 'Photoemission spectroscopy of LiF coated Al and Pt electrodes', Journal of Applied Physics **84**, 6729–6736 (1998) (cit. on pp. 26, 61, 67, 92, 110).

[76] P. D'Angelo, M. Barra, A. Cassinese, M. Maglione, P. Vacca, C. Minarini and A. Rubino, 'Electrical transport properties characterization of PVK (poly N-vinylcarbazole) for electroluminescent devices applications', Solid-State Electronics **51**, 123–129 (2007) (cit. on p. 26).

[77] Z. Li, Y. Liang, Z. Zhong, J. Qian, G. Liang, K. Zhao, H. Shi, S. Zhong, Y. Yin and W. Tian, 'A low-work-function, high-conductivity PEDOT:PSS electrode for organic solar cells with a simple structure', Synthetic Metals **210**, 363–366 (2015) (cit. on p. 26).

[78] J. Pan, J. Chen, Q. Huang, L. Wang and W. Lei, 'A highly efficient quantum dot light emitting diode via improving the carrier balance by modulating the hole transport', RSC Adv. Advances **7**, 43366–43372 (2017) (cit. on p. 26).

[79] H. Wu, Y. Zhang, X. Zhang, M. Lu, C. Sun, T. Zhang and W. W. Yu, 'Enhanced Stability and Performance in Perovskite Nanocrystal Light-Emitting Devices Using a ZnMgO Interfacial Layer', Advanced Optical Materials **5**, 1700377 (2017) (cit. on p. 27).

[80] C. Tang, X. Shen, X. Wu, Y. Zhong, J. Hu, M. Lu, Z. Wu, Y. Zhang, W. W. Yu and X. Bai, 'Optimizing the Performance of Perovskite Nanocrystal LEDs Utilizing Cobalt Doping on a ZnO Electron Transport Layer', J. Phys. Chem. Lett. **12**, 10112–10119 (2021) (cit. on p. 27).

[81] Y. Zou, T. Wu, F. Fu, S. Bai, L. Cai, Z. Yuan, Y. Li, R. Li, W. Xu, T. Song, Y. Yang, X. Gao, F. Gao and B. Sun, 'Thermal-induced interface degradation in perovskite light-emitting diodes', J. Mater. Chem. C **8**, 15079–15085 (2020) (cit. on p. 27).

[82] Y. Noguchi, K. Osada, K. Ninomiya, H. D. Gunawardana, K. R. Koswattage and H. Ishii, ‘Influence of intermolecular interactions on the formation of spontaneous orientation polarization in organic semiconducting films’, J Soc Inf Display **29**, 29–37 (2020) (cit. on pp. 27, 92).

[83] S. Hettler, M. Dries, P. Hermann, M. Obermair, D. Gerthsen and M. Malac, ‘Carbon contamination in scanning transmission electron microscopy and its impact on phase-plate applications’, Micron **96**, 38–47 (2017) (cit. on p. 30).

[84] Z. Dang, J. Shamsi, F. Palazon, M. Imran, Q. A. Akkerman, S. Park, G. Bertoni, M. Prato, R. Brescia and L. Manna, ‘In Situ Transmission Electron Microscopy Study of Electron Beam-Induced Transformations in Colloidal Cesium Lead Halide Perovskite Nanocrystals’, ACS Nano Nano **11**, 2124–2132 (2017) (cit. on p. 30).

[85] W. Brütting, *Physics of Organic Semiconductors* (WILEY-VCH, Oct. 2005) (cit. on p. 36).

[86] E.-L. Hsiang, Z. Yang, Q. Yang, Y.-F. Lan and S.-T. Wu, ‘Prospects and challenges of mini-LED, OLED, and micro-LED displays’, J Soc Inf Display **29**, 446–465 (2021) (cit. on p. 43).

[87] X. Deng, X. Wen, C. F. J. Lau, T. Young, J. Yun, M. A. Green, S. Huang and A. W. Y. Ho-Baillie, ‘Electric field induced reversible and irreversible photoluminescence responses in methylammonium lead iodide perovskite’, J. Mater. Chem. C **4**, 9060–9068 (2016) (cit. on p. 45).

[88] S. Bae, S. Kim, S.-W. Lee, K. J. Cho, S. Park, S. Lee, Y. Kang, H.-S. Lee and D. Kim, ‘Electric-Field-Induced Degradation of Methylammonium Lead Iodide Perovskite Solar Cells’, J. Phys. Chem. Lett. **7**, 3091–3096 (2016) (cit. on p. 45).

[89] G. Jones, W. R. Jackson and A. M. Halpern, ‘Medium effects on fluorescence quantum yields and lifetimes for coumarin laser dyes’, Chemical Physics Letters **72**, 391–395 (1980) (cit. on p. 45).

[90] K. Drexhage, ‘Fluorescence efficiency of laser dyes’, J. RES. NATL. BUR. STAN. SECT. A. **80A**, 421 (1976) (cit. on p. 45).

[91] M. C. Brennan, A. Forde, M. Zhukovskyi, A. J. Baublis, Y. V. Morozov, S. Zhang, Z. Zhang, D. S. Kilin and M. Kuno, ‘Universal Size-Dependent Stokes Shifts in Lead Halide Perovskite Nanocrystals’, J. Phys. Chem. Lett. **11**, 4937–4944 (2020) (cit. on p. 45).

[92] I. Papakonstantinou and C. Tummeltshammer, ‘Fundamental limits of concentration in luminescent solar concentrators revised: the effect of reabsorption and nonunity quantum yield’, Optica **2**, 841 (2015) (cit. on p. 45).

[93] W. Brütting, J. Frischeisen, T. D. Schmidt, B. J. Scholz and C. Mayr, ‘Device efficiency of organic light-emitting diodes: Progress by improved light outcoupling’, Phys. Status Solidi A **210**, 44–65 (2012) (cit. on p. 46).

[94] K.-H. Kim and S.-Y. Park, ‘Enhancing light-extraction efficiency of OLEDs with high- and low-refractive-index organic–inorganic hybrid materials’, Organic Electronics **36**, 103–112 (2016) (cit. on p. 46).

[95] Q. Xue, C. Lampe, T. Naujoks, K. Frank, M. Gramlich, M. Schoger, W. Vanderlinden, P. Reisbeck, B. Nickel, W. Brütting and A. S. Urban, ‘Doubly Stabilized Perovskite Nanocrystal Luminescence Downconverters’, Advanced Optical Materials **10**, 2102791 (2022) (cit. on pp. 46–48).

[96] Z. Chen, Z. Li, C. Zhang, X.-F. Jiang, D. Chen, Q. Xue, M. Liu, S. Su, H.-L. Yip and Y. Cao, ‘Recombination Dynamics Study on Nanostructured Perovskite Light-Emitting Devices’, Adv. Mater. **30**, 1801370 (2018) (cit. on p. 47).

[97] J. Liu, L. Guillemeney, B. Abécassis and L. Coolen, ‘Long Range Energy Transfer in Self-Assembled Stacks of Semiconducting Nanoplatelets’, Nano Lett. **20**, 3465–3470 (2020) (cit. on p. 47).

[98] K. Goushi, R. Kwong, J. J. Brown, H. Sasabe and C. Adachi, ‘Triplet exciton confinement and unconfinement by adjacent hole-transport layers’, Journal of Applied Physics **95**, 7798–7802 (2004) (cit. on p. 47).

[99] C. Murawski, K. Leo and M. C. Gather, ‘Efficiency Roll-Off in Organic Light-Emitting Diodes’, Adv. Mater. **25**, 6801–6827 (2013) (cit. on p. 47).

[100] J.-M. Tarascon and M. Armand, ‘Issues and challenges facing rechargeable lithium batteries’, Nature **414**, 359–367 (2001) (cit. on p. 52).

[101] L. Sim, F. Sentanin, A. Pawlicka, R. Yahya and A. Arof, ‘Development of polyacrylonitrile-based polymer electrolytes incorporated with lithium bis(trifluoromethane)sulfonimide for application in electrochromic device’, Electrochimica Acta **229**, 22–30 (2017) (cit. on p. 52).

[102] D. Mombrú, M. Romero, R. Faccio and Á. W. Mombrú, ‘Unraveling the Lithium Bis(trifluoromethanesulfonyl)imide (LiTFSI) Doping Mechanism of Regioregular Poly(3-hexylthiophene): Experimental and Theoretical Study’, J. Phys. Chem. C **124**, 7061–7070 (2020) (cit. on p. 52).

[103] A. Abate, T. Leijtens, S. Pathak, J. Teuscher, R. Avolio, M. E. Errico, J. Kirkpatrik, J. M. Ball, P. Docampo, I. McPherson and H. J. Snaith, 'Lithium salts as "redox active" p-type dopants for organic semiconductors and their impact in solid-state dye-sensitized solar cells', Phys. Chem. Chem. Phys. **15**, 2572 (2013) (cit. on p. 52).

[104] Z. Li, J. Tinkham, P. Schulz, M. Yang, D. H. Kim, J. Berry, A. Sellinger and K. Zhu, 'Acid Additives Enhancing the Conductivity of Spiro-OMeTAD Toward High-Efficiency and Hysteresis-Less Planar Perovskite Solar Cells', Adv. Energy Mater. **7**, 1601451 (2016) (cit. on p. 52).

[105] Z. Fang, H. He, L. Gan, J. Li and Z. Ye, 'Understanding the Role of Lithium Doping in Reducing Nonradiative Loss in Lead Halide Perovskites', Adv. Sci. **5**, 1800736 (2018) (cit. on p. 52).

[106] T. Wu, J. Li, Y. Zou, H. Xu, K. Wen, S. Wan, S. Bai, T. Song, J. A. McLeod, S. Duhm, F. Gao and B. Sun, 'High-Performance Perovskite Light-Emitting Diode with Enhanced Operational Stability Using Lithium Halide Passivation', Angew. Chem. Int. Ed. **59**, 4099–4105 (2020) (cit. on p. 52).

[107] H. Wu, J. Qiu, J. Wang, Y. Wen, Q. Wang, Z. Long, D. Zhou, Y. Yang and D. Wang, 'The dual-defect passivation role of lithium bromide doping in reducing the nonradiative loss in $CsPbX_3$ (X = Br and I) quantum dots', Inorg. Chem. Front. **8**, 658–668 (2021) (cit. on p. 52).

[108] J. M. Lee, B.-H. Kwon, H. I. Park, H. Kim, M. G. Kim, J. S. Park, E. S. Kim, S. Yoo, D. Y. Jeon and S. O. Kim, 'Exciton Dissociation and Charge-Transport Enhancement in Organic Solar Cells with Quantum-Dot/N-doped CNT Hybrid Nanomaterials', Adv. Mater. **25**, 2011–2017 (2013) (cit. on p. 54).

[109] Q. Sun, C. Zhao, Z. Yin, S. Wang, J. Leng, W. Tian and S. Jin, 'Ultrafast and High-Yield Polaronic Exciton Dissociation in Two-Dimensional Perovskites', J. Am. Chem. Soc. **143**, 19128–19136 (2021) (cit. on p. 54).

[110] X.-F. Peng, X.-Y. Wu, X.-X. Ji, J. Ren, Q. Wang, G.-Q. Li and X.-H. Yang, 'Modified Conducting Polymer Hole Injection Layer for High-Efficiency Perovskite Light-Emitting Devices: Enhanced Hole Injection and Reduced Luminescence Quenching', J. Phys. Chem. Lett. **8**, 4691–4697 (2017) (cit. on p. 54).

[111] T. Nguyen, P. L. Rendu, P. Long and S. D. Vos, 'Chemical and thermal treatment of PEDOT:PSS thin films for use in organic light emitting diodes', Surface and Coatings Technology **180-181**, 646–649 (2004) (cit. on p. 54).

[112] S. Olthof and K. Meerholz, 'Substrate-Dependent Electronic Structure and Film Formation of $MAPbI_3$ Perovskites', Scientific Reports **7**, 40267 (2017) (cit. on p. 54).

[113] Y.-L. Shi, F. Liang, Y. Hu, X.-D. Wang, Z.-K. Wang and L.-S. Liao, 'High-efficiency quantum dot light-emitting diodes employing lithium salt doped poly(9-vinylcarbazole) as a hole-transporting layer', J. Mater. Chem. C **5**, 5372–5377 (2017) (cit. on p. 54).

[114] K. Kim, J. Jeong, M. Kim, D. Kang, S. W. Cho, H. Lee and Y. Yi, 'Direct p-doping of Li-TFSI for efficient hole injection: Role of polaronic level in molecular doping', Applied Surface Science **480**, 565–571 (2019) (cit. on p. 54).

[115] W. Zhao and J. Sun, 'Triflimide ($HNTf_2$) in Organic Synthesis', Chem. Rev. **118**, 10349–10392 (2018) (cit. on p. 54).

[116] B. Zhao, Y. Lian, L. Cui, G. Divitini, G. Kusch, E. Ruggeri, F. Auras, W. Li, D. Yang, B. Zhu, R. A. Oliver, J. L. MacManus-Driscoll, S. D. Stranks, D. Di and R. H. Friend, 'Efficient light-emitting diodes from mixed-dimensional perovskites on a fluoride interface', Nat Electron **3**, 704–710 (2020) (cit. on p. 54).

[117] B. Ross, *Happy little accidents* (Kösel Verlag, Oct. 2017) (cit. on p. 54).

[118] M. A. Schwartz, 'The importance of stupidity in scientific research', Journal of Cell Science **121**, 1771–1771 (2008) (cit. on p. 54).

[119] L. R. Wilson and B. S. Richards, 'Measurement method for photoluminescent quantum yields of fluorescent organic dyes in polymethyl methacrylate for luminescent solar concentrators', Appl. Opt. **48**, 212 (2009) (cit. on p. 55).

[120] F. Krieg, Q. K. Ong, M. Burian, G. Raino, D. Naumenko, H. Amenitsch, A. Süess, M. J. Grotevent, F. Krumeich, M. I. Bodnarchuk, I. Shorubalko, F. Stellacci and M. V. Kovalenko, 'Stable Ultraconcentrated and Ultradilute Colloids of $CsPbX_3$ (X = Cl, Br) Nanocrystals Using Natural Lecithin as a Capping Ligand', J. Am. Chem. Soc. **141**, 19839–19849 (2019) (cit. on pp. 55, 78).

[121] C. Kirsch, T. Naujoks, P. Haizmann, P. Frech, H. Peisert, T. Chassé, W. Brütting and M. Scheele, 'Zwitterionic Carbazole Ligands Enhance the Stability and Performance of Perovskite Nanocrystals in Light Emitting Diodes', **15**, 32744–32752 (2023) (cit. on pp. 56, 79, 82, 84, 86, 105).

[122] Y. Sun, H. Zhang, K. Zhu, W. Ye, L. She, X. Gao, W. Ji and Q. Zeng, 'Research on the influence of polar solvents on $CsPbBr_3$ perovskite QDs', RSC Adv. Advances **11**, 27333–27337 (2021) (cit. on p. 56).

[123] J. Wahl, M. Engelmayer, M. Mandal, T. Naujoks, P. Haizmann, A. Maier, H. Peisert, D. Andrienko, W. Brütting and M. Scheele, 'Porphyrin Functionalization of $CsPbBrI_2$ /SiO_2Core–Shell Nanocrystals Enhances the Stability and Efficiency in Electroluminescent Devices', Advanced Optical Materials **10**, 2101945 (2021) (cit. on p. 56).

[124] K. Hills-Kimball, H. Yang, T. Cai, J. Wang and O. Chen, 'Recent Advances in Ligand Design and Engineering in Lead Halide Perovskite Nanocrystals', Advanced Science **8**, 2100214 (2021) (cit. on pp. 56, 78).

[125] Q. A. Akkerman, V. D'Innocenzo, S. Accornero, A. Scarpellini, A. Petrozza, M. Prato and L. Manna, 'Tuning the Optical Properties of Cesium Lead Halide Perovskite Nanocrystals by Anion Exchange Reactions', J. Am. Chem. Soc. **137**, 10276–10281 (2015) (cit. on p. 57).

[126] F. D. Stasio, S. Christodoulou, N. Huo and G. Konstantatos, 'Near-Unity Photoluminescence Quantum Yield in $CsPbBr_3$ Nanocrystal Solid-State Films via Postsynthesis Treatment with Lead Bromide', Chem. Mater. **29**, 7663–7667 (2017) (cit. on p. 57).

[127] J. Y. Woo, Y. Kim, J. Bae, T. G. Kim, J. W. Kim, D. C. Lee and S. Jeong, 'Highly Stable Cesium Lead Halide Perovskite Nanocrystals through in Situ Lead Halide Inorganic Passivation', Chem. Mater. **29**, 7088–7092 (2017) (cit. on p. 57).

[128] M. Liu, L. Ma, K. Xie, P. Zeng, S. Wei, F. Zhang, C. Li and F. Wang, 'Efficiently Improved Photoluminescence in Cesium Lead Halide Perovskite Nanocrystals by Using Bis(trifluoromethane)sulfonimide', J. Phys. Chem. Lett. **13**, 1519–1525 (2022) (cit. on pp. 57, 60).

[129] N. C. for Biotechnology Information, *PubChem Compound Summary for CID 260, Hydrogen bromide*, (2023) `https://pubchem.ncbi.nlm.nih.gov/compound/Hydrogen-bromide` (cit. on p. 57).

[130] H. Chu, H. Noh, Y.-J. Kim, S. Yuk, J.-H. Lee, J. Lee, H. Kwack, Y. Kim, D.-K. Yang and H.-T. Kim, 'Achieving three-dimensional lithium sulfide growth in lithium-sulfur batteries using high-donor-number anions', Nat Commun **10**, `10.1038/s41467-018-07975-4` (2019) (cit. on p. 57).

[131] A. Einstein, 'Über einen die Erzeugung und Verwandlung des Lichtes betreffenden heuristischen Gesichtspunkt', Ann. Phys. **322**, 132–148 (1905) (cit. on p. 60).

[132] Y. Park, V. Choong, Y. Gao, B. R. Hsieh and C. W. Tang, 'Work function of indium tin oxide transparent conductor measured by photoelectron spectroscopy', Appl. Phys. Lett. **68**, 2699–2701 (1996) (cit. on p. 60).

[133] K. Seki and H. Ishii, 'Photoemission studies of functional organic materials and their interfaces', Journal of Electron Spectroscopy and Related Phenomena **88-91**, 821–830 (1998) (cit. on p. 60).

[134] S. Olthof and K. Meerholz, 'Substrate-dependent electronic structure and film formation of $MAPbI_3$ perovskites', Sci Rep **7**, `10.1038/srep40267` (2017) (cit. on p. 60).

[135] F. Zu, C. M. Wolff, M. Ralaiarisoa, P. Amsalem, D. Neher and N. Koch, 'Unraveling the Electronic Properties of Lead Halide Perovskites with Surface Photovoltage in Photoemission Studies', ACS Appl. Mater. Interfaces **11**, 21578–21583 (2019) (cit. on p. 60).

[136] J. Endres, D. A. Egger, M. Kulbak, R. A. Kerner, L. Zhao, S. H. Silver, G. Hodes, B. P. Rand, D. Cahen, L. Kronik and A. Kahn, 'Valence and Conduction Band Densities of States of Metal Halide Perovskites: A Combined Experimental–Theoretical Study', J. Phys. Chem. Lett. **7**, 2722–2729 (2016) (cit. on pp. 60, 71).

[137] F. Zu, P. Amsalem, D. A. Egger, R. Wang, C. M. Wolff, H. Fang, M. A. Loi, D. Neher, L. Kronik, S. Duhm and N. Koch, 'Constructing the Electronic Structure of $CH_3NH_3PbI_3$ and $CH_3NH_3PbBr_3$ Perovskite Thin Films from Single-Crystal Band Structure Measurements', J. Phys. Chem. Lett. **10**, 601–609 (2019) (cit. on p. 60).

[138] S. M. Park, Y. H. Kim, Y. Yi, H.-Y. Oh and J. W. Kim, 'Insertion of an organic interlayer for hole current enhancement in inverted organic light emitting devices', Appl. Phys. Lett. **97**, 063308 (2010) (cit. on pp. 61, 92).

[139] M. Menzinger and R. Wolfgang, 'The Meaning and Use of the Arrhenius Activation Energy', Angew. Chem. Int. Ed. Engl. **8**, 438–444 (1969) (cit. on p. 64).

[140] H. Yang and N. Wu, 'Ionic conductivity and ion transport mechanisms of solid-state lithium-ion battery electrolytes: A review', Energy Science and Engineering **10**, 1643–1671 (2022) (cit. on p. 64).

[141] B. Roling, A. Happe, K. Funke and M. D. Ingram, 'Carrier Concentrations and Relaxation Spectroscopy: New Information from Scaling Properties of Conductivity Spectra in Ionically Conducting Glasses', Phys. Rev. Lett. **78**, 2160–2163 (1997) (cit. on p. 64).

[142] H.-J. Deiseroth, J. Maier, K. Weichert, V. Nickel, S.-T. Kong and C. Reiner, 'Li7PS6 and Li6PS5X (X: Cl, Br, I): Possible Three-dimensional Diffusion Pathways for Lithium Ions and Temperature Dependence of the Ionic Conductivity by Impedance Measurements', Z. anorg. allg. Chem. **637**, 1287–1294 (2011) (cit. on p. 64).

[143] A. A. Azli, N. S. A. Manan and M. F. Z. Kadir, 'Conductivity and Dielectric Studies of Lithium Trifluoromethanesulfonate Doped Polyethylene Oxide-Graphene Oxide Blend Based Electrolytes', Advances in Materials Science and Engineering **2015**, 1–10 (2015) (cit. on p. 65).

[144] X. Liu, H. Fan, J. Shi and Q. Li, 'Origin of anomalous giant dielectric performance in novel perovskite: $Bi_{0.5}$-xLaxNa$_{0.5}$-xLixTi$_1$-yMyO$_3$ (M = Mg^{2+}, Ga^{3+})', Sci Rep **5**, `10.1038/srep12699` (2015) (cit. on p. 65).

[145] X. Liu, M. Zhu, Z. Chen, B. Fang, J. Ding, X. Zhao, H. Xu and H. Luo, 'Structure and electrical properties of Li-doped $BaTiO_3$–$CaTiO_3$–$BaZrO_3$ lead-free ceramics prepared by citrate method', Journal of Alloys and Compounds **613**, 219–225 (2014) (cit. on p. 65).

[146] W. Li, Z. Man, J. Zeng, L. Zheng, G. Li and A. Kassiba, 'Relationship of Giant Dielectric Constant and Ion Migration in $CH_3NH_3PbI_3$ Single Crystal Using Dielectric Spectroscopy', J. Phys. Chem. C **124**, 13348–13355 (2020) (cit. on p. 65).

[147] J. Frischeisen, D. Yokoyama, A. Endo, C. Adachi and W. Brütting, 'Increased light outcoupling efficiency in dye-doped small molecule organic light-emitting diodes with horizontally oriented emitters', Organic Electronics **12**, 809–817 (2011) (cit. on p. 68).

[148] T. D. Schmidt, T. Lampe, D. S. M. R., P. I. Djurovich, M. E. Thompson and W. Brütting, 'Emitter Orientation as a Key Parameter in Organic Light-Emitting Diodes', Phys. Rev. Applied **8**, `10.1103/physrevapplied.8.037001` (2017) (cit. on p. 70).

[149] J. Jagielski, S. F. Solari, L. Jordan, D. Scullion, B. Blülle, Y.-T. Li, F. Krumeich, Y.-C. Chiu, B. Ruhstaller, E. J. G. Santos and C.-J. Shih, 'Scalable photonic sources using two-dimensional lead halide perovskite superlattices', Nat Commun **11**, `10.1038/s41467-019-14084-3` (2020) (cit. on p. 70).

[150] M. J. Jurow, T. Lampe, E. Penzo, J. Kang, M. A. Koc, T. Zechel, Z. Nett, M. Brady, L.-W. Wang, A. P. Alivisatos, S. Cabrini, W. Brütting and Y. Liu, 'Tunable Anisotropic Photon Emission from Self-Organized $CsPbBr_3$ Perovskite Nanocrystals', Nano Lett. **17**, 4534–4540 (2017) (cit. on p. 71).

[151] G. F. Samu, R. A. Scheidt, P. V. Kamat and C. Janáky, 'Electrochemistry and Spectroelectrochemistry of Lead Halide Perovskite Films: Materials Science Aspects and Boundary Conditions', Chem. Mater. **30**, 561–569 (2017) (cit. on p. 72).

[152] J. T. Mulder, I. du Fossé, M. A. Jazi, L. Manna and A. J. Houtepen, 'Electrochemical p-Doping of $CsPbBr_3$ Perovskite Nanocrystals', ACS Energy Lett. **6**, 2519–2525 (2021) (cit. on p. 72).

[153] R. A. Scheidt, C. Atwell and P. V. Kamat, 'Tracking Transformative Transitions: From $CsPbBr_3$ Nanocrystals to Bulk Perovskite Films', ACS Materials Lett. Materials Letters **1**, 8–13 (2019) (cit. on p. 75).

[154] W. Wu, M. Fang, L. Chao, L. Tao, H. Lu, B. Li, X. Ran, P. Li, Y. Xia, H. Zhang and Y. Chen, 'In situ nanocrystal seeding perovskite crystallization toward high-performance solar cells', Materials Today Energy **22**, 100855 (2021) (cit. on p. 75).

[155] F. Zhou, Z. Li, H. Chen, Q. Wang, L. Ding and Z. Jin, 'Application of perovskite nanocrystals (NCs)/quantum dots (QDs) in solar cells', Nano Energy **73**, 104757 (2020) (cit. on p. 75).

[156] D. Yang, B. Zhao, T. Yang, R. Lai, D. Lan, R. H. Friend and D. Di, 'Toward Stable and Efficient Perovskite Light-Emitting Diodes', Adv Funct Materials **32**, 2109495 (2021) (cit. on p. 75).

[157] J. D. Roo, M. Ibáñez, P. Geiregat, G. Nedelcu, W. Walravens, J. Maes, J. C. Martins, I. V. Driessche, M. V. Kovalenko and Z. Hens, 'Highly Dynamic Ligand Binding and Light Absorption Coefficient of Cesium Lead Bromide Perovskite Nanocrystals', ACS Nano Nano **10**, 2071–2081 (2016) (cit. on p. 76).

[158] J. Li, L. Xu, T. Wang, J. Song, J. Chen, J. Xue, Y. Dong, B. Cai, Q. Shan, B. Han and H. Zeng, '50-Fold EQE Improvement up to 6.27% of Solution-Processed All-Inorganic Perovskite $CsPbBr_3$QLEDs via Surface Ligand Density Control', Adv. Mater. **29**, 1603885 (2016) (cit. on pp. 76–78).

[159] C. Zou, Y. Liu, D. S. Ginger and L. Y. Lin, 'Suppressing Efficiency Roll-Off at High Current Densities for Ultra-Bright Green Perovskite Light-Emitting Diodes', ACS Nano Nano **14**, 6076–6086 (2020) (cit. on p. 77).

[160] A. Fakharuddin, M. K. Gangishetty, M. Abdi-Jalebi, S.-H. Chin, A. R. bin Mohd Yusoff, D. N. Congreve, W. Tress, F. Deschler, M. Vasilopoulou and H. J. Bolink, 'Perovskite light-emitting diodes', Nat Electron **5**, 203–216 (2022) (cit. on p. 77).

[161] S. M. Grimes, S. R. Johnston and D. N. Batchelder, 'Lead carbonate–phosphate system: solid–dilute solution exchange reactions in aqueous systems', Analyst **120**, 2741–2746 (1995) (cit. on p. 77).

[162] W.-k. Koh, S. Park and Y. Ham, 'Phosphonic Acid Stabilized Colloidal $CsPbX_3$(X=Br, I) Perovskite Nanocrystals and Their Surface Chemistry', ChemistrySelect **1**, 3479–3482 (2016) (cit. on p. 77).

[163] F. Krieg, S. T. Ochsenbein, S. Yakunin, S. ten Brinck, P. Aellen, A. Süess, B. Clerc, D. Guggisberg, O. Nazarenko, Y. Shynkarenko, S. Kumar, C.-J. Shih, I. Infante and M. V. Kovalenko, 'Colloidal $CsPbX_3$ (X = Cl, Br, I) Nanocrystals 2.0: Zwitterionic Capping Ligands for Improved Durability and Stability', ACS Energy Lett. Energy Letters **3**, 641–646 (2018) (cit. on pp. 78, 83).

[164] S. R. Smock, Y. Chen, A. J. Rossini and R. L. Brutchey, 'The Surface Chemistry and Structure of Colloidal Lead Halide Perovskite Nanocrystals', Acc. Chem. Res. **54**, 707–718 (2021) (cit. on p. 78).

[165] J. Ye, M. M. Byranvand, C. O. Martínez, R. L. Z. Hoye, M. Saliba and L. Polavarapu, 'Defect Passivation in Lead-Halide Perovskite Nanocrystals and Thin Films: Toward Efficient LEDs and Solar Cells', Angew Chem Int Ed **60**, 21636–21660 (2021) (cit. on p. 78).

[166] A. Pan, B. He, X. Fan, Z. Liu, J. J. Urban, A. P. Alivisatos, L. He and Y. Liu, 'Insight into the Ligand-Mediated Synthesis of Colloidal $CsPbBr_3$ Perovskite Nanocrystals: The Role of Organic Acid, Base, and Cesium Precursors', ACS Nano Nano **10**, 7943–7954 (2016) (cit. on p. 78).

[167] Y.-H. Kim, G.-H. Lee, Y.-T. Kim, C. Wolf, H. J. Yun, W. Kwon, C. G. Park and T.-W. Lee, 'High efficiency perovskite light-emitting diodes of ligand-engineered colloidal formamidinium lead bromide nanoparticles', Nano Energy **38**, 51–58 (2017) (cit. on p. 78).

[168] J. H. Park, A.-y. Lee, J. C. Yu, Y. S. Nam, Y. Choi, J. Park and M. H. Song, 'Surface Ligand Engineering for Efficient Perovskite Nanocrystal-Based Light-Emitting Diodes', ACS Appl. Mater. Interfaces **11**, 8428–8435 (2019) (cit. on p. 78).

[169] D. Jia, J. Chen, M. Yu, J. Liu, E. M. J. Johansson, A. Hagfeldt and X. Zhang, 'Dual Passivation of $CsPbI_3$ Perovskite Nanocrystals with Amino Acid Ligands for Efficient Quantum Dot Solar Cells', Small **16**, 2001772 (2020) (cit. on p. 79).

[170] J. He, H. Liu, Y. Dai, X. Ou, J. Wang, S. Tao, X. Zhang, P. Wang and D. Ma, 'Nonconjugated Carbazoles: A Series of Novel Host Materials for Highly Efficient Blue Electrophosphorescent OLEDs', J. Phys. Chem. C **113**, 6761–6767 (2009) (cit. on p. 79).

[171] Y. Lin, Y. Firdaus, F. H. Isikgor, M. I. Nugraha, E. Yengel, G. T. Harrison, R. Hallani, A. El-Labban, H. Faber, C. Ma, X. Zheng, A. Subbiah, C. T. Howells, O. M. Bakr, I. McCulloch, S. D. Wolf, L. Tsetseris and T. D. Anthopoulos, 'Self-Assembled Monolayer Enables Hole Transport Layer-Free Organic Solar Cells with 18% Efficiency and Improved Operational Stability', ACS Energy Lett. Energy Letters **5**, 2935–2944 (2020) (cit. on p. 79).

[172] W. Cho, Y. Kim, C. Lee, J. Park, Y.-S. Gal, J. W. Lee and S.-H. Jin, 'Single emissive layer white phosphorescent organic light-emitting diodes based on solution-processed iridium complexes', Dyes and Pigments **108**, 115–120 (2014) (cit. on p. 79).

[173] T. Hatakeyama, K. Shiren, K. Nakajima, S. Nomura, S. Nakatsuka, K. Kinoshita, J. Ni, Y. Ono and T. Ikuta, 'Ultrapure Blue Thermally Activated Delayed Fluorescence Molecules: Efficient HOMO-LUMO Separation by the Multiple Resonance Effect', Adv. Mater. **28**, 2777–2781 (2016) (cit. on p. 79).

[174] W. Wang, Z. Wu, T. Ye, S. Ding, K. Wang, Z. Peng and X. W. Sun, 'High-performance perovskite light-emitting diodes based on double hole transport layers', J. Mater. Chem. C **9**, 2115–2122 (2021) (cit. on p. 79).

[175] Y. Lu, Z. Wang, J. Chen, Y. Peng, X. Tang, Z. Liang, F. Qi and W. Chen, 'Tuning hole transport layers and optimizing perovskite films thickness for high efficiency $CsPbBr_3$ nanocrystals electroluminescence light-emitting diodes', Journal of Luminescence **234**, 117952 (2021) (cit. on p. 79).

[176] T. Förster, 'Zwischenmolekulare Energiewanderung und Fluoreszenz', Ann. Phys. **437**, 55–75 (1948) (cit. on pp. 81, 82).

[177] G. E. Johnson, 'Emission properties of vinylcarbazole polymers', The Journal of Chemical Physics **62**, 4697–4709 (1975) (cit. on p. 81).

[178] S. M. Bonesi, M. Mesaros, F. M. Cabrerizo, M. A. Ponce, G. M. Bilmes and R. Erra-Balsells, 'The photophysics of nitrocarbazoles used as UV-MALDI matrices: Comparative spectroscopic and optoacoustic studies of mononitro- and dinitrocarbazoles', Chemical Physics Letters **446**, 49–55 (2007) (cit. on p. 81).

[179] A. Ramar and R. Saraswathi, 'Synthesis and characterization of a charm-bracelet-type poly(N-vinylcarbazole)-C60 double-cable polymer', J Mater Sci **50**, 3740–3749 (2015) (cit. on p. 82).

[180] S. A. Bagnich, A. Rudnick, P. Schroegel, P. Strohriegl and A. Köhler, 'Triplet energies and excimer formation in meta and para linked carbazolebiphenyl matrix materials', Phil. Trans. R. Soc. A. **373**, 20140446 (2015) (cit. on p. 82).

[181] N. Bohr, 'Üer die Anwendung der Quantentheorie auf den Atombau', Z. Physik **13**, 117–165 (1923) (cit. on p. 85).

[182] P. J. Mohr, B. N. Taylor and D. B. Newell, 'CODATA Recommended Values of the Fundamental Physical Constants: 2010', Journal of Physical and Chemical Reference Data **41**, 043109 (2012) (cit. on p. 85).

[183] L. Brus, 'Electronic wave functions in semiconductor clusters: experiment and theory', J. Phys. Chem. **90**, 2555–2560 (1986) (cit. on p. 85).

[184] D. F. S. David J. Griffiths, *Introduction to Quantum Mechanics*, Third (Cambridge University Press, 2018) (cit. on p. 85).

[185] R. G. Niemann, A. G. Kontos, D. Palles, E. I. Kamitsos, A. Kaltzoglou, F. Brivio, P. Falaras and P. J. Cameron, 'Halogen Effects on Ordering and Bonding of $CH_3NH_3^+$ in $CH_3NH_3PbX_3$ (X = Cl, Br, I) Hybrid Perovskites: A Vibrational Spectroscopic Study', J. Phys. Chem. C **120**, 2509–2519 (2016) (cit. on p. 85).

[186] D. B. Straus and R. J. Cava, 'Tuning the Band Gap in the Halide Perovskite $CsPbBr_3$ through Sr Substitution', ACS Appl. Mater. Interfaces **14**, 34884–34890 (2022) (cit. on p. 85).

[187] R. W. Keyes, 'Correlation between Mobility and Effective Mass in Semiconductors', Journal of Applied Physics **30**, 454–454 (1959) (cit. on p. 87).

[188] C. Kittel, *Introduction to Solid State Physics*, 8th ed (Wiley, 2005) (cit. on p. 87).

[189] Y. Noguchi, K. Ninomiya and K. Sato, 'Charge-Carrier Dynamics and Exciton-Polaron Quenching Studied Using Simultaneous Observations of Displacement Current and Photoluminescence Intensity', J. Phys. Chem. C **126**, 18520–18527 (2022) (cit. on pp. 91, 97, 99).

[190] X. Wei, Y. Liu, T. Hu, Z. Li, J. Liu, R. Wang, H. Gao, X. Hu, G. Liu, P. Wang, C.-s. Lee and Y. Wang, 'Design of Efficient Exciplex Emitters by Decreasing the Energy Gap Between the Local Excited Triplet (3LE) State of the Acceptor and the Charge Transfer (CT) States of the Exciplex', Front. Chem. **7**, `10.3389/fchem.2019.00188` (2019) (cit. on pp. 92, 110).

[191] N. Ueno, Y. Kobayashi, T. Sekiguchi, H. Ikeura, K. Sugita, K. Honma, K. Tanaka, E. Ortí and R. Viruela, 'Valence bands of poly(methylmethacrylate) and photoion emission in vacuum ultraviolet region', Journal of Applied Physics **72**, 5423–5428 (1992) (cit. on p. 92).

[192] P. K. Sarkar, S. Bhattacharjee, M. Prajapat and A. Roy, 'Incorporation of SnO_2 nanoparticles in PMMA for performance enhancement of a transparent organic resistive memory device', RSC Adv. Advances **5**, 105661–105667 (2015) (cit. on p. 92).

[193] G. C. I. P. C. Ltd., *Techincal Datasheet Polymethylmethacrylat (PMMA), Gilbert Curry Industrial Plastics Co Ltd.* (2023) `https://www.theplasticshop.co.uk/plastic_technical_data_sheets/perspex_technical_properties_data_sheet.pdf` (cit. on p. 91).

[194] I. B. L. Ltd., *Techincal Datasheet Polymethylmethacrylat (PMMA), Iron Boar Labs Ltd.* (2023) `https://www.makeitfrom.com/material-properties/Polymethylmethacrylate-PMMA-Acrylic` (cit. on p. 91).

[195] K. Osada, K. Goushi, H. Kaji, C. Adachi, H. Ishii and Y. Noguchi, 'Observation of spontaneous orientation polarization in evaporated films of organic light-emitting diode materials', Organic Electronics **58**, 313–317 (2018) (cit. on p. 92).

[196] K. GmbH, *Techincal Datasheet Polymethylmethacrylat (PMMA), Kern GmbH*, (2023) `https://www.kern.de/cgi-bin/riweta.cgi?lng=1&nr=2610` (cit. on p. 93).

[197] Y.-S. Park, S. Lee, K.-H. Kim, S.-Y. Kim, J.-H. Lee and J.-J. Kim, 'Exciplex-Forming Co-host for Organic Light-Emitting Diodes with Ultimate Efficiency', Adv. Funct. Mater. **23**, 4914–4920 (2013) (cit. on p. 93).

[198] S. Lee, D. Limbach, K.-H. Kim, S.-J. Yoo, Y.-S. Park and J.-J. Kim, 'High efficiency and non-color-changing orange organic light emitting diodes with red and green emitting layers', Organic Electronics **14**, 1856–1860 (2013) (cit. on p. 93).

[199] P. I. Djurovich, E. I. Mayo, S. R. Forrest and M. E. Thompson, 'Measurement of the lowest unoccupied molecular orbital energies of molecular organic semiconductors', Organic Electronics **10**, 515–520 (2009) (cit. on p. 98).

[200] J. Sworakowski, 'How accurate are energies of HOMO and LUMO levels in small-molecule organic semiconductors determined from cyclic voltammetry or optical spectroscopy?', Synthetic Metals **235**, 125–130 (2018) (cit. on p. 98).

[201] V. K. Ravi, B. Mondal, V. V. Nawale and A. Nag, 'Don't Let the Lead Out: New Material Chemistry Approaches for Sustainable Lead Halide Perovskite Solar Cells', ACS Omega **5**, 29631–29641 (2020) (cit. on p. 103).

[202] T. Paul, S. Maiti, B. K. Chatterjee, P. Bairi, B. K. Das, S. Thakur and K. K. Chattopadhyay, 'Electrochemical Performance of 3D Network $CsPbBr_3$ Perovskite Anodes for Li-Ion Batteries: Experimental Venture with Theoretical Expedition', J. Phys. Chem. C **125**, 16892–16902 (2021) (cit. on p. 103).

[203] W.-B. Wu, Y.-C. Wong, Z.-K. Tan and J. Wu, ‘Photo-induced thiol coupling and C–H activation using nanocrystalline lead-halide perovskite catalysts’, Catal. Sci. Technol. **8**, 4257–4263 (2018) (cit. on p. 103).

[204] C. Tang, C. Chen, W. Xu and L. Xu, ‘Design of doped cesium lead halide perovskite as a photo-catalytic CO_2 reduction catalyst’, J. Mater. Chem. A **7**, 6911–6919 (2019) (cit. on p. 103).

[205] J. Hasnidawani, H. Azlina, H. Norita, N. Bonnia, S. Ratim and E. Ali, ‘Synthesis of ZnO Nanostructures Using Sol-Gel Method’, Procedia Chemistry **19**, 211–216 (2016) (cit. on p. 105).

[206] J. Maes, L. Balcaen, E. Drijvers, Q. Zhao, J. D. Roo, A. Vantomme, F. Vanhaecke, P. Geiregat and Z. Hens, ‘Light Absorption Coefficient of CsPbBr3 Perovskite Nanocrystals’, The Journal of Physical Chemistry Letters **9**, 3093–3097 (2018) (cit. on p. 106).

[207] S. Leyre, E. Coutino-Gonzalez, J. J. Joos, J. Ryckaert, Y. Meuret, D. Poelman, P. F. Smet, G. Durinck, J. Hofkens, G. Deconinck and P. Hanselaer, ‘Absolute Determination of Photoluminescence Quantum Efficiency using an Integrating Sphere Setup’, Review of Scientific Instruments **85**, 123115 (2014) (cit. on p. 107).

[208] N. B. Kotadiya, H. Lu, A. Mondal, Y. Ie, D. Andrienko, P. W. M. Blom and G.-J. A. H. Wetzelaer, ‘Universal strategy for Ohmic hole injection into organic semiconductors with high ionization energies’, Nature Mater **17**, 329–334 (2018) (cit. on pp. 109, 110).

[209] Q. Zhang, J. Li, K. Shizu, S. Huang, S. Hirata, H. Miyazaki and C. Adachi, ‘Design of Efficient Thermally Activated Delayed Fluorescence Materials for Pure Blue Organic Light Emitting Diodes’, J. Am. Chem. Soc. **134**, 14706–14709 (2012) (cit. on pp. 109, 110).

Software References

The referenced respective raw data and images used in this work are provided alongside this text. Please note that they are also published under the same license as this text, if not stated otherwise.

[S.1] *Rendered illustation of the $CsPbBr_3$ structure*, (2023) `src/img/CsPbBr3_struc.svg` (cit. on p. 10).

[S.2] *Rendered illustation of the $MAPbI_3$ structure*, (2023) `src/img/MaPbI3_struc.svg` (cit. on p. 10).

[S.3] *Rendered illustation of the $CsPbBr_3$ vials depending on halide content*, (2023) `src/img/solutions.svg` (cit. on p. 11).

[S.4] *Sketch for comparing the perovskite with other semiconductors concerning oscillator strength*, (2023) `src/img/ocillator_strength2.svg` (cit. on p. 11).

[S.5] *Figure for density of states investigation on $CsPbI_3$*, (2019) `src/img/CC_BY_4/DOS_of_CsPbI3_Tao_2019_upscaled.png` (cit. on p. 12).

[S.6] *Figure for investigation on dark and bright states in perovskites, Copyright 2023 by Springer Nature, license number 5544220541863*, (2018) `src/img/licensed/Becker_2018_Fig1_upscaled.png` (cit. on p. 16).

[S.7] *Python code for the calculation on the energy-gap of $CsPbBr_3$ NCs*, (2023) `src/data/DCzGPC_WD/CsPbBr3_QC_calc.ipynb` (cit. on pp. 15, 86).

[S.8] *Rendered illustation of the $CsPbBr_3$ surface paritally passivated*, (2023) `src/img/Ligands_attachment.svg` (cit. on p. 18).

[S.9] *Rendered illustation of the $CsPbBr_3$ full nanoparticle*, (2023) `src/img/CsPbBr3_NC_capped.png` (cit. on p. 20).

[S.10] *Sketch for an intuitive understanding of the unit smol*, (2023) `src/img/smol_sketch.svg` (cit. on p. 20).

[S.11] *Vectorgraphics of a suboptimal PeLED stack featuring TFB-TPBi*, (2023) `src/img/lhpnc-stack_ann_suboptimal.svg` (cit. on p. 26).

[S.12] *Vectorgraphics of an optimised PeLED stack featuring PVK-B3PYMPM*, (2023) `src/img/lhpnc-stack_ann.svg` (cit. on p. 26).

[S.13] *Vectorgraphics of the 4pi setup to measure the PLQY*, (2023) `src/img/PLQY.svg` (cit. on p. 31).

[S.14] *Vectorgraphics of the 2pi setup to measure the external PLQY or EQE*, (2023) `src/img/EQE.svg` (cit. on p. 31).

[S.15] *Vectorgraphics of the band alignment at a metal-semiconductor interface*, (2023) `src/img/depletion.svg` (cit. on p. 37).

[S.16] *Vectorgraphics of the DCM simulation plot*, (2023) `src/plot/DCM_plot/data_theo.pdf` (cit. on p. 39).

[S.17] *Python/matplotlib code for the DCM simulation plot*, (2023) `src/data/DCM_WD/Cap_Calc.ipynb` (cit. on p. 39).

[S.18] *Vectorgraphics of a conceptual LCD screen*, (2023) `src/img/lcd_concept.svg` (cit. on p. 44).

[S.19] *Vectorgraphics of a conceptual DC screen*, (2023) `src/img/dc_concept.svg` (cit. on p. 44).

[S.20] *Root Simulation file of the TOASTER Simulation of the bare down-converter device*, (2023) `src/data/DC_WD/TOASTER_SIM/mcbp_Downconvert_no_perov/BOOST.txt` (cit. on p. 46).

[S.21] *Root Simulation file of the TOASTER Simulation of the down-converter device with outcoupling layer*, (2023) `src/data/DC_WD/TOASTER_SIM/mcbp_Downconvert/BOOST.txt` (cit. on p. 46).

[S.22] *Python/matplotlib code for the spectra of down-converters*, (2023) `src/data/DC_WD/SpectraPlot.ipynb` (cit. on pp. 46, 48, 109, 110).

S.23 *Chemfig code for the P2VP polymer*, (2023) `src/chemfig/P2VP.chemfig` (cit. on p. 46).

S.24 *Vectorgraphics of power-dependent PLQY plot of down-converters*, (2023) `src/plot/DC_plot/plqy/DC_powerdep.pdf` (cit. on p. 46).

S.25 *Python/matplotlib code for the power-dependent PLQY of down-converters*, (2023) `src/data/DC_WD/PLQECalc_power_dep.ipynb` (cit. on pp. 46, 50).

S.26 *Vectorgraphics of a rendered schematic DC LED*, (2023) `src/img/SimplifiedStack.svg` (cit. on p. 48).

S.27 *Vectorgraphics of the spectra of down-converters*, (2023) `src/plot/DC_plot/pled/Spectrum.pdf` (cit. on p. 48).

S.28 *Photo of the bare pump LED for down-converters*, (2023) `src/plot/DC_plot/Cz-PS_cropped.png` (cit. on p. 48).

S.29 *Photo of the down-converters LED*, (2023) `src/plot/DC_plot/Micelles_cropped.png` (cit. on p. 48).

S.30 *Vectorgraphics of the jvl plot of down-converters*, (2023) `src/plot/DC_plot/pled/LXIV_CZ-PS-Downconverter_DC_OLED_CurrentDensity_and_Luminance.pdf` (cit. on p. 48).

S.31 *Vectorgraphics of the j–EQE plot of down-converters*, (2023) `src/plot/DC_plot/pled/LXIV_CZ-PS-Downconverter_DC_OLED_EQEvsCurrentDensity.pdf` (cit. on p. 48).

S.32 *Python/matplotlib code for the j–V–L plots of down-converters*, (2023) `src/data/DC_WD/OLEDPlot.ipynb` (cit. on pp. 48, 110).

S.33 *Chemfig code for the LiTFSI molecule*, (2023) `src/chemfig/LiTFSI.chemfig` (cit. on p. 51).

S.34 *Vectorgraphics of the situation at the valence injection region between metal and perovskite*, (2023) `src/img/p_doping_motivation.svg` (cit. on p. 51).

S.35 *Vectorgraphics of the substrate dependent PLQY plot*, (2023) `src/plot/litfsi_plot/plqy/underground.pdf` (cit. on p. 53).

S.36 *Vectorgraphics of the doping concentration dependent PLQY plot*, (2023) `src/plot/litfsi_plot/plqy/plqys_li_only_sol.pdf` (cit. on p. 53).

S.37 *Python/matplotlib code for the plqy of LiTFSI doped samples*, (2023) `src/data/LiTFSI_WD/PLQYPlot.ipynb` (cit. on pp. 53, 70).

S.38 *Vectorgraphics of the doping concentration dependent lifetimes of thin-films*, (2023) `src/plot/litfsi_plot/lt_film/enc_film_comp_with_ann.pdf` (cit. on p. 53).

S.39 *Vectorgraphics of the doping concentration dependent lifetimes of solutions*, (2023) `src/plot/litfsi_plot/lt_sol/sol_comp_with_ann.pdf` (cit. on p. 53).

S.40 *Python/matplotlib code for the lifetime plot of LiTFSI doped thin-films*, (2023) `src/data/LiTFSI_WD/LifetimePlot.ipynb` (cit. on pp. 53, 111, 112).

S.41 *Python/matplotlib code for the lifetime plot of LiTFSI doped solutions*, (2023) `src/data/LiTFSI_WD/LifetimePlot-Solution.ipynb` (cit. on pp. 53, 113, 114).

S.42 *Vectorgraphics of the spectra of LiTFSI doped green PNC thin-films*, (2023) `src/plot/litfsi_plot/spectra/spectrum_film.pdf` (cit. on p. 56).

S.43 *Vectorgraphics of the spectra of LiTFSI doped green PNC solutions*, (2023) `src/plot/litfsi_plot/spectra/spectrum_solution.pdf` (cit. on p. 56).

S.44 *Python/matplotlib code for the spectra of LiTFSI doped samples*, (2023) `src/data/LiTFSI_WD/SpectraPlot.ipynb` (cit. on pp. 56, 67, 74).

S.45 *SEM image of undoped green PNCs*, (2023) `src/plot/litfsi_plot/sem/native.png` (cit. on p. 58).

S.46 *SEM image of LiTFSI doped green PNCs*, (2023) `src/plot/litfsi_plot/sem/LiTFSI_1wt.png` (cit. on p. 58).

S.47 *Vectorgraphics of the XRD plot of LiTFSI doped green PNCs*, (2023) `src/plot/litfsi_plot/xrd/XRDofThinFilmsfilteredwithannotation.pdf` (cit. on p. 58).

S.48 *Python/matplotlib code for the XRD plots of LiTFSI doped PNCs on PVK on silicon*, (2023) `src/data/LiTFSI_WD/XRD_Plot.ipynb` (cit. on p. 58).

S.49 *SEM image of highly LiTFSI doped green PNCs*, (2023) `src/plot/litfsi_plot/sem/LiTFSI_27wt.png` (cit. on p. 58).

S.50 *Vectorgraphics of the UPS spectra of LiTFSI doped green PNC thin-films*, (2023) `src/plot/litfsi_plot/ups/UPS.pdf` (cit. on p. 59).

S.51 *Vectorgraphics of the illustration plot for the ups samples*, (2023) `src/plot/litfsi_plot/ups/UPS_levels.pdf` (cit. on p. 59).

S.52 *Python/matplotlib code for the UPS plot of LiTFSI doped thin-films*, (2023) `src/data/LiTFSI_WD/UPS_Plot.ipynb` (cit. on p. 59).

S.53 *Vectorgraphics of the stack illustration plot for the hole-only device*, (2023) `src/plot/litfsi_plot/stack/h_only-stack.pdf` (cit. on p. 61).

S.54 *Vectorgraphics of the stack illustration plot for the electron-only device*, (2023) `src/plot/litfsi_plot/stack/h_only-stack.pdf` (cit. on p. 61).

S.55 *Python/matplotlib code for the LiTFSI devices stack illustration plot*, (2023) `src/data/LiTFSI_WD/StackPlot.ipynb` (cit. on pp. 61, 67).

S.56 *Vectorgraphics of the j–V plot of LiTFSI doped-hole only devices*, (2023) `src/plot/litfsi_plot/single_carrier/9_LiTFSI_singlecarrier_hole_cb.pdf` (cit. on p. 62).

S.57 *Vectorgraphics of the j–V plot of LiTFSI doped electron-only devices*, (2023) `src/plot/litfsi_plot/single_carrier/9_LiTFSI_singlecarrier_electron_cb.pdf` (cit. on p. 62).

S.58 *Python/matplotlib code for the j–V plot of LiTFSI doped single carrier devices*, (2023) `src/data/LiTFSI_WD/SingleCarrierPlot.ipynb` (cit. on p. 62).

S.59 *Vectorgraphics of the temperature dependent j–E inplane plots of LiTFSI-doped samples*, (2023) `src/plot/litfsi_plot/inplane/Hysteresis.pdf` (cit. on p. 63).

S.60 *Vectorgraphics of the temperature dependent j–V inplane plots of the moderately LiTFSI-doped sample*, (2023) `src/plot/litfsi_plot/inplane/6smol_Cond_vs_T.pdf` (cit. on p. 63).

S.61 *Vectorgraphics of the temperature dependent j–V inplane plots of the highly LiTFSI-doped sample*, (2023) `src/plot/litfsi_plot/inplane/15smol_Cond_vs_T.pdf` (cit. on p. 63).

S.62 *Python/matplotlib code for the j–V inplane plots of LiTFSI doped TFT samples*, (2023) `src/data/LiTFSI_WD/InPlanePlot.ipynb` (cit. on pp. 63, 116).

S.63 *Vectorgraphics of the j–V–L plot of LiTFSI doped green PNCs*, (2023) `src/plot/litfsi_plot/pled/LITFSI-comp_1wtonly_OLED_CurrentDensity_and_Luminance_withoutErrors.pdf` (cit. on p. 67).

S.64 *Vectorgraphics of the j–EQE plot of LiTFSI doped green PNCs*, (2023) `src/plot/litfsi_plot/pled/LITFSI-comp_1wtonly_OLED_EQEvsCurrentDensity_withoutErrors.pdf` (cit. on p. 67).

S.65 *Vectorgraphics of the stack illustration plot for the PLED*, (2023) `src/plot/litfsi_plot/stack/lhpnc-stack.pdf` (cit. on p. 67).

S.66 *Vectorgraphics of the EL spectrum of LiTFSI doped green PNC LEDs*, (2023) `src/plot/litfsi_plot/spectra/Spectrum_green.pdf` (cit. on p. 67).

S.67 *Python/matplotlib code for the j–V–L plots of LiTFSI doped devices*, (2023) `src/data/LiTFSI_WD/OLEDPlot.ipynb` (cit. on pp. 67, 69, 74, 116, 117).

S.68 *Vectorgraphics of the j–V–L plot of LiTFSI doped green PNCs for all doping concentrations*, (2023) `src/plot/litfsi_plot/pled/LITFSI-comp_all_OLED_CurrentDensity_and_Luminance_withoutErrors.pdf` (cit. on p. 69).

S.69 *Vectorgraphics of the j–V–L plot of LiTFSI doped green PNCs with sweepback*, (2023) `src/plot/litfsi_plot/pled/LITFSI-comp_sweepback_cb.pdf` (cit. on p. 69).

S.70 *Vectorgraphics of the doping concentration dependent PLQY and EQE plot*, (2023) `src/plot/litfsi_plot/plqy/plqys_eqes.pdf` (cit. on p. 70).

S.71 *Vectorgraphics of the p-polarised ADPL spectrum of the LiTFSI doped samples*, (2023) `src/plot/litfsi_plot/adpl/adpl_comp_smol.pdf` (cit. on p. 70).

S.72 *Python/matplotlib code for the LiTFSI doped ADPL plots*, (2023) `src/data/LiTFSI_WD/ADPL_Plot.ipynb` (cit. on pp. 70, 118).

S.73 *Vectorgraphics of the j–V–L plot of LiTFSI doped red PNCs*, (2023) `src/plot/litfsi_plot/pled/LITFSI-comp_red_OLED_CurrentDensity_and_Luminance_withoutErrors.pdf` (cit. on p. 74).

S.74 *Vectorgraphics of the EL spectrum of LiTFSI doped red PNC LEDs*, (2023) `src/plot/litfsi_plot/spectra/Spectrum_red.pdf` (cit. on p. 74).

S.75 *Vectorgraphics of the EL spectrum of LiTFSI doped blue PNC LEDs*, (2023) `src/plot/litfsi_plot/spectra/Spectrum_blue.pdf` (cit. on p. 74).

S.76 *Vectorgraphics of the j–V–L plot of LiTFSI doped blue PNCs*, (2023) `src/plot/litfsi_plot/pled/LITFSI-comp_CKP30_OLED_CurrentDensity_and_Luminance_withoutErrors.pdf` (cit. on p. 74).

S.77 *Vectorgraphics of the sketch illustrating the ligand washing procedure*, (2023) `src/img/washing_concept.svg` (cit. on p. 76).

S.78 *Chemfig code for oleic acid*, (2023) `src/chemfig/OleicAcid.chemfig` (cit. on p. 76).

S.79 *Chemfig code for oleylamine*, (2023) `src/chemfig/Oleamine.chemfig` (cit. on p. 76).

S.80 *Vectorgraphics of the j–V–L plot of washed and lecithin treated perovskite devices*, (2023) `src/plot/dczgpc_plot/pled/DCzGPC-comp_nat_vs_washed_lecithin_OLED_CurrentDensity_and_Luminance_withoutErrors.pdf` (cit. on p. 77).

S.81 *Vectorgraphics of the j–V–L plot of washed and lecithin treated perovskite devices*, (2023) `src/plot/dczgpc_plot/pled/DCzGPC-comp_nat_vs_washed_lecithin_OLED_EQEvsLuminance_withoutErrors.pgf` (cit. on p. 77).

S.82 *Python/matplotlib code for the j–V–L plots of ligand engineered devices*, (2023) `src/data/DCzGPC_WD/OLEDPlot.ipynb` (cit. on pp. 77, 88).

S.83 *Chemfig code for dioleyl lecithin*, (2023) `src/chemfig/Lecithin.chemfig` (cit. on p. 79).

S.84 *Chemfig code for DCzGPC*, (2023) `src/chemfig/DCzGPC.chemfig` (cit. on p. 79).

S.85 *Vectorgraphics of the PL lifetime of DCzGPC specimen*, (2023) `src/plot/dczgpc_plot/streak_plot/TRPLLifetimeofDCzGPC.pdf` (cit. on p. 80).

S.86 *Vectorgraphics of the spectra plots of DCzGPC specimen*, (2023) `src/plot/dczgpc_plot/streak_plot/PLSpectraofDCzGPC.pdf` (cit. on p. 80).

S.87 *Python/matplotlib code for the PL lifetime and spectra plots of DCzGPC specimen*, (2023) `src/data/DCzGPC_WD/StreakPlot.ipynb` (cit. on p. 80).

S.88 *Vectorgraphics of the absorption spectra of DCzGPC treated $CsPbBr_2Cl$ solutions*, (2023) `src/plot/dczgpc_plot/uvvis_plot/Absorption_Spectrum.pdf` (cit. on p. 81).

S.89 *Vectorgraphics of the fluorescence spectra of DCzGPC treated $CsPbBr_2Cl$ solutions*, (2023) `src/plot/dczgpc_plot/uvvis_plot/PL_Emission_Spectrum.pdf` (cit. on p. 81).

S.90 *Python/matplotlib code for the UV-Vis plots of DCzGPC treated perovskite devices*, (2023) `src/data/DCzGPC_WD/UVVisPlot.ipynb` (cit. on pp. 81, 119).

S.91 *Python code for the calculation on the energy-gap of $CsPbBr_2Cl$ NCs*, (2023) `src/data/DCzGPC_WD/CsPbBr2Cl_QC_calc.ipynb` (cit. on p. 86).

S.92 *Vectorgraphics of the j–V–L plot of DCzGPC treated perovskite devices*, (2023) `src/plot/dczgpc_plot/pled/DCzGPC-comp_DCzGPC_OLED_CurrentDensity_and_Luminance_withoutErrors.pdf` (cit. on p. 88).

S.93 *Vectorgraphics of the j–V–L plot of DCzGPC treated perovskite devices*, (2023) `src/plot/dczgpc_plot/pled/DCzGPC-comp_DCzGPC_OLED_EQEvsLuminance_withoutErrors.pdf` (cit. on p. 88).

S.94 *Vectorgraphics of the EL spectra of DCzGPC treated perovskite devices*, (2023) `src/plot/dczgpc_plot/spectra/DCzGPC_EL_spectrum.pdf` (cit. on p. 88).

S.95 *Photo of the 26 wt.% DCzGPC treated PeLED*, (2023) `src/plot/dczgpc_plot/85pctSmol_at_8V_cropped.jpeg` (cit. on p. 88).

S.96 *Python/matplotlib code for the spectra of DCzGPC treated samples*, (2023) `src/data/DCzGPC_WD/SpectraPlot.ipynb` (cit. on p. 88).

S.97 *Vectorgraphics of the peak position of perovskite samples depending on DCzGPC treatment*, (2023) `src/plot/dczgpc_plot/spectra/linshift_PL_vs_EL.pdf` (cit. on p. 88).

S.98 *Vectorgraphics of the EL operational lifetime plot of DCzGPC treated perovskite LEDs*, (2023) `src/plot/dczgpc_plot/lt_plot/LifetimesofCKP.pdf` (cit. on p. 90).

S.99 *Vectorgraphics of the Conductivity depending on operational time of DCzGPC treated perovskite LEDs*, (2023) `src/plot/dczgpc_plot/lt_plot/LifetimesofCKP.pdf` (cit. on p. 90).

S.100 *Python/matplotlib code for the EL operational lifetime plot of DCzGPC treated perovskite LEDs*, (2023) `src/data/LiTFSI_WD/LifetimePlot.ipynb` (cit. on p. 90).

S.101 *Vectorgraphics of the DCM stack of the all-organic hole only MIS device*, (2023) `src/plot/dcm_plot/stack/dcm-h-neat-stack.pdf` (cit. on p. 92).

S.102 *Vectorgraphics of the DCM stack of the all-organic electron only MIS device*, (2023) `src/plot/dcm_plot/stack/dcm-e-neat-stack.pdf` (cit. on p. 92).

S.103 *Vectorgraphics of the DCM stack of the perovskite-organic hole only MIS device*, (2023) `src/plot/dcm_plot/stack/dcm-h-stack.pdf` (cit. on p. 92).

S.104 *Vectorgraphics of the DCM stack of the perovskite-organic electron only MIS device*, (2023) `src/plot/dcm_plot/stack/dcm-e-stack.pdf` (cit. on p. 92).

S.105 *Python/matplotlib code for the DCM stack illustrations.* (2023) `src/data/DCM_WD/StackPlot.ipynb` (cit. on p. 92).

S.106 *Vectorgraphics of the DCM on all-organic MIS devices*, (2023) `src/plot/dcm_plot/neat_only/neat.pdf` (cit. on p. 93).

S.107 *Python/matplotlib code for the DCM on all-organic MIS devices*, (2023) `src/data/DCM_WD/neat_DCM.ipynb` (cit. on p. 93).

S.108 *Vectorgraphics of the the DCM on native perovskite MIS devices*, (2023) `src/plot/dcm_plot/native_only/nativewashed.pdf` (cit. on p. 94).

S.109 *Python/matplotlib code for the DCM on native perovskite MIS devices*, (2023) `src/data/DCM_WD/native_DCM.ipynb` (cit. on pp. 94, 119).

S.110 *Vectorgraphics of the the DCM on lecithin treated perovskite MIS devices*, (2023) `src/plot/dcm_plot/lecithin_only/lecithinillumin.pdf` (cit. on p. 97).

S.111 *Python/matplotlib code for the DCM on lecithin treated perovskite MIS devices*, (2023) `src/data/DCM_WD/lecithin_DCM.ipynb` (cit. on p. 97).

S.112 *Vectorgraphics of the the DCM on LiTFSI treated perovskite MIS devices*, (2023) `src/plot/dcm_plot/LiTFSI_only/5wtLiTFSI.pdf` (cit. on p. 99).

S.113 *Python/matplotlib code for the DCM on LiTFSI treated perovskite MIS devices*, (2023) `src/data/DCM_WD/LiTFSI_DCM.ipynb` (cit. on p. 99).

S.114 *Python/matplotlib code for the stack illustration plot of the pump OLED for the down-converters*, (2023) `src/data/DC_WD/StackPlot.ipynb` (cit. on p. 110).

S.115 *Vectorgraphics of the stack plot of the pump OLED for the down-converters*, (2023) `src/plot/DC_plot/stack/dc-stack.pdf` (cit. on p. 110).

S.116 *Vectorgraphics of the jv radiance plot of down-converters*, (2023) `src/plot/DC_plot/pled/LXIV_CZ-PS-Downconverter_DC_OLED_CurrentDensity_and_Radiance.pdf` (cit. on p. 110).

S.117 *Vectorgraphics of the the Abs/EL/PL spectra and fits of down-converters*, (2023) `src/plot/DC_plot/pled/SpectrumAbsFit.pdf` (cit. on p. 110).

S.118 *Vectorgraphics of the the EL spectra and filled energy areas of down-converters*, (2023) `src/plot/DC_plot/pled/SpectrumDCE.pdf` (cit. on p. 110).

S.119 *Vectorgraphics of lifetime plot and fit of the native thin-film*, (2023) `src/plot/litfsi_plot/lt_film/enc_film_native_442_5mgpml_1D_lifetime.pdf` (cit. on p. 111).

S.120 *Vectorgraphics of lifetime plot and fit of the 0.6 smol pct. doped thin-film*, (2023) `src/plot/litfsi_plot/lt_film/enc_film_LiTFSi_442_5mgpml_1000ppm_1D_lifetime.pdf` (cit. on p. 111).

S.121 *Vectorgraphics of lifetime plot and fit of the 6 smol pct. doped thin-film*, (2023) `src/plot/litfsi_plot/lt_film/enc_film_LiTFSi_442_5mgpml_1pct_1D_lifetime.pdf` (cit. on p. 111).

S.122 *Vectorgraphics of lifetime plot and fit of the 57 smol pct. doped thin-film*, (2023) `src/plot/litfsi_plot/lt_film/enc_film_LiTFSi_442_5mgpml_10pct_1D_lifetime.pdf` (cit. on p. 111).

S.123 *Vectorgraphics of lifetime plot and fit of the 312 smol pct. doped thin-film*, (2023) `src/plot/litfsi_plot/lt_film/enc_film_LiTFSi_442_5mgpml_50pct_1D_lifetime.pdf` (cit. on p. 112).

S.124 *Vectorgraphics of bar plot of the average decay rate for each doped thin-film*, (2023) `src/plot/litfsi_plot/lt_film/solu_LiTFSi_442_5mgpml_50pct_1D_lifetime.pdf` (cit. on p. 112).

S.125 *Vectorgraphics of bar plot of the individual decay rates for each doped thin-film*, (2023) `src/plot/litfsi_plot/lt_film/solu_LiTFSi_442_5mgpml_50pct_1D_lifetime.pdf` (cit. on p. 112).

S.126 *Vectorgraphics of bar plot of the individual decay amplitudes for each doped thin-film*, (2023) `src/plot/litfsi_plot/lt_film/solu_LiTFSi_442_5mgpml_50pct_1D_lifetime.pdf` (cit. on p. 112).

S.127 *Vectorgraphics of lifetime plot and fit of the native solution*, (2023) `src/plot/litfsi_plot/lt_film/solu_native_442_5mgpml_1D_lifetime.pdf` (cit. on p. 113).

S.128 *Vectorgraphics of lifetime plot and fit of the 0.6 smol pct. doped solution*, (2023) `src/plot/litfsi_plot/lt_film/solu_LiTFSi_442_5mgpml_1000ppm_1D_lifetime.pdf` (cit. on p. 113).

S.129 *Vectorgraphics of lifetime plot and fit of the 6 smol pct. doped solution*, (2023) `src/plot/litfsi_plot/lt_film/solu_LiTFSi_442_5mgpml_1pct_1D_lifetime.pdf` (cit. on p. 113).

S.130 *Vectorgraphics of lifetime plot and fit of the 57 smol pct. doped solution*, (2023) `src/plot/litfsi_plot/lt_film/solu_LiTFSi_442_5mgpml_10pct_1D_lifetime.pdf` (cit. on p. 113).

S.131 *Vectorgraphics of lifetime plot and fit of the 312 smol pct. doped solution*, (2023) `src/plot/litfsi_plot/lt_film/solu_LiTFSi_442_5mgpml_50pct_1D_lifetime.pdf` (cit. on p. 114).

S.132 *Vectorgraphics of bar plot of the average decay rate for each doped solution*, (2023) `src/plot/litfsi_plot/lt_film/solu_LiTFSi_442_5mgpml_50pct_1D_lifetime.pdf` (cit. on p. 114).

S.133 *Vectorgraphics of bar plot of the individual decay rates for each doped solution*, (2023) `src/plot/litfsi_plot/lt_film/solu_LiTFSi_442_5mgpml_50pct_1D_lifetime.pdf` (cit. on p. 114).

S.134 *Vectorgraphics of bar plot of the individual decay amplitudes for each doped solution*, (2023) `src/plot/litfsi_plot/lt_film/solu_LiTFSi_442_5mgpml_50pct_1D_lifetime.pdf` (cit. on p. 114).

S.135 *Vectorgraphics of the XPS plot of the caesium region of LiTFSI doped green PNCs*, (2023) `src/plot/litfsi_plot/xps/xps_Cs.pdf` (cit. on p. 115).

S.136 *Vectorgraphics of the XPS plot of the lead region of LiTFSI doped green PNCs*, (2023) `src/plot/litfsi_plot/xps/xps_Pb.pdf` (cit. on p. 115).

S.137 *Vectorgraphics of the XPS plot of the bromine region of LiTFSI doped green PNCs*, (2023) `src/plot/litfsi_plot/xps/xps_br.pdf` (cit. on p. 115).

S.138 *Vectorgraphics of the XPS plot of the fluorine region of LiTFSI doped green PNCs*, (2023) `src/plot/litfsi_plot/xps/xps_f.pdf` (cit. on p. 115).

S.139 *Python/matplotlib code for the XPS plots of LiTFSI doped PNCs on PVK*, (2023) `src/data/LiTFSI_WD/XPS_Plot.ipynb` (cit. on p. 115).

S.140 *Vectorgraphics of the temperature dependent j–V inplane plots and fits on the moderately LiTFSI-doped sample*, (2023) `src/plot/litfsi_plot/inplane/6smolOnsetFits.pdf` (cit. on p. 116).

S.141 *Vectorgraphics of the temperature dependent j–V inplane plots and fits on the highly LiTFSI-doped sample*, (2023) `src/plot/litfsi_plot/inplane/15smolOnsetFits.pdf` (cit. on p. 116).

S.142 *Vectorgraphics of the L–EQE plot of LiTFSI doped green PNCs*, (2023) `src/plot/litfsi_plot/pled/LITFSI-comp_all_OLED_EQEvsLuminance_withoutErrors.pdf` (cit. on p. 116).

S.143 *Vectorgraphics of the j–EQE plot of LiTFSI doped green PNCs*, (2023) `src/plot/litfsi_plot/pled/LITFSI-comp_all_OLED_EQEvsCurrentDensity_withoutErrors.pdf` (cit. on p. 116).

S.144 *Vectorgraphics of the j–EQE plot of LiTFSI doped red PNCs*, (2023) `src/plot/litfsi_plot/pled/LITFSI-comp_red_OLED_EQEvsCurrentDensity_withoutErrors.pdf` (cit. on p. 117).

S.145 *Vectorgraphics of the j–EQE plot of LiTFSI doped blue PNCs*, (2023) `src/plot/litfsi_plot/pled/LITFSI-comp_CKP30_OLED_EQEvsCurrentDensity_withoutErrors.pdf` (cit. on p. 117).

S.146 *Vectorgraphics of the s-polarised ADPL spectrum with a fit of the native sample*, (2023) `src/plot/litfsi_plot/adpl/adpl_native_spol.pdf` (cit. on p. 118).

S.147 *Vectorgraphics of the s-polarised ADPL spectrum with a fit of the LiTFSI doped sample*, (2023) `src/plot/litfsi_plot/adpl/adpl_LiTFSI_spol.pdf` (cit. on p. 118).

S.148 *Vectorgraphics of the p-polarised ADPL spectrum with a fit of the native sample*, (2023) `src/plot/litfsi_plot/adpl/adpl_native_ppol.pdf` (cit. on p. 118).

S.149 *Vectorgraphics of the p-polarised ADPL spectrum with a fit of the LiTFSI doped sample*, (2023) `src/plot/litfsi_plot/adpl/adpl_LiTFSI_ppol.pdf` (cit. on p. 118).

S.150 *Folder with raw and simulation files for the ADPL analysis*, (2023) `src/data/LiTFSI_WD/adpl` (cit. on p. 118).

S.151 *Vectorgraphics of the fluorescence spectra of DCzGPC treated $CsPbBr_3$ solutions*, (2023) `src/plot/dczgpc_plot/uvvis_plot/PL_Emission_Spectrum_Green.pdf` (cit. on p. 119).

S.152 *Vectorgraphics of the fluorescence peak position of $CsPbBr_3$ solutions depending on DCzGPC treatment*, (2023) `src/plot/dczgpc_plot/uvvis_plot/linshift_verif_green.pdf` (cit. on p. 119).

S.153 *Vectorgraphics of the the DCM on native perovskite MIS devices after illumination*, (2023) `src/plot/dcm_plot/native_only/nativeillum3rd.pdf` (cit. on p. 119).

D. Acknowledgements

Finally, the following individuals are mentioned for their outstanding support during the course of this research project:

- **Prof. Dr. Wolfgang Brütting** for initiating the research in the mostly undiscovered topic of perovskite nanocrystals. Furthermore the challenges of spearheading this project would not have succeeded without his in-depth discussions, analysis and network of cooperators.
- **Prof. Dr. Henning Höppe** for his effort in reviewing this thesis and previous work as the additional assessor.
- **M. Sc. Roshini Jayabalan and B. Sc. Martin Waibel** for their remarkably fruitful contributions to this work while working as students on this project. Especially the friendly, humble and honest teamwork helped in advancing quickly, leading to amazing theses of their own.
- **Dr. Thomas Morgenstern** for his mentoring during the early phase of this project. Thomas guided me towards learning the fundamentals with his preliminary work; its cooperations and results enabled the application to LEDs.
- **Prof. Dr. Marcus Scheele, M. Sc. Christopher Kirsch and Dr. Jan Wahl** for the supervision and synthesis of some of the particles and the DCzGPC. Notably, Christopher assisted with his chemical insight on multiple occasions.
- **Prof. Yutaka Noguchi** for his kind assistance and insights about the displacement currents in MIS devices.
- **Prof. Dr. Alexander Urban and Dr. Carola Lampe** for the cooperation towards colour-conversion LEDs.
- **Prof. Ph. D. Denis Andrienko, Ph. D. Mukunda Mandal** for the aid in theoretical physics considerations.
- **Prof. Dr. Alexander Weber-Bargioni and Dr. Jonas Zipfel** for the very spontaneous introduction and help at the Lawrence National Laboratory in Berkeley, California. Work at the Molecular Foundry was supported by the Office of Science, Office of Basic Energy Sciences, of the U.S. Department of Energy under Contract No. DE-AC02-05CH11231.

- **DFG Project SPP 2196 and BaCaTeC** DFG for the trust in our group and consequent funding, and its extension and the BaCaTeC for the support to the research trip to Berkeley.
- **Chair of experimental physics and organic group** for continuous organisational, moral and interdisciplinary scientific support.
- **The community behind the open-source software** for their collaborative development of software, which enabled this work to be written proudly entirely on free software: images are created with blender and inkscape; the data analysis is performed with numpy, scipy and matplotlib; the typesetting is done on a linux operating system with lualatex.
- **UV-gradez** for the usual everyday-life and saving me from starvation with food and drinks organisation.
- **The one above all** Anna-Chiara my beloved wife, who knows more about this topic than many of the mentioned above, because of her infinite patience on listening and giving highly valuable non-natural scientific input. Miau!